

# **Terahertz Field Interaction and Ultrafast Dynamics in Donor-Acceptor Systems**

Inaugural dissertation  
of the Faculty of Science,  
University of Bern

presented by

**Elnaz Zyaee**

Supervisor of the doctoral thesis:  
Prof. Dr. Thomas Feurer

Institute of Applied Physics

Bern, 2025

This work is licensed under a Creative Commons Attribution 4.0 International License (CC BY 4.0). <https://creativecommons.org/licenses/by/4.0/>



# **Terahertz Field Interaction and Ultrafast Dynamics in Donor-Acceptor Systems**

Inaugural dissertation  
of the Faculty of Science,  
University of Bern

presented by

**Elnaz Zyaee**

Supervisor of the doctoral thesis:  
Prof. Dr. Thomas Feurer

Institute of Applied Physics

Accepted by the Faculty of Science.

Bern, 11.12.2025

The Dean:  
Prof. Dr. Jean-Louis Reymond



# Abstract

Developing electronic components from small collections of molecules, or even a single molecule, is the primary goal of molecular electronics. To achieve this, donor-acceptor systems are being explored as potential molecular switches, which function by using intramolecular charge transfer. Paracyclophanes (PCPs) serve as one of the proposed systems for studying and controlling through-space charge transfer. Achieving ultrafast control over these molecular states requires a fundamental understanding of both the interaction between the control field (e.g., terahertz (THz) electric field) and the molecule, and the excited state dynamics of the target molecules. This thesis addresses these prerequisites through foundational spectroscopic investigations.

First, time-resolved THz Stark spectroscopy was employed to gain essential insights into the interaction between intense, sub-picosecond THz electric fields and donor-acceptor molecules. Studies on a donor-acceptor system in non-polar solvent successfully demonstrated the extraction of changes in dipole moment and polarizability under ambient conditions, providing crucial data on the THz-driven response mechanism. The technique's robustness was further confirmed by extending measurements to model dyes in water as a highly polar solvent.

Second, the excited state dynamics of novel PCPs were characterized using femtosecond transient absorption spectroscopy, complemented by theoretical modeling (TD-DFT/CC2). Homo-PCPs were investigated to validate the theoretical framework, confirming its capability in reproducing the experimental data. Meanwhile, investigations of hetero-PCPs revealed ultrafast charge transfer dynamics, whose characteristics could be tuned through different linkers.

Together, these results provide essential groundwork for achieving THz field manipulation of molecular states on surfaces. The time-resolved THz Stark spectroscopy experiments help to understand the interaction of the THz field and donor-acceptor, while the transient absorption spectroscopy provides quantitative insight on charge transfer state lifetimes and relaxation pathways. Both experimental techniques were validated by theoretical studies. This comprehensive foundation is valuable for future experiments aimed at depositing these PCPs onto surfaces and controlling their molecular states with THz electric field.

# Acknowledgments

Thomas, there are no words strong enough to express my gratitude for everything you have done for me. Thank you for believing in me even when I doubted myself, for giving me the opportunity to work in your group, and for seeing potential in me long before I could see it myself. Your trust, patience, and guidance have shaped not only this thesis but also the person I have become through it. You have taught me far more than science; you have shown me how to think independently, to approach every obstacle with curiosity, and to turn challenges into opportunities for growth. You are, to me, the definition of an extraordinary mentor and an exceptional human being; wise, kind, and endlessly inspiring. Working with you has been one of the greatest privileges of my life, and I will always be grateful for the chance you gave me.

Hansi, thank you for always being there for me. From our daily lunches and fun conversations to the countless times you helped me fix the laser system or solve yet another mysterious problem in the setup. You were the person I could always rely on, no matter whether the issue was scientific or completely unrelated to work. Beyond all that, your humor and kindness made even long experimental days enjoyable. I am truly grateful for everything you have done and for all the great moments we shared, both in and outside the lab.

David and Bong Joo, thank you for everything I learned from you; from the many discussions in the lab to the practical tricks that made experiments actually work. I've learned not only about science but also from your dedication and thoughtful way of approaching every problem.

Vladislav and Camila, thank you for all the insightful discussions, meetings, and the valuable perspectives you shared. I truly learned a lot from you, your ideas and way of thinking have inspired me throughout this work.

A special thanks to the rest of the laser group, Alex, Andrea, Jabbar, Vivek, and Lukas. Thank you for the many helpful discussions, ideas, and good moments we shared in the group. I enjoyed learning from each of you and exchanging thoughts.

Thank you, Beatrice and Simone for handling administrative matters. You made everything run smoothly and with a smile. I appreciate all your support during my studies.

Many thanks to the electronics and mechanical workshops, especially Andres, for their support and for always finding practical solutions whenever something needed to be fixed, built, or improved.

I am grateful to Adrian Cavalieri and Robert Stanley for their support as second supervisor and external reviewer of this thesis, respectively.

Lastly, to my family and all my dear friends, thank you for surrounding me with love, patience, and encouragement through every step of this journey. You have been my anchor in difficult times and my greatest joy in moments of success. Your belief in me gave me strength, and your kindness

reminded me to stay grounded. I am grateful for your endless care, for listening, for laughing with me, and for reminding me that there is life and light beyond the lab. I am deeply grateful to have you all by my side.

A special part of this belongs to my dad, my true supporter, who is no longer with us but whose presence I still feel every day. His strength and quiet faith in me continue to guide and inspire me in everything I do.



# Contents

<b>Abstract</b>	<b>I</b>
<b>Acknowledgments</b>	<b>II</b>
<b>1 Introduction</b>	<b>1</b>
1.1 Overview of Ultrafast Spectroscopy . . . . .	2
1.1.1 Terahertz Spectroscopy . . . . .	3
1.1.2 Transient Absorption Spectroscopy . . . . .	3
1.2 Molecular Systems . . . . .	4
1.3 Outline of the Thesis . . . . .	4
<b>2 Experimental Techniques</b>	<b>10</b>
2.1 Generation and Detection of Terahertz Pulses in Nonlinear Crystals . . . . .	10
2.1.1 THz Generation via Optical Rectification . . . . .	11
2.1.2 Phase Matching and Tilted Pulse Front Pumping . . . . .	12
2.1.3 Detection of THz Pulses via Free-Space Electro-Optic Sampling . . . . .	14
2.2 Transient Absorption Spectroscopy . . . . .	15
2.2.1 Principles of Transient Absorption . . . . .	16
2.2.2 Relaxation Processes and Dynamics . . . . .	17
2.2.3 Data Analysis . . . . .	20
<b>3 Time-resolved THz Stark Spectroscopy of Molecules in Solution</b>	<b>25</b>
3.1 Introduction . . . . .	26
3.2 Results and Discussion . . . . .	28
3.2.1 Dynamics of the Stark Signature . . . . .	28
3.2.2 Comparison Between Conventional and THz Stark Spectroscopy . . . . .	31
3.2.3 Relevant Molecular Parameters . . . . .	33
3.3 Methods . . . . .	34
3.4 Supplemental Information . . . . .	35
3.4.1 Synthesis and Preparation of Molecular Systems . . . . .	35
3.4.2 Density Functional Theory Calculations . . . . .	36
3.4.3 Conventional Stark Spectroscopy . . . . .	38
3.4.4 THz Stark Spectroscopy . . . . .	38
3.4.5 Additional THz Stark Spectroscopy Results . . . . .	42

3.4.6	Characterization of THz Pulses . . . . .	44
3.4.7	Liptay Analysis . . . . .	45
3.4.8	Local Field Correction Factor . . . . .	48
3.4.9	THz Stark Spectroscopy Results of Anthanthrene in EtOAc . . . . .	48
<b>4</b>	<b>Time-resolved Terahertz Stark Spectroscopy of Molecules in Water</b>	<b>61</b>
4.1	Introduction . . . . .	62
4.2	Results and Discussion . . . . .	63
4.2.1	Dynamics of the Stark Signature . . . . .	63
4.2.2	Relevant Molecular Parameters . . . . .	66
4.3	Conclusion . . . . .	67
4.4	Supplemental Information . . . . .	68
4.4.1	THz Stark Spectroscopy Setup . . . . .	68
4.4.2	Sample Preparation . . . . .	68
4.4.3	Data Acquisition and Analysis . . . . .	68
4.4.4	Polarization Anisotropy . . . . .	70
4.4.5	Background Measurements . . . . .	70
4.4.6	Local Field Correction Factor . . . . .	71
4.4.7	Computational Methods . . . . .	72
<b>5</b>	<b>An Accurate Modeling of the Optical and Electronic Properties of the Paracyclophanes</b>	<b>79</b>
5.1	Introduction . . . . .	80
5.2	Computational Methods . . . . .	81
5.3	Experimental Methods . . . . .	83
5.3.1	Femtosecond Transient Absorption Spectroscopy (fTAS) . . . . .	83
5.4	Results and Discussion . . . . .	83
5.4.1	Structural Properties . . . . .	83
5.4.2	Optical Properties of the Monomeric Units . . . . .	84
5.4.3	Optical Properties of the Homoparacyclophanes . . . . .	87
5.4.4	Transient Absorption . . . . .	92
5.4.5	Electrochemical Properties . . . . .	93
5.5	Conclusions . . . . .	94
5.6	Supplementary Information . . . . .	95
<b>6</b>	<b>Tuning Charge Transfer in Novel NDI-Pyrene Paracyclophanes: The Role of Interchromophore Distance and Linker Structure</b>	<b>116</b>
6.1	Introduction . . . . .	117
6.2	Results and Discussion . . . . .	118
6.2.1	Synthesis and Characterization . . . . .	118
6.2.2	Structure of the Paracyclophanes . . . . .	119
6.2.3	Optical Properties . . . . .	120
6.2.4	Electrochemical Properties . . . . .	121
6.3	Theoretical Study . . . . .	123



6.3.1	Absorption Properties of Paracyclophanes . . . . .	124
6.4	Fluorescence . . . . .	128
6.5	Transient Absorption . . . . .	129
6.6	Supplementary Information . . . . .	133
<b>7</b>	<b>Conclusion and Outlook</b>	<b>151</b>

# List of Figures

1.1	<b>Schematic representation of the PCP structures investigated in this work.</b>	4
2.1	<b>Schematic of optical (a) and THz spectra (b) for optical rectification.</b> Frequency pairs within the optical spectrum map to THz outputs at corresponding difference frequencies $\Omega =  \omega_j - \omega_i $ .	11
2.2	<b>The effect of velocity matching on THz field amplification.</b> <b>a</b> Linear amplification of the THz field as the optical group and THz phase velocities are matched. <b>b</b> Destructive interference of THz waves from two nonlinear slices separated by the walk-off distance $l_w$ . Dotted curves show the individual contributions.	12
2.3	<b>Schematic of tilted pulse front pumping in LiNbO<sub>3</sub>.</b> A diffraction grating and imaging optics generate a tilted optical pulse front that matches the THz phase velocity.	13
2.4	<b>Schematic of a standard free space EO sampling setup.</b> Probe polarization states, without <b>a</b> and with <b>b</b> the THz field, are shown before and after the polarization optics.	14
2.5	<b>Characterization of the THz pulse used in this work.</b> <b>a</b> The temporal waveform of the electric field, generated via tilted pulse front pumping in LiNbO <sub>3</sub> and measured at the sample position by electro optic sampling in ZnTe. <b>b</b> The corresponding amplitude spectrum obtained from a Fourier transform, showing a center frequency of 0.5 THz.	15
2.6	<b>Schematic of a basic femtosecond transient absorption spectroscopy setup.</b>	16
2.7	<b>Schematic representation of TA signal contributions.</b> Negative bands originate from ground state bleaching (GSB) and stimulated emission (SE), whereas positive bands arise from excited state absorption (ESA). The total measured $\Delta A$ spectrum results from the superposition of these processes. The inset illustrates the corresponding electronic energy-level diagram, indicating the origin of GSB, SE, and ESA transitions.	18
2.8	<b>Perrin-Jablonski diagram illustrating the relaxation pathways of an excited molecule.</b> Solid arrows represent radiative processes (absorption, fluorescence, phosphorescence), while dashed arrows denote non-radiative processes (internal conversion, intersystem crossing, vibrational relaxation).	19
2.9	<b>A representative plot of singular values from an SVD analysis.</b> The number of values clearly above the noise floor ( $p$ ) is determined to select the basis vectors for the subsequent global fit.	21

3.1	<b>Electric field induced Stark effect and experimental concept.</b> Electric field induced Stark shift due to a difference in ground- and excited state dipole ( <b>a</b> ), i.e. linear Stark effect, and polarizability ( <b>b</b> ), i.e. quadratic Stark effect. For an isotropic distribution of molecules the ground state absorption band versus energy $A(E)$ broadens in the case of the linear Stark effect with the difference signal $\Delta A(E)$ resembling the second order derivative of the absorption band. In the case of the quadratic Stark effect the ground state absorption band shifts resulting in a difference signal $\Delta A(E)$ that is proportional to the first order derivative of absorption band. <b>c</b> Schematic representation of the experimental setup. The femtosecond supercontinuum probe pulse is scanned in time across the collinear single-cycle THz pulses and its spectrum is recorded by a spectrometer. . . . .	27
3.2	<b>THz Stark signal of TTF-BTD with parallel orientation.</b> <b>a</b> False-color plot of the measured change in absorption spectrum as a function of time delay between THz and probe pulse and wavelength. <b>b</b> Time-averaged (between the two green dotted lines) change in absorption versus wavelength (green solid curve) compared to the scaled first (black dashed curve) and second order derivative (black dotted curve) of the ground state absorption spectrum. <b>c</b> Spectral average of the change in absorption between the purple dotted (purple curve) and red dotted lines (red curve) in <b>a</b> . The red curve is compared to the scaled square of the measured THz electric field $E_{\text{THz}}^2$ (black dashed curve). <b>d</b> Chemical structure of TTF-BTD. . . . .	28
3.3	<b>THz Stark signal of anthanthrene with parallel orientation.</b> <b>a</b> False-color plot of the measured change in absorption spectrum as a function of time delay between THz and probe pulse and wavelength. <b>b</b> Time-averaged (between the two green dotted lines) change in absorption versus wavelength (green solid curve) compared to the scaled first (black dashed curve) and second order derivative (black dotted curve) of the ground state absorption spectrum. <b>c</b> Spectral average of the change in absorption between the purple dotted (purple curve) and red dotted lines (red curve) in <b>a</b> . The red curve is compared to the scaled square of the measured THz electric field $E_{\text{THz}}^2$ (black dashed curve). <b>d</b> Chemical structure of anthanthrene. . . . .	30
3.4	<b>Comparison of conventional and THz Stark spectroscopy.</b> <b>a,b</b> Low temperature (77 K) and room temperature (295 K) absorption spectra of (a) TTF-BTD and (b) anthanthrene. <b>c,d</b> Conventional Stark spectra measured at 77 K for two values of the angle $\chi$ between the polarization of the THz and the probe pulses. <b>e,f</b> THz Stark spectra recorded at room temperature for parallel and perpendicular orientation of THz and probe polarization. For direct comparison the y-scale is in units of $\Delta\epsilon$ scaled to an electric field of 1 MV/cm. The grey dotted vertical lines are guides to the eye and help to visualize the shift of the spectra at the different temperatures. . . . .	32
3.5	<b>Molecular orbitals of anthanthrene.</b> With reference to the main text, we draw the reader's attention to the HOMO→LUMO transition in particular. . . . .	37
3.6	<b>THz Stark spectroscopy.</b> High-field single-cycle THz waveforms were generated via tilted-pulse-front pumping in LiNbO <sub>3</sub> and the fs-SC probe pulses were generated in CaF <sub>2</sub> . The probe pulses passed collinearly with the THz pulses through the sample and were analyzed by a spectrometer. A chopper running at 500 Hz alternated between THz waveform on and off. . . . .	39

3.7	<b>Measured color-coded Stark map for anthanthrene versus time delay and wavelength before a and after b GVD correction.</b> The black solid curve indicates the fitted 3rd order polynomial representing the GVD, which turns into a vertical line after GVD correction. . . . .	40
3.8	<b>Background measurement with pure toluene for a parallel and b perpendicular orientation of THz and probe pulses.</b> Spectral average of the change in absorption between the purple dotted lines as a function of time delay for c parallel and d perpendicular orientation. . . . .	41
3.9	<b>THz Stark signal of TTF-BTD with perpendicular orientation. a</b> False-color plot of the measured change in absorption spectrum as a function of time delay between THz and probe pulse and wavelength. <b>b</b> Time-averaged (between the two green dotted lines) change in absorption versus wavelength (green solid curve) compared to the scaled first (black dashed curve) and second order derivative (black dotted curve) of the ground state absorption spectrum. <b>c</b> Spectral average of the change in absorption between the purple dotted (purple curve) and red dotted lines (red curve) in <b>a</b> . The red curve is compared to the scaled square of the measured THz electric field $E_{\text{THz}}^2$ (black dashed curve). <b>d</b> Chemical structure of TTF-BTD. . . . .	42
3.10	<b>THz Stark signal of anthanthrene with perpendicular orientation. a</b> False-color plot of the measured change in absorption spectrum as a function of time delay between THz and probe pulse and wavelength. <b>b</b> Time-averaged (between the two green dotted lines) change in absorption versus wavelength (green solid curve) compared to the scaled first (black dashed curve) and second order derivative (black dotted curve) of the ground state absorption spectrum. <b>c</b> Spectral average of the change in absorption between the purple dotted (purple curve) and red dotted lines (red curve) in <b>a</b> . The red curve is compared to the scaled square of the measured THz electric field $E_{\text{THz}}^2$ (black dashed curve). <b>d</b> Chemical structure of anthanthrene. . . . .	43
3.11	<b>a Measured electro-optic signal at the sample position and b corresponding spectrum.</b> . . . . .	44
3.12	<b>TTF-BTD conventional Stark and THz-Stark spectra fitting a, b</b> Ground state absorption spectrum $\epsilon$ of TTF-BTD sample at 77 K ( <b>a</b> ) and at 295 K ( <b>b</b> ). The dots represent the data points and the black solid curves represents the fits. <b>c, d</b> Measured Stark spectra for two different incidence angles (dots) and corresponding fits (black solid curves) for the conventional Stark measurement <b>c</b> and THz-Stark measurement <b>d</b> . For better visualization, the curves for $\chi = 90^\circ$ are arbitrarily shifted along the $\Delta\epsilon$ -axis. <b>e, f</b> Contribution of the zeroth (solid curve), first (dashed curve) and second (dotted curve) order derivative line form for the Stark spectra for $\chi = 90^\circ$ . . . . .	46

3.13	<b>Anthanthrene conventional Stark and THz-Stark spectra fitting</b> <b>a, b</b> Ground state absorption spectrum $\epsilon$ of anthanthrene sample at 77 K ( <b>a</b> ) and at 295 K ( <b>b</b> ). The dots represent the data points and the black solid curves represents the fits. <b>c, d</b> Measured Stark spectra for two different incidence angles (dots) and corresponding fits (black solid curves) for the conventional Stark measurement <b>c</b> and THz-Stark measurement <b>d</b> . For better visualization, the curves for $\chi = 90^\circ$ are arbitrarily shifted along the $\Delta\epsilon$ -axis. <b>e, f</b> Contribution of the zeroth (solid curve), first (dashed curve) and second (dotted curve) order derivative line form for the Stark spectra for $\chi = 90^\circ$ . . . . .	47
3.14	<b>THz Stark signal of anthanthrene in EtOAc with parallel orientation.</b> <b>a</b> False-color plot of the measured change in absorption spectrum as a function of time delay between THz and probe pulse and wavelength. <b>b</b> Time-averaged (between the two green dotted lines) change in absorption versus wavelength (green solid curve) compared to the scaled first (black dashed curve) and second order derivative (black dotted curve) of the ground state absorption spectrum. <b>c</b> Spectral average of the change in absorption between the purple dotted (purple curve) and red dotted lines (red curve) in <b>a</b> . . . . .	49
3.15	<b>THz Stark signal of anthanthrene in EtOAc with perpendicular orientation.</b> <b>a</b> False-color plot of the measured change in absorption spectrum as a function of time delay between THz and probe pulse and wavelength. <b>b</b> Time-averaged (between the two green dotted lines) change in absorption versus wavelength (green solid curve) compared to the scaled first (black dashed curve) and second order derivative (black dotted curve) of the ground state absorption spectrum. <b>c</b> Spectral average of the change in absorption between the purple dotted (purple curve) and red dotted lines (red curve) in <b>a</b> . . . . .	50
3.16	<b>Comparison of THz Stark signal of Anthanthrene in toluene and EtOAc.</b> <b>a</b> absorption spectra of Anthanthrene in toluene (blue) and EtOAc (red). <b>b,c</b> THz Stark spectra of Anthanthrene ( <b>b</b> ) in toluene ( <b>c</b> ) in EtOAc recorded for parallel and perpendicular orientation of THz and probe polarization. For direct comparison the y-scale is in units of $\Delta\epsilon$ scaled to an electric field of 1 MV/cm. The grey dotted vertical lines are guides to the eye and help to visualize the shift of the spectra at the different temperatures. . . . .	51
4.1	<b>THz Stark response of Malachite Green in parallel orientation.</b> <b>a</b> False-color map of the measured change in absorption spectrum as a function of wavelength and of probe delay relative to the THz pulse. <b>b</b> Spectral trace obtained by averaging the signal between the red dashed lines in <b>a</b> (red solid curve), compared to the total fit (black dash-dotted curve), the first-order derivative (grey dashed curve), and the second-order derivative (grey dotted curve) of the ground state absorption spectrum. <b>c</b> Temporal evolution of the spectrally integrated Stark signal (blue curve), averaged across the spectral range indicated by the blue dashed lines in <b>a</b> , compared to the squared THz electric field profile $E_{\text{THz}}^2$ (purple dashed curve). <b>d</b> Chemical structure formula of Malachite Green. . . . .	64

4.2	<b>THz Stark response of Methyl Orange in parallel orientation.</b> <b>a</b> False-color map of the measured change in absorption spectrum as a function of wavelength and of probe delay relative to the THz pulse. <b>b</b> Spectral trace obtained by averaging the signal between the red dashed lines in <b>a</b> (red solid curve), compared to the total fit (black dash-dotted curve), the first-order derivative (grey dashed curve), and the second-order derivative (grey dotted curve) of the ground state absorption spectrum. <b>c</b> Temporal evolution of the spectrally integrated Stark signal (blue curve), averaged across the spectral range indicated by the blue dashed lines in <b>a</b> , compared to the squared THz electric field profile $E_{\text{THz}}^2$ (purple dashed curve). <b>d</b> Chemical structure of Methyl Orange. . . . .	65
4.3	<b>Molar absorption coefficient and its modulation.</b> The plots combine the absorption spectra (blue line, right y-axes) and THz Stark responses (left y-axes) of Malachite Green ( <b>a</b> ) and Methyl Orange ( <b>b</b> ), measured at room temperature. The Stark spectra are plotted as $\Delta\epsilon$ , recorded for parallel (brown) and perpendicular (orange) orientations of the THz and probe polarizations, and scaled to an electric field strength of 1 MV/cm. . . . .	66
4.4	<b>Experimental setup for THz Stark spectroscopy with a reference-corrected supercontinuum detection.</b> Single-cycle THz pulses are produced by tilted-pulse-front excitation in LiNbO <sub>3</sub> and are spatially overlapped with femtosecond SC probe pulses generated in CaF <sub>2</sub> . The probe beam was split before the sample, with one arm passing through the sample while the other serving as a reference to improve signal-to-noise ratio. Both probe and reference spectra are recorded by a spectrometer. A mechanical chopper operating at 500 Hz periodically blocked the THz beam, enabling alternating acquisition of THz-on and THz-off signals for differential detection. . . . .	69
4.5	<b>a, b Overlay of the parallel TRTSS spectrum (solid blue curve) with the best-scaled perpendicular spectrum (red dashed curve) of Malachite Green and Methyl Orange respectively.</b> . . . . .	70
4.6	<b>a and b <math>\Delta A(\lambda, t)</math> map.</b> Broad, nearly wavelength-independent response of pure water at time zero, for parallel and perpendicular geometry, respectively. No derivative structure or band center zero-crossing, consistent with non-resonant Kerr/electrostriction rather than Stark signature. <b>c and d wavelength-averaged <math>\Delta A(t)</math>.</b> Temporal evolution of the signal, averaged across the spectral range indicated by the blue dashed lines, for parallel and perpendicular geometry, respectively. . . . .	71
4.7	<b>Band-averaged TRTSS traces with the probe analyzer at 0° and 90° measured for pure water.</b> An opposite signal sign is observed with the rotation of the polarizer (Kerr birefringence). . . . .	72
4.8	<b>Comparison of the natural transition orbitals and transition densities between TD-DFT with wB97XD DFT functional with 6-31+G(d,p) basis and CC2 calculation with def2-TZVPPD in vaccum.</b> TD-DFT orbitals and densities results agree well with the CC2 results except for the Methyl Orange second and third excited states are exchanged. The natural transition orbitals keep the same shape also in the water solution modeled as polarizable continuum environment. . . . .	73



5.1	<b>Structures of the studied paracyclophanes.</b>	84
5.2	<b>Optical spectra and corresponding electronic excitations of the monomeric units. (a)</b> Computed and experimental absorption and fluorescence spectra of NDI, Pyrene and Pyrene with <sup>t</sup> BuPh and Ada linkers. The computed spectra show excellent agreement with the experimental ones without inclusion of arbitrary shifts. <b>(b)</b> Transition densities and natural transition orbitals for the lowest excited states of the monomeric units.	86
5.3	<b>Optical spectra and corresponding electronic excitations of the homoparacyclophanes. (a)</b> Computed and experimental absorption and fluorescence spectra of NDI, Pyrene and bis(aminomethyl)Pyrene homo-paracyclophanes. <b>(b)</b> Monomeric and NDI-Ada-NDI transition density for the corresponding lowest excited states. The green arrows represents the orientation of the transition dipole from the separate aromatic units. The lowest excited state of the H-type dimer is optically dark with unit transition dipoles oriented in opposite directions whereas the second excited state is bright with unit dipoles aligned. <b>(c)</b> Natural transition orbitals for the monomeric NDI and the second excited state for the NDI-Ada-NDI paracyclophane.	89
5.4	<b>Frenkel exciton model for the homo-paracyclophanes. (a)</b> Representation of the Frenkel exciton Hamiltonian and decomposition into LE-LE and CT-LE blocks. <b>(b)</b> Representation of the paracyclophane as two separate units embedded in a dielectric environment. The blue area represents the solvent cavity. <b>(c)</b> Comparison of the exciton couplings between locally excited states computed from the Poisson-TrESP method and from diabaticization of the supermolecule excited states with correlation coefficient 0.997. <b>(d)</b> Correlation between calculated LE-CT couplings and corresponding molecular orbital overlaps between the individual separate units with correlation coefficient of 0.983 and 0.964 for the NDI and Pyrene based PCPs, respectively.	91
5.5	<b>a Transient absorption spectra of NDI-<sup>t</sup>BuPh-NDI and NDI-Ada-NDI recorded at various time delays excited at 380 nm. b</b> Corresponding decay associated spectra (DASs).	92
5.6	<b>Absorption and fluorescence spectra for the NDI computed with Duschinsky rotation.</b>	96
5.7	<b>Comparison of the ground state and excimer geometry for the Pyrene homoparacyclophane with ethyl and propyl linkers.</b>	97
5.8	<b>Experimental setup for transient absorption spectroscopy (TAS) with a reference-corrected supercontinuum detection.</b> Pump pulses were generated in a non-collinear optical parametric amplifier (NOPA) and are spatially overlapped with femtosecond SC probe pulses generated in CaF <sub>2</sub> . A mechanical chopper running at 2 kHz periodically interrupted the pump beam, allowing sequential acquisition of pump-on and pump-off traces for differential measurements.	98
5.9	<b>Synthetic route to homoparacyclophanes and monomeric units with linkers.</b>	99
5.10	<b>Cyclic voltammogram and differential pulse voltammogram of NDI-Ada-NDI.</b>	101
5.11	<b>Cyclic voltammogram and differential pulse voltammogram of Pyrene-Ada.</b>	101
5.12	<b>Cyclic voltammogram and differential pulse voltammogram of NDI-<sup>t</sup>BuPh.</b>	102
5.13	<b>HNMR Ada-CN.</b>	102

5.14	<b>CNMR Ada-CN.</b>	103
5.15	<b>HNMR Ada-NH<sub>2</sub>.</b>	104
5.16	<b>CNMR Ada-NH<sub>2</sub>.</b>	105
5.17	<b>HNMR Ada-NHBoc.</b>	106
5.18	<b>CNMR Ada-NHBoc.</b>	107
5.19	<b>HNMR Ada-NHBoc-py semicircle.</b>	108
5.20	<b>HNMR of NDI-Ada-NDI.</b>	109
5.21	<b>HNMR of NDI-<sup>t</sup>BuPh monomer.</b>	110
6.1	<b>Schematic representation of the different PCP structures investigated in this work.</b>	118
6.2	<b>Synthetic routes to NDI-Ada-Py, NDI-<sup>t</sup>BuPh-Py, and NDI-Ph-Py cyclophanes and structures of reference compounds.</b>	119
6.3	<b>Partial <sup>1</sup>H NMR spectra of NDI-Ref, NDI-<sup>t</sup>BuPh-Py, and <sup>t</sup>BuPh-Py in CDCl<sub>3</sub>.</b>	120
6.4	<b>Optimized geometries for the three D-A paracyclophanes.</b>	120
6.5	<b>Absorption spectra of PCPs and their reference compounds in CH<sub>2</sub>Cl<sub>2</sub> at room temperature.</b>	122
6.6	<b>Cyclic voltammograms of the different PCPs with their reference compounds measured in DCM with TBAPF<sub>6</sub> (0.1M) as the supporting electrolyte. Pt working electrode, glassy carbon as counter electrode, scan rate 0.1 V min<sup>-1</sup>.</b>	123
6.7	<b>Comparison of the experimental and computed absorption spectra.</b> Except of the broadening peak and slightly different redistribution of intensities among the vibronic modes the computed spectra quantitatively well agree with the experimental ones and all the observed effects are well captures.	125
6.8	<b>Absorption spectra decomposed to the individual transitions for the three different linkers.</b>	128
6.9	<b>The proposed exciton relaxation pathways for different excitation wavelengths of the NDI-Ada-Py based on a comparison of the computed and experimental fluorescence spectra.</b> Solid arrows indicate system excitation and fluorescence, while dashed lines show exciton relaxation. The red dashed lines represent expected relaxation pathways that could not be validated from the comparison of the experimental and computed spectra due to the small transition dipole moment of the final CT states.	130
6.10	<b>Ultrafast excited state dynamics of NDI-Ada-Py upon excitation at 400 nm. a</b> Transient absorption spectra of NDI-Ada-NDI recorded at various time delays. <b>b</b> Corresponding decay associated spectra (DASs).	131
6.11	<b>Ultrafast excited state dynamics of NDI-Ada-Py upon excitation at 380 nm. a</b> Transient absorption spectra of NDI-Ada-NDI recorded at various time delays. <b>b</b> Corresponding decay associated spectra (DASs).	132
6.12	<b>Ultrafast excited state dynamics of NDI-Ada-Py upon excitation at 260 nm. a</b> Transient absorption spectra of NDI-Ada-NDI recorded at various time delays. <b>b</b> Corresponding decay associated spectra (DASs).	132
6.13	<b>Synthetic procedures for NDI-Ada-Pyrene</b>	133
6.14	<b>Synthetic procedures for NDI-<sup>t</sup>BuPh-Pyrene</b>	134



6.15	Synthetic procedures for NDI-Ph-Pyrene . . . . .	135
6.16	Fluorescence spectra of NDI-Ada-Pyrene and reference compound Pyrene-Ada ( $\lambda_{exc} = 290$ nm) and excitation spectra of Pyrene-Ada. . . . .	136
6.17	Fluorescence spectra of NDI-Ada-Pyrene and reference compound NDI- <sup>t</sup> BuPh ( $\lambda_{exc} = 380$ nm) and excitation spectra of Pyrene-NDI- <sup>t</sup> BuPh. . . . .	136
6.18	Fluorescence and excitation spectra of reference compound Pyrene-Ada ( $\lambda_{exc} = 450$ nm). . . . .	137
6.19	Fluorescence and excitation spectra of NDI-Ada-Pyrene ( $\lambda_{exc} = 460$ nm). . . .	137
6.20	Cyclic voltammogram of NDI-Ada-Pyrene. . . . .	138
6.21	Differential pulse voltammograms of NDI-Ada-Pyrene. . . . .	138
6.22	HNMR NDI-Ada-Pyrene. . . . .	139
6.23	CNMR NDI-Ada-Pyrene. . . . .	140
6.24	DEPT135 NDI-Ada-Pyrene. . . . .	141
6.25	Iso-surface representation of the transition density of the NDI-Ph-Pyrene lowest charge transfer (CT) state $S_1$ . The positive part (red) of the transition density is localized on the NDI unit, whereas the negative part (blue) is localized on the pyrene moiety. This spatial separation leads to a transition dipole moment oriented perpendicular to the planes of the NDI and pyrene units. . . . .	142
6.26	Comparison of the NTO analysis between TD-DFT with $\omega B97XD$ functional and the corresponding states from CC2 method for the excited states of the NDI-Ada-Pyrene paracyclophane. . . . .	143
6.27	Comparison of the NTO analysis between TD-DFT with $\omega B97XD$ functional and the corresponding states from CC2 method for the excited states of the NDI-Ph-Pyrene paracyclophane. . . . .	144
6.28	Natural Transition Orbital analysis for the NDI-Ada-Pyrene and NDI-Ph-Pyrene paracyclophane hetero-structures together with corresponding adiabatic energies. . . . .	145
6.29	Individual fragments for calculation of the couplings between transition densities and molecular orbital overlaps for the paracyclophane homo- and hetero-structures. . . . .	145

# List of Tables

3.1	Comparison of relevant molecular parameters as calculated via DFT or measured by conventional and THz Stark spectroscopy. . . . .	33
3.2	Ground state transitions of anthanthrene with wavelength, oscillator strength, and major contributing molecular orbitals calculated using TD-DFT. . . . .	36
3.3	$\Delta\alpha$ computed by TD-DFT with an aug-cc-pVDZ basis set. . . . .	37
3.4	Comparison of relevant molecular parameters as calculated via DFT or measured by conventional and THz Stark spectroscopy in different solvents. . . . .	48
4.1	Comparison of relevant molecular parameters as calculated via TD-DFT and measured via THz Stark spectroscopy. . . . .	67
4.2	Polarization anisotropy metrics from derivative-only diagnostics. . . . .	70
4.3	Comparison of the electronic properties for the first excited state between the TD-DFT and CC2 approach. $E_{ge}$ and $\mu_{ge}$ correspond to the vertical excitation energy and transition dipole moment, respectively, between the ground and first excited state $S_1$ , while $\Delta\mu$ and $\text{Tr}(\Delta\alpha)$ represent the difference between excited and ground state dipole moment and isotropic polarizability, respectively. . . . .	74
4.4	Comparison of the electronic properties for different solvation schemes within the TD-DFT approach using the wB97XD functional and 6-31+G(d,p) basis set. . . . .	74
5.1	Redox properties for the monomeric units and homoparacyclophanes. . . . .	94
6.1	Electrochemical data of the target compound and references. Redox potentials (V) vs. Ag/AgCl in $\text{CH}_2\text{Cl}_2$ . . . . .	124
6.2	Transition dipole and excitation energy decomposition into individual contributions. . . . .	129

# Chapter 1

## Introduction

The continuous miniaturization of microelectronic components, as outlined by Moore's Law, is nearing its inherent physical limits<sup>1</sup>. Moore's Law states that the number of transistors on a chip doubles approximately every two years, resulting in a continuous reduction of transistor size<sup>1</sup>. As silicon-based component dimensions shrink to the nanometer scale, quantum mechanical effects such as electron tunneling through insulating barriers and power dissipation become dominant and classical physics no longer suffices to describe the relevant physical processes<sup>2</sup>. Molecular electronics presents one of the most compelling routes forward, proposing the use of single molecules or molecular ensembles as the fundamental building blocks of electronic components such as wires, diodes, switches, and memory elements<sup>3,4</sup>. Molecules offer valuable advantages; their inherent size approaches the ultimate limit of miniaturization and the most importantly, variety of chemical synthesis allows for tailoring specific electronic properties<sup>5</sup>. This approach promises not only to continue the trend of miniaturization but also to unlock novel functionalities based on the quantum states inherent to molecular structures<sup>3,6</sup>.

A key goal in molecular electronics is the creation of molecular memory elements, that can be switched between at least two stable or quasi-stable states, known as bi-stability<sup>3</sup>. Bi-stability can be achieved by external stimuli such as light, electric fields, or chemical changes. In particular, light offers ultrafast and contact-free control of bi-stable systems such as photo-isomerization, different spin configurations, or charge transfer<sup>5,7</sup>. The charge transfer can occur within a single donor-acceptor structure (intramolecular), or between different molecules (intermolecular), resulting in transient charge separated and the formation of radical species<sup>7,8</sup>. However, transforming a bi-stable molecule into a functional device requires its integration onto a conductive surface<sup>9</sup>. A typical molecular device consists of a functional molecule positioned between two conductive electrodes, forming a single-molecule junction<sup>3,10</sup>. The performance of such a device, its conductivity, stability, and switching speed, is not solely determined by the intrinsic properties of the molecule itself. Rather, it is also governed by the dynamics at the molecule-surface interface<sup>3,11</sup>. The electronic coupling between the molecular orbitals and the band structure of the electrodes dictates the efficiency of charge transfer<sup>3,10</sup>. Furthermore, the lifetime of charge transfer is linked to relaxation pathways influenced by the substrate. These pathways can involve coupling to a variety of collective excitations within the surface like plasmons<sup>12</sup>.

This research is motivated by controlling molecular states with external fields. The achievement of this requires an external field that is both extremely fast and sufficiently strong to act as

a transient electrical bias<sup>13,14</sup>. The electric field of a terahertz (THz) pulse is an ideal candidate for this purpose. It can act on a molecule within sub-picosecond timescales faster than most typical relaxation processes<sup>9,14,15</sup>. Pioneering experiments combining scanning tunnelling microscopy with THz pulses (THz-STM) have highlighted the potential of using THz fields for the control of molecular systems<sup>9,16,17</sup>.

However, before such advanced control techniques can be applied, a deep understanding of both the molecule's response to the controlling field and its excited state behavior is required. Specifically, one must characterize how the molecule's electronic structure interacts with the THz field and learn the pathways and timescales of its relaxation processes, which necessitates foundational spectroscopic investigations.

To this end, this thesis employs two spectroscopic approaches, time-resolved THz Stark spectroscopy and transient absorption spectroscopy. The THz frequency range itself offers unique spectroscopic insights. As THz pulses can act as strong electric field, time-resolved THz Stark spectroscopy utilizes this capability to directly measure how a molecule's absorption spectrum is modified by the THz field in real-time. This reveals electronic properties, such as changes in dipole moment and polarizability, providing insight into the molecule's electronic response under the influence of the fields. Understanding THz-molecule interaction is a vital first step. Second, it is essential to understand how the molecule behaves after excitation. Femtosecond transient absorption spectroscopy provides this information by tracking population dynamics following photoexcitation and it allows measurement of the lifetimes of excited states, identification of transient species (like charge transfer states), and determination of the kinetics for various relaxation processes (e.g., charge separation, recombination, intersystem crossing). This dynamic information reveals how the molecule dissipates energy and how long it stays in specific states.

## 1.1 Overview of Ultrafast Spectroscopy

The study of chemical and physical processes following photoexcitation is fundamental to understanding a vast variety of phenomena. The processes in a molecule after absorbing light, such as electron transfer, charge separation, bond breaking/formation, and structural rearrangements, occur on incredibly short timescales, typically spanning from femtoseconds ( $10^{-15}$  s) to nanoseconds ( $10^{-9}$  s)<sup>18,19</sup>. Accessing these ultrafast dynamics requires experimental techniques that can resolve with temporal resolution comparable to the molecular processes.

Ultrafast laser spectroscopy, particularly utilizing femtosecond laser pulses, has revolutionized our ability to observe these processes in real-time<sup>19</sup>. Pump-probe techniques form the fundamental basis of time-resolved spectroscopy. In this approach, an initial "pump" pulse excites the system, creating a non-equilibrium state (e.g., an electronic excited state), and a subsequent, time-delayed "probe" pulse measures the system's evolution as it relaxes back towards equilibrium. By varying the time delay between the pump and probe pulses, the dynamics of the system can be studied, providing a insight into the lifetimes of transient states, their kinetics, and the spectral signatures of intermediates<sup>20,21</sup>.

### 1.1.1 Terahertz Spectroscopy

Electromagnetic radiation in the terahertz (THz) frequency range plays a crucial role in the thesis presented here. This spectral region, typically defined as 0.1 to 10 THz (corresponding to wavelengths from 3 mm down to 30  $\mu\text{m}$  and photon energies from 0.4 meV to 40 meV), lies between the microwave and infrared domains and is particularly significant due to its ability to interact with a wide range of low-energy excitations in materials<sup>13</sup>.

Historically, this spectral region was referred to as the "THz gap" due to the challenges in efficiently generating and detecting radiation in this range compared to the well-established neighboring microwave and infrared domains<sup>22</sup>. However, advances over the past few decades, largely driven by the development of ultrafast femtosecond laser technology, have led to robust methods for generating coherent THz pulses, for instance, via optical rectification in nonlinear crystals or emission from photoconductive antennas<sup>23,24</sup>. Equally important has been the development of phase-sensitive detection techniques, such as free-space electro-optic sampling, allowing for the measurement of the THz electric field waveform, not just its intensity<sup>22</sup>.

The availability of intense, phase-stable, single- or few-cycle THz pulses has revolutionized the field, moving beyond linear spectroscopy towards nonlinear interactions and the control of matter<sup>14</sup>. With peak electric fields reaching hundreds of kV/cm to several MV/cm, THz pulses can exert strong forces on charged particles and molecular dipoles<sup>24</sup>. The phase-stability ensures that the electric field waveform is identical from one laser shot to the next, which is a requirement for coherently controlling molecular dynamics<sup>15</sup>. Furthermore, the single- or few-cycle pulses allows for an impulsive excitation, where the duration of the driving field is shorter than the molecular rotational periods being probed<sup>14,15</sup>. Unlike optical pulses which primarily interact with electronic transitions, THz pulses can couple to and drive rotational or vibrational degrees of freedom<sup>15</sup>. Furthermore, the sub-picosecond duration of the electric field allows it to act as an impulsive bias, driving systems far from equilibrium and potentially accessing transient states of matter<sup>14,25</sup>. This capability of THz pulses to act as transient electric field is utilized in time-resolved THz Stark spectroscopy, a technique employed in this work where the THz pulse serves as the perturbing field to make changes in molecular electronic properties.

### 1.1.2 Transient Absorption Spectroscopy

In addition to technique using THz pulses, femtosecond Transient Absorption Spectroscopy (fTAS) is a widely established pump-probe method primarily used to track the population dynamics of electronic states following photoexcitation, typically in the UV-Visible-NIR spectral range<sup>21,26</sup>. The pump pulse initiates a photochemical or photophysical process by promoting molecules to an excited electronic state. The broadband probe pulse then measures the change in absorbance of the sample as a function of time delay and wavelength<sup>21,27</sup>.

The resulting signal contains contributions from ground state bleaching (GSB), stimulated emission (SE), and excited state absorption (ESA). Analyzing the temporal evolution of these spectral features allows for the measurement of excited state lifetimes, the identification of intermediate species, and the determination of relaxation pathways such as internal conversion, inter-system crossing, charge transfer, and vibrational cooling<sup>26,27</sup>. TAS provides crucial information about "what states are populated and for how long," which is essential for understanding the in-

trinsic relaxation behavior of molecules relevant to fields like photovoltaics, photocatalysis, and molecular electronics<sup>26,27</sup>.

## 1.2 Molecular Systems

Having introduced the key spectroscopic methods, we now present the molecular systems explored in this work. Molecules featuring electron-donating (D) and electron-accepting (A) moieties covalently linked together provide a framework for studying charge transfer processes<sup>7</sup>. Upon excitation, these D-A systems can undergo intramolecular charge transfer, leading to a state with charge separation ( $D^+-A^-$ )<sup>7,10</sup>. The lifetime of this charge transfer state are critical for potential device applications. However, controlling and optimizing this state requires a molecular structure that allows for precise tuning of the D-A interaction.

In this work, paracyclophanes (PCPs), consisting two or more aromatic  $\pi$ -units arranged in a cofacial geometry and connected by rigid or semi-rigid linkers, were explored. By incorporating D (e.g., Pyrene) and A (e.g., Naphthalene diimide) units within the PCP structure, the distance and relative orientation between the donor and acceptor can be precisely controlled through chemical synthesis<sup>28</sup>. This structural control allows for investigation of through-space electronic coupling and its influence on charge transfer dynamics. Furthermore, the linker units can be designed to act as "molecular feet", providing a built-in strategy to control the distance and electronic coupling between the functional  $\pi$ -systems and a conductive substrate upon surface deposition.

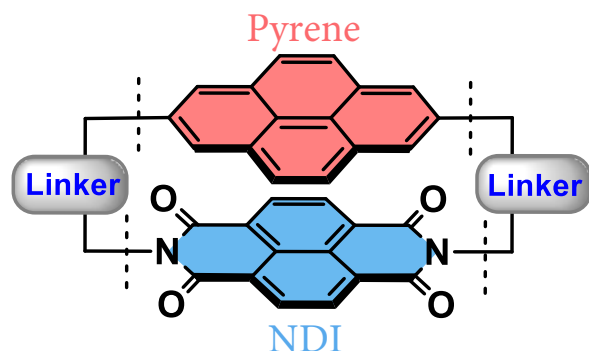


Figure 1.1: Schematic representation of the PCP structures investigated in this work.

## 1.3 Outline of the Thesis

This cumulative thesis summarizes the research I conducted during my PhD studies. The work is structured as a series of foundational investigations aimed at the long-term goal of investigating molecule-surface interactions in the presence of THz electric fields. The thesis is focused into two main parts; first, developing an understanding of THz field interactions with molecules in solution, and second, performing the essential excited state characterization of donor-acceptor paracyclophane systems designed for this purpose. The thesis is organized as follows:

- **Chapter 2: "Experimental Techniques"**

This chapter provides the necessary technical background for the two primary spectroscopic methods employed throughout this work; time-resolved THz Stark spectroscopy and femtosecond transient absorption spectroscopy. It covers the principles of THz pulse generation and detection as well as the fundamentals of pump-probe techniques for studying ultrafast molecular dynamics.

- **Chapter 3: "Time-resolved THz Stark Spectroscopy of Molecules in Solution"**

*(Published in Nature Communications)*

This chapter describes how THz electric fields interact with donor-acceptor molecule. We demonstrate time-resolved THz Stark spectroscopy on a D-A system in a non-polar solvent, successfully extracting key electronic parameters.

This work was a large collaboration between the Institute of Applied Physics and the Department of Chemistry, Biochemistry and Pharmaceutical Sciences at the University of Bern, the University of Oslo, and Temple University in USA. My contribution was performing experiments, analyzing the data, and contributing to the manuscript.

- **Chapter 4: "Time-resolved Terahertz Stark Spectroscopy of Molecules in Water"**

*(In preparation for submission)*

This chapter presents an extension of the time-resolved THz Stark spectroscopy method to test its limits and robustness in the most challenging of environments.

This work was a collaboration with the Laboratory of Computational Chemistry and Biochemistry at EPFL. I performed the THz Stark spectroscopy measurements, analyzed the data, and writing of the manuscript.

- **Chapter 5: "An Accurate Modeling of the Optical and Electronic Properties of the Paracyclophanes"**

*(In preparation for submission)*

This chapter focuses on homo-paracyclophanes (homo-PCPs) and establishes the combined experimental and computational methodology required to understand their characteristics, and the theoretical framework for modeling these systems is validated.

This work was a collaboration between the Institute of Applied Physics, the Laboratory of Computational Chemistry and Biochemistry (EPFL), and the Department of Chemistry, Biochemistry and Pharmaceutical Sciences at the University of Bern. My primary contribution involved interpreting the excited state dynamics of these homo-PCPs. To achieve this, I performed the femtosecond TAS measurements and conducted the detailed kinetic analysis, providing insights into processes.

- **Chapter 6: "Tuning Charge Transfer in Novel NDI-Pyrene Paracyclophanes: The Role of Interchromophore Distance and Linker Structure"**

*(In preparation for submission)*

This chapter represents the synthesis of the target D-A hetero-paracyclophanes (NDI-Pyrene) with different linkers and applying the validated theoretical models to them. This work



successfully presents the ultrafast intramolecular charge transfer dynamics, quantifies the relaxation lifetimes.

This work was a collaboration between the Institute of Applied Physics, the Laboratory of Computational Chemistry and Biochemistry (EPFL), and the Department of Chemistry, Biochemistry and Pharmaceutical Sciences at the University of Bern. My contribution focused on understanding the complex excited state dynamics and intramolecular charge transfer mechanisms in these hetero-PCPs. I performed the TAS measurements across different excitation wavelengths and carried out the kinetic analysis to quantify state lifetimes and learn about relaxation pathways.

The chapters based on manuscripts that are still in preparation may be subject to minor modifications or additional analyses prior to their submission for publication.

## Additional Work

During my PhD, I also contributed to the following projects and publications which are not included as chapters in this thesis:

- D. Rohrbach, L. Beéry, S. J. Mousavi, H.-M. Frey, B. J. Kang, **E. Zyaee**, Z. Zeng and T. Feurer, “THz-induced gas alignment in field enhancing waveguides,” *Opt. Express* **33**(2), 3315–3326 (2025). DOI:10.1364/OE.543482.

*This work demonstrated that using a THz waveguide significantly enhances the signal for THz-induced alignment of gas molecules by increasing the interaction length and locally enhancing the field strength, enabling detailed studies of alignment dynamics.*

- D. Rohrbach, B. J. Kang, **E. Zyaee**, and T. Feurer, “Wideband dispersion-free THz waveguide platform featuring field-enhancement,” *Sci. Rep.* **13**, 14949 (2023). DOI: 10.1038/s41598-023-41843-6.

*This paper presents the design and characterization of a novel metallic double-ridged THz waveguide platform exhibiting low loss, minimal dispersion, efficient coupling, and field enhancement.*

- A. S. Morillo-Candas, S. M. Augustin, E. Prat, A. Sarracini, J. Knurr, S. Zerdane, Z. Sun, N. Yang, M. Rebholz, H. Zhang, Y. Deng, X. Xie, **E. Zyaee**, D. Rohrbach, A. Cannizzo, A. Al-Haddad, K. A. Schnorr, C. Ott, T. Feurer, C. Bostedt, T. Pfeifer, G. Knopp, “Coherent nonlinear X-ray four-photon interaction with core-shell electrons,” *Nature* (Accepted).

*This study demonstrates coherent nonlinear four-wave mixing involving core-shell electrons using broadband X-ray pulses from a Free-Electron Laser, observing background-free signals including X-ray electronic Raman processes in neon, paving the way for multidimensional X-ray spectroscopy.*



## Bibliography

- [1] M. Mitchell Waldrop. The chips are down for Moore’s law. *Nature*, 530(7589):144–147, 2016. doi: 10.1038/530144a.
- [2] Mark Lundstrom. Moore’s law forever? *Science*, 299(5604):210–211, 2003. doi: 10.1126/science.1079567. URL <https://doi.org/10.1126/science.1079567>.
- [3] C. Joachim, J. K. Gimzewski, and A. Aviram. Electronics using hybrid-molecular and mono-molecular devices. *Nature*, 408:541–548, 2000. URL <https://doi.org/10.1038/35046000>.
- [4] G. Cuniberti, G. Fagas, and K. Richter, editors. *Introducing Molecular Electronics*. Springer, Berlin, Heidelberg, 2005. doi: 10.1007/b101525. URL <https://doi.org/10.1007/b101525>.
- [5] Dong Xiang, Xiaolong Wang, Chuancheng Jia, Takhee Lee, and Xuefeng Guo. Molecular-scale electronics: From concept to function. *Chemical Reviews*, 116(7):4318–4440, 2016. doi: 10.1021/acs.chemrev.5b00680. URL <https://doi.org/10.1021/acs.chemrev.5b00680>.
- [6] James R. Heath and Mark A. Ratner. Molecular electronics. *Physics Today*, 56(5):43–49, 2003. doi: 10.1063/1.1583533.
- [7] A. Aviram and M. A. Ratner. Molecular rectifiers. *Chem. Phys. Lett.*, 29(2):277–283, 1974. URL [https://doi.org/10.1016/0009-2614\(74\)85031-1](https://doi.org/10.1016/0009-2614(74)85031-1).
- [8] S. Mishra, D. Beyer, K. Eimre, J. Liu, R. Berger, O. Gröning, C. A. Pignedoli, K. Müllen, R. Fasel, J. Ma, and P. Ruffieux. Topological frustration induces unconventional magnetism in a nanographene. *Angewandte Chemie International Edition*, 59:12041–12046, 2020.
- [9] T. L. Cocker, V. Jelic, M. Gupta, S. J. Molesky, J. A. J. Burgess, G. De Los Reyes, L. V. Titova, Y. Y. Tsui, M. R. Freeman, and F. A. Hegmann. An ultrafast terahertz scanning tunnelling microscope. *Nature Photonics*, 7:620–625, 2013. doi: <https://doi.org/10.1038/nphoton.2013.151>. URL <https://doi.org/10.1038/nphoton.2013.151>.
- [10] Abraham Nitzan and Mark A. Ratner. Electron transport in molecular wire junctions. *Science*, 300(5624):1384–1389, 2003. doi: 10.1126/science.1081572. URL <https://doi.org/10.1126/science.1081572>.
- [11] Michael Thoss and Ferdinand Evers. Perspective: Theory of quantum transport in molecular junctions. *The Journal of Chemical Physics*, 148(3):030901, 2018. doi: 10.1063/1.5003306. URL <https://doi.org/10.1063/1.5003306>.
- [12] Z. He, F. Li, Y. Liu, F. Yao, L. Xu, X. Han, and K. Wang. Principle and applications of the coupling of surface plasmons and excitons. *Applied Sciences*, 10(5):1774, 2020. URL <https://doi.org/10.3390/app10051774>.

- [13] M. Tonouchi. Cutting-edge terahertz technology. *Nature Photonics*, 1(2):97–105, 2007. doi: 10.1038/nphoton.2007.3. URL <https://doi.org/10.1038/nphoton.2007.3>.
- [14] Tobias Kampfrath, Koichiro Tanaka, and Keith A. Nelson. Resonant and nonresonant control over matter and light by intense terahertz transients. *Nature Photonics*, 7:680–690, 2013. doi: 10.1038/nphoton.2013.184. URL <https://doi.org/10.1038/nphoton.2013.184>.
- [15] S. Fleischer, Y. Zhou, R. W. Field, and K. A. Nelson. Molecular orientation and alignment by intense single-cycle THz pulses. *Physical Review Letters*, 107(16):163603, 2011. doi: 10.1103/PhysRevLett.107.163603. URL <https://doi.org/10.1103/PhysRevLett.107.163603>.
- [16] T. L. Cocker, D. Peller, P. Yu, J. Repp, and R. Huber. Tracking the ultrafast motion of a single molecule by femtosecond orbital imaging. *Nature*, 539:263–267, 2016. URL <https://doi.org/10.1038/nature19816>.
- [17] D. Peller, L. Z. Kastner, T. Buchner, C. Roelcke, F. Albrecht, N. Moll, R. Huber, and J. Repp. Sub-cycle atomic-scale forces coherently control a single-molecule switch. *Nature*, 585:58–62, 2020. URL <https://doi.org/10.1038/s41586-020-2620-2>.
- [18] Martin Klessinger and Josef Michl. *Excited States and Photochemistry of Organic Molecules*. Wiley-VCH, New York, 1995. ISBN 978-0-471-18576-5.
- [19] Ahmed H. Zewail. Femtochemistry: Atomic-scale dynamics of the chemical bond. *The Journal of Physical Chemistry A*, 104(24):5660–5694, 2000. doi: 10.1021/jp001460h. URL <https://doi.org/10.1021/jp001460h>.
- [20] Shaul Mukamel. *Principles of Nonlinear Optical Spectroscopy*. Oxford University Press, New York, 1995. ISBN 978-0195132915.
- [21] R. Berera, R. van Grondelle, and J. T. M. Kennis. Ultrafast transient absorption spectroscopy: principles and application to photosynthetic systems. *Photosynthesis Research*, 101(2-3): 105–118, 2009. doi: 10.1007/s11120-009-9454-y. URL <https://doi.org/10.1007/s11120-009-9454-y>.
- [22] Yun-Shik Lee. *Principles of Terahertz Science and Technology*. Springer US, 2009. ISBN 978-0-387-09539-4. doi: 10.1007/978-0-387-09540-0.
- [23] Matthias C. Hoffmann and József A. Fülöp. Intense ultrashort terahertz pulses: generation and applications. *Journal of Physics D: Applied Physics*, 44(8):083001, 2011. doi: 10.1088/0022-3727/44/8/083001. URL <https://doi.org/10.1088/0022-3727/44/8/083001>.
- [24] József András Fülöp, Stelios Tzortzakis, and Tobias Kampfrath. Laser-driven strong-field terahertz sources. *Advanced Optical Materials*, 8(3):1900681, 2020. doi: 10.1002/adom.201900681. URL <https://doi.org/10.1002/adom.201900681>.

- [25] Dongfang Zhang, Arya Fallahi, Michael Hemmer, Xiaojun Wu, Moein Fakhari, Yi Hua, Huseyin Cankaya, Anne-Laure Calendron, Luis E. Zapata, Nicholas H. Matlis, and Franz X. Kärtner. Segmented terahertz electron accelerator and manipulator (steam). *Nature Photonics*, 12:336–342, 2018. doi: 10.1038/s41566-018-0138-z. URL <https://doi.org/10.1038/s41566-018-0138-z>.
- [26] Minh-Huong Ha-Thi, Gotard Burdzinski, Thomas Pino, and Pascale Changuenet. Transient absorption spectroscopy in inorganic systems. In Xiuhua Wang and Jianbao Li, editors, *Springer Handbook of Inorganic Photochemistry*, pages 107–130. Springer International Publishing, Cham, Switzerland, 2022. doi: 10.1007/978-3-030-63713-2\_5. URL [https://doi.org/10.1007/978-3-030-63713-2\\_5](https://doi.org/10.1007/978-3-030-63713-2_5).
- [27] Andrea Cannizzo, Ana María Blanco-Rodríguez, Amal El Nahhas, Jan Šebera, Sašo Zálíš, Antonín Viček, Jr., and Mostafa Chergui. Femtosecond fluorescence and intersystem crossing in rhenium(i) carbonyl–bipyridine complexes. *Journal of the American Chemical Society*, 130(28):8967–8975, 2008. doi: 10.1021/ja710763w. URL <https://doi.org/10.1021/ja710763w>.
- [28] Heinz A. Staab, Daqing Zhang, and Christoph Krieger. New electron donor–acceptor compounds, 51. [3](n,n′)-1,8;4,5-naphthalenetetracarboxdiimido-[3](2,7)pyrenophane and its [4,4] cyclophane homologue. *Liebigs Annalen der Chemie*, 1997(8):1551–1556, 1997. doi: 10.1002/jlac.199719970735. URL <https://doi.org/10.1002/jlac.199719970735>.

# Chapter 2

## Experimental Techniques

The investigations presented in this thesis rely on advanced ultrafast spectroscopic methods capable of probing molecular dynamics and electronic properties on femtosecond to picosecond timescales. This chapter introduces the technical basics of the two main experimental methods, time-resolved Terahertz Stark spectroscopy and transient absorption spectroscopy (TAS). Understanding the principles behind the generation and detection of intense terahertz (THz) pulses is crucial for interpreting the experiments presented in Chapters 3 and 4, where the THz pulse acts as a strong electric field perturbation. Similarly, the TAS principles, including data acquisition and analysis, is essential for understanding the excited state dynamics of the paracyclophane systems discussed in Chapters 5 and 6.

Section 2.1 presents the methods used for generating intense, single-cycle THz pulses, focusing on optical rectification via tilted-pulse-front pumping in  $\text{LiNbO}_3$ , and phase-sensitive detection using free-space electro-optic sampling. Section 2.2 outlines the principles of TAS, describes the various photophysical processes contributing to the measured signal, discusses common relaxation pathways observed, and explains the data analysis techniques, including Singular Value Decomposition (SVD) and Global Fitting, used to extract kinetic information.

### 2.1 Generation and Detection of Terahertz Pulses in Nonlinear Crystals

The generation of single-cycle terahertz (THz) pulses has been largely enabled by harnessing the nonlinear optical responses of certain crystals when they interact with ultrashort laser pulses from femtosecond lasers. Among the various techniques, Optical Rectification (OR) in non-centrosymmetric crystals serves as a mechanism for generating THz radiation, while the Pockels effect, is utilized for its coherent detection via free-space electro-optic sampling (EOS). In this section, we provide an overview of these concepts with emphasis on tilted pulse front pumping in Lithium Niobate ( $\text{LiNbO}_3$ ) for generating THz pulses and the principles of phased-resolved detection by EOS.

### 2.1.1 THz Generation via Optical Rectification

Optical rectification is a second-order nonlinear optical effect, a special case of difference frequency generation (DFG), which can produce a quasi-DC or low-frequency polarization within a nonlinear medium when illuminated by an intense optical field. When the optical field is from an ultrashort laser pulse with a broad spectrum, OR generates a time-varying polarization that follows the pulse's intensity envelope. This transient polarization acts as a source, radiating an electromagnetic pulse with a spectral bandwidth in the THz range<sup>1,2</sup>. Figure 2.1 shows components of the optical pulse at  $\omega_i$  and  $\omega_j = \omega_i + \Omega$  undergo difference frequency mixing, generating a THz component at  $\Omega = |\omega_j - \omega_i|$ .

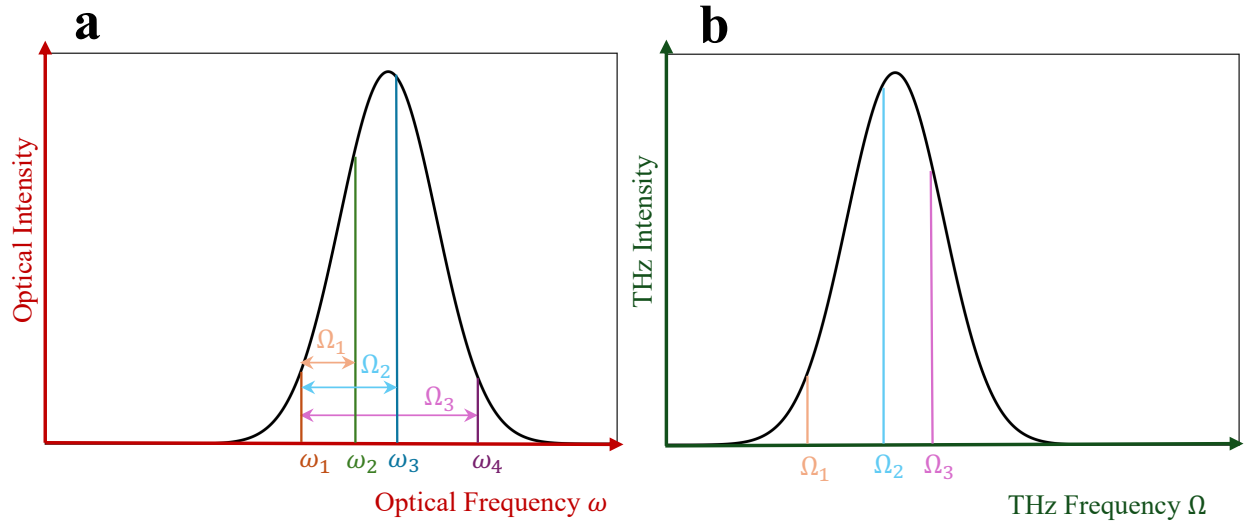


Figure 2.1: **Schematic of optical (a) and THz spectra (b) for optical rectification.** Frequency pairs within the optical spectrum map to THz outputs at corresponding difference frequencies  $\Omega = |\omega_j - \omega_i|$ .

For an optical pulse with a time-varying envelope  $E_0(t)$ , this rectified polarization  $P^{(2)}(t)$  tracks the pulse intensity envelope. This time-varying polarization becomes the source of the emitted THz radiation<sup>2</sup>. The relationship between the induced second-order polarization and the driving electric field is described using the second-order nonlinear susceptibility tensor,  $\chi_{ijk}^{(2)}$ . For optical rectification, the polarization is given by

$$P_i^{(2)}(\Omega) = \sum_{j,k} \epsilon_0 \chi_{ijk}^{(2)}(\Omega, \omega + \Omega, -\omega) E_j(\omega + \Omega) E_k^*(\omega). \quad (2.1)$$

The tensor elements  $\chi_{ijk}^{(2)}$  depend on the crystal's symmetry. For many common crystals used in THz generation, such as Lithium Niobate ( $\text{LiNbO}_3$ ), the tensor has only a few non-zero, independent elements<sup>3</sup>. The specific orientation of the crystal relative to the polarization of the incident optical pulse is therefore critical for maximizing the efficiency of THz generation.

### 2.1.2 Phase Matching and Tilted Pulse Front Pumping

As the optical pulse propagates through the nonlinear crystal, it continuously generates a THz wave. The total emitted THz field at the crystal's exit face is the coherent sum of the radiation from all points along the propagation path. For this summation to be constructive and lead to efficient THz generation, a phase-matching condition must be met<sup>1,2</sup>. In a frequency-domain picture, the general condition for phase matching (momentum conservation) requires equality of the wave vectors

$$k_{\text{opt}}(\omega) - k_{\text{opt}}(\omega - \Omega) = k_{\text{THz}}(\Omega). \quad (2.2)$$

In the time-domain picture this corresponds to velocity matching, meaning the group velocity of

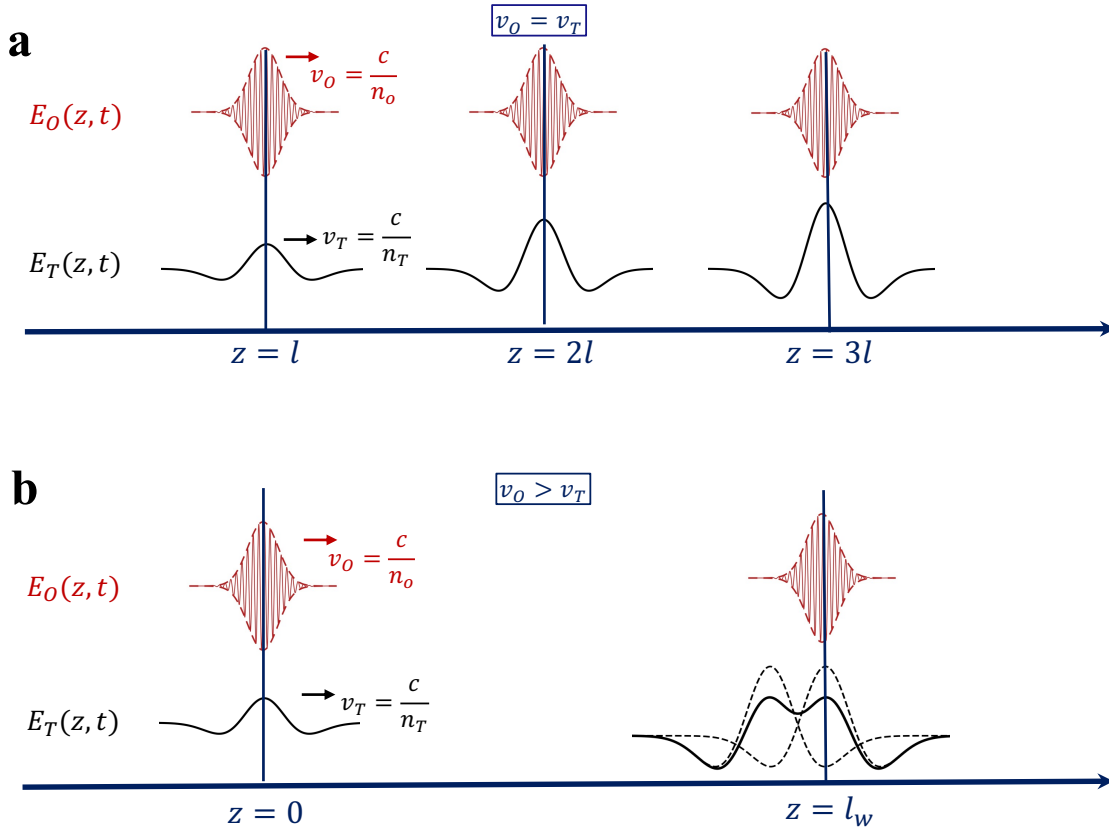


Figure 2.2: **The effect of velocity matching on THz field amplification.** **a** Linear amplification of the THz field as the optical group and THz phase velocities are matched. **b** Destructive interference of THz waves from two nonlinear slices separated by the walk-off distance  $l_w$ . Dotted curves show the individual contributions.

the optical pump pulse,  $v_O = c/n_{g,O}$ , must match the phase velocity of the generated THz wave,  $v_T = c/n_{Ph,T}$ . Here,  $n_{g,O}$  is the optical group index at the pump frequency and  $n_{Ph,T}$  is the THz phase index. This condition,  $n_{g,O} \approx n_{Ph,T}$ , ensures that the newly generated THz pulses remain in phase with the optical pump pulse as they travel together through the crystal, allowing for constructive interference and linear amplification of the THz field<sup>1,2</sup>.



For 800 nm pumping, the optimum tilt angle is approximately  $\theta_c \approx 64^\circ$ <sup>2</sup>. The tilt is introduced using a diffraction grating followed by imaging optics that reimage the angularly dispersed beam into the LiNbO<sub>3</sub> crystal. The resulting geometry enables efficient phase matching over millimeter scale interaction lengths, allowing emission of intense single-cycle THz pulses with peak fields exceeding 1 MV/cm.

### 2.1.3 Detection of THz Pulses via Free-Space Electro-Optic Sampling

Free space electro-optic (EO) sampling is a coherent, phase-resolved detection technique that measures the time-dependent electric field of a THz pulse,  $E_{\text{THz}}(t)$ . It is based on the Pockels effect, which is the inverse process of optical rectification. In the Pockels effect, a low-frequency or DC electric field, in this case the field of the THz pulse, induces birefringence in a noncentrosymmetric crystal<sup>2</sup>. This birefringence is proportional to the THz field strength. The principle of EOS is

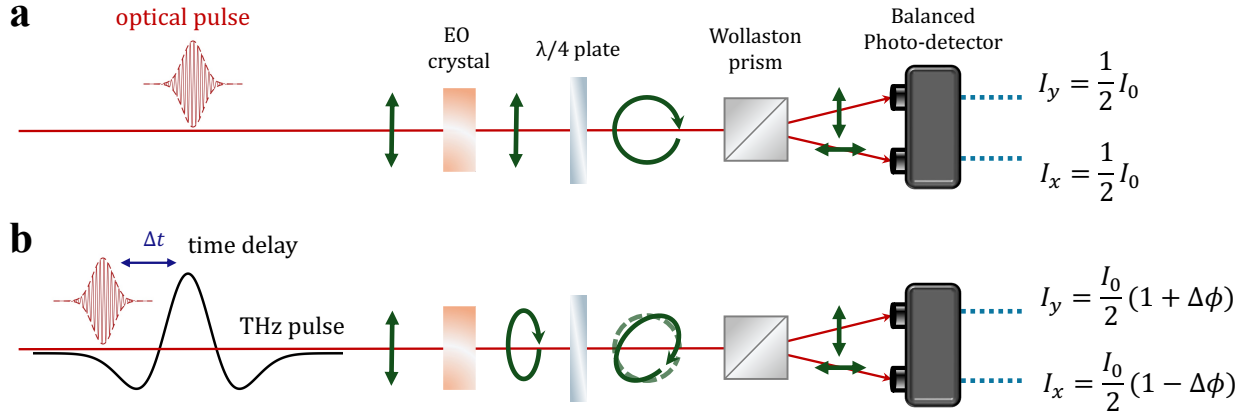


Figure 2.4: **Schematic of a standard free space EO sampling setup.** Probe polarization states, without **a** and with **b** the THz field, are shown before and after the polarization optics.

illustrated in Figure 2.4. The THz pulse and a time-delayed, linearly polarized optical probe pulse are collinearly focused onto an electro-optic crystal (e.g., ZnTe)<sup>4</sup>. The electric field of the THz pulse,  $E_{\text{THz}}$ , induces a transient birefringence in the crystal, altering its refractive index, meaning it creates a temporary difference between the refractive indices along two orthogonal axes ( $n_x \neq n_y$ ). This birefringence causes a phase retardation,  $\Delta\phi$ , between the components of the probe pulse polarized parallel and perpendicular to the THz field. This phase retardation is linearly proportional to the instantaneous THz field strength

$$\Delta\phi = \frac{\omega L}{c} n_o^3 r_{41} E_{\text{THz}}, \quad (2.5)$$

where  $\omega$  is the probe frequency,  $L$  is the crystal thickness,  $n_o$  is the optical refractive index, and  $r_{41}$  is the electro-optic coefficient of the crystal<sup>2</sup>. Selecting the crystal thickness requires balancing sensitivity against bandwidth. A thicker crystal increases the interaction length, yielding a stronger signal. However, it also worsens the "walk-off" caused by the velocity mismatch between the group velocity of the optical probe and the phase velocity of THz pulse. This temporal



smearing attenuates high frequency components, thus reducing the detection bandwidth. A thinner crystal is therefore used to minimize this mismatch and preserve a broad bandwidth.

This THz induced polarization change, from linear to slightly elliptical, is then analyzed. The probe beam passes through a quarter-wave plate and a Wollaston prism, which separates it into two orthogonal polarization components. These components are directed onto a pair of balanced photodiodes. The differential signal measured by the photodiodes,  $I_s = I_{\perp} - I_{\parallel}$ , is directly proportional to the instantaneous electric field of the THz pulse at the moment the probe pulse traversed the crystal,

$$I_s \propto I_0 \Delta\phi \propto E_{THz}. \quad (2.6)$$

By varying the time delay,  $\Delta t$ , between the THz and probe pulses, the entire temporal profile of the THz electric field can be sampled, providing both its amplitude and phase information.

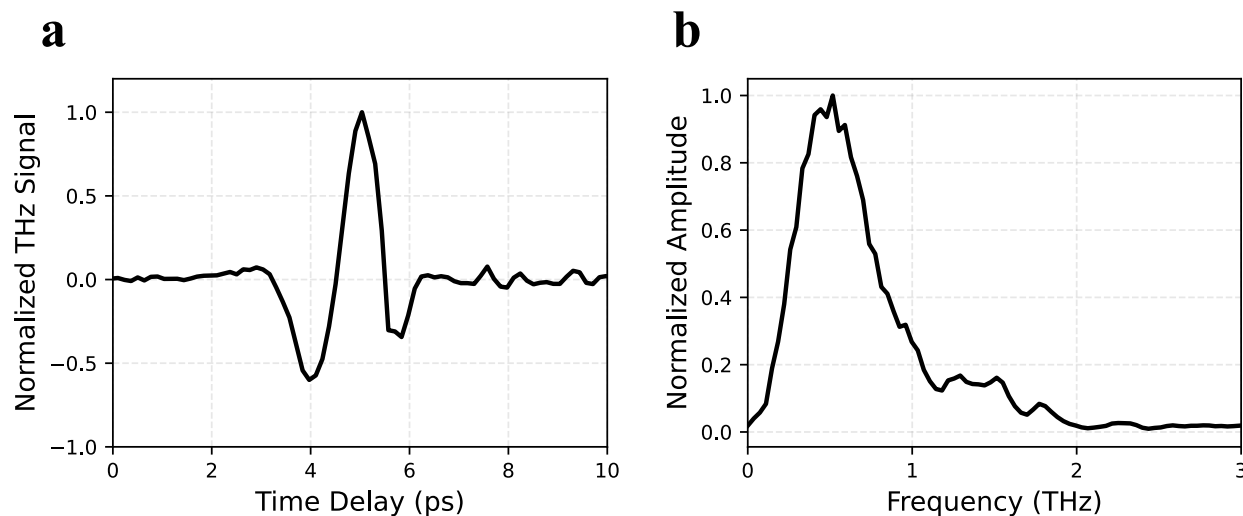


**Figure 2.5: Characterization of the THz pulse used in this work.** **a** The temporal waveform of the electric field, generated via tilted pulse front pumping in LiNbO<sub>3</sub> and measured at the sample position by electro optic sampling in ZnTe. **b** The corresponding amplitude spectrum obtained from a Fourier transform, showing a center frequency of 0.5 THz.

The output of our tilted pulse front setup in LiNbO<sub>3</sub>, characterized using free space electro-optic sampling in a 100  $\mu\text{m}$  thick ZnTe crystal, is shown in Figure 2.5. The measured time domain waveform of the THz electric field is a nearly single cycle pulse with a duration of approximately 2 picoseconds, as seen in Figure 2.5a. The corresponding amplitude spectrum, calculated via a Fourier transform of the temporal data, is presented in Figure 2.5b. The spectrum is centered at 0.5 THz and has a broad bandwidth suitable for the spectroscopic experiments described in this work.

## 2.2 Transient Absorption Spectroscopy

Photochemical reactions originate from an electronically excited state, a high energy configuration reached when a molecule absorbs a photon. Exploring the chemical and physical processes initiated by photoexcitation is key to understanding a wide range of fundamental phenomena. The

journey of a molecule after absorbing a photon is a complex cascade of competing events governed by the principles of photophysics and photochemistry<sup>5</sup>. The initial events that dictate the fate of a molecule after absorbing a photon occur on incredibly short timescales, typically from femtoseconds ( $10^{-15}$  s) to nanoseconds ( $10^{-9}$  s). Accessing these events requires experimental techniques with temporal resolution<sup>5</sup>.

Transient Absorption Spectroscopy (TAS), or pump-probe spectroscopy, enables the real-time observation of ultrafast molecular dynamics. It uses ultrashort laser pulses to excite molecules into a non-equilibrium state and monitor their evolution over time. The technique reveals excited state lifetimes, relaxation dynamics, and the formation of transient species<sup>6,7</sup>.

This chapter provides an overview of the principles and applications of femtosecond Transient Absorption Spectroscopy. We will begin by description of a typical experimental setup. The core of the section will focus on the variety of relaxation processes that can be studied using TAS, including vibrational cooling, internal conversion, and intersystem crossing. Finally, we will discuss the methods used to analyze the complex data of these experiments.

### 2.2.1 Principles of Transient Absorption

To observe the ultrafast events in photochemical reactions, a UV-vis transient absorption spectroscopy which provides femtosecond temporal resolution, is used. In femtosecond transient absorption spectroscopy, the excitation source is typically an amplified ultrashort pulse laser system. Such systems are most commonly based on Ti:Sapphire technology and provide pulses with durations shorter than 100 fs at repetition rates in the range of 1-10 kHz. The general layout is depicted in Figure 2.6.

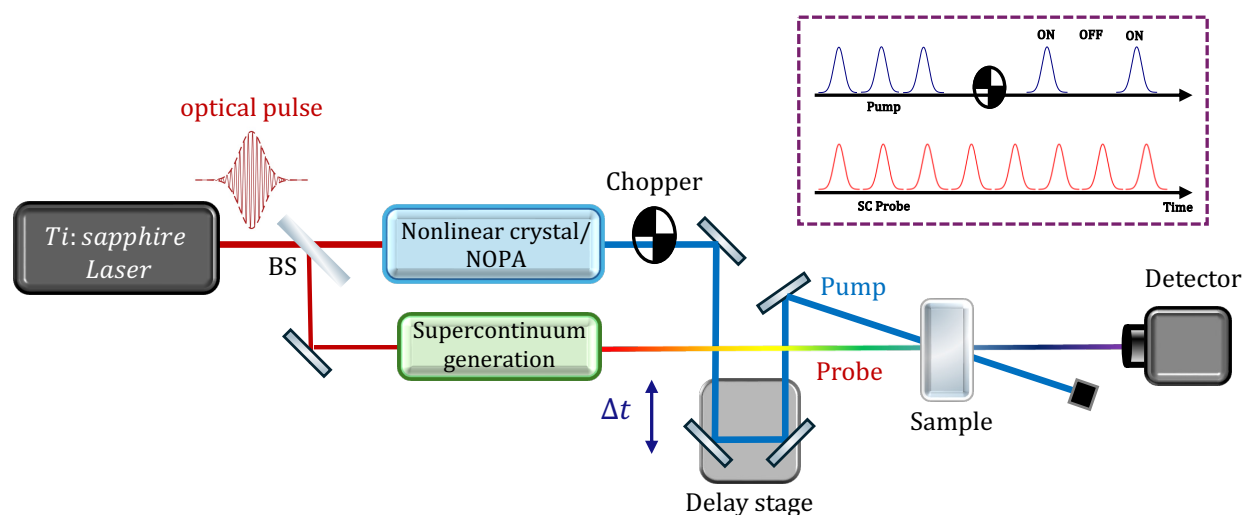


Figure 2.6: **Schematic of a basic femtosecond transient absorption spectroscopy setup.**

Transient absorption spectroscopy measures the time dependent change of the intensity of the probe beam transmitted by the sample after photoexcitation. The measured signal expressed as the differential absorbance  $\Delta A$ , defined as the absorbance of the photoexcited (pumped) sample minus the absorbance of the sample in its ground state (unpumped)

$$\Delta A(\lambda, t) = A_{\text{pumped}}(\lambda, t) - A_{\text{unpumped}}(\lambda, t) = -\log_{10} \left( \frac{I_{\text{pumped}}(\lambda, t)}{I_{\text{unpumped}}(\lambda, t)} \right), \quad (2.7)$$

where  $\lambda$  is the probe wavelength,  $t$  is the time delay between the pump and probe pulses,  $I_{\text{pumped}}$  and  $I_{\text{unpumped}}$  are the probe intensity transmitted by the sample with and without the pump respectively<sup>6</sup>.

The  $\Delta A$  signal is a composite of several distinct photophysical contributions, reflecting contributions of the different states created by the pump, which can be positive namely excited state absorption or negative, ground state bleaching, and stimulated emission. These processes are schematically depicted in Figure 2.7, which shows their origin in the context of electronic energy levels.

1. **Ground State Bleach (GSB):** The pump pulse excites a fraction of the molecules from the ground state  $S_0$  to an excited state  $S_n$ . This depletion of the ground state population reduces the sample's ability to absorb light at wavelengths corresponding to the ground state absorption band. This results in a negative  $\Delta A$  signal that spectrally mirrors the steady state absorption spectrum<sup>6,8</sup>.
2. **Excited State Absorption (ESA):** Once populated, the excited state (e.g.,  $S_1$ ) can itself absorb a probe photon, promoting the molecule to a higher excited state  $S_n$ . This is a new absorption feature that is absent in the unpumped sample and therefore appears as a positive  $\Delta A$  signal<sup>6,8</sup>.
3. **Stimulated Emission (SE):** The probe pulse can stimulate the excited molecule to relax back to the ground state, emitting a photon. This adds intensity to the transmitted probe beam, effectively appearing as a negative absorbance. The SE spectrum typically resembles a mirror image of the steady state fluorescence spectrum<sup>6,8</sup>.

By recording the full  $\Delta A$  spectrum at a series of pump-probe time delays, a complete two-dimensional data map is constructed.

### 2.2.2 Relaxation Processes and Dynamics

The time-resolved data from a TAS experiment provides information about the various relaxation pathways available to a photoexcited molecule. Upon absorbing a photon of appropriate energy, a molecule is promoted from its ground electronic state ( $S_0$ ) to a higher singlet excited state ( $S_n$ ). From this highly energetic and unstable state, the molecule seeks to dissipate its excess energy through several competing pathways<sup>6</sup>. These processes are summarized schematically in the Perrin-Jablonski diagram (Figure 2.8) and are described in more detail below.

#### Vibrational and Solvent Relaxation

Immediately after photoexcitation to a high energy vibronic level of an electronic state  $S_n$ , the molecule has significant excess vibrational energy. The relaxation from this "hot" state is a complex, multi-step process that occurs on a timescale of tens of femtoseconds to a few picoseconds. In solution, this involves two primary non-radiative pathways:

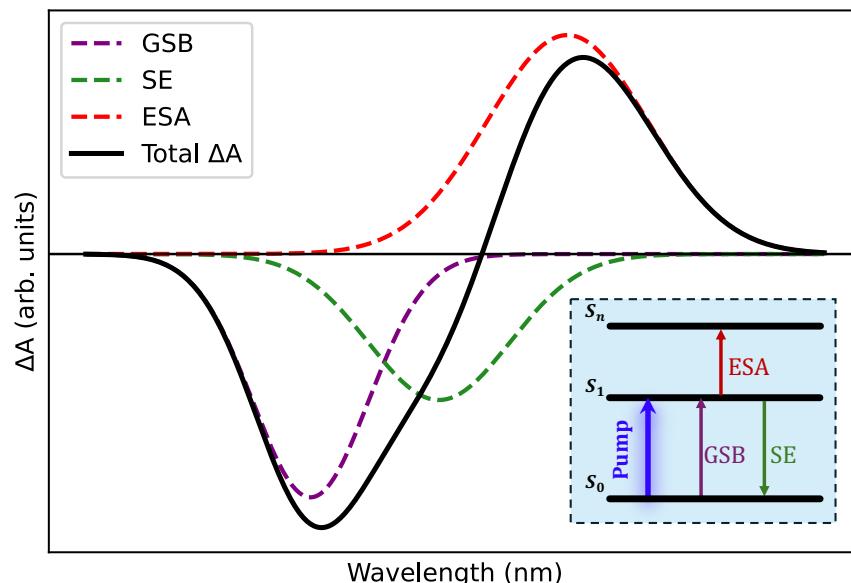


Figure 2.7: **Schematic representation of TA signal contributions.** Negative bands originate from ground state bleaching (GSB) and stimulated emission (SE), whereas positive bands arise from excited state absorption (ESA). The total measured  $\Delta A$  spectrum results from the superposition of these processes. The inset illustrates the corresponding electronic energy-level diagram, indicating the origin of GSB, SE, and ESA transitions.

- **Vibrational Relaxation (VR):** The excess vibrational energy, initially localized in Franck-Condon active modes, rapidly redistributes among all the vibrational modes of the molecule<sup>6,8</sup>.
- **Solvent Reorganization:** If the molecule's dipole moment changes upon excitation (which is especially true for charge-transfer states), the polar solvent molecules must reorient themselves to stabilize the new charge distribution. This reorientation process is also an ultrafast relaxation pathway<sup>8</sup>.

In TAS data, these combined effects (vibrational cooling and solvent reorganization) are often difficult to separate and are observed as a dynamic shift or narrowing of the ESA and SE bands. As the molecule cools to the bottom of the excited state potential well, the spectral features sharpen and may shift to the blue or red as the molecule finds its new equilibrium geometry<sup>6,8</sup>.

### Electronic State Transitions

After these initial cooling and relaxation processes have brought the molecule to the bottom of the excited state potential well, the subsequent evolution is governed by electronic transitions between states of different energy and spin multiplicity. These transitions determine the ultimate fate of the excitation and can proceed through a variety of radiative and non-radiative channels. The most relevant electronic processes are outlined below.

- **Internal Conversion (IC):** This is a non radiative, isoenergetic transition between two electronic states of the same spin multiplicity (e.g.,  $S_2 \rightarrow S_1$  or  $S_1 \rightarrow S_0$ ). IC is typically ultrafast

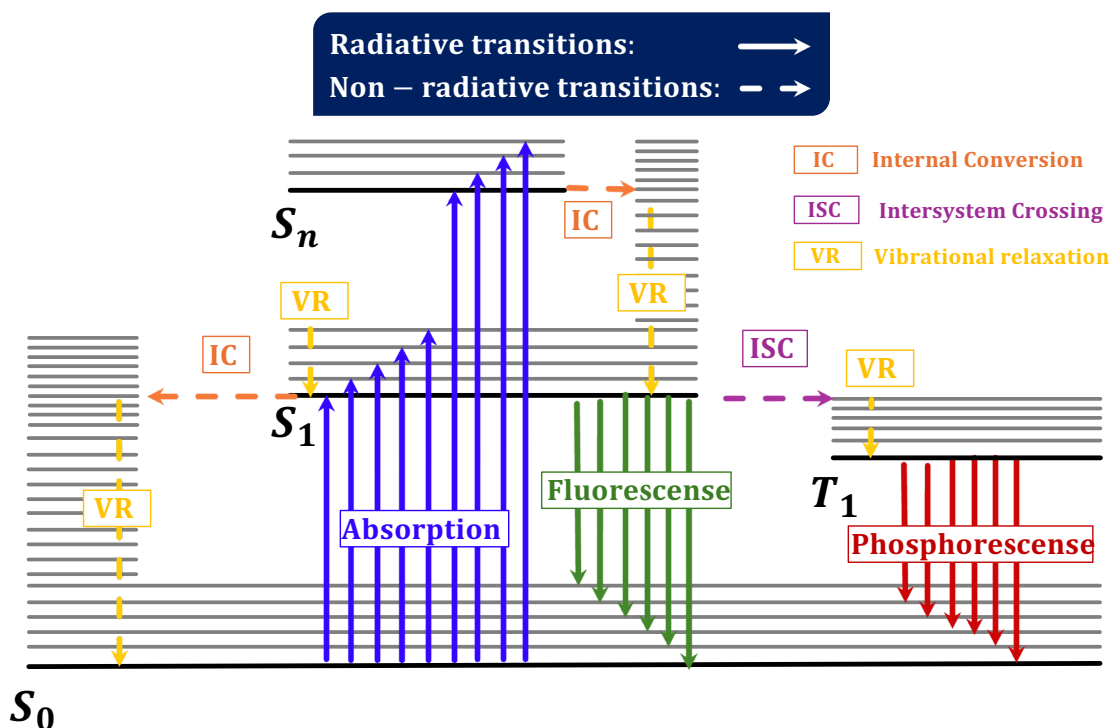


Figure 2.8: **Perrin-Jablonski diagram illustrating the relaxation pathways of an excited molecule.** Solid arrows represent radiative processes (absorption, fluorescence, phosphorescence), while dashed arrows denote non-radiative processes (internal conversion, intersystem crossing, vibrational relaxation).

between upper excited states ( $S_n \rightarrow S_1 < 10$  ps) but much slower from  $S_1$  to  $S_0$ , governed by the energy gap law (larger energy gaps lead to slower rates). In TAS, internal conversion is observed as the decay of the ESA from the higher excited state ( $S_n$ ). Depending on the system, this process may be accompanied by the appearance of new ESA or SE signals associated with the lower state ( $S_1$ )<sup>6,8</sup>.

- **Intersystem Crossing (ISC):** This is a non radiative transition between two electronic states of different spin multiplicity, most commonly from a singlet state to a triplet state (e.g.,  $S_1 \rightarrow T_1$ ). While spin forbidden, ISC can be efficient, especially in molecules containing heavy atoms that enhance spin-orbit coupling. ISC rates vary widely, from picoseconds to microseconds. TAS can track ISC by observing the decay of the  $S_1$  spectral features (ESA and SE) and the simultaneous rise of a new, often very long-lived ESA feature corresponding to the triplet state<sup>6,8</sup>.
- **Fluorescence and Phosphorescence:** These are radiative decay processes from  $S_1 \rightarrow S_0$  and  $T_1 \rightarrow S_0$ , respectively. While TAS primarily measures changes in absorption, the lifetime of the  $S_1$  state measured by TAS (via the decay of its ESA and SE signals) should match the fluorescence lifetime measured by other techniques<sup>6,8</sup>.

### 2.2.3 Data Analysis

The raw data from a time-resolved transient absorption experiment forms a two-dimensional matrix,  $A(\lambda, t)$ , containing the differential absorbance as a function of both probe wavelength ( $\lambda$ ) and pump-probe time delay ( $t$ ). One can analyze the data that involve examining kinetic traces at a few selected wavelengths corresponding to spectral maxima or minima. However, such an approach is often insufficient and can be misleading. Kinetic traces at single wavelengths can be distorted by overlapping positive (excited state absorption) and negative (ground state bleaching, stimulated emission) signals, or by dynamic spectral shifts caused by processes like vibrational relaxation or solvent reorganization.

To extract a physically meaningful model, a global fitting (GF) is employed<sup>9,10</sup>. This method analyzes the entire dataset simultaneously, fitting all wavelengths and time delays to a kinetic model. The fundamental assumption is that the overall temporal evolution of the system can be described as a sum of a discrete number of independent, first-order kinetic processes<sup>9,10</sup>. This powerful approach ensures that the determined lifetimes are consistent across the entire spectrum and allows for the deconvolution of spectrally overlapping components.

To improve computational efficiency and suppress noise without losing relevant information, the global fit is performed on a reduced dataset generated via Singular Value Decomposition (SVD).

A time-resolved spectrum, represented by the data matrix  $A(\lambda, t)$ , can be described as the sum of the true signal matrix,  $\hat{A}(\lambda, t)$ , which contains all information about the spectral evolution, and a matrix  $\Xi(\lambda, t)$ , which consists of stochastic, normally-distributed noise with a mean of zero<sup>8</sup>,

$$A(\lambda, t) = \hat{A}(\lambda, t) + \Xi(\lambda, t). \quad (2.8)$$

Without prior knowledge of the system's temporal evolution, we can assume that the signal matrix  $\hat{A}$  can be factorized as a superposition of the contributions of  $p$  different components. This is known as the bilinear model assumption<sup>10</sup>:

$$\hat{A}(\lambda, t) = \sum_{l=1}^p \epsilon_l(\lambda) c_l(t) \quad (2.9)$$

where  $\epsilon_l(\lambda)$  is the spectral distribution and  $c_l(t)$  is the temporal evolution of the  $l$ -th component. This model implies that the temporal evolution of each component's spectrum involves changes in amplitude only, not in band shape<sup>11,12</sup>. For a data matrix  $A$  composed of discrete wavelengths  $\lambda_i$  and time delays  $t_k$ , this is expressed as:

$$A(\lambda_i, t_k) = \sum_{l=1}^p \epsilon_l(\lambda_i) c_l(t_k) + \Xi(\lambda_i, t_k). \quad (2.10)$$

SVD is the procedure used to determine the number of significant components,  $p$ , and to separate the signal from the noise contribution. SVD decomposes the experimental data matrix  $A(\lambda, t)$  into the product of three matrices:

$$A = USV^T, \quad (2.11)$$

where  $U$  is an orthogonal matrix whose columns are the basis spectra,  $S$  is a diagonal matrix containing the singular values ( $s_i$ ), and  $V^T$  is an orthogonal matrix whose rows contain the corresponding basis kinetic traces. The singular values are ordered in descending magnitude ( $s_1 > s_2 > \dots$ ) and represent the weight of each component pair ( $U_i, V_i$ ) in the overall decomposition.

A plot of the singular values versus their index (Figure 2.9) is used to determine the number of components that are significantly different from the noise. Typically, a sharp drop or "elbow" is observed, separating a small number of large singular values (representing the signal) from a large number of small, slowly decaying values (representing the noise). The number of significant singular values, denoted here as  $p$ , provides a robust, model-free estimate of the data's rank and indicates the number of basis vectors that are sufficient to describe the observed dynamics<sup>8,11,12</sup>.

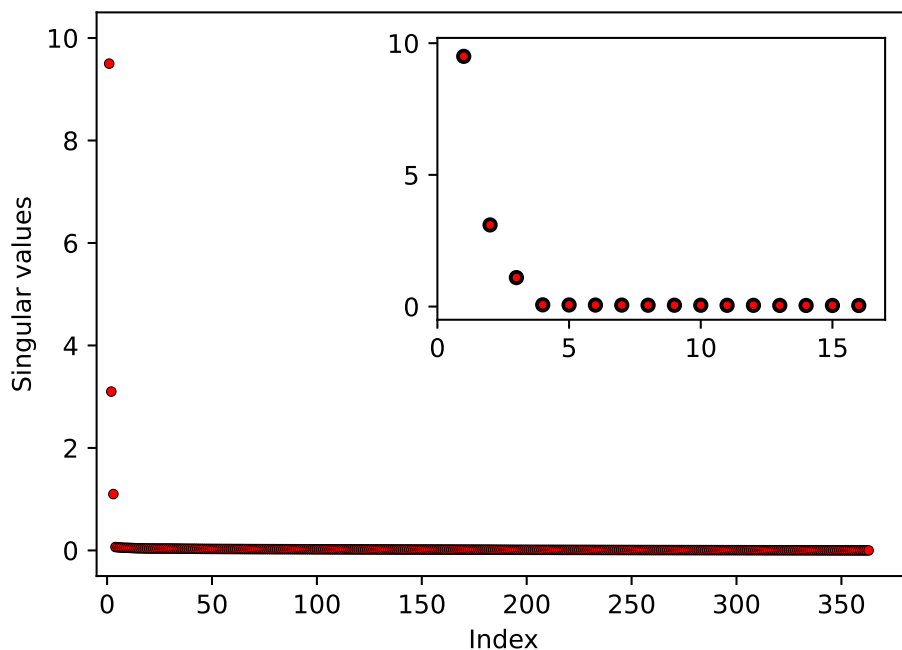


Figure 2.9: **A representative plot of singular values from an SVD analysis.** The number of values clearly above the noise floor ( $p$ ) is determined to select the basis vectors for the subsequent global fit.

The spectral and kinetic basis vectors produced by SVD are mathematical constructs and are not, in general, directly representative of a physical process. To extract a physically meaningful interpretation, a kinetic model must be assumed, which is then fitted to the basis vectors<sup>8,13</sup>. For the intramolecular relaxation processes studied in this work, a model governed by a sum of exponential decays is the most reasonable choice. The temporal evolution is thus described by:

$$\tilde{V}_i = \left[ \sum_{j=1}^k a_{ij} e^{-t/\tau_j} \right] \otimes \text{IRF}(t) \quad (2.12)$$

where  $k$  is the number of exponential decays,  $\tau_j$  are the lifetimes, and  $a_{ij}$  are the amplitudes. The Gaussian term describes the convolution with the Instrument Response Function (IRF), where

$\Delta_{IRF}$  is the full width at half-maximum and  $t_0$  is the time-zero. The explicit analytical expression for this convolution is given by<sup>9</sup>:

$$S(t) = \frac{\exp(-kt)}{2} \exp\left(k\left(t_0 + \frac{k\sigma^2}{2}\right)\right) \left[1 + \operatorname{erf}\left(\frac{t - (t_0 + k\sigma^2)}{\sigma\sqrt{2}}\right)\right], \quad (2.13)$$

where  $k = 1/\tau$ , and the IRF width  $\sigma = \Delta_{IRF}/(2\sqrt{2\ln 2})$ .

In a Global Fit (GF) analysis, all significant kinetic basis traces ( $\tilde{V}_i$ ) are fitted simultaneously to equation 2.12, where the lifetimes ( $\tau_j$ ) are treated as common (global) parameters for all traces. This procedure yields the coefficients  $a_{i,j}$ , which are then used to calculate the Decay-Associated Spectra (DAS). The DAS, which correspond to the characteristic lifetimes  $\tau_j$ , are constructed by summing the properly weighted spectral basis vectors ( $U_i$ ):

$$\text{DAS}_{j=1\dots k} = \sum_{i=1}^p a_{i,j} \cdot s_i \cdot U_i \quad (2.14)$$

The resulting DASs contain the spectral contribution corresponding to each characteristic lifetime  $\tau_j$ . As mentioned, this approach assumes no time-dependent changes in the spectral band shapes within the data. By examining the series of DAS, from the fastest process to the slowest, one can reconstruct the cascade of events following photoexcitation. A DAS with both positive and negative features, often represents the transition from one transient species to another; the positive portion signifies the decay of the precursor species, while the negative portion signifies the rise of the successor species. The final component represents the spectrum of any photoproducts or long-lived states that can persist beyond the temporal window of the measurement.

## Summary

This chapter presents the experimental methodologies used for the work presented in this thesis. The generation of intense, phase-stable, single-cycle THz pulses via optical rectification, particularly using the tilted-pulse-front pumping scheme in LiNbO<sub>3</sub>, was described, along with their coherent detection through electro-optic sampling. These techniques form the basis for the time-resolved THz Stark spectroscopy experiments discussed in Chapter 3 and 4. Furthermore, the principles of femtosecond Transient Absorption Spectroscopy (fTAS) were outlined, covering the pump-probe scheme, the origins of transient signals (GSB, SE, ESA), typical excited state relaxation processes, and the common methods for analyzing the resulting complex datasets, namely Singular Value Decomposition and Global Fitting to extract Decay-Associated Spectra (DAS) relevant to Chapter 5 and 6.



## Bibliography

- [1] József András Fülöp, Stelios Tzortzakis, and Tobias Kampfrath. Laser-driven strong-field terahertz sources. *Advanced Optical Materials*, 8(3):1900681, 2020. doi: 10.1002/adom.201900681. URL <https://doi.org/10.1002/adom.201900681>.
- [2] Yun-Shik Lee. *Principles of Terahertz Science and Technology*, volume 129 of *Springer Series in Optical Sciences*. Springer US, Boston, MA, 2009. ISBN 978-0-387-09540-0. doi: 10.1007/978-0-387-09540-0.
- [3] L. Xu, X.-C. Zhang, and D. H. Auston. Terahertz beam generation by femtosecond optical pulses in electro-optic materials. *Applied Physics Letters*, 61(15):1784–1786, 1992. doi: 10.1063/1.108426. URL <https://doi.org/10.1063/1.108426>.
- [4] Nick C. J. van der Valk, Paul C. M. Planken, Anton N. Buijserd, and Huib J. Bakker. Influence of pump wavelength and crystal length on the phase matching of optical rectification. *J. Opt. Soc. Am. B*, 22(8):1714–1718, Aug 2005. doi: 10.1364/JOSAB.22.001714. URL <https://opg.optica.org/josab/abstract.cfm?URI=josab-22-8-1714>.
- [5] Martin Klessinger and Josef Michl. *Excited States and Photochemistry of Organic Molecules*. Wiley-VCH, 1st edition, 1995. ISBN 978-0-471-18576-5.
- [6] Minh-Huong Ha-Thi, Gotard Burdzinski, Thomas Pino, and Pascale Changenet. Transient absorption in inorganic systems. 2022. doi: 10.1007/978-3-030-63713-2\_5. URL <https://hal.science/hal-02991509>.
- [7] X. Qin, G. Zhang, L. Chen, Q. Wang, G. Wang, H. Zhang, Y. Li, and C. Liu. A review: Principles and applications of high-pressure in situ time-resolved transient absorption spectroscopy. *Ultrafast Science*, 4(Article 0044), 2024. doi: 10.34133/ultrafastscience.0044. URL <https://doi.org/10.34133/ultrafastscience.0044>. Submitted 16 July 2023; Accepted 2 October 2023; Published 1 February 2024.
- [8] Nina Schönbächler. *Steady State and Time-resolved Raman and Absorption Spectroscopies for Chemical Recognition and Molecular Dynamical Studies*. PhD thesis, Universität Bern, Bern, Switzerland, 2013.
- [9] Chavdar Slavov, Helvi Hartmann, and Josef Wachtveitl. Implementation and evaluation of data analysis strategies for time-resolved optical spectroscopy. *Analytical Chemistry*, 87(4):2328–2336, 2015. doi: 10.1021/ac504348h. URL <https://doi.org/10.1021/ac504348h>.
- [10] C. Ruckebusch, M. Sliwa, P. Pernot, A. de Juan, and R. Tauler. Comprehensive data analysis of femtosecond transient absorption spectra: A review. *Journal of Photochemistry and Photobiology C: Photochemistry Reviews*, 13(1):1–27, 2012. doi: 10.1016/j.jphotochemrev.2011.10.002. URL <https://doi.org/10.1016/j.jphotochemrev.2011.10.002>.

- [11] Andrea Cannizzo, Ana María Blanco-Rodríguez, Amal El Nahhas, Jan Šebera, Sašo Záliš, Antonín Viček, Jr., and Mostafa Chergui. Femtosecond fluorescence and intersystem crossing in rhenium(i) carbonyl–bipyridine complexes. *Journal of the American Chemical Society*, 130(28):8967–8975, 2008. doi: 10.1021/ja710763w. URL <https://doi.org/10.1021/ja710763w>.
- [12] M. Nazari, C. D. Bösch, A. Rondi, A. Francés-Monerris, M. Marazzi, E. Lognon, M. Gazzetto, S. M. Langenegger, R. Häner, T. Feurer, A. Monari, and A. Cannizzo. Ultrafast dynamics in polycyclic aromatic hydrocarbons: the key case of conical intersections at higher excited states and their role in the photophysics of phenanthrene monomer. *Phys. Chem. Chem. Phys.*, 21:16981–16988, 2019. doi: 10.1039/C9CP03147B. URL <https://doi.org/10.1039/C9CP03147B>.
- [13] Maryam Nazari Haghighi Pashaki, Nina Mosimann-Schönbächler, Aaron Riede, Michela Gazzetto, Ariana Rondi, and Andrea Cannizzo. Two-dimensional ultrafast transient absorption spectrograph covering deep-ultraviolet to visible spectral region optimized for biomolecules. *Methods and Applications in Fluorescence*, 9(4):045001, 2021. doi: 10.1088/2515-7647/ac0805. URL <https://doi.org/10.1088/2515-7647/ac0805>.

# Chapter 3

## Time-resolved THz Stark Spectroscopy of Molecules in Solution

Bong Joo Kang<sup>1,2</sup>, Egmont J. Rohwer<sup>1</sup>, David Rohrbach<sup>1</sup>, Elnaz Zyaee<sup>1</sup>, Maryam Akbarimoosavi<sup>1</sup>, Zoltan Ollmann<sup>1</sup>, Gleb Sorokhov<sup>3</sup>, Alex Borgoo<sup>4</sup>, Michele Cascella<sup>4</sup>, Andrea Cannizzo<sup>1</sup>, Silvio Decurtins<sup>3</sup>, Robert J. Stanley<sup>5</sup>, Shi-Xia Liu<sup>3</sup>, Thomas Feurer<sup>1</sup>

<sup>1</sup> Institute of Applied Physics, University of Bern, 3012 Bern, Switzerland

<sup>2</sup> Division of Advanced Materials, Korea Research Institute of Chemical Technology (KRICT), 34114 Daejeon, Republic of Korea

<sup>3</sup> Department of Chemistry, Biochemistry and Pharmaceutical Sciences, University of Bern, 3012 Bern, Switzerland

<sup>4</sup> Department of Chemistry and Hylleraas Centre for Quantum Molecular Sciences, University of Oslo, N-0315 Oslo, Norway

<sup>5</sup> Department of Chemistry, Temple University, Philadelphia, PA 19122, USA

This work has been published in Nature Communications: <https://doi.org/10.1038/s41467-024-48164-w>.

---

### Abstract

For decades, it was considered all but impossible to perform Stark spectroscopy on molecules in a liquid solution, because their concomitant orientation to the applied electric field results in overwhelming background signals. A way out was to immobilize the solute molecules by freezing the solvent. While mitigating solute orientation, freezing removes the possibility to study molecules in liquid environments at ambient conditions. Here we demonstrate time-resolved THz Stark spectroscopy, utilizing intense single-cycle terahertz pulses as electric field source. At THz frequencies, solute molecules have no time to orient their dipole moments. Hence, dynamic Stark spectroscopy on the time scales of molecular vibrations or rotations in both non-polar and polar solvents at arbitrary temperatures is now possible. We verify THz Stark spectroscopy for two judiciously selected molecular systems and compare the results to conventional Stark spectroscopy and first principle calculations.

---

## 3.1 Introduction

Stark spectroscopy is an invaluable tool to reveal information about physicochemical properties of molecules<sup>1,2,3,4,5,6,7,8,9</sup>. Sufficiently strong electric fields modify absorption spectra of isotropic ensembles of molecules if ground and excited state energy eigenvalues of the respective optical transition shift in energy due to the interaction with the applied electric field. In most cases, the interaction can be treated as a perturbation and expanded in a power series of the electric field. To first order, Stark spectroscopy reveals information on the electric dipoles, and to second order, on the induced dipoles, i.e. on the polarizabilities, of the two states. The former is referred to as the linear Stark effect (Fig. 3.1a), the latter is called the quadratic Stark effect (Fig. 3.1b). It is important to note that only a nonzero difference between ground and excited state dipole or polarizability results in a modified absorption spectrum, and consequently, only those differences can be extracted from a measurement. While a change in dipole moment, for instance, reflects the degree of charge separation or charge transfer associated with the transition, a change in polarizability describes the sensitivity of a transition to an external electric field<sup>2</sup>. These effects are also known as electro-chromism<sup>5</sup> and a corresponding measurement gives insight in, for instance, photo-induced electron or charge transfer<sup>10,11,12,13,14</sup>, nonlinear material properties<sup>2,4,8,15</sup>, biological organization and energy tuning<sup>16,17,18,19,20,21</sup>, or solvato-chromism. Also, vibrational Stark spectroscopy of CO or CN ligands has developed into an important tool to measure in situ electric field strength in various chemical environments<sup>22</sup>. In addition, more recent research results revived the interest in the observation of transient Stark responses in solids, gases, or other media such as polymers, quantum dots, and TMDC<sup>23,24,25,26,27</sup>. However, transient Stark spectroscopy of molecules in solution at room temperature has not yet been demonstrated, because a successful measurement of molecules in solution is subject to some preconditions.

Conventional Stark spectroscopy uses low frequency (kHz) electric fields, which oscillate much slower than typical rotation times of molecules in solution. Hence, molecules must be immobilized in order to avoid alignment of their dipoles along the applied electric field, otherwise this poling effect would result in an overwhelming increase of the overall absorption and obscure any Stark signatures. Typically, this is achieved by freezing the solvent, which limits the range of solvents that can be used since these need to form optical glasses to avoid scattering of probe light. Moreover, freezing prevents molecules to be characterized in their natural, liquid or physiological environment. Finally, the sample geometry, with the electrodes on the front- and backside of the sample cuvette, leads to a non-optimal geometry with the angle between the polarization of the Stark field and the probe being far from the ideal value of 0 deg (typically 50 to 60 deg)<sup>28</sup>.

Here, we demonstrate that increasing the frequency of the oscillating electric field to the terahertz (THz) regime removes all of the above mentioned constraints and disadvantages of conventional Stark spectroscopy. Since a number of years it became possible to generate phase stable single- or few-cycle THz pulses with sufficiently strong electric fields (up to or even exceeding 1 MV/cm) to induce measurable Stark shifts as well as femtosecond supercontinuum (fs-SC) probe pulses to time-resolve those transient Stark signatures<sup>29,30</sup>. A schematic of the experimental realization is shown in Fig. 3.1c. Scanning the time delay between probe pulse and the THz waveform allows for the measurement of Stark signatures for positive or negative electric fields and from zero field up to the peak field strength of the THz pulse (see Supplementary Information 4). At

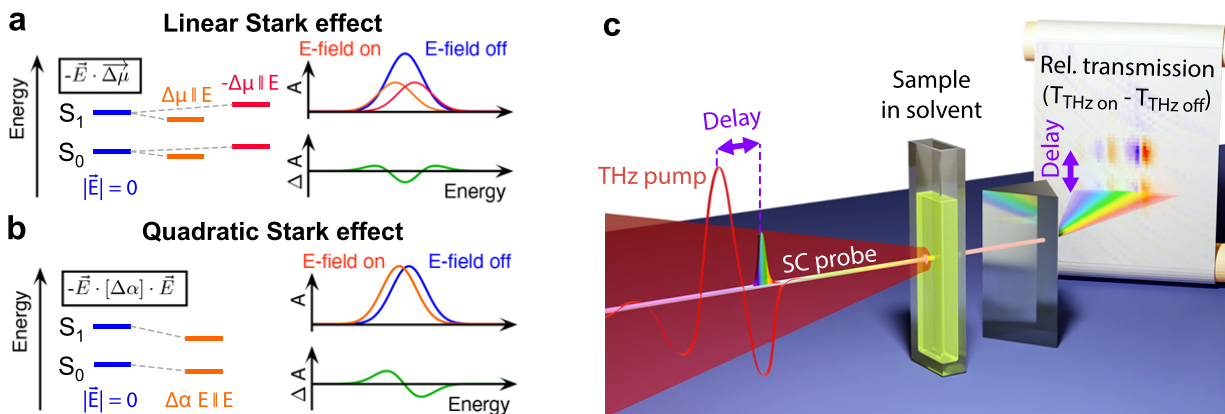


**Figure 3.1: Electric field induced Stark effect and experimental concept.** Electric field induced Stark shift due to a difference in ground- and excited state dipole (a), i.e. linear Stark effect, and polarizability (b), i.e. quadratic Stark effect. For an isotropic distribution of molecules the ground state absorption band versus energy  $A(E)$  broadens in the case of the linear Stark effect with the difference signal  $\Delta A(E)$  resembling the second order derivative of the absorption band. In the case of the quadratic Stark effect the ground state absorption band shifts resulting in a difference signal  $\Delta A(E)$  that is proportional to the first order derivative of absorption band. **c** Schematic representation of the experimental setup. The femtosecond supercontinuum probe pulse is scanned in time across the collinear single-cycle THz pulses and its spectrum is recorded by a spectrometer.

THz frequencies the electric field oscillates faster than typical molecular rotation times in solution, hence for the first time, time-resolved Stark spectroscopy of molecules is performed without freezing the sample. Consequently, virtually any solvent can be used and molecules can be studied in their natural chemical or biological environment. Moreover, a wider temperature range becomes accessible, especially temperatures above the freezing point of the solvent but also room temperature or higher. The THz frequency of the field source also entails a higher dielectric breakdown allowing for electric field strengths, which were impossible to attain previously<sup>31,32,33</sup>. At such field strengths, for instance, transition polarizability or hyper-polarizability may play a more important role, particularly for weakly allowed transitions. Such higher-order electric field effects may require a new theoretical concept, especially when the applied electric field can no longer be treated as a perturbation to the system's Hamiltonian or when magnetic effects need to be considered. THz Stark spectroscopy offers additional minor advantages, i.e., the sample thickness can be substantially increased and is limited only by absorption or velocity matching between the THz and the probe pulse. Additionally, arbitrary angles between the electric field vector and the probe polarization can be used and the absence of electrodes avoids potential redox chemistry in the pristine sample.

For the present THz Stark spectroscopic study, we selected two molecules to separately study the dynamics for linear and quadratic Stark effect and for comparison we performed quantum chemical calculations as well as conventional Stark spectroscopy. One molecule consists of a strong electron donor tetrathiafulvalene and an electron acceptor benzothiadiazole, showing an energetically low-lying intramolecular charge transfer state with a substantial change in dipole moment. The other is an anthanthrene derivative tetrasubstituted with silyl-protected acetylene

groups to extend its  $\pi$ -conjugation, leading to an intense and sharp absorption band with a large change in polarizability.

## 3.2 Results and Discussion

### 3.2.1 Dynamics of the Stark Signature

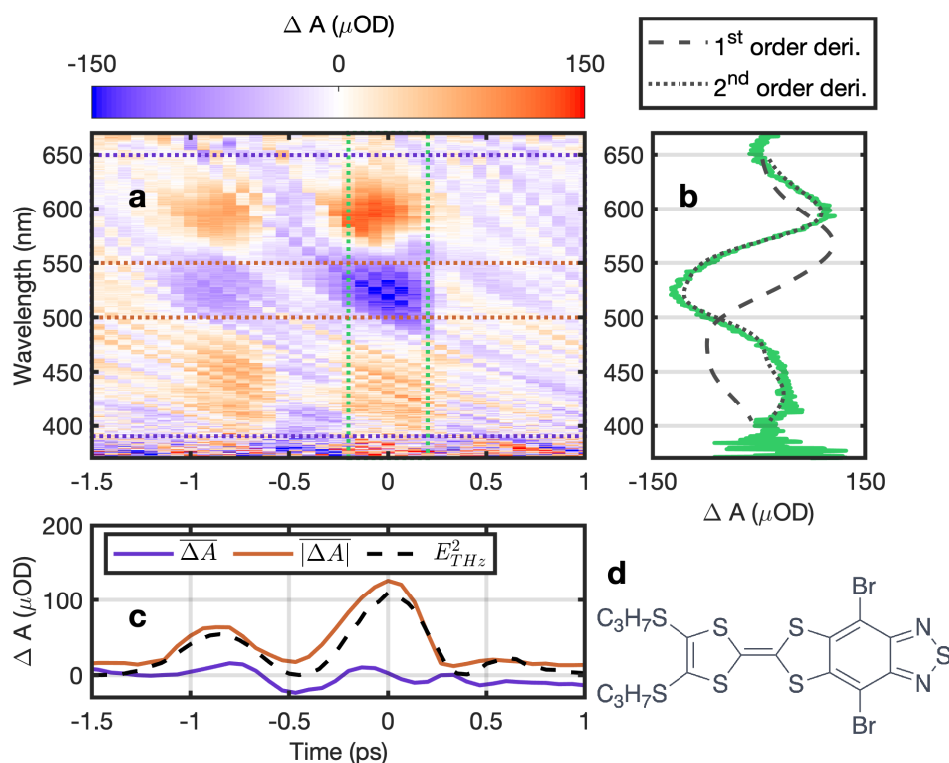


Figure 3.2: **THz Stark signal of TTF-BTD with parallel orientation.** **a** False-color plot of the measured change in absorption spectrum as a function of time delay between THz and probe pulse and wavelength. **b** Time-averaged (between the two green dotted lines) change in absorption versus wavelength (green solid curve) compared to the scaled first (black dashed curve) and second order derivative (black dotted curve) of the ground state absorption spectrum. **c** Spectral average of the change in absorption between the purple dotted (purple curve) and red dotted lines (red curve) in **a**. The red curve is compared to the scaled square of the measured THz electric field  $E_{\text{THz}}^2$  (black dashed curve). **d** Chemical structure of TTF-BTD.

We first discuss the experimental results of a molecule with a pronounced intramolecular charge transfer (ICT) character, namely an annulated electron donor-acceptor compound. Thereby, tetrathiafulvalene (TTF) acts as a strong donor and benzothiadiazole (BTD) equally as an acceptor within the compact and planar dyad<sup>34,35</sup>. The bromine functionalization of BTD increases its



acceptor strength and the propyl chains on TTF act as solubilizing groups (Fig. 3.2d) (see Supplementary Information 1). Figure 3.2a shows the color-coded THz-induced change in absorption  $\Delta A(\tau, \lambda)$  in TTF-BTD versus time delay  $\tau$  and wavelength  $\lambda$  for parallel polarization orientation between probe pulse and THz waveform (corresponding results for a perpendicular orientation are provided in the Supplementary Information 5). The color scale indicates the difference in absorption in units of optical density (OD). The two-dimensional distribution reveals both temporal and spectral characteristics of the THz field-induced Stark shift with a time and wavelength resolution of approximately 100 fs and 0.5 nm. Time zero is set arbitrarily to the maximum change in absorption  $\Delta A_{\text{max}}$ . The two peaks of the single-cycle THz pulse are well resolved with zero signal at the zero-crossing of the THz electric field. The measured spectra around the peaks of the THz field indicate a spectral broadening of the rather broad  $S_0 - S_1$  absorption band between 390 nm to 650 nm, which is not unusual for ICT transitions.

Calculating the margin along the delay axis between the two green dotted vertical lines results in the average Stark signal versus wavelength (green curve in Fig. 3.2b). Note that all measurements had the background signal (from pure toluene in the cuvette) subtracted. Comparing the measured signal to the scaled first- and second-order derivative of the ground state absorption curve reveals that the Stark signature is dominated by a first order Stark contribution (black dotted curve) revealing a linear Stark effect caused by a change in dipole moment between ground and excited state. Additionally, we calculate two margins along the wavelength axis, first between the purple dotted horizontal lines resulting in the purple curve in (Fig. 3.2c), and second between the two red dotted horizontal lines yielding the red curve in (Fig. 3.2c). The margin over the entire transition (purple curve) versus time delay is essentially zero confirming that no alignment of molecules to the applied THz field occurs. The residual small signal is most likely due to an imperfect correction of the group velocity dispersion in the fs-SC (see Supplementary Information 4) as well as a sensitivity level of 20  $\mu\text{OD}$  due to fs-SC fluctuations. These findings constitute an important result as they demonstrate that THz Stark spectroscopy can be applied to molecules in solution without the need to freeze the solvent. The red curve, averaged over one of the peaks in the Stark spectrum, indicates that the instantaneous Stark signal scales as the square of the THz field which is in agreement with Liptay's derivation of the linear and the quadratic Stark effect of an ensemble of molecules with isotropic orientation.

The second molecule, anthanthrene<sup>36</sup>, is a  $\pi$ -conjugated organic molecule of interest due to its semiconducting properties and potential applications in light emitting diodes or solar cells. The structure of anthanthrene is shown in Fig. 3.3d. It constitutes an interesting building block for organic electronics and Stark spectroscopy has the potential to reveal some of its relevant physico-chemical properties. The transient Stark signal of the  $S_0 - S_1$  transition of anthanthrene in toluene is shown in Fig. 3.3. The polarization between probe pulse and the THz waveform was parallel and the corresponding results for perpendicular polarization are provided in the Supplementary Information 5. Additional THz Stark spectroscopy results. The electronic transition shows a well separated vibrational progression, hence all vibrational bands are treated as one transition within our detection window. Margins are calculated following the same recipe as outlined above. A comparison of the time averaged Stark signature (Fig. 3.3b green curve) with the scaled first- (black dashed curve) and second-order derivative (black dotted curve) of the ground state absorption reveals a mostly quadratic Stark effect related to a difference in polarizability of ground and excited state. It also suggests that ground and excited state dipoles are, very likely based on symmetry

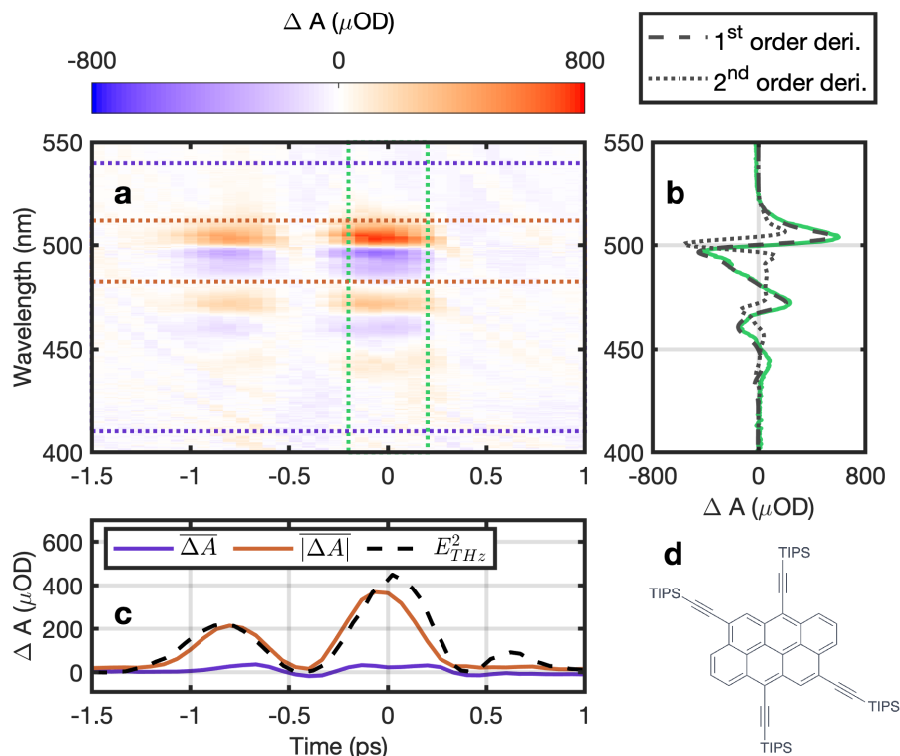


Figure 3.3: **THz Stark signal of anthanthrene with parallel orientation.** **a** False-color plot of the measured change in absorption spectrum as a function of time delay between THz and probe pulse and wavelength. **b** Time-averaged (between the two green dotted lines) change in absorption versus wavelength (green solid curve) compared to the scaled first (black dashed curve) and second order derivative (black dotted curve) of the ground state absorption spectrum. **c** Spectral average of the change in absorption between the purple dotted (purple curve) and red dotted lines (red curve) in **a**. The red curve is compared to the scaled square of the measured THz electric field  $E_{\text{THz}}^2$  (black dashed curve). **d** Chemical structure of anthanthrene.

arguments, negligible or similar in value. The two margins along the wavelength axis shown in Fig. 3.3c (purple and red curves) confirm that poling effects can be excluded, hence the sample maintains an isotropic distribution throughout, confirming again that the THz field oscillation is faster than the rotation time of investigated molecule in solution.

That is, both molecules show a pronounced instantaneous Stark signature, which is well-matched to either the first- or the second-order derivative of the ground state absorption band, suggesting a dominant quadratic or linear Stark effect, respectively. In both cases, the Stark signal is proportional to the square of the THz electric field in agreement with Liptay formalism (see Supplementary Information 7) tracing the picosecond single-cycle THz waveform and we identify no measurable hysteresis or memory effect.



### 3.2.2 Comparison Between Conventional and THz Stark Spectroscopy

For both molecules the Stark spectra for parallel and perpendicular polarization between probe pulse and THz waveform are fitted simultaneously and analyzed using the formalism outlined by Liptay<sup>5,37</sup> to extract relevant molecular parameters, such as differences in dipole moment or polarizability. We compare the results to those obtained from conventional Stark spectroscopy (see Supplementary Information 3) and those calculated from Density Functional Theory (DFT). DFT also provides molecular orbitals and associated energies for further discussion of results, specifically the charge redistribution associated with an excitation (see Supplementary Information 2). Recall that conventional Stark spectroscopy is done at 77 K, that is well below the freezing temperature of toluene, whereas THz Stark spectroscopy can be performed in principle at any temperature, but here is done at room temperature. To account for different optical path lengths, sample concentrations or electric field strength in the two measurement techniques, we compare the change in molar attenuation coefficient  $\Delta\epsilon$  scaled to 1 MV/cm rather than the change in absorption.

The ground state absorption spectra of TTF-BTD and anthanthrene in toluene are shown in Fig. 3.4a and b for 77 K (blue curves) and room temperature (red curves). The DFT calculations suggest that TTF-BTD exhibits a broad absorption band due to a substantial ICT in the excited state. Anthanthrene, on the other hand, exhibits relatively narrow absorption features with an evident vibronic progression and DFT calculations mainly suggest a change in polarizability. When decreasing the temperature from 300 K to 77 K toluene is known to increase its effective polarity due to an increase in density<sup>38</sup>. While in TTF-BTD this results in a blue-shift of the absorption peak from 514 nm to 505 nm due to the solvent's instantaneous electronic polarizability<sup>39</sup>, in anthanthrene this leads to a increased stabilization of the energy levels and an associated red-shift of the lowest vibronic mode of the  $S_0 - S_1$  HOMO - LUMO transition from 500 nm to 505 nm. Irrespective of molecule, thermal broadening of the absorption features is evident for increasing temperatures. Both effects illustrate the importance of fitting Stark spectra with ground state absorption spectra recorded at the same temperature.

Figure 3.4c and d show the change in molar attenuation coefficient  $\Delta\epsilon$  scaled to 1 MV/cm for TTF-BTD and anthanthrene as measured by conventional Stark spectroscopy for a relative orientation between probe pulse and THz waveform polarization of 56 deg/61 deg (blue solid curve) and 90 deg (blue dashed curve). Note, that angles smaller than 56 deg are difficult to realize due to above mentioned geometrical constraints. The corresponding results of the THz Stark spectroscopy are shown in Fig. 3.4e and f. THz results were averaged over a 467 fs time window around the larger peak of the THz pulse. Unlike conventional Stark spectroscopy, the THz variant has no geometrical constraints and allows for angles down to 0 deg, which helps to improve the dynamic range of measurement as well as the accuracy of the Liptay analysis. Except for the temperature related blue- or red-shift and the different minimal angle, the Stark signatures of both methodologies are in excellent agreement with each other. The peak change in molar attenuation coefficient for TTF-BTD is slightly lower in the THz measurement due to the thermal broadening of the absorption spectrum at room temperature.

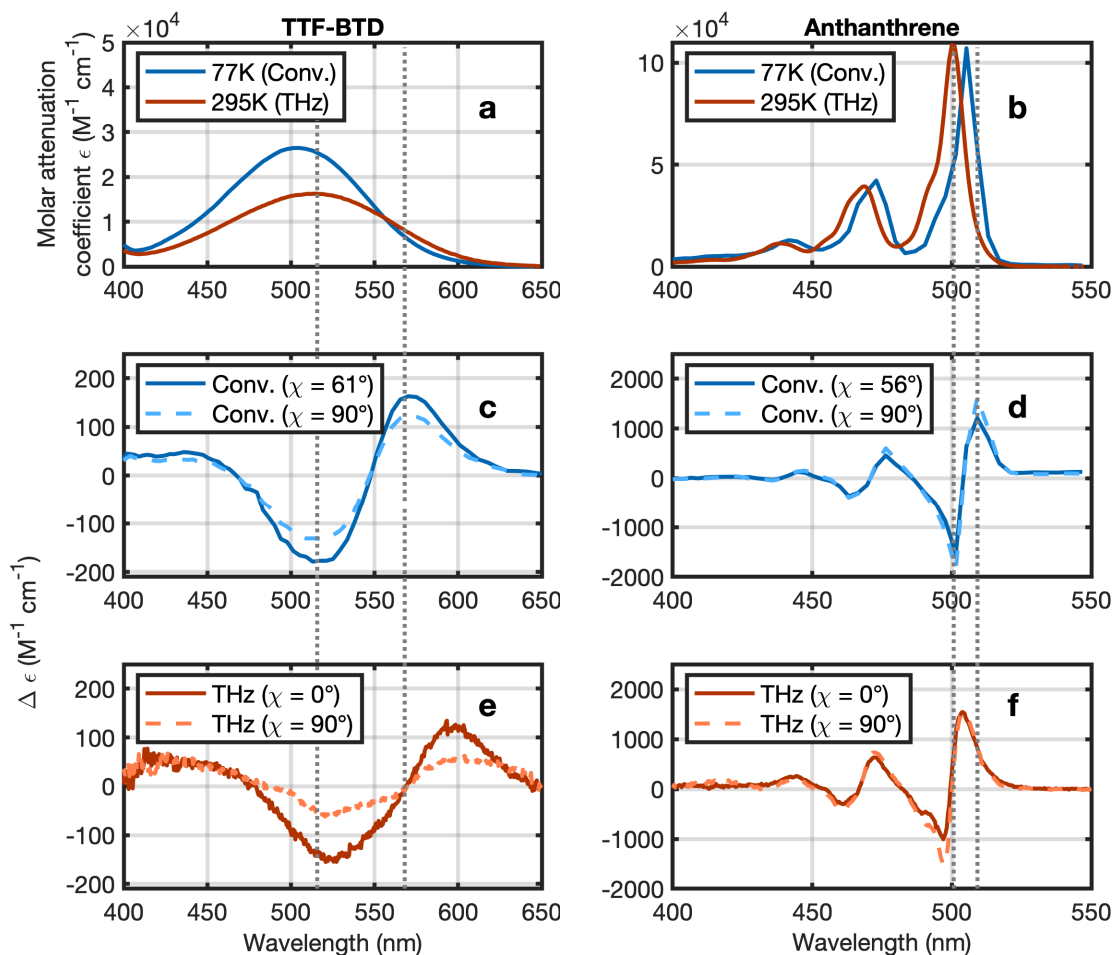


Figure 3.4: **Comparison of conventional and THz Stark spectroscopy.** **a,b** Low temperature (77 K) and room temperature (295 K) absorption spectra of (a) TTF-BTD and (b) anthanthrene. **c,d** Conventional Stark spectra measured at 77 K for two values of the angle  $\chi$  between the polarization of the THz and the probe pulses. **e,f** THz Stark spectra recorded at room temperature for parallel and perpendicular orientation of THz and probe polarization. For direct comparison the y-scale is in units of  $\Delta\epsilon$  scaled to an electric field of 1 MV/cm. The grey dotted vertical lines are guides to the eye and help to visualize the shift of the spectra at the different temperatures.

### 3.2.3 Relevant Molecular Parameters

A more rigorous comparison becomes available after analyzing the spectra in Fig. 3.4 following the Liptay protocol. It reveals the change in dipole moment,  $\Delta\mu$ , the angle between the change in dipole moment and the transition dipole moment  $m$ ,  $\zeta$ , the average change in polarizability,  $\text{Tr}(\Delta\alpha)$ , and the change in polarizability parallel to the transition dipole moment  $m$ ,  $m \Delta\alpha m$ . The latter consistently showed large fitting errors and is not reported here. Table 3.1 summarizes these molecular parameters calculated from DFT as well as measured and extracted via the Liptay analysis of both Stark spectroscopy methodologies.

Table 3.1: Comparison of relevant molecular parameters as calculated via DFT or measured by conventional and THz Stark spectroscopy.

Parameter	DFT	Conventional Stark	THz-Stark
<b>TTF-BTD: tetrathiafulvalene-benzothiadiazole</b>			
$\Delta\mu$ (D)	16.2	$14.7 \pm 0.1$	$15.3 \pm 1.8$
$\zeta$ ( $^\circ$ )	$\approx 0$	$24.8 \pm 0.2$	$18.7 \pm 1.1$
<b>Anthanthrene: 4,6,10,12-tetrakis(triisopropylsilylethynyl)anthanthrene</b>			
$\text{Tr}(\Delta\alpha)$ ( $\text{\AA}^3$ )	457	$363 \pm 20$	$296 \pm 70$

The agreement within the error bars in all molecular parameters extracted from the two Stark spectroscopy modalities is remarkable and confirms that both techniques deliver results which are in quantitative agreement with each other. The biggest source of error comes from the uncertainty of the electric field applied to the sample (see Supplementary Information 6). Furthermore, the experimental results are in reasonable agreement with DFT calculations given the fact that the solvent environment can only be treated approximately if at all. Including the solvent effect in the DFT calculations for TTF-BTD leads to marginal modifications to the molecular geometry as compared to the gas phase and details can be found in reference<sup>37</sup>. The mismatch in measured and calculated angle  $\zeta$  most likely is due to these structural modifications, but may be also a result of temperature affecting electrostatic interactions and molecular geometry<sup>37,40</sup>. For the anthanthrene, the DFT calculations were performed at 0 K and without solvent effects, nevertheless, the experimental results agree very well with the DFT calculations. Hence, neither the low polarity of the solvent nor the increased temperature seem to drastically affect the dipole moment or the electronic polarizability of the molecule.

In conclusion, we have demonstrated that THz Stark spectroscopy indeed reveals the same physicochemical properties of molecules as conventional Stark spectroscopy, but at the same time opens hitherto inaccessible opportunities, because it is not subjected to the same limitations that apply to conventional Stark spectroscopy. Geometrical constraints are removed allowing for arbitrary angles between probe pulse and THz waveform polarization, no electrodes are required, which helps to avoid potential redox chemistry in the pristine sample, and the much higher frequency of THz waveforms allows for higher electric field strengths before the threshold for dielectric breakdown is reached. Most importantly however, THz Stark spectroscopy removes the

need to immobilize the molecular ensemble by freezing the solvent. Although this study demonstrates time-resolved THz spectroscopy for two specific molecules in a non-polar environment, the method is not limited to that. As also shown in a recent report on transient THz field-induced broadening of absorption bands, which was published during the reviewing process,<sup>41</sup> this opens up interesting future applications to study samples also in polar natural environments. Hence, molecules or bio-molecules can now be studied in their natural environment and at relevant temperatures. Our findings are based on measurements of two molecules relevant in the context of molecular electronics.

In addition, THz Stark spectroscopy allows us to observe transient or non-equilibrium electronic properties of molecules with sub-100 fs resolution. Consequently, THz Stark spectroscopy can be used to study molecular ensembles at conditions not accessible to conventional Stark spectroscopy, for instance, within a much increased range of temperatures or in different non-polar or polar solvents, even those that do not form transparent glasses at low temperatures. Today's high-field THz sources generate field strengths in excess of 1 MV/cm and even higher fields when combined with field enhancement structures so that higher-order Stark contributions become observable, such as hysteresis effects originating from electron-phonon couplings. Higher order Stark contributions are impossible to access via conventional Stark spectroscopy but are relevant to model electron dynamics induced by external or local fields (e.g. charge and electron transfer) or to refine quantum chemistry codes. Moreover, the intrinsic time resolution of around 100 fs facilitates studies on the time-dependent physicochemical properties of a molecule during its photo-cycle, specifically it allows for Stark spectroscopy of excited states.

### 3.3 Methods

**THz Stark spectrometer** The THz Stark spectrometer was designed to record the change in absorption  $\Delta A(\tau, \lambda) = A_{\text{THz on}}(\tau, \lambda) - A_{\text{THz off}}(\tau, \lambda)$  as a function of time delay between the THz waveform and the probe pulse  $\tau$  and of wavelength  $\lambda$ . The recorded Stark maps  $\Delta A(\tau, \lambda)$  were subsequently corrected for the fs-SC group velocity dispersion and the background resulting from the pure solvent (see Supplementary Information 4). The analysis of the Stark spectra, here at maximum electric field,  $\Delta A(\lambda)$ , was outlined in reference<sup>5</sup>. After having identified the Stark-active transitions, the Stark spectra were subsequently analyzed with the Liptay formalism, which links the molar absorption  $\Delta\epsilon(\bar{\nu})$  as a function of wavenumber to the ground state absorption spectrum  $\epsilon(\bar{\nu})$ . The model assumes a fixed angle between electric field and probe polarization and an isotropic distribution of transition dipole moments, which is achieved by freezing the sample in conventional Stark spectroscopy. The ground state absorption spectra and two Stark spectra for different probe polarizations were fitted simultaneously with a weighted sum of the zeroth, first, and second order derivative of the ground state absorption spectrum.

$$\Delta\epsilon(\bar{\nu}) = f_l^2 |\mathbf{E}|^2 \left\{ a\epsilon(\bar{\nu}) + b \frac{d}{d\bar{\nu}} \left( \frac{\epsilon(\bar{\nu})}{\bar{\nu}} \right) + c \frac{d^2}{d\bar{\nu}^2} \left( \frac{\epsilon(\bar{\nu})}{\bar{\nu}} \right) \right\}. \quad (3.1)$$

From the fit parameters  $a$ ,  $b$ , and  $c$  we extracted the trace of the polarizability tensor, its projection along the transition dipole moment, the angle between the applied electric field and the probe polarization, the change in dipole moment, and the angle between the change in dipole moment and

the transition dipole moment. An important ingredient to the fit is the THz electric field strength  $|E|$  in the sample at which the probe pulse interrogates the molecular system. In order to account for all experimental effects we first measured the THz electric field in air and then performed finite difference time-domain simulations to determine the time dependence of the THz electric field experienced by the probe pulse in the complex cuvette/liquid environment. We found that the time dependence is almost identical, however with the peak electric field strength being reduced by a factor of 0.7 due to Fresnel reflections and Fabry-Perot effects. Hence, the maximum field in the sample was reduced to 280(17) kV cm<sup>-1</sup>. The electric field experienced by the molecules is further modified by the local field correction factor  $f_l$ , which is a measure of how the solvent cavity affects the field inside the cavity containing the molecule<sup>42,43,44</sup>. We estimated the local field correction factors for TTF-BTD and anthanthrene to 1.30 and 1.33 for conventional Stark spectroscopy and to 1.26 and 1.29 respectively for THz Stark spectroscopy (see Supplementary Information 8).

## 3.4 Supplemental Information

### 3.4.1 Synthesis and Preparation of Molecular Systems

The two molecular systems were selected because they show either a pronounced change in dipole moment, which allows us to unambiguously observe the linear Stark effect, or a pronounced change in polarizability, which allows us to observe the quadratic Stark effect. In addition, both molecules are relevant in the field of molecular electronics and the extracted physicochemical properties are relevant in their own right.

The first molecular system is fused heterocyclic tetrathiafulvalene<sup>45,46,47,48,49</sup> - benzothiadiazole<sup>50,51,52</sup> (TTF-BTD) with Br substituted at the 4 and 8 positions of BTD<sup>53</sup>. This molecule is known to undergo intramolecular charge transfer<sup>54,55</sup> with a correspondingly large change in dipole moment upon excitation of the HOMO-LUMO transition. The relatively broad absorption band centered around 500 nm is a typical signature of such intramolecular charge transfer.

The second molecular system is the 4,6,10,12-tetrakis(triisopropylsilyl)ethynyl-anthanthrene compound<sup>36</sup>, which bears a graphene-like aromatic skeleton and is well-known for its quantum interference effect on the single molecule conductance,<sup>56,57,58</sup> and for its versatile chromophoric properties in organic electronics<sup>59,60,61,62,63</sup>. It exhibits optically allowed transitions with significant oscillator strengths in the spectral range around 500 nm.

For all experiments, toluene was used as solvent because it has a low polarity and forms a transparent optical glass at 77 K, which is mandatory for the conventional Stark measurements. The low polarity limits effects due to varying solvent polarity at different temperatures and the potential for THz field-induced orientation of the solvent. For conventional Stark measurements, the sample concentration was 1 mM for TTF-BTD and 0.45 mM for anthanthrene. The sample concentration for the THz Stark measurements was 1 mM for TTF-BTD and 0.5 mM for anthanthrene. In the THz Stark experiment, a spectro-sil quartz flow cell from Starna Scientific was used with a sample thickness of 200  $\mu$ m and a wall thickness of 200  $\mu$ m. Even though a flow cell is not specifically needed, it helped to suppress air bubble formation. Furthermore, any potential effects due to toluene evaporation are reduced.

While the ground state absorption spectra in conventional Stark spectroscopy were measured

directly with the Stark spectroscopy apparatus (with no applied electric field at low temperature), the room temperature ground state absorption spectra were recorded separately with a spectrophotometer (Perkin-Elmer Lambda 750 Spectrometer, 1 mm thick cuvette).

### 3.4.2 Density Functional Theory Calculations

We performed DFT calculations of both systems to gain further insight into the charge redistribution between the molecular orbitals involved in the observed optical transitions and the associated energies. While details on our DFT computations on TTF-BTD have already been published elsewhere<sup>37</sup>, we here present methods and results on the second system anthanthrene. The molecular geometries of anthanthrene were optimised at the Kohn-Sham DFT level. We used the PBE0<sup>64</sup> or the B3LYP<sup>65</sup> functionals to approximate the exchange-correlation energy in combination with the 6-31+G(d,p) basis set<sup>66</sup>. The excitation energies were computed by time-dependent DFT (TD-DFT)<sup>67</sup>. The properties of excited states were obtained as higher-order response properties of the ground state. Specifically, the polarizability of an excited state was determined by first converging the electronic energy of the ground state and then by computing the double residue of the cubic response function as described in reference<sup>68</sup> and implemented in the DALTON software package<sup>69</sup>. Table 3.2 summarizes possible transitions originating from the ground  $S_0$  state with corresponding wavelength, oscillator strength, major molecular orbital contributions, and transition dipole moment. Molecular orbitals and associated energies involved in the calculated transitions for the sample are illustrated in Fig. 3.5.

Table 3.2: Ground state transitions of anthanthrene with wavelength, oscillator strength, and major contributing molecular orbitals calculated using TD-DFT.

Excited State	Wavelength (nm)	Oscillator Strength	Major Contributions (%)
$S_1$	500.2	0.4846	HOMO $\rightarrow$ LUMO (pure)
$S_2$	419.7	0.0000	HOMO-1 $\rightarrow$ LUMO (36) HOMO $\rightarrow$ LUMO+1 (13)
$S_3$	402.8	0.0000	HOMO-1 $\rightarrow$ LUMO (13) HOMO $\rightarrow$ LUMO+1 (36)
$S_4$	395.2	0.0087	HOMO-2 $\rightarrow$ LUMO (27) HOMO $\rightarrow$ LUMO+2 (22) HOMO-3 $\rightarrow$ LUMO (3)
$S_5$	333.0	0.6133	HOMO-2 $\rightarrow$ LUMO (20) HOMO-1 $\rightarrow$ LUMO+1 (2) HOMO $\rightarrow$ LUMO+2 (22)
$S_6$	315.4	0.0366	HOMO-3 $\rightarrow$ LUMO (33) HOMO $\rightarrow$ LUMO+2 (2) HOMO $\rightarrow$ LUMO+3 (12)

The average isotropic change in polarizability over the transitions was calculated using both PBE0 and B3LYP functionals. We checked convergence with the basis set (using aug-cc-PVTZ



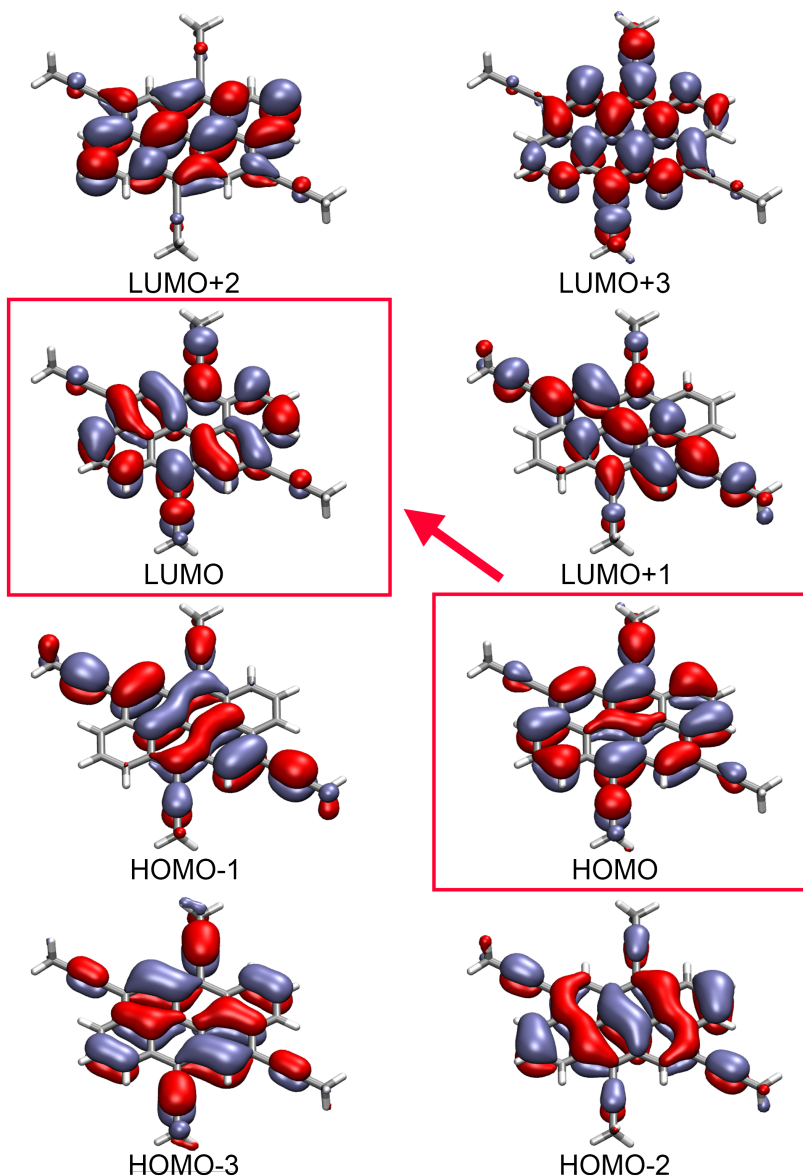


Figure 3.5: **Molecular orbitals of anthanthrene.** With reference to the main text, we draw the reader’s attention to the HOMO→LUMO transition in particular.

Table 3.3:  $\Delta\alpha$  computed by TD-DFT with an aug-cc-pVDZ basis set.

State	Wavelength (PBE0)	Wavelength (B3LYP)	Tr( $\Delta\alpha$ ) (B3LYP)
$S_1$	500.2 nm	518.8 nm	457 Å <sup>3</sup>
$S_5$	333.0 nm	347.0 nm	333 Å <sup>3</sup>

and daug-cc-PDVZ). We verified that using aug-cc-PVDZ the basis set error affects the quantitative

result by less than 1%. In addition, note that the lowest energy transition  $S_0 \rightarrow S_1$  splits in a well-separated vibronic progression.

### 3.4.3 Conventional Stark Spectroscopy

To understand the limitations of conventional field Stark spectroscopy we will describe the technique in general terms here. A more detailed description of the specific Stark spectrometer used, along with technical details can be found in a previous publication<sup>37</sup>. Typically, a high voltage source is connected to transparent electrodes (indium tin oxide: ITO) on the inner front and back surface of the sample cell. The front and the back window are separated by a Kapton spacer with a thickness of 25  $\mu\text{m}$  and the sample cavity is filled by injection with the sample solution. The sample is then mounted in a cooled Dewar at 77 K to freeze the solvent. Freezing the sample is also a common work-around to increase the breakdown voltage and prevent unwanted redox chemistry. During the experiments, a 3.5 kHz sinusoidal signal is applied across a cell. While for TTF-BTD the applied voltage was  $V_{\text{rms}} = 250 \text{ V}$  (with a peak field of 141 kV/cm), for anthanthrene the applied voltage was  $V_{\text{rms}} = 150 \text{ V}$  (with a peak field of 85 kV/cm). A lamp and monochromator provide tunable probe light. The electric field-induced transmission changes are monitored at twice the AC frequency by a lock-in amplifier. The difference between the in- and out-of-phase components is plotted as a function of monochromator wavelength, resulting in a Stark spectrum. The cell can be rotated about a vertical axis within the Dewar to facilitate different relative angles between the applied field and the probe light polarization. The polarization of the probe light is set with a Glan-Taylor prism.

### 3.4.4 THz Stark Spectroscopy

This section describes in detail all relevant steps to extract the molecular physicochemical constants. We start with a brief description of the experimental apparatus and the data recorded by it. Next, we outline how we correct for the group velocity dispersion of the probe pulses and give a detailed account of the background subtraction protocol. A further important ingredient for the analysis is the THz electric field strength in the sample and we determine it by a combination of measurements and finite difference time domain simulations. Finally, the measurements are analyzed by the Liptay formalism, which is briefly described toward the end.

#### Experimental setup

Figure 3.6 shows a schematic of the experimental setup. The high-field single-cycle THz waveforms were generated via tilted-pulse-front pumping in  $\text{LiNbO}_3$  and the time-delayed femtosecond supercontinuum (fs-SC) probe pulses came from white-light generation in a 5-mm-thick  $\text{CaF}_2$  crystal, which was mounted in a continuously moving mount in order to avoid photo-darkening. In detail, a 1 kHz Ti:sapphire regenerative amplifier (Legend Elite Duo Femto, Coherent) delivering 90 fs pulses with an average power of 8 W at 800 nm was used to produce the single-cycle THz waveforms by optical rectification in a prism-cut  $\text{LiNbO}_3$  crystal<sup>70,71</sup>. The THz waveforms were imaged to the sample position by a combination of two lenses with focal lengths of 100 mm and 50 mm, resulting in a 2:1 demagnification.



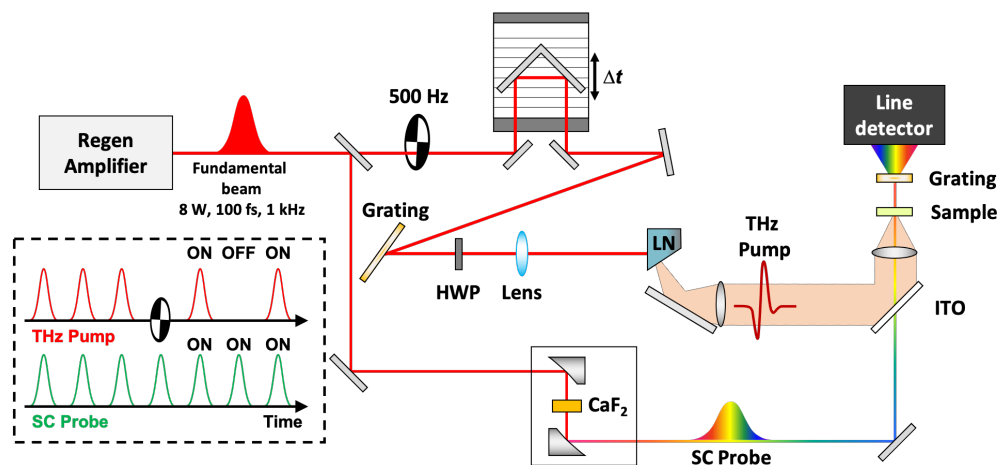


Figure 3.6: **THz Stark spectroscopy.** High-field single-cycle THz waveforms were generated via tilted-pulse-front pumping in  $\text{LiNbO}_3$  and the fs-SC probe pulses were generated in  $\text{CaF}_2$ . The probe pulses passed collinearly with the THz pulses through the sample and were analyzed by a spectrometer. A chopper running at 500 Hz alternated between THz waveform on and off.

THz waveform and fs-SC probe pulses were combined collinearly with an indium tin oxide (ITO) coated glass slide, which acts as a mirror at THz frequencies but is transparent at optical frequencies. The relative polarization between the THz waveform and the probe pulse was adjusted by an achromatic half-wave plate in the probe arm and both were subsequently focused to the sample using a TPX lens. The probe beam waist was set to  $w_{\text{SC}} \approx 17 \mu\text{m}$ , which is more than one order of magnitude smaller than the THz beam waist of  $w_{\text{THz}} \approx 1 \text{ mm}$ , and thus probes an area of almost constant THz electric field strength at the center of the THz spot. After the sample, the probe spectrum was analyzed with a 1024-pixel CMOS array (Glaz-I, Synertronic Designs) on a pulse-to-pulse basis. A phase-locked chopper blocked every other THz waveform and from two consecutive probe spectra (with and without THz) the change in absorption, i.e.  $\Delta A(\lambda) = A_{\text{THz on}}(\lambda) - A_{\text{THz off}}(\lambda) = -\log_{10}(T_{\text{THz on}}(\lambda)/T_{\text{THz off}}(\lambda))$ , was calculated as a function of wavelength  $\lambda$ . In order to realize a sufficiently high signal-to-noise ratio we typically averaged more than 5000 pulse pairs. From a number of such measurements for different time delays  $\tau$  between the THz waveform and the probe pulse, we construct two-dimensional color-coded Stark maps  $\Delta A(\tau, \lambda)$  as shown in Fig. 3.7a.

### Group velocity dispersion correction

The fs-SC probe pulses experience group velocity dispersion (GVD) due to a number of dispersive optical elements through which they have to propagate. As a result, each spectral component has a different effective time delay with respect to the THz waveform. Since the total GVD is independent of sample and polarization, it can be corrected for. As an example, Fig. 3.7a shows the measured and color-coded Stark signals (anthanthrene) versus time delay between probe pulse and THz waveform and wavelength of probe pulse. The black solid curve shows the 3rd order polynomial fitting, which is subsequently used for GVD correction. The GVD correction was confirmed by measuring the cross-phase modulation in a quartz substrate at the sample position.

In essence, all rows of data are shifted by a time delay that is given by the 3rd order polynomial curve and Fig. 3.7b shows the data after GVD correction. All measurements on the solid curve shown in Fig. 3.7a now have the same corrected time delay.

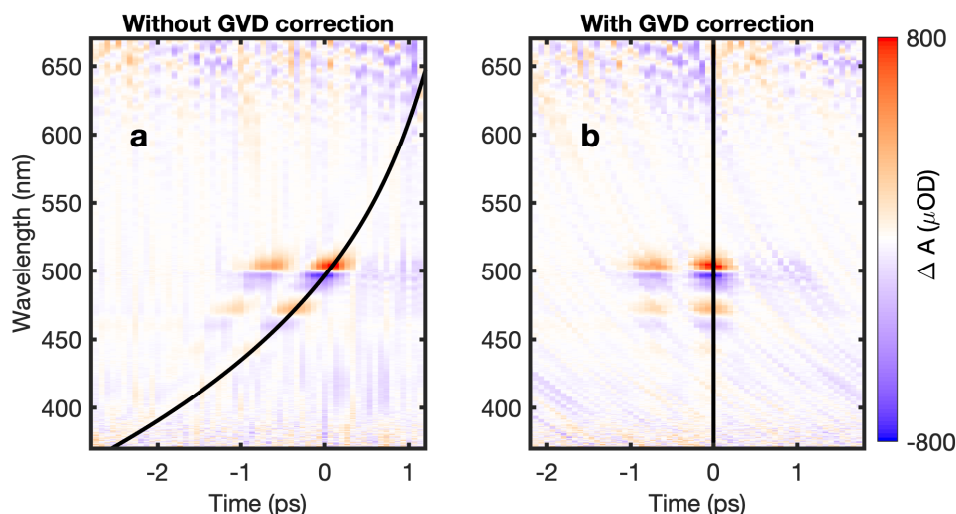


Figure 3.7: **Measured color-coded Stark map for anthanthrene versus time delay and wavelength before a and after b GVD correction.** The black solid curve indicates the fitted 3rd order polynomial representing the GVD, which turns into a vertical line after GVD correction.

### Background measurements

To characterize the measurement background, we recorded signals for the pure solvent. Figure 3.8 shows the spectra for parallel and perpendicular orientation of THz and probe polarization. For all time delays, the measurement is dominated by random noise. Note that the GVD correction introduces an apparent parabolic structure. Around time delay zero we find a positive signal for all wavelength, which is attributed to a THz Kerr effect observed in low-polar liquids<sup>72</sup>. In Fig. 3.8c,d the two signals integrated along the wavelength axis are shown as function of time delay. In agreement with theory, the signal for parallel orientation is larger than that for perpendicular orientation. For all measurements presented in this paper, we subtracted this background signal before plotting and analysing the data.

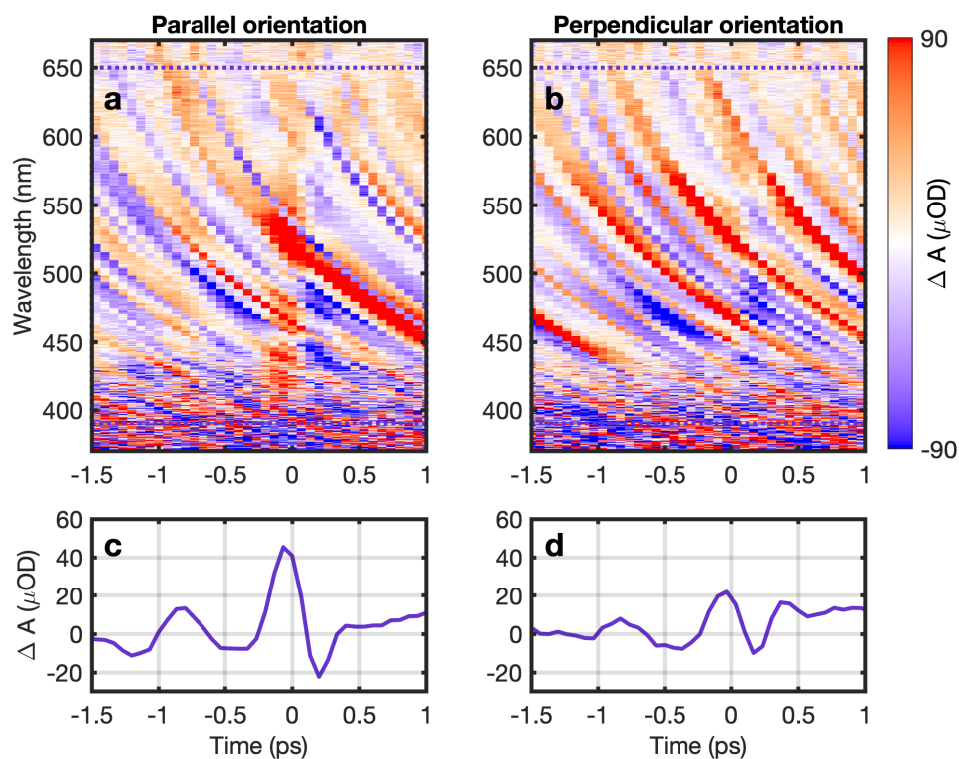


Figure 3.8: **Background measurement with pure toluene for a parallel and b perpendicular orientation of THz and probe pulses.** Spectral average of the change in absorption between the purple dotted lines as a function of time delay for **c** parallel and **d** perpendicular orientation.

### 3.4.5 Additional THz Stark Spectroscopy Results

In the main text we only show results for parallel polarization between THz waveform and probe pulse. However, the Liptay analysis requires Stark signals for two different relative polarization orientations, ideally but not necessarily parallel and perpendicular. Hence, for completeness we here show the signals for perpendicular orientation. While Fig. 3.9 shows the perpendicular orientation for TTF-BTD, Fig. 3.10 shows the corresponding results for anthanthrene.

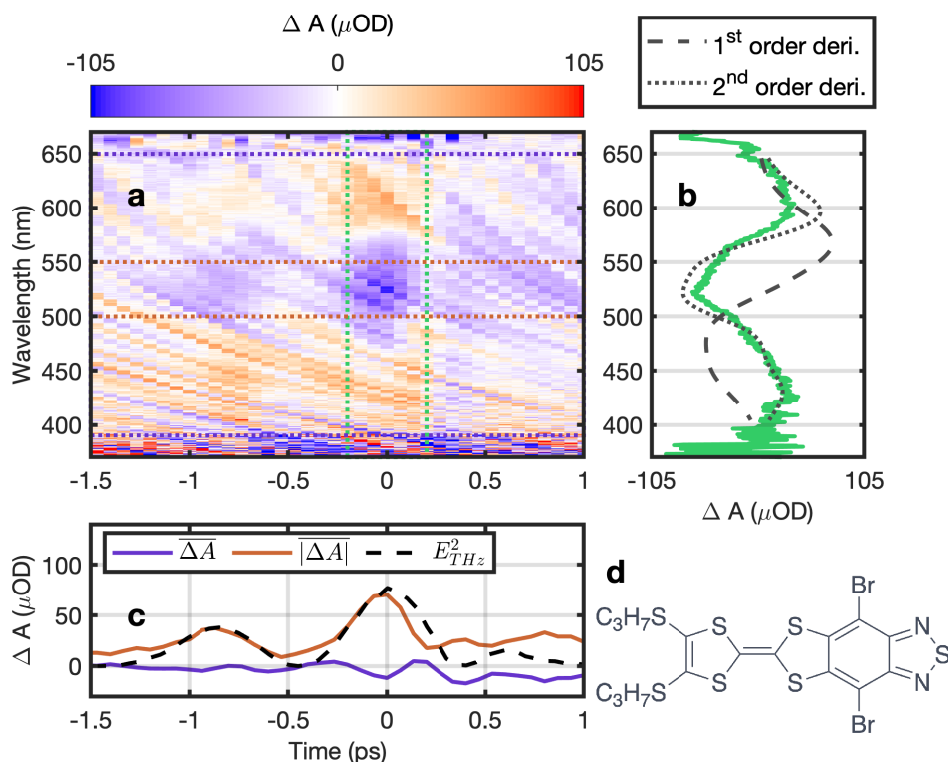


Figure 3.9: **THz Stark signal of TTF-BTD with perpendicular orientation.** **a** False-color plot of the measured change in absorption spectrum as a function of time delay between THz and probe pulse and wavelength. **b** Time-averaged (between the two green dotted lines) change in absorption versus wavelength (green solid curve) compared to the scaled first (black dashed curve) and second order derivative (black dotted curve) of the ground state absorption spectrum. **c** Spectral average of the change in absorption between the purple dotted (purple curve) and red dotted lines (red curve) in **a**. The red curve is compared to the scaled square of the measured THz electric field  $E_{\text{THz}}^2$  (black dashed curve). **d** Chemical structure of TTF-BTD.

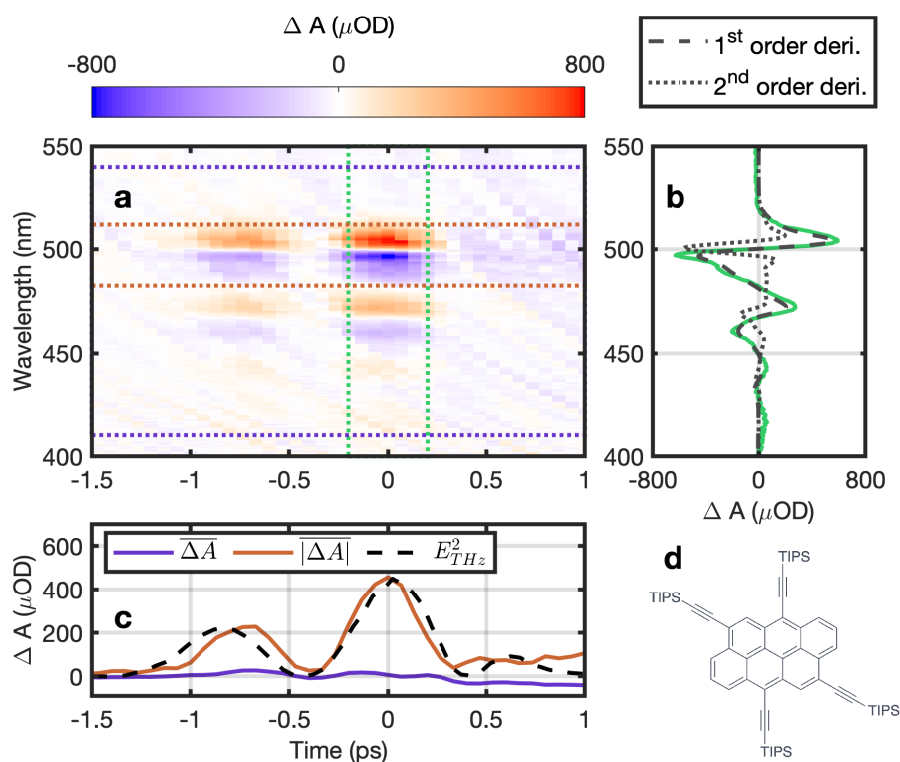


Figure 3.10: **THz Stark signal of anthanthrene with perpendicular orientation.** **a** False-color plot of the measured change in absorption spectrum as a function of time delay between THz and probe pulse and wavelength. **b** Time-averaged (between the two green dotted lines) change in absorption versus wavelength (green solid curve) compared to the scaled first (black dashed curve) and second order derivative (black dotted curve) of the ground state absorption spectrum. **c** Spectral average of the change in absorption between the purple dotted (purple curve) and red dotted lines (red curve) in **a**. The red curve is compared to the scaled square of the measured THz electric field  $E_{\text{THz}}^2$  (black dashed curve). **d** Chemical structure of anthanthrene.

### 3.4.6 Characterization of THz Pulses

To determine the THz electric field strength in air we assume that the spatio-temporal electric field can be expressed in a product  $E(x, y, t) = E_0 g_x(x) g_y(y) f(t)$ , where  $E_0$  is the peak electric field strength and  $g_x(x)$ ,  $g_y(y)$ , and  $f(t)$  are spatially and temporally dependent functions normalized to a peak value of one. The peak electric field strength  $E_0$  was determined from three measurements, i.e. the average power  $P_{avg}$  at a repetition rate of  $f_{rep}$ , the spatial profiles  $g_x^2(x)$  and  $g_y^2(y)$ , and the time dependence  $f(t)$  and is calculated via

$$E_0 = \sqrt{\frac{P_{avg}}{\epsilon_0 c f_{rep} \int_{-\infty}^{\infty} g_x^2(x) dx \int_{-\infty}^{\infty} g_y^2(y) dy \int_{-\infty}^{\infty} f^2(t) dt}}, \quad (3.2)$$

where  $\epsilon_0$  is the vacuum permittivity and  $c$  is the speed of light in vacuum. The average power was recorded by a calibrated THz power meter (with a resolution of 50  $\mu$ W and a relative error of  $\pm 12\%$ ), the spatial profiles were extracted from two perpendicular knife-edge measurements, and the time dependence was measured by electro-optic sampling in a 0.3-mm-thick GaP  $\langle 110 \rangle$  crystal. Note that all measurements are taken at the sample position. The maximum THz power was measured to 3.6 mW at 1 kHz repetition rate, the THz spot was nearly Gaussian with a beam waist of 1 mm in x- as well as in y-direction, and the measured electro-optic signal<sup>73,74,75</sup> and the corresponding spectrum are shown in Fig. 3.11a and b. Inserting the three measurements in Eq.(3.2) results in a peak electric field of  $E_0 = (400 \pm 24)$  kV/cm in air. The corresponding THz spectral amplitude shows a center frequency of 0.5 THz with a bandwidth of 0.7 THz (FWHM). The optical system was in ambient atmosphere, hence the absorption feature around 1.1 THz is due to the water vapor absorption.

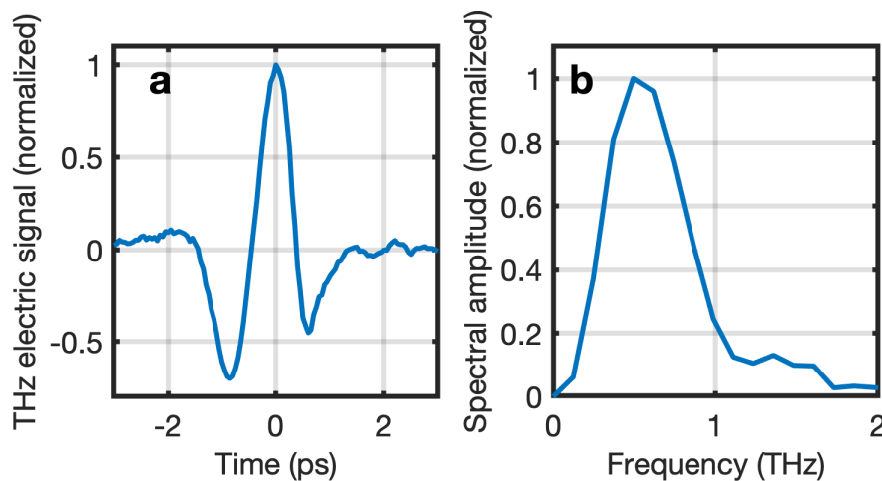


Figure 3.11: **a** Measured electro-optic signal at the sample position and **b** corresponding spectrum.

The effective field strength, at which the probe pulse interrogates the molecular system, is typically smaller because of a number of effects. The dominating reduction factor comes from the geometry and material of the cuvette. For instance, Fresnel reflections or Fabry-Perot interferences at or within the cuvette limit the maximum electric field strength. Some solvents also have a

no-negligible THz absorption coefficient and consequently reduce the electric field strength exponentially along the probe's propagation direction. Moreover, several effects lead to a smearing and averaging of the signal, such as the finite size of the probe interrogating the sample at different THz electric field strengths or the finite duration of the probe pulse and the group velocity mismatch between THz waveform and probe pulse. In order to account for all these effects we performed finite difference time-domain simulations propagating the THz waveform together with a time delayed probe pulse through the sample cuvette. We found that the time dependence of the THz electric field experienced by the probe pulse is almost identical to the free space THz waveform, however the peak electric field strength is reduced by a factor of 0.7 resulting in a maximum electric field of  $E_0 = (280 \pm 17)$  kV/cm in the sample.

### 3.4.7 Liptay Analysis

The following analysis closely follows the recipe outlined in reference<sup>5</sup>. After having identified the Stark-active transitions, the Stark spectra are subsequently analyzed with the Liptay formalism (for details also see references<sup>37</sup> and<sup>28</sup>). The analytic expression derived by Liptay links the molar absorption  $\Delta\epsilon(\bar{\nu})$  as a function of wavenumber to the square of the electric field  $\mathbf{E}$  and ground state absorption spectrum  $\epsilon(\bar{\nu})$

$$\Delta\epsilon(\bar{\nu}) = f_l^2 |\mathbf{E}|^2 \left\{ A_\chi \epsilon(\bar{\nu}) + \frac{B_\chi}{15hc} \bar{\nu} \frac{d}{d\bar{\nu}} \left( \frac{\epsilon(\bar{\nu})}{\bar{\nu}} \right) + \frac{C_\chi}{30h^2c^2} \bar{\nu} \frac{d^2}{d\bar{\nu}^2} \left( \frac{\epsilon(\bar{\nu})}{\bar{\nu}} \right) \right\}, \quad (3.3)$$

where  $h$  is Planck's constant and  $c$  the speed of light. The model assumes an isotropic distribution of transition dipole moments, which is provided by freezing the sample in conventional Stark spectroscopy. The measured Stark spectra are fitted with a weighted combination of the zeroth, first, and second order derivative of the ground state absorption spectrum. The coefficient  $A_\chi$  is determined by the transition polarizability and/or the transition hyperpolarizability of the sample, which can usually be neglected for immobilized samples. The second and third coefficients are given by

$$B_\chi = \frac{5}{2} \text{Tr}(\underline{\Delta\alpha}) + (3 \cos^2 \chi - 1) \left( \frac{3}{2} \mathbf{m} \underline{\Delta\alpha} \mathbf{m} - \frac{1}{2} \text{Tr}(\underline{\Delta\alpha}) \right) \quad (3.4)$$

$$C_\chi = |\Delta\mu|^2 \{ 5 + (3 \cos^2 \chi - 1) (3 \cos^2 \zeta - 1) \}, \quad (3.5)$$

where  $\text{Tr}(\underline{\Delta\alpha})$  is the trace of the polarizability tensor,  $\mathbf{m} \underline{\Delta\alpha} \mathbf{m}$  is its projection along the transition dipole moment,  $\chi$  is the angle between the applied electric field and the probe polarization,  $\Delta\mu$  is the change in dipole moment and  $\zeta$  is the angle between the change in dipole moment and the transition dipole moment.

The molecular parameters are extracted by simultaneously fitting the ground state absorption spectra and two Stark spectra for different probe polarizations. Figure 3.12 shows the measured data (dotted curves) and the corresponding fits (black solid curves) for the TTF-BTD sample. Figure 3.12a and Fig. 3.12c show the results for the conventional Stark measurement at 77 K, while Fig. 3.12b and Fig. 3.12d show the results for the THz-Stark measurement at 295 K (same data as shown in Fig. 4 in the main text). For both experiments we find reasonable agreement



between the fits and the measured data with a slightly better fit quality for the conventional Stark measurements. Figure 3.12e and Fig. 3.12f separately show the contribution of the zeroth, first and second order contribution to the fitted Stark signal for  $\chi = 90^\circ$ . The contribution of the zeroth order  $\hat{A}_\chi$  is multiplied by 10 and we find negligible contribution to the Stark signal for both the conventional and the THz experiment, which confirms that the alignment of molecules due to the electric field is negligible.

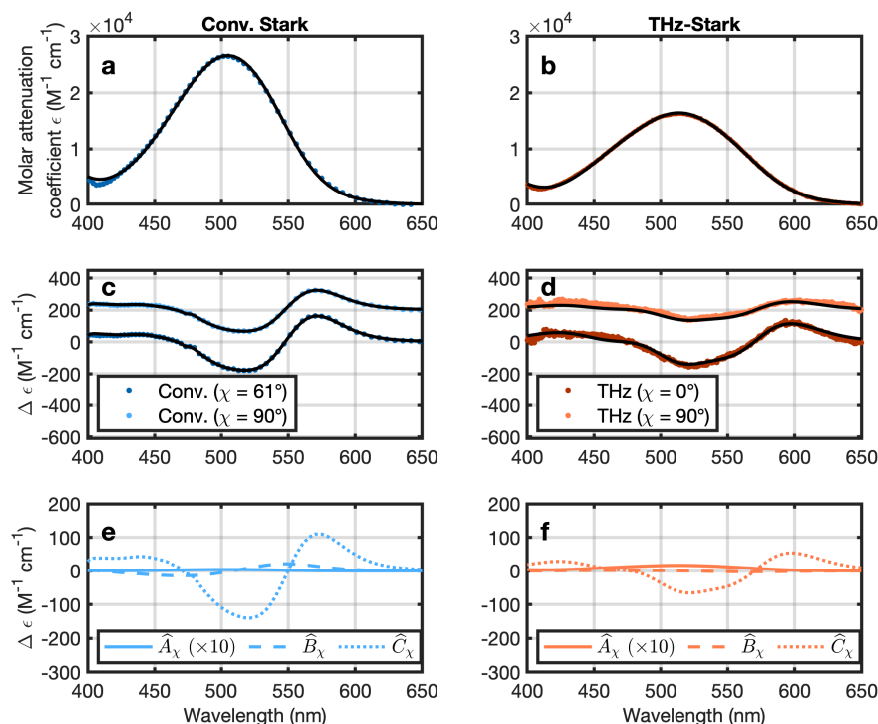


Figure 3.12: **TTF-BTD conventional Stark and THz-Stark spectra fitting** **a, b** Ground state absorption spectrum  $\epsilon$  of TTF-BTD sample at 77 K (**a**) and at 295 K (**b**). The dots represent the data points and the black solid curves represents the fits. **c, d** Measured Stark spectra for two different incidence angles (dots) and corresponding fits (black solid curves) for the conventional Stark measurement **c** and THz-Stark measurement **d**. For better visualization, the curves for  $\chi = 90^\circ$  are arbitrarily shifted along the  $\Delta\epsilon$ -axis. **e, f** Contribution of the zeroth (solid curve), first (dashed curve) and second (dotted curve) order derivative line form for the Stark spectra for  $\chi = 90^\circ$ .

The same fitting results are shown in Fig. 3.13 for the anthanthrene sample. Also here we find reasonable agreement between the fits and the measured data for both conventional and THz Stark spectroscopy.



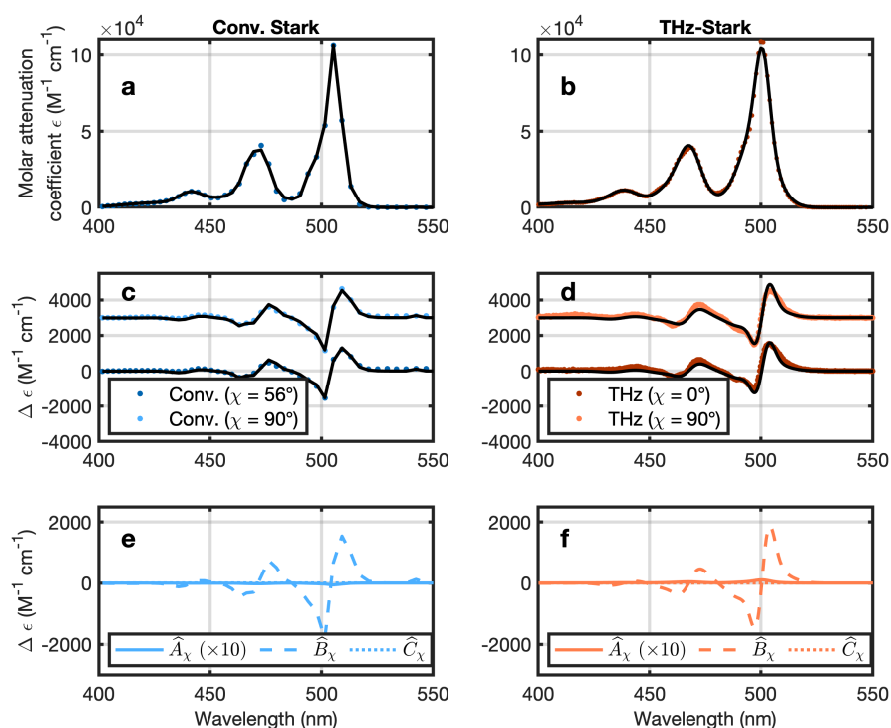


Figure 3.13: **Anthanthrene conventional Stark and THz-Stark spectra fitting** **a, b** Ground state absorption spectrum  $\epsilon$  of anthanthrene sample at 77 K (**a**) and at 295 K (**b**). The dots represent the data points and the black solid curves represents the fits. **c, d** Measured Stark spectra for two different incidence angles (dots) and corresponding fits (black solid curves) for the conventional Stark measurement **c** and THz-Stark measurement **d**. For better visualization, the curves for  $\chi = 90^\circ$  are arbitrarily shifted along the  $\Delta\epsilon$ -axis. **e, f** Contribution of the zeroth (solid curve), first (dashed curve) and second (dotted curve) order derivative line form for the Stark spectra for  $\chi = 90^\circ$ .

### 3.4.8 Local Field Correction Factor

The local field correction factor gives a measure of how the solvent cavity affects the field inside the cavity when an external electric field is applied. The calculations were done in analogy to those described in literature<sup>42,43,44</sup>. We approximated the molecule as occupying a cavity with an ellipsoidal shape. For anthanthrene we estimate the ellipsoid axes to 15 Å, 15 Å, and 3 Å, while for the TTB-BTD we estimate them to 15 Å, 7 Å, and 3 Å. Note that reasonable variation of these parameters has only minor effects to the local field correction factor. Based on literature, the dielectric constant of toluene at 77 K and zero frequency is 2.52<sup>76</sup>, while at room temperature and 400 GHz it is 2.27<sup>77</sup>. The local field correction factors  $f_l$  for TTF-BTD and anthanthrene are estimated to be 1.30 and 1.33 respectively for conventional Stark spectroscopy and to be 1.26 and 1.29 respectively for THz Stark spectroscopy. Hence, the fitted values  $\text{Tr}(\Delta\alpha)$  have to be divided by  $f_l^2$  and  $\Delta\mu$  by  $f_l$  before the numbers can be compared with the DFT calculation.

### 3.4.9 THz Stark Spectroscopy Results of Anthanthrene in EtOAc

To demonstrate that the transient THz Stark effect can be studied in a different solvent with different polarity, we measured the same solute Anthanthrene in the solvent ethyl acetate (EtOAc). The relative polarity of EtOAc is about 0.228 and the relative polarity of toluene is about 0.099. To apply Liptay analysis, Stark signals were measured for two different relative polarization orientations. While Fig. 3.14 shows the parallel orientation for Anthanthrene in EtOAc, Fig. 3.15 shows the perpendicular orientation for Anthanthrene in EtOAc. Although the relative polarity increased by a factor of 2.3, the result of EtOAc gives a similar Stark signature to those measured for solutes in toluene as shown in Fig. 3.16. The blue shift in the ground state absorption is attributed to the solvent's instantaneous electronic polarizability. Note that the solute we used is a non-polar solute and cannot be dissolved in more polar solvents.

Then, we compared quantitatively the extracted molecular parameters as calculated via DFT or measured by conventional and THz Stark spectroscopy summarized in Table 3.1.

Table 3.4: Comparison of relevant molecular parameters as calculated via DFT or measured by conventional and THz Stark spectroscopy in different solvents.

Parameter	DFT	Conventional Stark (Toluene)	THz-Stark (Toluene)	THz-Stark (EtOAc)
<b>Anthanthrene: 4,6,10,12-tetrakis(triisopropylsilylethynyl)anthanthrene</b>				
$\text{Tr}(\Delta\alpha)$ (Å <sup>3</sup> )	457	$363 \pm 20$	$296 \pm 70$	$229 \pm 53$

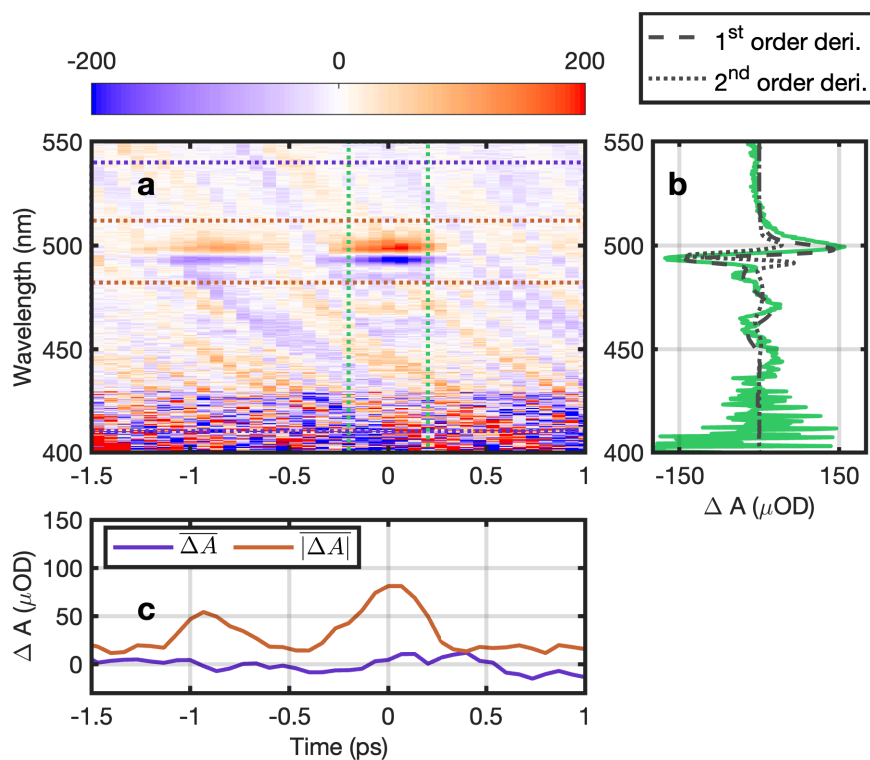


Figure 3.14: **THz Stark signal of anthanthrene in EtOAc with parallel orientation.** **a** False-color plot of the measured change in absorption spectrum as a function of time delay between THz and probe pulse and wavelength. **b** Time-averaged (between the two green dotted lines) change in absorption versus wavelength (green solid curve) compared to the scaled first (black dashed curve) and second order derivative (black dotted curve) of the ground state absorption spectrum. **c** Spectral average of the change in absorption between the purple dotted (purple curve) and red dotted lines (red curve) in **a**.

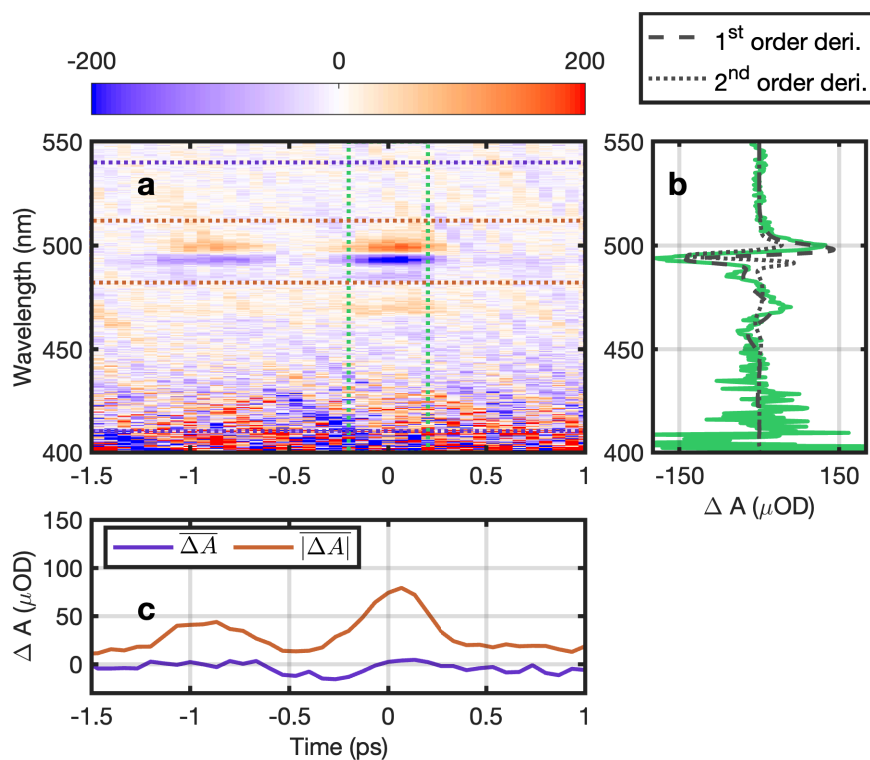


Figure 3.15: **THz Stark signal of anthanthrene in EtOAc with perpendicular orientation.** **a** False-color plot of the measured change in absorption spectrum as a function of time delay between THz and probe pulse and wavelength. **b** Time-averaged (between the two green dotted lines) change in absorption versus wavelength (green solid curve) compared to the scaled first (black dashed curve) and second order derivative (black dotted curve) of the ground state absorption spectrum. **c** Spectral average of the change in absorption between the purple dotted (purple curve) and red dotted lines (red curve) in **a**.

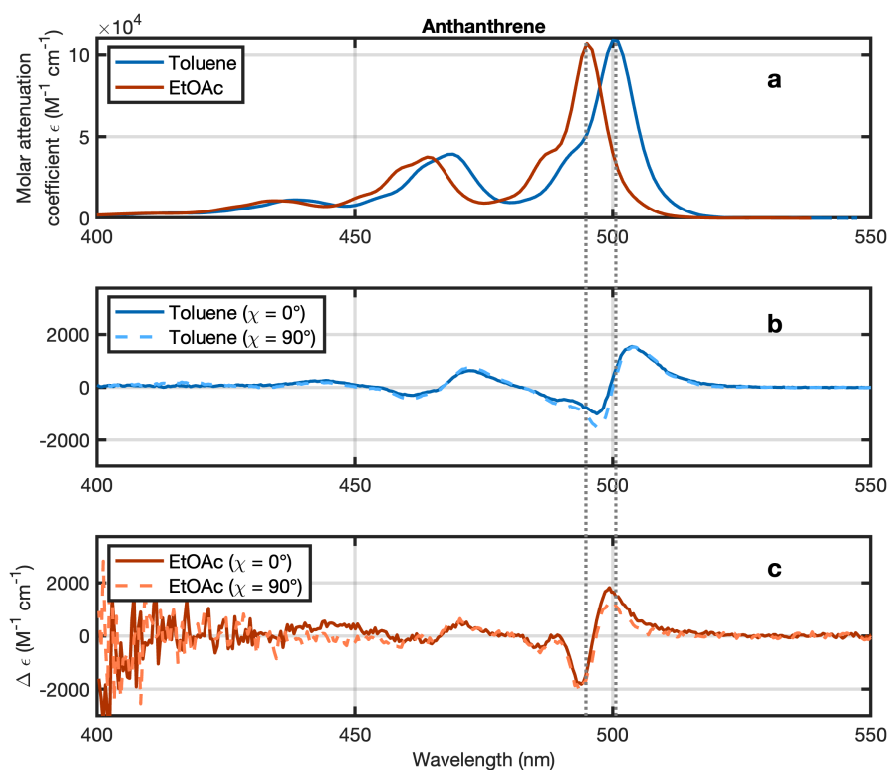


Figure 3.16: **Comparison of THz Stark signal of Anthanthrene in toluene and EtOAc.** **a** absorption spectra of Anthanthrene in toluene (blue) and EtOAc (red). **b,c** THz Stark spectra of Anthanthrene (b) in toluene (c) in EtOAc recorded for parallel and perpendicular orientation of THz and probe polarization. For direct comparison the y-scale is in units of  $\Delta \epsilon$  scaled to an electric field of 1 MV/cm. The grey dotted vertical lines are guides to the eye and help to visualize the shift of the spectra at the different temperatures.

## Bibliography

- [1] Bruce S Brunschwig, Carol Creutz, and Norman Sutin. Electroabsorption spectroscopy of charge transfer states of transition metal complexes. *Coord. Chem. Rev.*, 177(1):61–79, 1998. ISSN 0010-8545. doi: [https://doi.org/10.1016/S0010-8545\(98\)00188-X](https://doi.org/10.1016/S0010-8545(98)00188-X). URL <https://www.sciencedirect.com/science/article/pii/S001085459800188X>.
- [2] Gerold U Bublit, Rafael Ortiz, Seth R Marder, and Steven G Boxer. Stark Spectroscopy of Donor/Acceptor Substituted Polyenes. *J. Am. Chem. Soc.*, 119(14):3365–3376, apr 1997. ISSN 0002-7863. doi: 10.1021/ja9640814. URL <https://doi.org/10.1021/ja9640814>.
- [3] Toshifumi Iimori, Ryuichi Ito, Nobuhiro Ohta, and Hideyuki Nakano. Stark Spectroscopy of Rubrene. I. Electroabsorption Spectroscopy and Molecular Parameters. *J. Phys. Chem. A*, 120(25):4307–4313, jun 2016. ISSN 1089-5639. doi: 10.1021/acs.jpca.6b02625. URL <https://doi.org/10.1021/acs.jpca.6b02625>.
- [4] Laba Karki, Fredrick W Vance, Joseph T Hupp, Steven M LeCours, and Michael J Therien. Electronic Stark Effect Studies of a Porphyrin-Based Push-Pull Chromophore Displaying a Large First Hyperpolarizability: State-Specific Contributions to  $\beta$ . *J. Am. Chem. Soc.*, 120(11):2606–2611, mar 1998. ISSN 0002-7863. doi: 10.1021/ja973593v. URL <https://doi.org/10.1021/ja973593v>.
- [5] Wolfgang Liptay. Electrochromism and Solvatochromism. *Angew. Chemie Int. Ed. English*, 8(3):177–188, mar 1969. ISSN 0570-0833. doi: <https://doi.org/10.1002/anie.196901771>. URL <https://doi.org/10.1002/anie.196901771>.
- [6] Sarah A Locknar and Linda A Peteanu. Investigation of the Relationship between Dipolar Properties and Cis-Trans Configuration in Retinal Polyenes: A Comparative Study Using Stark Spectroscopy and Semiempirical Calculations. *J. Phys. Chem. B*, 102(21):4240–4246, may 1998. ISSN 1520-6106. doi: 10.1021/jp980562t. URL <https://doi.org/10.1021/jp980562t>.
- [7] R Mathies and L Stryer. Retinal has a highly dipolar vertically excited singlet state: implications for vision. *Proc. Natl. Acad. Sci. U. S. A.*, 73(7):2169–2173, jul 1976. ISSN 0027-8424. doi: 10.1073/pnas.73.7.2169. URL <https://pubmed.ncbi.nlm.nih.gov/1065867https://www.ncbi.nlm.nih.gov/pmc/articles/PMC430480/>.
- [8] Raymond F Pauszek, Goutham Kodali, Stuart T Caldwell, Brian Fitzpatrick, Nada Y Zainalabdeen, Graeme Cooke, Vincent M Rotello, and Robert J Stanley. Excited State Charge Redistribution and Dynamics in the Donor- $\pi$ -Acceptor Flavin Derivative ABFL. *J. Phys. Chem. B*, 117(49):15684–15694, dec 2013. ISSN 1520-6106. doi: 10.1021/jp406420h. URL <https://doi.org/10.1021/jp406420h>.
- [9] Brandt C Pein, Chee Kong Lee, Liang Shi, JiaoJian Shi, Wendi Chang, Harold Y Hwang, Jennifer Scherer, Igor Coropceanu, Xiaoguang Zhao, Xin Zhang, Vladimir Bulović, Mounqi G

- Bawendi, Adam P Willard, and Keith A Nelson. Terahertz-Driven Stark Spectroscopy of CdSe and CdSe–CdS Core–Shell Quantum Dots. *Nano Lett.*, 19(11):8125–8131, nov 2019. ISSN 1530-6984. doi: 10.1021/acs.nanolett.9b03342. URL <https://doi.org/10.1021/acs.nanolett.9b03342>.
- [10] Nancy Hopkins and Robert J Stanley. Measurement of the Electronic Properties of the Flavoprotein Old Yellow Enzyme (OYE) and the OYE:p-Cl Phenol Charge-Transfer Complex Using Stark Spectroscopy. *Biochemistry*, 42(4):991–999, feb 2003. ISSN 0006-2960. doi: 10.1021/bi0268908. URL <https://doi.org/10.1021/bi0268908>.
- [11] Dennis H Oh and Steven G Boxer. Stark effect spectra of Ru(diimine)<sub>3</sub><sup>2+</sup> complexes. *J. Am. Chem. Soc.*, 111(3):1130–1131, feb 1989. ISSN 0002-7863. doi: 10.1021/ja00185a054. URL <https://doi.org/10.1021/ja00185a054>.
- [12] J R Reimers and N S Hush. Electronic properties of transition-metal complexes determined from electroabsorption (Stark) spectroscopy. 2. Mononuclear complexes of ruthenium (II). *J. Phys. Chem.*, 95(24):9773–9781, 1991.
- [13] Yeung-gyo K Shin, Bruce S Brunschwig, Carol Creutz, and Norman Sutin. Toward a Quantitative Understanding of Dipole-Moment Changes in Charge-Transfer Transitions: Electroabsorption Spectroscopy of Transition-Metal Complexes. *J. Am. Chem. Soc.*, 117(33):8668–8669, aug 1995. ISSN 0002-7863. doi: 10.1021/ja00138a024. URL <https://doi.org/10.1021/ja00138a024>.
- [14] Vittoria Roiati, Edoardo Mosconi, Andrea Listorti, Silvia Colella, Giuseppe Gigli, and Filippo De Angelis. Stark Effect in Perovskite/TiO<sub>2</sub> Solar Cells: Evidence of Local Interfacial Order. *Nano Lett.*, 14(4):2168–2174, apr 2014. ISSN 1530-6984. doi: 10.1021/nl500544c. URL <https://doi.org/10.1021/nl500544c>.
- [15] Mohan Singh Mehata, Chain-Shu Hsu, Yuan-Pern Lee, and Nobuhiro Ohta. Electroabsorption and Electrophotoluminescence of Poly(2,3-diphenyl-5-hexyl-p-phenylene vinylene). *J. Phys. Chem. C*, 116(28):14789–14795, jul 2012. ISSN 1932-7447. doi: 10.1021/jp302666f. URL <https://doi.org/10.1021/jp302666f>.
- [16] Arindam Chowdhury, Linda A. Peteanu, M. Adam Webb, and Glen R. Loppnow. Stark spectroscopic studies of blue copper proteins: Azurin. *J. Phys. Chem. B*, 105(2):527–534, jan 2001. ISSN 15206106. doi: 10.1021/jp0025227. URL <https://doi.org/10.1021/jp0025227>.
- [17] Goutham Kodali, Salim U Siddiqui, and Robert J Stanley. Charge Redistribution in Oxidized and Semiquinone E. coli DNA Photolyase upon Photoexcitation: Stark Spectroscopy Reveals a Rationale for the Position of Trp382. *J. Am. Chem. Soc.*, 131(13):4795–4807, apr 2009. ISSN 0002-7863. doi: 10.1021/ja809214r. URL <https://doi.org/10.1021/ja809214r>.
- [18] David J Lockhart and Steven G Boxer. Stark effect spectroscopy of Rhodobacter sphaeroides and Rhodopseudomonas viridis reaction centers. *Proc. Natl. Acad. Sci.*, 85(1):107–111, jan

1988. doi: 10.1073/pnas.85.1.107. URL <https://doi.org/10.1073/pnas.85.1.107>.
- [19] M Lösche, G Feher, and M Y Okamura. The Stark effect in reaction centers from *Rhodobacter sphaeroides* R-26 and *Rhodopseudomonas viridis*. *Proc. Natl. Acad. Sci.*, 84(21):7537–7541, nov 1987. doi: 10.1073/pnas.84.21.7537. URL <https://doi.org/10.1073/pnas.84.21.7537>.
- [20] L L Premvardhan, M A van der Horst, K J Hellingwerf, and R van Grondelle. Stark spectroscopy on photoactive yellow protein, E46Q, and a nonisomerizing derivative, probes photo-induced charge motion. *Biophys. J.*, 84(5):3226–3239, may 2003. ISSN 00063495. URL <https://www.proquest.com/scholarly-journals/stark-spectroscopy-on-photoactive-yellow-protein/docview/215702186/se-2https://libkey.io/libraries/528/openurl?genre=article&au=Premvardhan%2C+L+L%3BM+A+van+der+Horst%3BHellingwerf%2C+K+J%3BR+van+Grondelle&aula>.
- [21] Oscar J G Somsen, Vladimir Chernyak, Raoul N Frese, Rienk van Grondelle, and Shaul Mukamel. Excitonic Interactions and Stark Spectroscopy of Light Harvesting Systems. *J. Phys. Chem. B*, 102(44):8893–8908, oct 1998. ISSN 1520-6106. doi: 10.1021/jp981114o. URL <https://doi.org/10.1021/jp981114o>.
- [22] Niraj Verma, Yunwen Tao, Wenli Zou, Xia Chen, Xin Chen, Marek Freindorf, and Elfi Kraka. A Critical Evaluation of Vibrational Stark Effect (VSE) Probes with the Local Vibrational Mode Theory. *Sensors*, 20(8):2358, 2020. doi: 10.3390/s20082358.
- [23] Christian Schmidt, Johannes Bühler, A-C Heinrich, Jonas Allerbeck, Reinold Podzimski, Daniel Berghoff, Torsten Meier, W Gero Schmidt, Christian Reichl, Werner Wegscheider, et al. Signatures of transient wannier-stark localization in bulk gallium arsenide. *Nature Communications*, 9(1):2890, 2018.
- [24] T Barmashova, A Luchinin, A Murzanev, A Sidorov, A Stepanov, A Veselov, and A Vodopyanov. Studies of terahertz discharge in noble gases using a michelson interferometer. In *Journal of Physics: Conference Series*, volume 1697, page 012220. IOP Publishing, 2020.
- [25] Toshiki Yamada, Takahiro Kaji, Chiyumi Yamada, and Akira Otomo. Terahertz wave detection by the stark effect in nonlinear optical polymers. *Japanese Journal of Applied Physics*, 58(4):040901, 2019.
- [26] Moritz B Heindl, Nicholas Kirkwood, Tobias Lauster, Julia A Lang, Markus Retsch, Paul Mulvaney, and Georg Herink. Ultrafast imaging of terahertz electric waveforms using quantum dots. *Light: Science & Applications*, 11(1):5, 2022.
- [27] Yuki Kobayashi, Christian Heide, Amalya C Johnson, Vishal Tiwari, Fang Liu, David A Reis, Tony F Heinz, and Shambhu Ghimire. Floquet engineering of strongly driven excitons in monolayer tungsten disulfide. *Nature Physics*, 19(2):171–176, 2023.



- [28] Gerold U Bublitx and Steven G Boxer. STARK SPECTROSCOPY: Applications in Chemistry, Biology, and Materials Science. *Annu. Rev. Phys. Chem.*, 48(1):213–242, oct 1997. ISSN 0066-426X. doi: 10.1146/annurev.physchem.48.1.213. URL <https://doi.org/10.1146/annurev.physchem.48.1.213>.
- [29] Sabine Keiber, Shawn Sederberg, Alexander Schwarz, Michael Trubetskov, Volodymyr Pervak, Ferenc Krausz, and Nicholas Karpowicz. Electro-optic sampling of near-infrared waveforms. *Nat. Photonics*, 10(3):159–162, 2016. ISSN 1749-4893. doi: 10.1038/nphoton.2015.269. URL <https://doi.org/10.1038/nphoton.2015.269>.
- [30] Matthias Knorr, Jürgen Raab, Maximilian Tauer, Philipp Merkl, Dominik Peller, Emanuel Wittmann, Eberhard Riedle, Christoph Lange, and Rupert Huber. Phase-locked multi-terahertz electric fields exceeding 13 MV/cm at a 190 kHz repetition rate. *Opt. Lett.*, 42(21):4367–4370, 2017. doi: 10.1364/OL.42.004367. URL <https://opg.optica.org/ol/abstract.cfm?URI=ol-42-21-4367>.
- [31] H M Jones and E E Kunhardt. Pulsed dielectric breakdown of pressurized water and salt solutions. *J. Appl. Phys.*, 77(2):795–805, jan 1995. ISSN 0021-8979. doi: 10.1063/1.359002. URL <https://doi.org/10.1063/1.359002>.
- [32] Z Krasucki and Frank Philip Bowden. Breakdown of liquid dielectrics. *Proc. R. Soc. London. Ser. A. Math. Phys. Sci.*, 294(1438):393–404, oct 1966. doi: 10.1098/rspa.1966.0214. URL <https://doi.org/10.1098/rspa.1966.0214>.
- [33] Dongfang Zhang, Arya Fallahi, Michael Hemmer, Xiaojun Wu, Moein Fakhari, Yi Hua, Huseyin Cankaya, Anne-Laure Calendron, Luis E Zapata, Nicholas H Matlis, and Franz X Kärtner. Segmented terahertz electron accelerator and manipulator (STEAM). *Nat. Photonics*, 12(6):336–342, 2018. ISSN 1749-4893. doi: 10.1038/s41566-018-0138-z. URL <https://doi.org/10.1038/s41566-018-0138-z>.
- [34] Anneliese Amacher, Hewei Luo, Zitong Liu, Martin Bircher, Michele Cascella, Jürg Hauser, Silvio Decurtins, Deqing Zhang, and Shi-Xia Liu. Electronic tuning effects via cyano substitution of a fused tetrathiafulvalene–benzothiadiazole dyad for ambipolar transport properties. *RSC Adv.*, 4(6):2873–2878, 2014. doi: 10.1039/C3RA46784H. URL <http://dx.doi.org/10.1039/C3RA46784H>.
- [35] Flavia Pop, Anneliese Amacher, Narcis Avarvari, Jie Ding, Latevi Max Lawson Daku, Andreas Hauser, Marius Koch, Jürg Hauser, Shi-Xia Liu, and Silvio Decurtins. Tetrathiafulvalene-Benzothiadiazoles as Redox-Tunable Donor–Acceptor Systems: Synthesis and Photophysical Study. *Chem. – A Eur. J.*, 19(7):2504–2514, feb 2013. ISSN 0947-6539. doi: <https://doi.org/10.1002/chem.201202742>. URL <https://doi.org/10.1002/chem.201202742>.
- [36] Jean-Benoît Giguère, Quentin Verolet, and Jean-François Morin. 4,10-Dibromoanthanthrone as a New Building Block for p-Type, n-Type, and Ambipolar  $\pi$ -Conjugated Materials. *Chem. – A Eur. J.*, 19(1):372–381, jan 2013. ISSN 0947-6539. doi: <https://doi.org/10.1002/chem.201202878>. URL <https://doi.org/10.1002/chem.201202878>.

- [37] Egmont J Rohwer, Maryam Akbarimoosavi, Steven E Meckel, Xunshan Liu, Yan Geng, Latévi Max Lawson Daku, Andreas Hauser, Andrea Cannizzo, Silvio Decurtins, Robert J Stanley, Shi-Xia Liu, and Thomas Feurer. Dipole Moment and Polarizability of Tunable Intramolecular Charge Transfer States in Heterocyclic  $\pi$ -Conjugated Molecular Dyads Determined by Computational and Stark Spectroscopic Study. *J. Phys. Chem. C*, 122(17): 9346–9355, may 2018. ISSN 1932-7447. doi: 10.1021/acs.jpcc.8b02268. URL <https://doi.org/10.1021/acs.jpcc.8b02268>.
- [38] Gerold U Bublitz and Steven G Boxer. Effective Polarity of Frozen Solvent Glasses in the Vicinity of Dipolar Solutes. *J. Am. Chem. Soc.*, 120(16):3988–3992, apr 1998. ISSN 0002-7863. doi: 10.1021/ja971665c. URL <https://doi.org/10.1021/ja971665c>.
- [39] Maryam Akbarimoosavi, Egmont Rohwer, Ariana Rondi, Jihane Hankache, Yan Geng, Silvio Decurtins, Andreas Hauser, Shi-Xia Liu, Thomas Feurer, and Andrea Cannizzo. Tunable Lifetimes of Intramolecular Charge-Separated States in Molecular Donor–Acceptor Dyads. *J. Phys. Chem. C*, 123(14):8500–8511, apr 2019. ISSN 1932-7447. doi: 10.1021/acs.jpcc.8b11066. URL <https://doi.org/10.1021/acs.jpcc.8b11066>.
- [40] Ariana Rondi, Yuseff Rodriguez, Thomas Feurer, and Andrea Cannizzo. Solvation-Driven Charge Transfer and Localization in Metal Complexes. *Acc. Chem. Res.*, 48(5):1432–1440, may 2015. ISSN 0001-4842. doi: 10.1021/ar5003939. URL <https://doi.org/10.1021/ar5003939>.
- [41] Poonam Singh, Jia Zhang, Dieter Engel, Benjamin P. Fingerhut, and Thomas Elsaesser. Transient terahertz stark effect: A dynamic probe of electric interactions in polar liquids. *The Journal of Physical Chemistry Letters*, 14(24):5505–5510, 2023. doi: 10.1021/acs.jpclett.3c01079. URL <https://doi.org/10.1021/acs.jpclett.3c01079>. PMID: 37289958.
- [42] Antoine Aubret, Michel Orrit, and Florian Kulzer. Understanding Local-Field Correction Factors in the Framework of the Onsager-Böttcher Model. *ChemPhysChem*, 20(3):345–355, feb 2019. ISSN 1439-4235. doi: <https://doi.org/10.1002/cphc.201800923>. URL <https://doi.org/10.1002/cphc.201800923>.
- [43] Robert J Stanley and M Salim Siddiqui. A Stark Spectroscopic Study of N(3)-Methyl, N(10)-Isobutyl-7,8-Dimethylisoalloxazine in Nonpolar Low-Temperature Glasses: Experiment and Comparison with Calculations. *J. Phys. Chem. A*, 105(49):11001–11008, dec 2001. ISSN 1089-5639. doi: 10.1021/jp011971j. URL <https://doi.org/10.1021/jp011971j>.
- [44] Lavanya Premvardhan and Linda Peteanu. Electroabsorption measurements and ab initio calculations of the dipolar properties of 2-(2'-hydroxyphenyl)-benzothiazole and -benzoxazole: two photostabilizers that undergo excited-state proton transfer. *Chem. Phys. Lett.*, 296(5):521–529, 1998. ISSN 0009-2614. doi: [https://doi.org/10.1016/S0009-2614\(98\)01048-3](https://doi.org/10.1016/S0009-2614(98)01048-3). URL <https://www.sciencedirect.com/science/article/pii/S0009261498010483>.

- [45] Michael Bendikov, Fred Wudl, and Dmitrii F Perepichka. Tetrathiafulvalenes, Oligoacenenes, and Their Buckminsterfullerene Derivatives: The Brick and Mortar of Organic Electronics. *Chem. Rev.*, 104(11):4891–4946, nov 2004. ISSN 0009-2665. doi: 10.1021/cr030666m. URL <https://doi.org/10.1021/cr030666m>.
- [46] Nazario Martín. Tetrathiafulvalene: the advent of organic metals. *Chem. Commun.*, 49(63): 7025–7027, 2013. ISSN 1359-7345. doi: 10.1039/C3CC00240C. URL <http://dx.doi.org/10.1039/C3CC00240C>.
- [47] Jincai Wu, Nathalie Dupont, Shi-Xia Liu, Antonia Neels, Andreas Hauser, and Silvio Decurtins. Imidazole-annulated tetrathiafulvalenes exhibiting pH-tuneable intramolecular charge transfer and redox properties. *Chem. Asian J.*, 4(3):392–399, mar 2009. ISSN 1861-471X (Electronic). doi: 10.1002/asia.200800322.
- [48] Jesse J Bergkamp, Silvio Decurtins, and Shi-Xia Liu. Current advances in fused tetrathiafulvalene donor–acceptor systems. *Chem. Soc. Rev.*, 44(4):863–874, 2015. ISSN 0306-0012. doi: 10.1039/C4CS00255E. URL <http://dx.doi.org/10.1039/C4CS00255E>.
- [49] José L Segura and Nazario Martín. New Concepts in Tetrathiafulvalene Chemistry. *Angew. Chem. Int. Ed. Engl.*, 40(8):1372–1409, apr 2001. ISSN 1521-3773 (Electronic). doi: 10.1002/1521-3773(20010417)40:8<1372::aid-anie1372>3.0.co;2-i.
- [50] K. R. Justin Thomas, J. T. Lin, M Velusamy, Y.T. Tao, and C.H. Chuen. Color Tuning in Benzo[1,2,5]thiadiazole-Based Small Molecules by Amino Conjugation/Deconjugation: Bright Red-Light-Emitting Diodes. *Adv. Funct. Mater.*, 14(1):83–90, jan 2004. ISSN 1616-301X. doi: <https://doi.org/10.1002/adfm.200304486>. URL <https://doi.org/10.1002/adfm.200304486>.
- [51] Yongzhen Wu and Weihong Zhu. Organic sensitizers from D– $\pi$ –A to D–A– $\pi$ –A: effect of the internal electron-withdrawing units on molecular absorption, energy levels and photovoltaic performances. *Chem. Soc. Rev.*, 42(5):2039–2058, 2013. ISSN 0306-0012. doi: 10.1039/C2CS35346F. URL <http://dx.doi.org/10.1039/C2CS35346F>.
- [52] Colin R Belton, Alexander L Kanibolotsky, James Kirkpatrick, Clara Orofino, Saadeldin E T Elmasly, Paul N Stavrinou, Peter J Skabara, and Donal D C Bradley. Location, Location, Location - Strategic Positioning of 2,1,3-Benzothiadiazole Units within Trigonal Quaterfluorene-Truxene Star-Shaped Structures. *Adv. Funct. Mater.*, 23(22):2792–2804, jun 2013. ISSN 1616-301X. doi: <https://doi.org/10.1002/adfm.201202644>. URL <https://doi.org/10.1002/adfm.201202644>.
- [53] Flavia Pop, François Riobé, Sabine Seifert, Thomas Cauchy, Jie Ding, Nathalie Dupont, Andreas Hauser, Marius Koch, and Narcis Avarvari. Tetrathiafulvalene-1,3,5-triazines as (Multi)Donor–Acceptor Systems with Tunable Charge Transfer: Structural, Photophysical, and Theoretical Investigations. *Inorg. Chem.*, 52(9):5023–5034, may 2013. ISSN 0020-1669. doi: 10.1021/ic3027336. URL <https://doi.org/10.1021/ic3027336>.

- [54] Pere Alemany, Enric Canadell, Yan Geng, Jürg Hauser, Piero Macchi, Karl Krämer, Silvio Decurtins, and Shi-Xia Liu. Exploring the Electronic Structure of an Organic Semiconductor Based on a Compactly Fused Electron Donor–Acceptor Molecule. *ChemPhysChem*, 16(7): 1361–1365, may 2015. ISSN 1439-4235. doi: <https://doi.org/10.1002/cphc.201500090>. URL <https://doi.org/10.1002/cphc.201500090>.
- [55] Yan Geng, Raphael Pfattner, Antonio Campos, Jürg Hauser, Vladimir Laukhin, Joaquim Puigdollers, Jaume Veciana, Marta Mas-Torrent, Concepció Rovira, Silvio Decurtins, and Shi-Xia Liu. A Compact Tetrathiafulvalene–Benzothiadiazole Dyad and Its Highly Symmetrical Charge-Transfer Salt: Ordered Donor  $\pi$ -Stacks Closely Bound to Their Acceptors. *Chem. – A Eur. J.*, 20(23):7136–7143, jun 2014. ISSN 0947-6539. doi: <https://doi.org/10.1002/chem.201304688>. URL <https://doi.org/10.1002/chem.201304688>.
- [56] Colin J Lambert and Shi-Xia Liu. A Magic Ratio Rule for Beginners: A Chemist’s Guide to Quantum Interference in Molecules. *Chem. – A Eur. J.*, 24(17):4193–4201, mar 2018. ISSN 0947-6539. doi: <https://doi.org/10.1002/chem.201704488>. URL <https://doi.org/10.1002/chem.201704488>.
- [57] Yan Geng, Sara Sangtarash, Cancan Huang, Hatef Sadeghi, Yongchun Fu, Wenjing Hong, Thomas Wandlowski, Silvio Decurtins, Colin J Lambert, and Shi-Xia Liu. Magic Ratios for Connectivity-Driven Electrical Conductance of Graphene-like Molecules. *J. Am. Chem. Soc.*, 137(13):4469–4476, apr 2015. ISSN 0002-7863. doi: 10.1021/jacs.5b00335. URL <https://doi.org/10.1021/jacs.5b00335>.
- [58] Marjan Famili, Chuancheng Jia, Xunshan Liu, Peiqi Wang, Iain M Grace, Jian Guo, Yuan Liu, Ziyang Feng, Yiliu Wang, Zipeng Zhao, Silvio Decurtins, Robert Häner, Yu Huang, Shi-Xia Liu, Colin J Lambert, and Xiangfeng Duan. Self-Assembled Molecular-Electronic Films Controlled by Room Temperature Quantum Interference. *Chem*, 5(2):474–484, 2019. ISSN 2451-9294. doi: <https://doi.org/10.1016/j.chempr.2018.12.008>. URL <https://www.sciencedirect.com/science/article/pii/S2451929418305710>.
- [59] Yan Geng, Chenyi Yi, Martin Peter Bircher, Silvio Decurtins, Michele Cascella, Michael Grätzel, and Shi-Xia Liu. Anthanthrene dye-sensitized solar cells: influence of the number of anchoring groups and substitution motif. *RSC Adv.*, 5(119):98643–98652, 2015. doi: 10.1039/C5RA21917E. URL <http://dx.doi.org/10.1039/C5RA21917E>.
- [60] Jean-Benoît Giguère, Niyazi Serdar Sariciftci, and Jean-François Morin. Polycyclic anthanthrene small molecules: semiconductors for organic field-effect transistors and solar cells applications. *J. Mater. Chem. C*, 3(3):601–606, 2015. ISSN 2050-7526. doi: 10.1039/C4TC02137A. URL <http://dx.doi.org/10.1039/C4TC02137A>.
- [61] Lei Zhang, Bright Walker, Feng Liu, Nicholas S Colella, Stefan C B Mannsfeld, James J Watkins, Thuc-Quyen Nguyen, and Alejandro L Briseno. Triisopropylsilylethynyl-functionalized dibenzo[def,mno]chrysene: a solution-processed small molecule for bulk heterojunction solar cells. *J. Mater. Chem.*, 22(10):4266–4268, 2012. ISSN 0959-9428. doi: 10.1039/C2JM14998B. URL <http://dx.doi.org/10.1039/C2JM14998B>.

- [62] Bipin K Shah, Douglas C Neckers, Jianmin Shi, Eric W Forsythe, and David Morton. Anthanthrene Derivatives as Blue Emitting Materials for Organic Light-Emitting Diode Applications. *Chem. Mater.*, 18(3):603–608, feb 2006. ISSN 0897-4756. doi: 10.1021/cm052188x. URL <https://doi.org/10.1021/cm052188x>.
- [63] Bipin K Shah, Douglas C Neckers, Jianmin Shi, Eric W Forsythe, and David Morton. Photophysical Properties of Anthanthrene-Based Tunable Blue Emitters. *J. Phys. Chem. A*, 109(34):7677–7681, sep 2005. ISSN 1089-5639. doi: 10.1021/jp052337z. URL <https://doi.org/10.1021/jp052337z>.
- [64] Carlo Adamo and Vincenzo Barone. Toward reliable density functional methods without adjustable parameters: The PBE0 model. *J. Chem. Phys.*, 110(13):6158–6170, mar 1999. ISSN 0021-9606. doi: 10.1063/1.478522. URL <https://doi.org/10.1063/1.478522>.
- [65] Axel D Becke. Density-functional thermochemistry. III. The role of exact exchange. *J. Chem. Phys.*, 98(7):5648–5652, apr 1993. ISSN 0021-9606. doi: 10.1063/1.464913. URL <https://doi.org/10.1063/1.464913>.
- [66] W J Hehre, R Ditchfield, and J A Pople. Self—Consistent Molecular Orbital Methods. XII. Further Extensions of Gaussian—Type Basis Sets for Use in Molecular Orbital Studies of Organic Molecules. *J. Chem. Phys.*, 56(5):2257–2261, mar 1972. ISSN 0021-9606. doi: 10.1063/1.1677527. URL <https://doi.org/10.1063/1.1677527>.
- [67] Erich Runge and E K U Gross. Density-Functional Theory for Time-Dependent Systems. *Phys. Rev. Lett.*, 52(12):997–1000, mar 1984. doi: 10.1103/PhysRevLett.52.997. URL <https://link.aps.org/doi/10.1103/PhysRevLett.52.997>.
- [68] Branislav Jansik, Dan Jonsson, Pawel Sałek, and Hans Ågren. Calculations of static and dynamic polarizabilities of excited states by means of density functional theory. *J. Chem. Phys.*, 121(16):7595–7600, oct 2004. ISSN 0021-9606. doi: 10.1063/1.1794635. URL <https://aip.scitation.org/doi/abs/10.1063/1.1794635>.
- [69] Kestutis Aidas, Celestino Angeli, Keld L Bak, Vejbjørn Bakken, Radovan Bast, Linus Boman, Ove Christiansen, Renzo Cimiraglia, Sonia Coriani, Pål Dahle, Erik K Dalskov, Ulf Ekström, Thomas Enevoldsen, Janus J Eriksen, Patrick Ettenhuber, Berta Fernández, Lara Ferrighi, Heike Fliegl, Luca Frediani, Kasper Hald, Asger Halkier, Christof Hättig, Hanne Heiberg, Trygve Helgaker, Alf Christian Hennum, Hinne Hettema, Eirik Hjertenæs, Stinne Høst, Ida-Marie Høyvik, Maria Francesca Iozzi, Branislav Jansík, Hans Jørgen Aa. Jensen, Dan Jonsson, Poul Jørgensen, Joanna Kauczor, Sheela Kirpekar, Thomas Kjærgaard, Wim Klopper, Stefan Knecht, Rika Kobayashi, Henrik Koch, Jacob Kongsted, Andreas Krapp, Kasper Kristensen, Andrea Ligabue, Ola B Lutnæs, Juan I Melo, Kurt V Mikkelsen, Rolf H Myhre, Christian Neiss, Christian B Nielsen, Patrick Norman, Jeppe Olsen, Jógvan Magnus H Olsen, Anders Osted, Martin J Packer, Filip Pawłowski, Thomas B Pedersen, Patricio F Provasi, Simen Reine, Zilvinas Rinkevicius, Torgeir A Ruden, Kenneth Ruud, Vladimir V Rybkin, Pawel Sałek, Claire C M Samson, Alfredo Sánchez de Merás, Trond Saue, Stephan P A



- Sauer, Bernd Schimmelpfennig, Kristian Sneskov, Arnfinn H Steindal, Kristian O Sylvester-Hvid, Peter R Taylor, Andrew M Teale, Erik I Tellgren, David P Tew, Andreas J Thorvaldsen, Lea Thøgersen, Olav Vahtras, Mark A Watson, David J D Wilson, Marcin Ziolkowski, and Hans Ågren. The Dalton quantum chemistry program system. *WIREs Comput. Mol. Sci.*, 4 (3):269–284, may 2014. ISSN 1759-0876. doi: <https://doi.org/10.1002/wcms.1172>. URL <https://doi.org/10.1002/wcms.1172>.
- [70] János Hebling, Gábor Almási, Ida Z Kozma, and Jürgen Kuhl. Velocity matching by pulse front tilting for large-area THz-pulse generation. *Opt. Express*, 10(21):1161–1166, 2002. doi: 10.1364/OE.10.001161. URL <http://opg.optica.org/oe/abstract.cfm?URI=oe-10-21-1161>.
- [71] J A Fülöp, Z Ollmann, Cs. Lombosi, C Skrobol, S Klingebiel, L Pálfalvi, F Krausz, S Karsch, and J Hebling. Efficient generation of THz pulses with 0.4 mJ energy. *Opt. Express*, 22(17):20155–20163, aug 2014. doi: 10.1364/OE.22.020155. URL <http://www.opticsexpress.org/abstract.cfm?URI=oe-22-17-20155>.
- [72] Mohsen Sajadi, Martin Wolf, and Tobias Kampfrath. Transient birefringence of liquids induced by terahertz electric-field torque on permanent molecular dipoles. *Nat. Commun.*, 8(1):14963, 2017. ISSN 2041-1723. doi: 10.1038/ncomms14963. URL <https://doi.org/10.1038/ncomms14963>.
- [73] Q Wu and X.-C. Zhang. Free-space electro-optic sampling of terahertz beams. *Appl. Phys. Lett.*, 67(24):3523–3525, dec 1995. ISSN 0003-6951. doi: 10.1063/1.114909. URL <https://doi.org/10.1063/1.114909>.
- [74] Ajay Nahata, Aniruddha S Weling, and Tony F Heinz. A wideband coherent terahertz spectroscopy system using optical rectification and electro-optic sampling. *Appl. Phys. Lett.*, 69(16):2321–2323, oct 1996. ISSN 0003-6951. doi: 10.1063/1.117511. URL <https://doi.org/10.1063/1.117511>.
- [75] Fabian D J Brunner, Jeremy A Johnson, Sebastian Grübel, Andrés Ferrer, Steven L Johnson, and Thomas Feurer. Distortion-free enhancement of terahertz signals measured by electro-optic sampling. I. Theory. *J. Opt. Soc. Am. B*, 31(4):904–910, 2014. doi: 10.1364/JOSAB.31.000904. URL <http://opg.optica.org/josab/abstract.cfm?URI=josab-31-4-904>.
- [76] Héctor Isnardi. Die Dielektrizitätskonstante von Flüssigkeiten in ihrer Temperaturabhängigkeit. *Zeitschrift für Phys.*, 9(1):153–179, 1922. ISSN 0044-3328. doi: 10.1007/BF01326964. URL <https://doi.org/10.1007/BF01326964>.
- [77] Cecilie Rønne, Kasper Jensby, Brian J Loughnane, John Fourkas, O Faurskov Nielsen, and Søren R Keiding. Temperature dependence of the dielectric function of C<sub>6</sub>H<sub>6</sub>(l) and C<sub>6</sub>H<sub>5</sub>CH<sub>3</sub>(l) measured with THz spectroscopy. *J. Chem. Phys.*, 113(9):3749–3756, aug 2000. ISSN 0021-9606. doi: 10.1063/1.1287737. URL <https://doi.org/10.1063/1.1287737>.

# Chapter 4

## Time-resolved Terahertz Stark Spectroscopy of Molecules in Water

Elnaz Zyaee<sup>1</sup>, Vladislav Slama<sup>2</sup>, Seyyed Jabbar Mousavi<sup>1</sup>, David Rohrbach<sup>1</sup>, Ursula Röthlisberger<sup>2</sup>, Thomas Feurer<sup>1</sup>

<sup>1</sup> Institute of Applied Physics, University of Bern, 3012 Bern, Switzerland

<sup>2</sup> Laboratory of Computational Chemistry and Biochemistry, École Polytechnique Fédérale de Lausanne (EPFL)

[This work is in preparation for submission.](#)

---

### Abstract

Stark spectroscopy is a powerful method for probing molecular dipole moment changes, charge transfer dynamics, and polarizability under applied electric fields. Time-Resolved Terahertz Stark Spectroscopy (TRTSS), which employs intense single-cycle terahertz (THz) pulses to induce transient Stark shifts, overcomes key limitations of conventional approaches. Unlike static or low-frequency fields, THz pulses oscillate much faster than typical molecular rotation times, effectively preventing dipole reorientation and enabling measurements in solutions at ambient conditions. Here, we extend TRTSS to the most polar solvent and report the first demonstration of Stark spectroscopy in water at room temperature. Using Malachite Green and Methyl Orange as model systems, we observe THz-induced spectral modulations in water, demonstrating that TRTSS can successfully reveal field-induced changes even in highly polar, hydrogen-bonded environments. These results demonstrate that direct field-molecule interactions can be quantified by TRTSS, even within water's complex and highly polar hydrogen-bonded network. By demonstrating TRTSS in water, this work significantly broadens the applicability of this technique, establishing it as a versatile tool for investigating molecular dynamics in chemically and biologically relevant environments. Furthermore, it opens new opportunities for studying biomolecular Stark effects in aqueous systems, with implications for ultrafast spectroscopy, electrochemistry, and bioelectronics.

---

## 4.1 Introduction

Understanding how molecules respond to external electric fields provides fundamental insight into their electronic structure, charge distribution, and interactions with their environment. Stark spectroscopy has long been an essential tool for probing these properties by analyzing electric-field-induced spectral shifts, revealing information about dipole moments, polarizabilities, and charge transfer processes<sup>1,2,3,4,5</sup>. However, conventional Stark spectroscopy typically relies on low-frequency (kHz) electric fields applied through electrodes, necessitating cryogenic immobilization of samples to avoid rotational and alignment effects<sup>6,7,8</sup>. This limitation restricts the range of solvents that can be used, often excluding biologically and chemically relevant polar environments such as water, where solvation effects play a crucial role in molecular behavior<sup>6,7</sup>.

Recently, terahertz (THz) Stark spectroscopy has emerged as a powerful alternative, utilizing ultrafast, phase-stable THz pulses to transiently induce Stark shifts without requiring sample freezing<sup>5,9,10,11,12,13</sup>. In our previous work, we demonstrated that THz Stark spectroscopy enables precise measurements of dipole moment changes and polarizabilities in non-polar and weakly polar solvents under ambient conditions<sup>11</sup>. Around the same time, Singh et al. reported the THz Stark spectroscopy of a prototypical organic dye, Betaine-30 (B-30), in two aprotic polar solvents: chloroform ( $\text{CHCl}_3$ ) and dimethylsulfoxide ( $\text{C}_2\text{H}_6\text{SO}$ , DMSO)<sup>12</sup>. More recently, they also employed THz Stark spectroscopy to monitor the electric dipole changes of wild-type bacteriorhodopsin (BR) and a BR D85T mutant upon electronic excitation<sup>13</sup>. However, the applicability of this technique to water, a highly polar solvent, has not yet been explored.

Extending TRTSS to water presents fundamental challenges. First, its high dielectric constant ( $\approx 80$  at room temperature) could significantly screen the applied electric field, potentially reducing the Stark effect experienced by solvated molecules<sup>14,15,16</sup>. Second, strong THz absorption by water, due to intermolecular hydrogen bonding and dipolar relaxation raises concerns about effective field penetration and whether the induced Stark shifts remain detectable<sup>17,18</sup>. Finally, the dynamic solvent reorganization around chromophores in aqueous environments introduces additional complexities in interpreting molecular Stark responses, as solvent interactions may contribute to the observed field-induced shifts<sup>6,19</sup>.

In this study, we demonstrate that THz Stark spectroscopy is not only feasible in water but also provides valuable molecular insights previously inaccessible with conventional Stark methods. Using Malachite Green and Methyl Orange as model systems, we show that clear Stark signals can be detected even in the most polar environment, enabling precise measurements of dipole moment changes and polarizabilities in water. Liptay analysis of our experimental THz Stark spectroscopy data provides evidence for mixed Stark behavior, showing close agreement with the time-dependent density functional theory (TD-DFT) calculations. Our findings suggest that THz Stark spectroscopy can serve as a powerful tool for investigating electrostatic interactions in biological and chemical systems under physiological conditions, including protein electrostatics and ultrafast charge transfer processes.



## 4.2 Results and Discussion

### 4.2.1 Dynamics of the Stark Signature

This study presents the THz-induced Stark response of two dyes dissolved in water, Malachite Green (Figure 4.1) and Methyl Orange (Figure 4.2). To isolate the response of each dye, and to remove the nonresonant Kerr/electrostriction background and any cell contributions, a reference measurement on pure water (See Fig 4.6) was performed under identical conditions (cell, path length, polarization, THz energy) and subtracted from the sample data. The residual reports the stark parameters of the dye solution phase in water. Figure 4.1 presents the THz-induced Stark response of Malachite Green, measured with the probe polarization aligned parallel to the THz electric field polarization (parallel orientation). Figure 4.1a shows a false-color map of the measured change in absorption ( $\Delta A$ ) as a function of probe wavelength and time delay between the THz and probe pulses. The strongest absorption modulation is observed around 440-550 nm, at time zero, indicating a field-driven Stark shift. Figure 4.1b illustrates the time-averaged spectral response (red solid curve), computed over the spectral window highlighted by the red dashed lines in panel a. The Stark spectrum is well described by a weighted sum of spectral derivatives. The total fit (black dash-dotted curve) closely follows the first derivative of the steady state absorption (grey dashed curve), with only a small second-derivative mixture (grey dotted curve). This indicates that the observed Stark signal does not conform strictly to a purely linear or quadratic Stark effect rather a response dominated by the change in polarizability (quadratic Stark effect) with a minor contribution from the dipole moment changes (linear Stark effect).

Figure 4.1c depicts the time-domain evolution of the Stark signal, obtained by averaging over the spectral region marked by the blue dashed lines in panel a. The absorption change (blue curve) exhibits a strong temporal correlation with the squared THz field envelope,  $E_{\text{THz}}^2$  (purple dashed curve). Finally, Figure 4.1d displays the chemical structure of Malachite Green. The signal's derivative like lineshape and its temporal evolution tracking the squared THz field  $E_{\text{THz}}^2$  validates TRTSS as a quantitative method for probing of the change in dipole moment ( $\Delta\mu$ ) and polarizability change ( $\Delta\alpha$ ) in solution. These results demonstrate sufficient sensitivity to resolve sub-picosecond, field-induced modulations in molecules in solution.

Figure 4.2 presents the THz Stark response of Methyl Orange in water measured with the probe polarization parallel to the THz electric field polarization, further demonstrating the applicability of TRTSS in highly polar solvents. The false-color plot in Figure 4.2a illustrates the time-dependent spectral modulation, showing absorption changes in the 500-580 nm range. These spectral features appear around time zero, indicating a direct interaction between the THz electric field and the molecular dipole or polarizability.

Figure 4.2b displays the time-averaged Stark spectrum (red solid line), overlaid with a total fit (black dash-dotted line), and the first- and second-order derivatives (grey dashed and dotted lines, respectively) of the ground state absorption spectrum. The presence of both linear (dipole moment-driven) and quadratic (polarizability-driven) Stark components suggests a mixed Stark behavior. Figure 4.2c depicts the spectrally averaged change in absorption as a function of time (blue curve), computed over the spectral region between the blue dashed lines in panel a. The temporal profile closely follows the squared THz field envelope,  $E_{\text{THz}}^2$  (purple dashed curve). Finally, Figure 4.2d shows the molecular structure of Methyl Orange, highlighting the electronic environment that gives

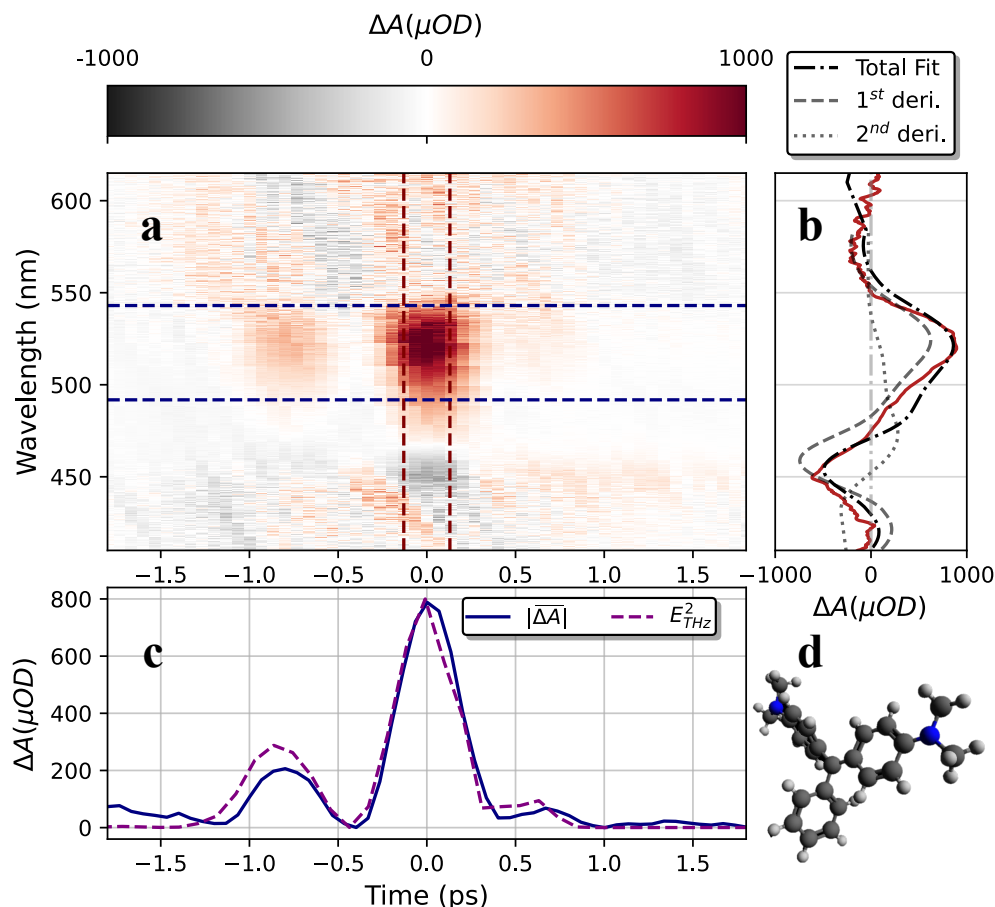
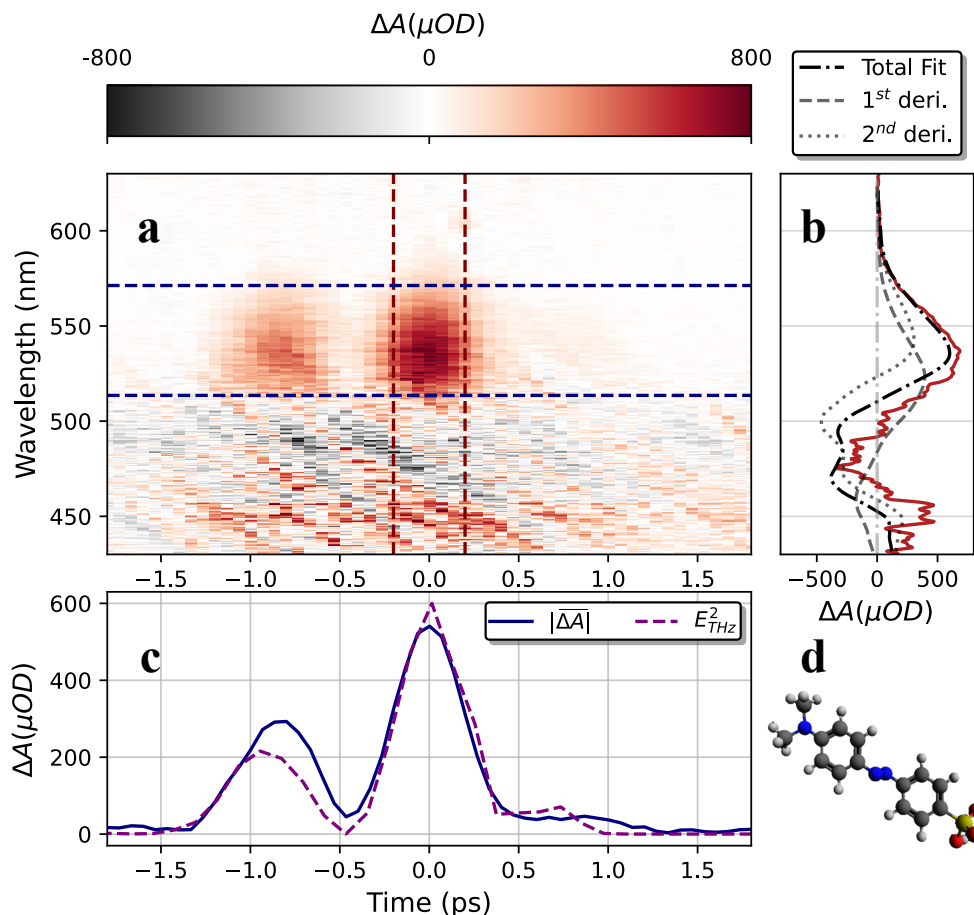


Figure 4.1: **THz Stark response of Malachite Green in parallel orientation.** **a** False-color map of the measured change in absorption spectrum as a function of wavelength and of probe delay relative to the THz pulse. **b** Spectral trace obtained by averaging the signal between the red dashed lines in **a** (red solid curve), compared to the total fit (black dash-dotted curve), the first-order derivative (grey dashed curve), and the second-order derivative (grey dotted curve) of the ground state absorption spectrum. **c** Temporal evolution of the spectrally integrated Stark signal (blue curve), averaged across the spectral range indicated by the blue dashed lines in **a**, compared to the squared THz electric field profile  $E_{THz}^2$  (purple dashed curve). **d** Chemical structure formula of Malachite Green.

rise to the observed THz-induced response. Figure 4.3 presents the molar absorption coefficients and their THz-induced modulations for Malachite Green (**a**) and Methyl Orange (**b**) in water at room temperature (295 K). The plots combine the ground state absorption spectra (blue lines, right y-axes) with the corresponding THz Stark spectra (left y-axes), recorded for both parallel (red) and perpendicular (orange) orientations of the THz and probe polarizations. The Stark signals  $\Delta\epsilon(\lambda)$  are scaled to an effective field strength of 1 MV/cm.

For Malachite Green, the absorption spectrum in our sample has a peak near 550 nm and is blue-shifted relative to dilute literature values, consistent with some degree of self-aggregation<sup>20</sup>.



**Figure 4.2: THz Stark response of Methyl Orange in parallel orientation.** **a** False-color map of the measured change in absorption spectrum as a function of wavelength and of probe delay relative to the THz pulse. **b** Spectral trace obtained by averaging the signal between the red dashed lines in **a** (red solid curve), compared to the total fit (black dash-dotted curve), the first-order derivative (grey dashed curve), and the second-order derivative (grey dotted curve) of the ground state absorption spectrum. **c** Temporal evolution of the spectrally integrated Stark signal (blue curve), averaged across the spectral range indicated by the blue dashed lines in **a**, compared to the squared THz electric field profile  $E_{THz}^2$  (purple dashed curve). **d** Chemical structure of Methyl Orange.

Accordingly, we analyze Malachite Green with a monomer plus aggregate derivative basis. Derivative decomposition identifies a polarizability-dominated mixed Stark response (first-derivative term), with a smaller contribution from the second derivative (change in dipole moment) term. Using separate derivatives for monomer and aggregate improves the residuals and indicates that the aggregate like component mainly contributes to the  $\text{Tr}(\Delta\alpha)$  term.

Methyl Orange in water exhibits a broad band centered at 465 nm. Unlike Malachite Green, Methyl Orange behaves monomerically, thus the extracted parameters reflect the monomer in bulk water. The corresponding TRTSS spectra, with a zero crossing near the absorption maximum,

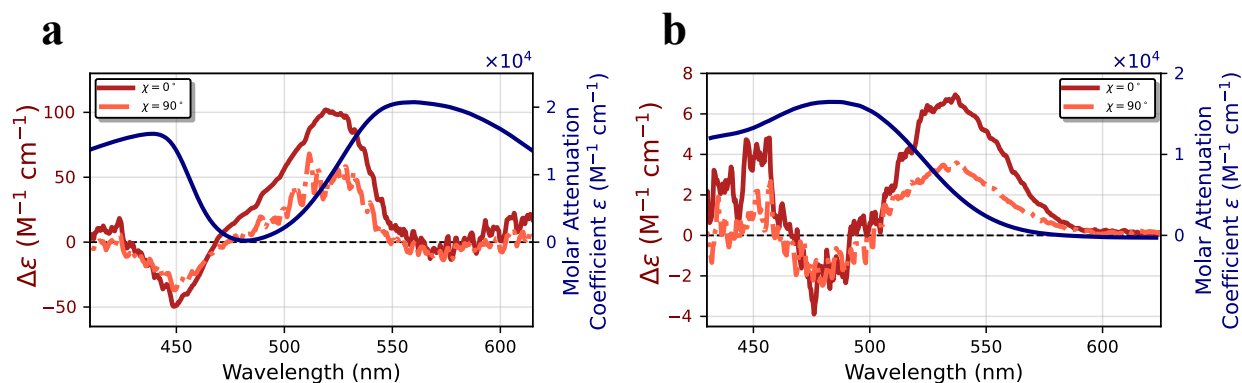


Figure 4.3: **Molar absorption coefficient and its modulation.** The plots combine the absorption spectra (blue line, right y-axes) and THz Stark responses (left y-axes) of Malachite Green (**a**) and Methyl Orange (**b**), measured at room temperature. The Stark spectra are plotted as  $\Delta\epsilon$ , recorded for parallel (brown) and perpendicular (orange) orientations of the THz and probe polarizations, and scaled to an electric field strength of 1 MV/cm.

are in an excellent agreement with a mixed Liptay fit. The first derivative term is the leading contribution, while the second derivative term is smaller yet required to capture the asymmetry of the modulation.

The characteristic spectral features and the field-dependent response confirm that the THz Stark effect can be effectively employed to probe molecular charge redistribution and polarizability changes in organic chromophores in water.

## 4.2.2 Relevant Molecular Parameters

A detailed comparison is achieved by analyzing the spectra using the established Liptay formalism<sup>6</sup>. This method enables the extraction of key molecular parameters such as the change in the dipole moment,  $\Delta\mu$ , the angle  $\zeta$  between  $\Delta\mu$  and the transition dipole moment  $m$ , the average change in polarizability,  $\text{Tr}(\Delta\alpha)$ , and the component of the polarizability change along  $m$ , expressed as  $m; \Delta\alpha; m$ . Table 4.1 summarizes key molecular parameters for Malachite Green and Methyl Orange, determined from Time-Dependent Density-Functional Theory (TD-DFT) calculations and extracted experimentally via Liptay analysis of THz Stark spectroscopy data.

Malachite Green in water displays a blue-shifted, broadened band relative to dilute literature values, consistent with partial self-aggregation<sup>20</sup>. Accordingly, we fit a mixture basis with monomer and aggregate derivatives. The retrieved parameters are  $\Delta\mu = 5.6 \pm 1.2D$  and  $\zeta = 36.3 \pm 1.1^\circ$ , together with  $\text{Tr}(\Delta\alpha) = -57.3 \pm 15.4 \text{ \AA}^3$  and  $m\Delta\alpha m = -37.7 \pm 8.9 \text{ \AA}^3$  reported in Table 4.1. TD-DFT on an isolated monomer model predicts a positive  $\text{Tr}(\Delta\alpha)$ . However, the negative  $\text{Tr}(\Delta\alpha)$  indicates a smaller average polarizability in the excited state relative to the ground state. In Stark analysis, this corresponds to a dominant first derivative component with the negative sign. We tentatively attribute the observed negative  $\text{Tr}(\Delta\alpha)$  to the formation of H-aggregates. In such structures, strong excitonic coupling between dye molecules produces a blue-shifted absorption band and creates delocalized exciton states that are shared across several chromophores<sup>20</sup>. At

the same time, the dense packing imposes significant structural and electrostatic constraints on the individual molecules within the aggregate<sup>21,22</sup>. It is plausible that this rigid and highly structured environment is the dominant factor affecting the Stark response. While the exciton state is delocalized, these strong local constraints could constrain the collective electron cloud, making it less deformable than that of an isolated monomer. This would effectively lower the polarizability of the  $S_1$  excited state, yielding a negative  $\text{Tr}(\Delta\alpha)$ .

In contrast, Methyl Orange behaves monomerically in water, therefore a single-species fit suffices. We obtain  $\Delta\mu = 6.2 \pm 1.8D$ ,  $\zeta = 24.8 \pm 2.1^\circ$ ,  $\text{Tr}(\Delta\alpha) = 115.3 \pm 17.2 \text{ \AA}^3$ , and  $m\Delta\alpha m = 79.9 \pm 12.5 \text{ \AA}^3$ . The TD-DFT calculations reproduce the experimental trends. For Methyl Orange the  $S_1$  state is strong charge transfer (CT), so TD-DFT already predicts a large  $|\Delta\mu|$ <sup>23</sup>. In water, polar solvation and hydrogen bonding stabilize both  $S_0$  and  $S_1$  in a correlated way along the same CT axis; this does not strongly change the difference  $\Delta\mu = \mu_e - \mu_g$ . The deviation between experimental and theoretical  $\zeta$  values probably arises from structural modifications, with additional influence from temperature dependent electrostatic and geometric effects<sup>24,25</sup>.

These results provide further support for the mixed Stark behavior observed in both samples, where contributions from both linear (dipole-driven) and quadratic (polarizability-driven) Stark effects were evident. The quantitative extraction of molecular Stark parameters from THz spectroscopy further validates the applicability of THz Stark spectroscopy in polar environments, demonstrating its potential for characterizing solvated molecular systems under ambient conditions.

Table 4.1: Comparison of relevant molecular parameters as calculated via TD-DFT and measured via THz Stark spectroscopy.

Parameter	Malachite Green		Methyl Orange	
	TD-DFT	THz-Stark	TD-DFT	THz-Stark
$\Delta\mu$ (D)	4.2	$5.6 \pm 1.2$	8.7	$6.2 \pm 1.8$
$\zeta$ ( $^\circ$ )	90	$36.3 \pm 1.1$	9	$24.8 \pm 2.1$
$\text{Tr}(\Delta\alpha)$ ( $\text{\AA}^3$ )	32	$-57.3 \pm 15.4$	92	$115.3 \pm 17.2$
$m\Delta\alpha m/m^2$ ( $\text{\AA}^3$ )	32	$-37.7 \pm 8.9$	91	$79.9 \pm 12.5$

## 4.3 Conclusion

In this study, we have demonstrated for the first time that TRTSS can be successfully applied to highly polar solvents such as water under ambient conditions. Our findings confirm that solvent polarity and hydrogen bonding do not fundamentally limit the ability to measure Stark shifts in solution, significantly expanding the applicability of TRTSS beyond non-polar solvents like toluene.

By investigating Malachite Green and Methyl Orange, we observed clear Stark signals that exhibit a combination of linear (dipole-driven) and quadratic (polarizability-driven) effects, suggesting the mixed Stark response of these molecules. The agreement between the experimental

results and the TD-DFT calculations provides further evidence for the observed mixed Stark behavior.

These results mark a major advancement for THz Stark spectroscopy, an invaluable tool for determining the electronic properties of molecules, proving that the technique can be applied to liquid-phase samples without freezing, even in highly polar solvents. Moreover, our findings establish TRTSS as a versatile and solvent-compatible spectroscopic tool, paving the way for new explorations in biophysics, ultrafast electrochemistry, and solution-phase quantum dynamics. Future work will explore more complex molecular systems, including biological molecules and electrochemical interfaces, where solvent interactions play a crucial role. Additionally, expanding the method to higher-field THz pulses Stark spectroscopy could provide deeper insights into nonlinear Stark effects and transient electronic structures in solution-phase dynamics.

## 4.4 Supplemental Information

### 4.4.1 THz Stark Spectroscopy Setup

Time-Resolved THz Stark Spectroscopy (TRTSS) was performed using a single-cycle terahertz (THz) pulse to induce transient Stark shifts in molecular absorption spectra. Figure 4.4 provides an overview of the experimental setup. The THz pulses were generated via optical rectification in a LiNbO<sub>3</sub> crystal using a tilted-pulse-front scheme. A synchronized femtosecond supercontinuum probe pulse, generated through white-light continuum generation in a CaF<sub>2</sub> crystal, was used to monitor Stark-induced absorption changes. The probe and THz pulses were spatially overlapped and temporally delayed to scan the Stark response as a function of time delay. The transmitted probe spectra were detected using a 1024-pixel CMOS array, with a reference line to enable shot-to-shot normalization and enhance the signal to noise ratio.

### 4.4.2 Sample Preparation

Methyl Orange and Malachite Green were dissolved in deionized water at concentrations optimized for strong but non-saturating absorption in the visible spectral range. The solutions were placed in a quartz cuvette with a 100  $\mu\text{m}$  path length, ensuring minimal absorption from water itself while maintaining sufficient signal strength. All measurements were performed at room temperature (295 K) to demonstrate TRTSS applicability in solution systems.

### 4.4.3 Data Acquisition and Analysis

To extract molecular Stark parameters, we performed a Liptay analysis by decomposing the Stark spectra into a linear combination of the absorption spectrum and its derivatives. Following established methods, the derivatives were obtained by direct numerical differentiation of the experimental absorption spectrum. To minimize noise, the data were smoothed with a Savitzky-Golay filter while preserving curvature and peak intensities<sup>6</sup>. As discussed by Bublitx and Boxer, when multiple absorption bands with different electro-optic parameters contribute, a deconvolution approach,



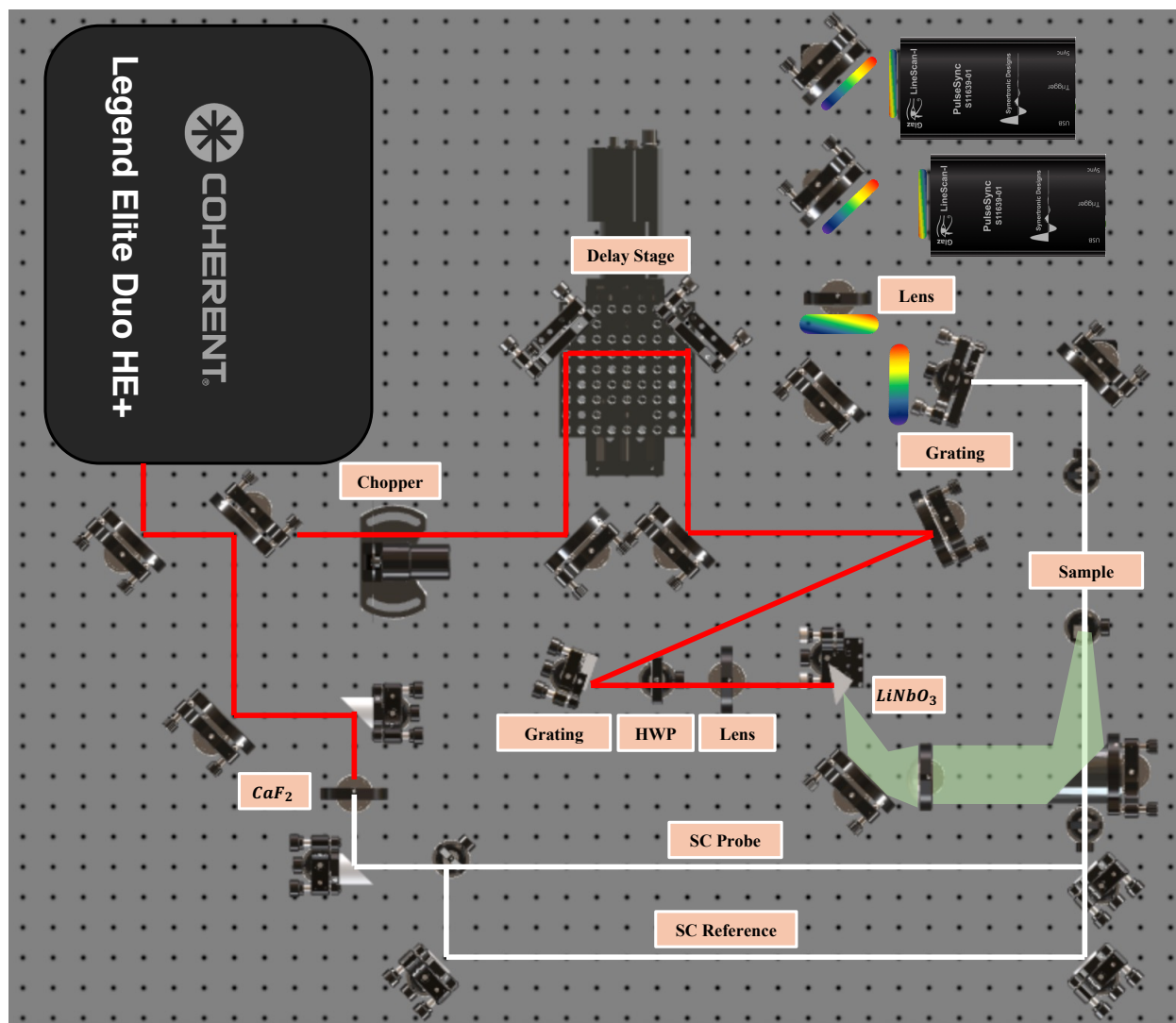


Figure 4.4: **Experimental setup for THz Stark spectroscopy with a reference-corrected supercontinuum detection.** Single-cycle THz pulses are produced by tilted-pulse-front excitation in LiNbO<sub>3</sub> and are spatially overlapped with femtosecond SC probe pulses generated in CaF<sub>2</sub>. The probe beam was split before the sample, with one arm passing through the sample while the other serving as a reference to improve signal-to-noise ratio. Both probe and reference spectra are recorded by a spectrometer. A mechanical chopper operating at 500 Hz periodically blocked the THz beam, enabling alternating acquisition of THz-on and THz-off signals for differential detection.

fitting the absorption as a sum of band components and using their analytical derivatives, provides an equivalent but species resolved basis<sup>6</sup>. Consistent with this, we used the direct derivative method for Methyl Orange (single dominant band), whereas Malachite Green was modeled with separate monomer/aggregate species to account for overlapping bands. The extracted Stark parameters, including  $\Delta\mu$ ,  $\zeta$ ,  $\text{Tr}(\Delta\alpha)$ , and  $m\Delta\alpha m/m^2$ , were determined from best fits of the derivative

components and compared with TD-DFT values to assess accuracy.

#### 4.4.4 Polarization Anisotropy

For an isotropic solution, Liptay theory predicts that the electroabsorption spectra recorded with probe polarization parallel and perpendicular to the THz field have the same linear combination of  $A(\nu)$ ,  $A'(\nu)$ , and  $A''(\nu)$ , differing only by geometry factors, thus the ratio  $R(\lambda) = \Delta\epsilon_{\parallel}(\lambda)/\Delta\epsilon_{\perp}(\lambda)$  is wavelength-independent<sup>6,26</sup>. We evaluate  $R(\lambda)$  from the derivative reconstructions within the absorption band and report the band-median with interquartile range (IQR). We obtain,  $R_{\text{MG}} = 1.75 \pm 0.28$  (IQR), and  $R_{\text{MO}} = 1.02 \pm 0.23$  (IQR), both ratios are flat across the band.

Table 4.2: Polarization anisotropy metrics from derivative-only diagnostics.

Sample	$R_{\text{median}}$ (IQR)	Best scale $s$
Malachite Green	1.75 (1.62-1.90)	1.73
Methyl Orange	1.02 (0.85-1.08)	0.97

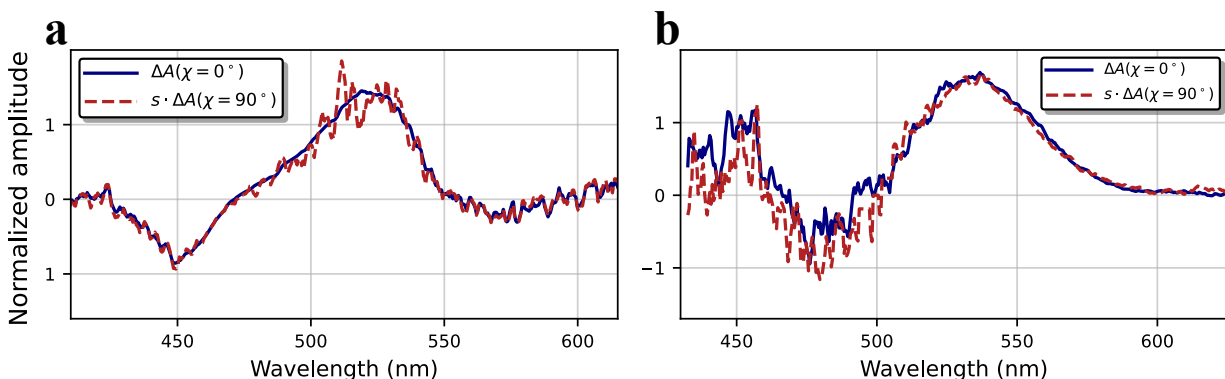


Figure 4.5: **a, b Overlay of the parallel TRTSS spectrum (solid blue curve) with the best-scaled perpendicular spectrum (red dashed curve) of Malachite Green and Methyl Orange respectively.**

To visualize the constraint, we overlay the parallel spectrum ( $\chi = 0^\circ$ ) with the best scaled perpendicular spectrum  $s \cdot (\chi = 90^\circ)$  in Figure 4.5.

#### 4.4.5 Background Measurements

A pure water TRTSS dataset was measured under identical conditions (cell, path length, THz/probe polarizations, fluences). The response is spectrally featureless across 400-650 nm, as shown in Figure 4.6. Since liquid water has no electronic absorption in this spectral window, it cannot yield a Stark electroabsorption lineshape. Intense THz fields can reorient permanent dipoles and



induce transient birefringence in liquids, i.e., a Kerr response; we observe this in pure water<sup>27</sup>. Its apparent sign and amplitude change with polarization angle ( $0^\circ/90^\circ$ ), as expected for a birefringent Kerr signal.

Figure 4.7 demonstrates the polarization control measurements for pure water. The band-averaged signal changes sign when the polarizer is rotated by  $90^\circ$ , as expected for Kerr birefringence.

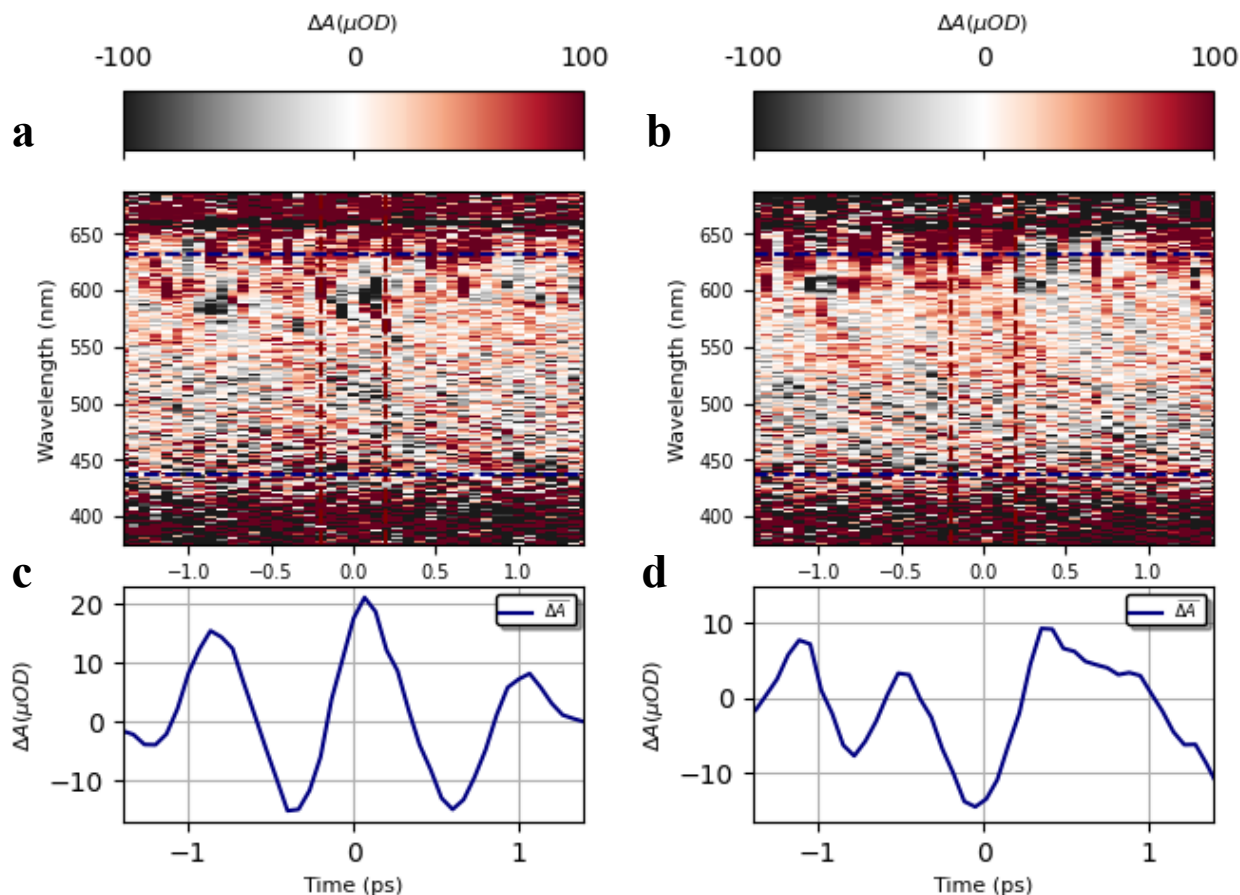


Figure 4.6: **a and b**  $\Delta A(\lambda, t)$  **map**. Broad, nearly wavelength-independent response of pure water at time zero, for parallel and perpendicular geometry, respectively. No derivative structure or band center zero-crossing, consistent with non-resonant Kerr/electrostriction rather than Stark signature. **c and d** **wavelength-averaged**  $\Delta A(t)$ . Temporal evolution of the signal, averaged across the spectral range indicated by the blue dashed lines, for parallel and perpendicular geometry, respectively.

#### 4.4.6 Local Field Correction Factor

The electric field a molecule experiences inside a solvent is different from the field applied to the bulk liquid. To correct for this, we used a standard local field factor  $f_L$  to relate the macroscopic field to the actual field at the molecule<sup>28,29,30</sup>. Based on the properties of water at our THz frequency, we calculated a correction factor of  $f_L = 1.36$ . Dividing measured change in dipole

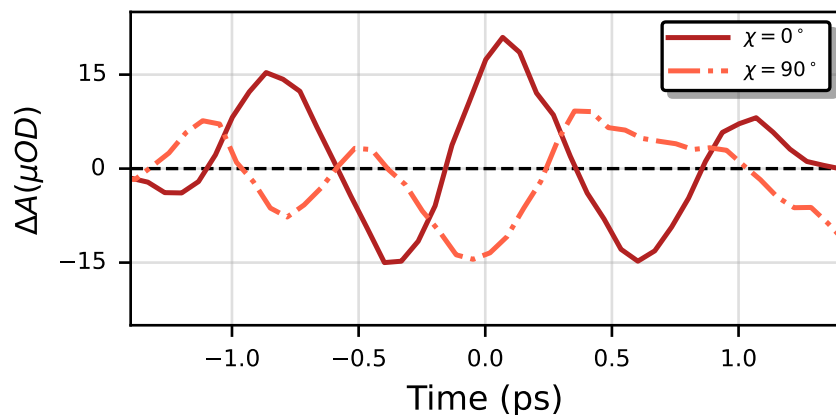


Figure 4.7: **Band-averaged TRTSS traces with the probe analyzer at  $0^\circ$  and  $90^\circ$  measured for pure water.** An opposite signal sign is observed with the rotation of the polarizer (Kerr birefringence).

moment  $\Delta\mu$  by this factor ( $f_L$ ) and the change in polarizability  $\text{Tr}(\Delta\alpha)$  by its square  $f_L^2$ , allows for a better comparison with theory by accounting for the solvent's dielectric screening, but it does not remove the effects of direct molecule-solvent interactions.

#### 4.4.7 Computational Methods

Electronic structure calculations were performed with Gaussian 16 software. First, the ground state geometries were optimized using a DFT description with B3LYP functional and 6-31+G(d,p) basis set. The counterion is expected to be solvated in water, and hence be close to the molecule. Therefore, the charge of Malachite Green was set to +1 and the charge of Methyl Orange to -1. The ground and excited state properties including electronic dipole moment, polarizabilities, transition dipole moment and energies were computed with the range-separated wB97XD functional and the same basis set as for the geometry optimization. The solvent effects were included within the polarizable continuum model (PCM) both for the conformational analysis and for the calculation of excitation properties. The ability of the selected functional to describe the mixed charge transfer (CT) and locally excited (LE) states was validated by comparing the vacuum properties with the CC2 approach with def2-TZVPPD, which was shown to provide similar precision for both the CT and LE states (Fig. S4.8 and Table S4.3). In the next step, we investigated the solvent effects on the electronic properties by comparison of the gas phase properties with the nonequilibrium linear response solvation, including only fast response of the electronic degrees of freedom, and the equilibrium solvation including nuclei relaxation effects (Table S4.4). In order to validate the computed excited state properties and visualize the effects of the environment, we computed absorption spectra for the two studied systems and three different solvation schemes and compared them with the experiment.

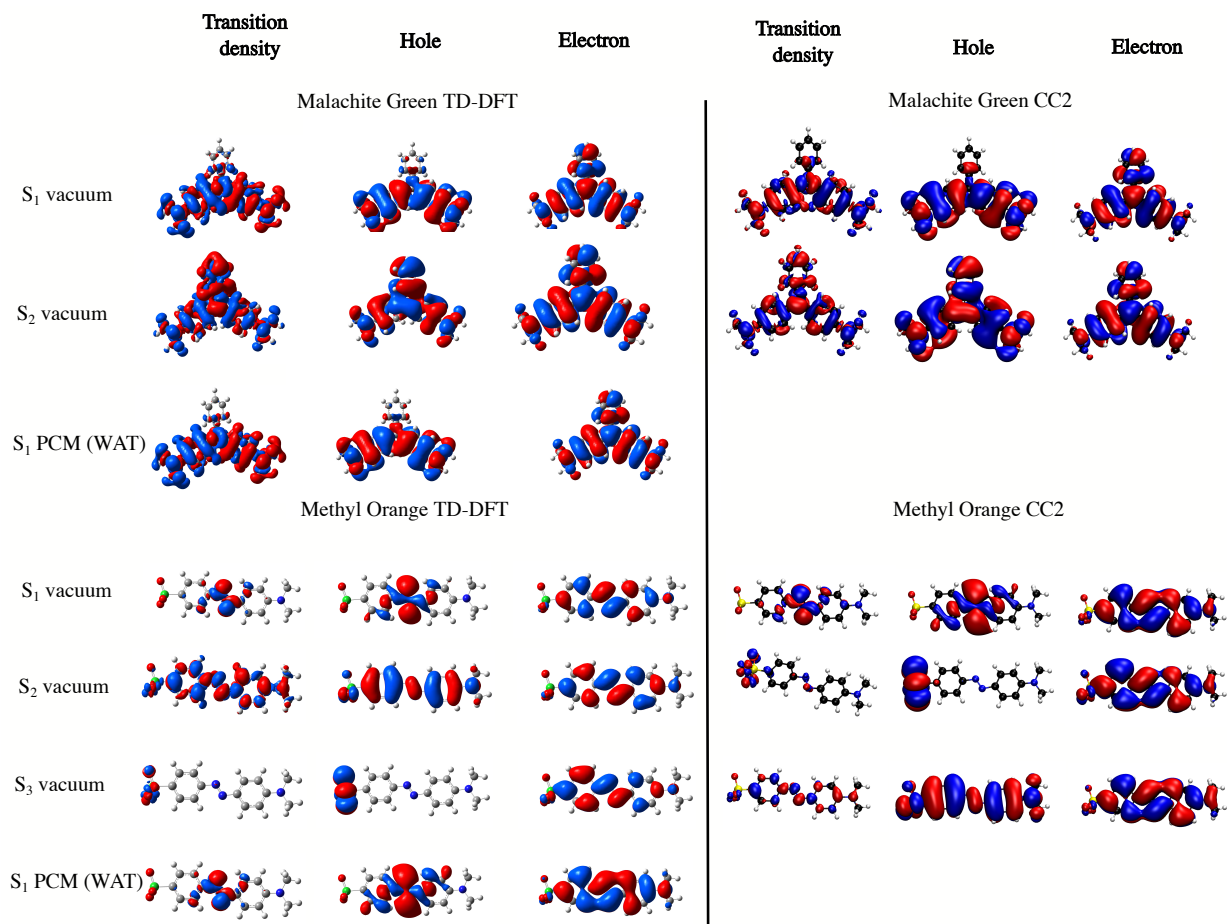


Figure 4.8: Comparison of the natural transition orbitals and transition densities between TD-DFT with wB97XD DFT functional with 6-31+G(d,p) basis and CC2 calculation with def2-TZVPPD in vacuum. TD-DFT orbitals and densities results agree well with the CC2 results except for the Methyl Orange second and third excited states are exchanged. The natural transition orbitals keep the same shape also in the water solution modeled as polarizable continuum environment.

Table 4.3: Comparison of the electronic properties for the first excited state between the TD-DFT and CC2 approach.  $E_{ge}$  and  $\mu_{ge}$  correspond to the vertical excitation energy and transition dipole moment, respectively, between the ground and first excited state  $S_1$ , while  $\Delta\mu$  and  $\text{Tr}(\Delta\alpha)$  represent the difference between excited and ground state dipole moment and isotropic polarizability, respectively.

Property	wB97XD (B3LYP geom)	CC2 (B3LYP geom)	CC2 (CC2 geom)
<b>Malachite Green</b>			
$E_{ge}$ (eV)	2.766	2.236	2.232
$\mu_{ge}$ (D)	(9.66, 0.0, 0.05)	(11.27, 0.0, 0.00)	(11.20, 0.0, 0.00)
$\Delta\mu$ (D)	(0.0, -2.47, 0.0)	(0.0, -2.29, 0.0)	(0.0, -2.42, 0.0)
<b>Methyl Orange</b>			
$E_{ge}$ (eV)	3.609	3.423	3.236
$\mu_{ge}$ (D)	(9.12, 0.0, 0.0)	(9.69, 0.0, 0.00)	(9.86, 0.0, 0.00)
$\Delta\mu$ (D)	(-2.21, -0.10, 0.05)	(5.53, -0.20, -0.10)	(-6.24, -0.25, -0.03)

Table 4.4: Comparison of the electronic properties for different solvation schemes within the TD-DFT approach using the wB97XD functional and 6-31+G(d,p) basis set.

Property	Gas phase	Non-equilibrium Solv.	Equilibrium Solv.
<b>Malachite Green</b>			
$E_{ge}$ (eV)	2.766	2.603	2.359
$\mu_{ge}$ (D)	(9.66, 0.0, 0.05)	(10.65, 0.0, -0.05)	(12.35, 0.0, 0.08)
$\Delta\mu$ (D)	(0.0, -2.47, 0.0)	(0.0, -3.72, 0.0)	(0.0, -4.17, 0.0)
$\text{Tr}(\Delta\alpha_{\text{diag}})$ ( $\text{\AA}^3$ )	(8.9, 0.8, 0.5)	(31.7, -0.7, 0.7)	(31.8, -0.7, 0.7)
<b>Methyl Orange</b>			
$E_{ge}$ (eV)	3.609	3.364	3.191
$\mu_{ge}$ (D)	(9.12, 0.0, 0.0)	(9.68, 0.04, 0.08)	(10.58, -0.05, 0.10)
$\Delta\mu$ (D)	(-2.21, -0.10, 0.05)	(-8.16, 0.25, -0.05)	(-8.70, 0.23, -0.05)
$\text{Tr}(\Delta\alpha_{\text{diag}})$ ( $\text{\AA}^3$ )	(103.4, 0.6, 1.0)	(82.4, 0.6, 0.7)	(90.6, 0.4, 0.7)

## Bibliography

- [1] Bruce S Brunschwig, Carol Creutz, and Norman Sutin. Electroabsorption spectroscopy of charge transfer states of transition metal complexes. *Coord. Chem. Rev.*, 177(1):61–79, 1998. ISSN 0010-8545. doi: [https://doi.org/10.1016/S0010-8545\(98\)00188-X](https://doi.org/10.1016/S0010-8545(98)00188-X). URL <https://www.sciencedirect.com/science/article/pii/S001085459800188X>.
- [2] Gerold U Bublitz, Rafael Ortiz, Seth R Marder, and Steven G Boxer. Stark Spectroscopy of Donor/Acceptor Substituted Polyenes. *J. Am. Chem. Soc.*, 119(14):3365–3376, apr 1997. ISSN 0002-7863. doi: 10.1021/ja9640814. URL <https://doi.org/10.1021/ja9640814>.
- [3] Toshifumi Iimori, Ryuichi Ito, Nobuhiro Ohta, and Hideyuki Nakano. Stark Spectroscopy of Rubrene. I. Electroabsorption Spectroscopy and Molecular Parameters. *J. Phys. Chem. A*, 120(25):4307–4313, jun 2016. ISSN 1089-5639. doi: 10.1021/acs.jpca.6b02625. URL <https://doi.org/10.1021/acs.jpca.6b02625>.
- [4] Wolfgang Liptay. Electrochromism and Solvatochromism. *Angew. Chemie Int. Ed. English*, 8(3):177–188, mar 1969. ISSN 0570-0833. doi: <https://doi.org/10.1002/anie.196901771>. URL <https://doi.org/10.1002/anie.196901771>.
- [5] Brandt C Pein, Chee Kong Lee, Liang Shi, JiaoJian Shi, Wendi Chang, Harold Y Hwang, Jennifer Scherer, Igor Coropceanu, Xiaoguang Zhao, Xin Zhang, Vladimir Bulović, Mouni G Bawendi, Adam P Willard, and Keith A Nelson. Terahertz-Driven Stark Spectroscopy of CdSe and CdSe–CdS Core–Shell Quantum Dots. *Nano Lett.*, 19(11):8125–8131, nov 2019. ISSN 1530-6984. doi: 10.1021/acs.nanolett.9b03342. URL <https://doi.org/10.1021/acs.nanolett.9b03342>.
- [6] G. U. Bublitz and S. G. Boxer. Stark spectroscopy: applications in chemistry, biology, and materials science. *Annual Review of Physical Chemistry*, 48:213–242, 1997. doi: 10.1146/annurev.physchem.48.1.213.
- [7] Steven S. Andrews and Steven G. Boxer. Vibrational stark effects of nitriles. i. methods and experimental results. *The Journal of Physical Chemistry A*, 104(51):11853–11863, 2000. doi: 10.1021/jp002242r.
- [8] Steven S. Andrews and Steven G. Boxer. A liquid nitrogen immersion cryostat for optical measurements. *Review of Scientific Instruments*, 71(9):3567–3569, 2000. doi: 10.1063/1.1287343.
- [9] Sabine Keiber, Shawn Sederberg, Alexander Schwarz, Michael Trubetskov, Volodymyr Pervak, Ferenc Krausz, and Nicholas Karpowicz. Electro-optic sampling of near-infrared waveforms. *Nat. Photonics*, 10(3):159–162, 2016. ISSN 1749-4893. doi: 10.1038/nphoton.2015.269. URL <https://doi.org/10.1038/nphoton.2015.269>.

- [10] Matthias Knorr, Jürgen Raab, Maximilian Tauer, Philipp Merkl, Dominik Peller, Emanuel Wittmann, Eberhard Riedle, Christoph Lange, and Rupert Huber. Phase-locked multi-terahertz electric fields exceeding 13 MV/cm at a 190 kHz repetition rate. *Opt. Lett.*, 42(21): 4367–4370, 2017. doi: 10.1364/OL.42.004367. URL <https://opg.optica.org/ol/abstract.cfm?URI=ol-42-21-4367>.
- [11] Bong Joo Kang, Egmont J Rohwer, David Rohrbach, Elnaz Zyaee, Maryam Akbarimoosavi, Zoltan Ollmann, Gleb Sorohhov, Alex Borgoo, Michele Cascella, Andrea Cannizzo, et al. Time-resolved thz stark spectroscopy of molecules in solution. *Nature Communications*, 15 (1):4212, 2024.
- [12] Poonam Singh, Jia Zhang, Dieter Engel, Benjamin P. Fingerhut, and Thomas Elsaesser. Transient terahertz stark effect: A dynamic probe of electric interactions in polar liquids. *The Journal of Physical Chemistry Letters*, 14(24):5505–5510, 2023. doi: 10.1021/acs.jpclett.3c01079. URL <https://doi.org/10.1021/acs.jpclett.3c01079>. PMID: 37289958.
- [13] Jia Zhang, Poonam Singh, Dieter Engel, Benjamin P. Fingerhut, Matthias Broser, Peter Hegemann, and Thomas Elsaesser. Ultrafast terahertz stark spectroscopy reveals the excited-state dipole moments of retinal in bacteriorhodopsin. *Proceedings of the National Academy of Sciences*, 121(26):e2319676121, 2024. doi: 10.1073/pnas.2319676121. URL <https://www.pnas.org/doi/abs/10.1073/pnas.2319676121>.
- [14] M. Uematsu and E. U. Franck. Static dielectric constant of water and steam. *Journal of Physical and Chemical Reference Data*, 9(4):1291–1306, 10 1980. ISSN 0047-2689. doi: 10.1063/1.555632. URL <https://doi.org/10.1063/1.555632>.
- [15] William J. Ellison. Permittivity of pure water, at standard atmospheric pressure, over the frequency range 0–25 thz and the temperature range 0–100 °c. *Journal of Physical and Chemical Reference Data*, 36(1):1–18, 2007. doi: 10.1063/1.2360986.
- [16] Cyrus G. Malmberg and Arthur A. Maryott. Dielectric constant of water from 0 0 to 100 0 c. 1956. URL <https://api.semanticscholar.org/CorpusID:7145199>.
- [17] J. T. Kindt and C. A. Schmuttenmaer. Far-infrared dielectric properties of polar liquids probed by femtosecond terahertz pulse spectroscopy. *The Journal of Physical Chemistry*, 100(24): 10373–10379, 1996. ISSN 0022-3654. doi: 10.1021/jp960141g.
- [18] Jens Neu and Charles A. Schmuttenmaer. Tutorial: An introduction to terahertz time domain spectroscopy (thz-tds). *Journal of Applied Physics*, 124(23):231101, 12 2018. ISSN 0021-8979. doi: 10.1063/1.5047659. URL <https://doi.org/10.1063/1.5047659>.
- [19] Joshua D. Slocum and Lauren J. Webb. Measuring electric fields in biological matter using the vibrational stark effect of nitrile probes. *Annual Review of Physical Chemistry*, 69(Volume 69, 2018):253–271, 2018. ISSN 1545-1593. doi: <https://doi.org/10.1146/annurev-physchem-052516-045011>. URL <https://www.annualreviews.org/content/journals/10.1146/annurev-physchem-052516-045011>.

- [20] Frank C. Spano. The spectral signatures of frenkel polarons in h- and j-aggregates. *Accounts of Chemical Research*, 43(3):429–439, 2010. doi: 10.1021/ar900233v.
- [21] Jun Chen, C. C. W. Law, Jacky W. Y. Lam, Yong Dong, S. M. F. Lo, Ian D. Williams, Daoben Zhu, and Ben Zhong Tang. Synthesis, light emission, nanoaggregation, and restricted intramolecular rotation of 1,1-substituted 2,3,4,5-tetraphenylsiloles. *Chemistry of Materials*, 15(7):1535–1546, 2003. doi: 10.1021/cm021715z.
- [22] Jun Mei, Nathan L. C. Leung, Ryan T. K. Kwok, Jacky W. Y. Lam, and Ben Zhong Tang. Aggregation-induced emission: Together we shine, united we soar! *Chemical Reviews*, 115(21):11718–11940, 2015. doi: 10.1021/acs.chemrev.5b00263.
- [23] Christoph Nançoz, Giuseppe Licari, Joseph S. Beckwith, Magnus Soederberg, Bogdan Dereka, Arnulf Rosspeintner, Oleksandr Yushchenko, Romain Letrun, Sabine Richert, Bernhard Lang, and Eric Vauthey. Influence of the hydrogen-bond interactions on the excited-state dynamics of a push–pull azobenzene dye: the case of methyl orange. *Phys. Chem. Chem. Phys.*, 20:7254–7264, 2018. doi: 10.1039/C7CP08390D. URL <http://dx.doi.org/10.1039/C7CP08390D>.
- [24] Egmont J Rohwer, Maryam Akbarimoosavi, Steven E Meckel, Xunshan Liu, Yan Geng, Latévi Max Lawson Daku, Andreas Hauser, Andrea Cannizzo, Silvio Decurtins, Robert J Stanley, Shi-Xia Liu, and Thomas Feurer. Dipole Moment and Polarizability of Tunable Intramolecular Charge Transfer States in Heterocyclic  $\pi$ -Conjugated Molecular Dyads Determined by Computational and Stark Spectroscopic Study. *J. Phys. Chem. C*, 122(17):9346–9355, may 2018. ISSN 1932-7447. doi: 10.1021/acs.jpcc.8b02268. URL <https://doi.org/10.1021/acs.jpcc.8b02268>.
- [25] Ariana Rondi, Yuseff Rodriguez, Thomas Feurer, and Andrea Cannizzo. Solvation-Driven Charge Transfer and Localization in Metal Complexes. *Acc. Chem. Res.*, 48(5):1432–1440, may 2015. ISSN 0001-4842. doi: 10.1021/ar5003939. URL <https://doi.org/10.1021/ar5003939>.
- [26] Erko Jalviste and Nobuhiro Ohta. Theoretical foundation of electroabsorption spectroscopy: Self-contained derivation of the basic equations with the direction cosine method and the euler angle method. *Journal of Photochemistry and Photobiology C: Photochemistry Reviews*, 8(1):30–46, 2007. ISSN 1389-5567. doi: <https://doi.org/10.1016/j.jphotochemrev.2007.01.001>. URL <https://www.sciencedirect.com/science/article/pii/S1389556707000275>.
- [27] Mohsen Sajadi, Martin Wolf, and Tobias Kampftrath. Transient birefringence of liquids induced by terahertz electric-field torque on permanent molecular dipoles. *Nat. Commun.*, 8(1):14963, 2017. ISSN 2041-1723. doi: 10.1038/ncomms14963. URL <https://doi.org/10.1038/ncomms14963>.
- [28] Antoine Aubret, Michel Orrit, and Florian Kulzer. Understanding Local-Field Correction Factors in the Framework of the Onsager-Böttcher Model. *ChemPhysChem*, 20(3):345–355,



feb 2019. ISSN 1439-4235. doi: <https://doi.org/10.1002/cphc.201800923>. URL <https://doi.org/10.1002/cphc.201800923>.

[29] Lars Onsager. Electric moments of molecules in liquids. *Journal of the American Chemical Society*, 58(8):1486–1493, 1936. doi: 10.1021/ja01299a050.

[30] John David Jackson. *Classical Electrodynamics*. Wiley, New York, 3rd edition, 1998.



# Chapter 5

## An Accurate Modeling of the Optical and Electronic Properties of the Paracyclophanes

Vladislav Slama<sup>1</sup>, Elnaz Zyaee<sup>2</sup>, Camila Negrete-Vergara<sup>3</sup>, Hans-Martin Frey<sup>2</sup>, Shi-Xia Liu<sup>3</sup>,  
Thomas Feurer<sup>2</sup>, Ursula Röthlisberger<sup>1</sup>

<sup>1</sup> Laboratory of Computational Chemistry and Biochemistry, École Polytechnique Fédérale de Lausanne (EPFL)

<sup>2</sup> Institute of Applied Physics, University of Bern

<sup>3</sup> Department of chemistry, biochemistry and pharmaceutical sciences, University of Bern

[This work is in preparation for submission.](#)

---

### Abstract

Aromatic  $\pi$ -stacking interactions play an important role in both natural and artificial systems, influencing processes such as charge separation in photosynthesis and charge transport in organic semiconductors. Controlling the geometry and distance between aromatic units is therefore crucial for tuning intermolecular interactions and charge transfer efficiency. Due to their well-defined stacking geometry, paracyclophanes (PCPs) composed of two or more aromatic units connected by rigid linkers, provide an ideal platform for a systematic study of such effects. Despite extensive experimental studies of PCPs, a comprehensive and quantitatively validated theoretical description linking the structure with the electronic and optical properties is still missing. Here, we present an extensive computational and experimental investigation of the electronic and optical properties of homo-PCPs containing naphthalene diimide (NDI) or Pyrene chromophores linked by bridges of varying length and rigidity. We introduce a robust methodology for an accurate simulation of the absorption and fluorescence spectra of PCPs based on a combined TD-DFT and CC2 approach, achieving excellent quantitative agreement with experiment. We also present and validate a fragment based description of PCPs based on the Frenkel exciton model. Such approach is valuable not only for interpretation of the electronic and optical properties of PCPs, but it can also significantly reduce the cost of the calculation while maintaining the accuracy of the supermolecular approach. This work establishes a quantitatively reliable framework linking structure, excitonic coupling, and charge transfer interactions in PCPs with optical properties, providing design principles for next-generation optoelectronic materials.

---

## 5.1 Introduction

Aromatic stacking interactions play an important role in many fields ranging from biology to supramolecular chemistry and materials science. In biological systems  $\pi$ -stacking contributes to protein stability, ligand-receptor binding (e.g. in dopamine receptors)<sup>1,2</sup>, and molecular orbital overlap of aromatic systems is crucial for charge separation in the photosynthetic reaction center<sup>3</sup>. In artificial systems, such as organic electronic devices or artificial light harvesting systems,  $\pi$ -stacking enhances molecular orbital overlap, which is critical for charge transport and charge transfer (CT) state formation<sup>4,5,6,7</sup>. The efficiency of CT state formation and intermolecular charge transport in organic semiconductors is governed by electronic coupling<sup>8</sup>, which depends on the degree of molecular orbital overlap between neighboring molecules. This overlap, in turn, is determined by the relative distance and orientation of the molecules. Therefore, significant efforts have been devoted towards the development of molecular systems that exhibit close packing and well-defined orientations to tailor intermolecular interaction to specific applications.

A promising class of compounds featuring face-to-face aromatic stacking and well-defined mutual geometry are paracyclophanes (PCPs)<sup>9,10,11</sup>. These molecules consist of two or more aromatic units connected by linkers (e.g. alkyl chains or phenylene bridges), resulting in a rigid structure. The electronic and optical properties of PCPs are governed by both the choice of the aromatic subunits and the linkers, which defines the interunit distance as well as the relative orientation of the two aromatic systems. Homoparacyclophanes (homo-PCPs), composed of identical aromatic units, have been explored as building blocks for the construction of conductive polymers, molecular wires, and light-emitting diodes<sup>10,12,13</sup>. In contrast, heteroparacyclophanes formed by aromatic units with electron donor and acceptor properties exhibit pronounced CT interactions. The ability to tune CT state properties in these systems is particularly relevant for applications in organic photovoltaics (OPV) and organic field-effect transistors (OFET)<sup>12,14</sup>.

Despite extensive experimental studies of PCPs, a comprehensive and quantitatively validated theoretical description linking molecular structure with electronic and optical properties, particularly for larger systems, is still missing. Most of the theoretical investigations to date have focused on ground state properties and molecular orbital analyses, or time dependent density functional theory (TD-DFT) calculations of excited states in the gas phase<sup>15,16,17,18</sup>. The lack of quantitative accuracy is largely due to the challenges in the theoretical description of CT states, which are characterized by spatially separated electrons and holes with small molecular orbital overlap resulting in low transition dipole moments, and a strong dependence on geometry and environment. Conventional TD-DFT approaches employing generalized gradient approximation (GGA) or hybrid functionals often fail for CT states because of their incorrect asymptotic behavior, necessitating the use of higher-level methods with significantly greater computational cost<sup>19,20</sup>. Although employing range-separated hybrid functionals partially mitigate this deficiency of the TDDFT approach, in many cases they still do not achieve fully quantitative accuracy<sup>21</sup>.

In this work, we present a computational methodology for a quantitative description of the electronic properties of PCPs. The redox properties are calculated using DFT-based approaches and validated against experimental measurements. Excited state properties are evaluated using a combination of an approximate coupled cluster method (CC2) and linear-response TD-DFT with range-separated functionals. The calculated excited states are used to simulate absorption and

fluorescence spectra and to rationalize the observed excited state dynamics of PCP systems. We also investigate solvent effects on both redox and excited state properties and demonstrate that accurate inclusion of solvation is essential for a quantitative agreement with experimental data. Furthermore, we show that the electronic properties of homo-PCPs can effectively be described as interacting monomeric units embedded in a polarizable environment, following the Frenkel exciton model. This approach substantially reduces computational cost, enables the treatment of larger systems, and facilitates the rational design of novel PCPs with tailored properties.

Finally, we validate the proposed methodology by comparing computed optical spectra with experimental results for a series of homo-PCPs containing naphthalene diimide (NDI) or Pyrene units connected by linkers of varying length, thereby covering a range of interunit distances and orientations. The resulting quantitative agreement confirms the robustness of the computational approach. Importantly, an accurate theoretical description of the electronic and optical properties of PCPs is not only essential for understanding their behavior in different environments but it is also critical for the rational design of new molecules with targeted functionalities.

## 5.2 Computational Methods

To compare the electronic and optical properties of the monomeric NDI and Pyrene units with those of the corresponding homo-PCPs, the molecular structures were optimized at the DFT level using the B3LYP functional and the 6-31+G(p,d) basis set. Solvent effects were included through the polarizable continuum model (PCM) with equilibrium solvation, employing dichloromethane ( $\text{CH}_2\text{Cl}_2$ ) as the solvent. Since the lowest excited state of Pyrene with transition dipole moment oriented along its short molecular axis ( $^1L_b$ ) exhibits partial double-excitation character and the Pyrene with amine-containing linkers show partial charge transfer (CT) character, a two-step procedure was employed to compute the excited state properties of PCPs containing Pyrene units.

In the first step, excited state properties were calculated in the gas phase at CC2 level with a def2-TZVPD basis set as implemented in Turbomole 7.1.1<sup>22</sup>, and at the TD-DFT level using the range-separated  $\omega$ B97XD functional with the same basis set as implemented in Gaussian 16<sup>23</sup>, both at the same DFT geometry. The CC2 method provides similar accuracy for the locally excited (LE) state energies for both the NDI and Pyrene units (including states with partial double excitation character) as for the CT states in the PCPs. While TD-DFT with range separated hybrid functionals generally fails to reproduce the absolute energies of CT states and the excited states of Pyrene with partial double excitation character, it correctly describes their molecular orbital (MO) composition and symmetry. Using a natural transition orbital (NTO) analysis, CC2 excited states were mapped onto their TD-DFT counterparts. This mapping was used to obtain energy correction factors for the states computed at the TD-DFT level of theory.

In the second step, excited states are recomputed at the TD-DFT level with the  $\omega$ B97XD functional including solvent effects at the same geometry as in the gas phase calculation, using the Gaussian 16 software package<sup>23</sup>. Solvent effects were incorporated within the PCM approach where the implicit non-equilibrium solvation was applied for the excited states, the linear response approach was used for LE states, and a state-specific solvation model was adopted for the states with significant CT character. Analysis of the MO composition of the excited states and the NTOs was used to map the solvated excited states to their gas phase counterparts. The final excitation

energies of the solvated systems were obtained from the TD-DFT calculation with nonequilibrium solvation, corrected by the corresponding energy difference between TD-DFT and CC2 from the gas phase. This two-step approach effectively overcomes the inherent limitations of TD-DFT for CT states and yields quantitatively accurate excitation energies for solvated molecules without the need for empirical energy shifts. Conceptually, this method can be regarded as a CC2 gas-phase calculation corrected by solvent-induced energy shifts computed at the TD-DFT level.

This two-step procedure was necessary because the current implementation of the CC2 method in Turbomole 7.1.1<sup>22</sup> does not support explicit inclusion of solvent effects in a state-specific manner, a feature that turned out to be essential for an accurate description of solvent effects on CT states.

Optical spectra were simulated using the vertical gradient (VG) approximation combined with the cumulant expansion formalism<sup>24</sup>. This method is widely applied in the modeling of organic molecules and super-molecular systems and accounts for vibronic effects in optical spectra without requiring extensive explicit sampling of the molecular geometries. It also enables combination of different theoretical methods for describing electronic excitations (CC2) and solvent effects (TD-DFT). Within this framework, the absorption  $\alpha(\omega)$  and fluorescence  $I(\omega)$  spectra are obtained as a sum over excited states:

$$\alpha(\omega) \propto \omega \sum_i |\mu_{gi}|^2 D_i(\omega), \quad (5.1)$$

$$I(\omega) \propto \omega^2 \sum_i p_i |\mu_{gi}|^2 \tilde{D}_i(\omega), \quad (5.2)$$

where  $p_i$  corresponds to the Boltzmann factor  $p_i = \exp\left[-\frac{\varepsilon_i}{k_B T}\right] / \sum_j \exp\left[-\frac{\varepsilon_j}{k_B T}\right]$  and  $\mu_{gi}$  is the transition dipole moment between the ground and  $i$ -th electronic excited state.

The homogeneous lineshape  $D_i(\omega)$  and fluorescence lineshape  $\tilde{D}_i(\omega)$  are obtained in the cumulant expansion formalism as:

$$D_i(\omega) = \int_{-\infty}^{\infty} e^{-i(\omega_{gi}-\omega)t - g_i(t)} dt, \quad (5.3)$$

$$\tilde{D}_i(\omega) = \int_{-\infty}^{\infty} e^{-i(\omega_{gi}-\omega)t + 2i\lambda_i t - g_i^*(t)} dt, \quad (5.4)$$

where  $g_i(t)$  is the lineshape function of the excited state  $i$  and  $\lambda_i$  is the corresponding reorganization energy. The lineshape function  $g_i(t)$  can be obtained from the spectral density  $J_i(\omega)$  of the excited state  $i$  as:

$$g_i(t) = \int_0^{\infty} d\omega \frac{J_i(\omega)}{\pi\omega^2} \left[ \coth\left(\frac{\beta\hbar\omega}{2}\right) (\cos(\omega t) - 1) - i(\sin(\omega t) - \omega t) \right] \quad (5.5)$$

More details regarding the calculation of the spectral densities  $J_i(\omega)$  are described in the Supporting Information (SI).

## 5.3 Experimental Methods

### 5.3.1 Femtosecond Transient Absorption Spectroscopy (fTAS)

Femtosecond transient absorption (TAS) measurements were performed using a Ti:sapphire regenerative amplifier system (800 nm central wavelength, 87 fs pulse duration, 4 kHz repetition rate, 0.55 mJ per pulse). Pump pulses were generated in a noncollinear optical parametric amplifier (NOPA) seeded with white light from the fundamental output. The NOPA output at 760 nm was frequency-doubled in a 0.1 mm BBO crystal to produce excitation pulses centered at 380 nm. The pump pulse energy at the sample was maintained at 0.5  $\mu$ J to avoid multiphoton effects. The probe pulse was generated as a supercontinuum (420-750 nm) in a 5 mm CaF<sub>2</sub> plate and collinearly overlapped with the pump in the sample. The instrument response function (IRF) was determined to be 200 fs (FWHM). The temporal delay between pump and probe pulses was controlled with a motorized delay stage, covering delays up to 1.9 ns. A detailed information about the transient absorption together with the schematic representation of the setup are provided in SI and Figure 5.8.

## 5.4 Results and Discussion

### 5.4.1 Structural Properties

The geometries of the monomeric units and the homo-PCP were optimized using DFT, including solvent effects of CH<sub>2</sub>Cl<sub>2</sub> via the PCM approach. The resulting PCP geometries are strongly influenced by both the structure of the individual aromatic units and the nature of the linkers.

For the PCPs containing NDI units, three types of linkers were investigated: adamantane (Ada), tert-butylphenyl (<sup>t</sup>BuPh) and cyclohexane (cyc). The <sup>t</sup>BuPh linker provides higher flexibility, allowing for the incorporation of units with slightly different lengths facilitating the parallel stacking of the NDI units. In contrast, the rigid Ada linker enforces a more constrained geometry, resulting in a pronounced inclination of the aromatic unit planes. For the NDI-<sup>t</sup>BuPh-NDI homodimer, two nearly isoenergetic lowest-energy conformers were identified, corresponding to the cis and trans orientations of the linkers, Figure 5.1. The trans orientation promotes nearly parallel stacking of the NDI units, while the cis conformation leads to an inclination of approximately 18°. The inclination is even more pronounced for the NDI-Ada-NDI homodimer, reaching a value around 47°.

In the NDI homo-PCP with the shortest cyclohexane linker, the interunit distance near the linker is 2.9 Å, which is smaller than the sum of the van der Waals radii for two carbon atoms (approximately 3.4 Å). This close proximity results in steric repulsion between the NDI units, which suppresses inclination and induces bending of the overall structure. As a consequence, the interunit distance increases to approximately 4.0 Å at the center of the PCP, Figure 5.1. This value is slightly larger than the interplanar distance observed in the crystalline state (around 3.3 Å), likely due to the absence of the intermolecular crystal packing constraints in solution. The calculated mutual rotation of 9° of the NDI units on the other hand agrees well with the previously reported crystal structure in Ref. 25.

A similar structural behavior is observed for PCPs containing Pyrene units. The linkers examined in this case include ethyl, propyl, bis(aminomethyl)adamantane, and bis(aminomethyl)tert-butylphenyl. The linkers bearing amine groups were selected because of their influence on the lowest excited state of Pyrene; the amine acts as an electron donor, introducing partial CT character to this state. PCPs with *t*BuPh and Ada linkers exhibit parallel arrangement of the Pyrene units, with interplanar separations of 5.1 Å and 4.1 Å, respectively. As in the case of the NDI-based PCPs, the *t*BuPh-linked Pyrene dimers also yield cis and trans isomers with similar energies. The shortest ethyl and propyl linkers lead to bent geometries, with interunit distances of about 4.1 Å at the center of the PCP and slightly shorter distances near the linkers, analogously to the behavior observed for the NDI-cyc-NDI system.

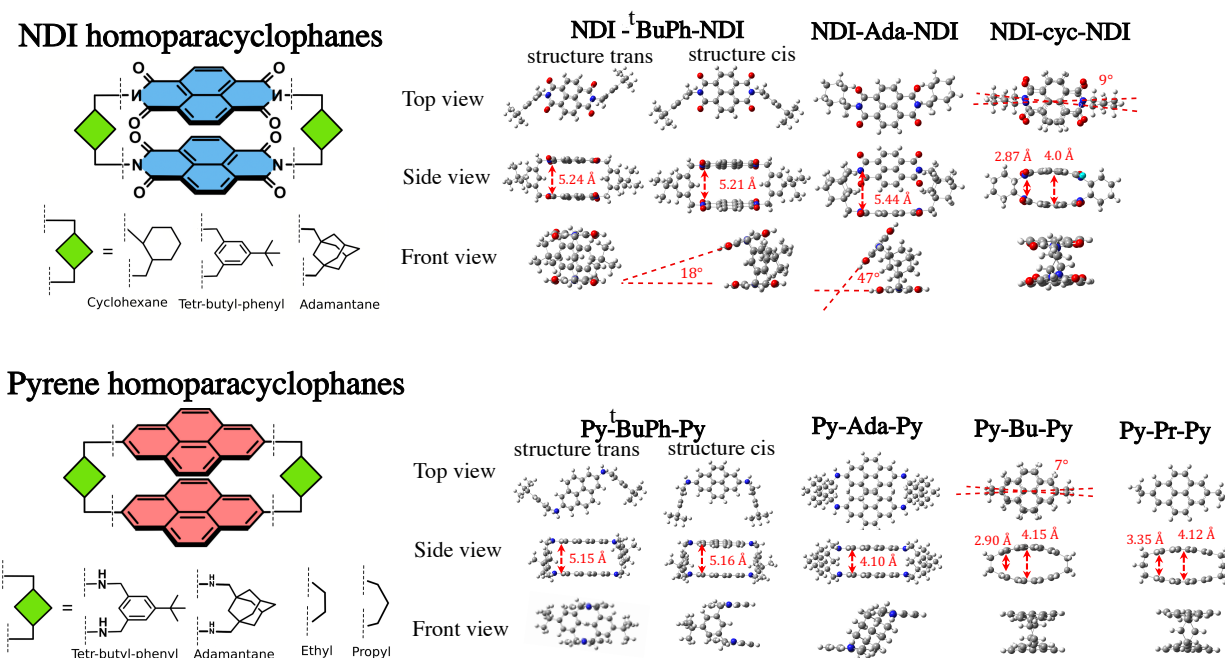


Figure 5.1: Structures of the studied paracyclophanes.

## 5.4.2 Optical Properties of the Monomeric Units

Before analyzing the "double-decker" PCPs and elucidating the origin and dynamics of their excited states, it is instructive to first examine the excited state properties of the individual molecular building blocks themselves. Studying the monomers separately allows for a clear distinction between inter-unit excitations within the PCP and intra-unit excitations localized on the individual monomeric units. The optical spectra of the NDI and Pyrene monomers, together with a molecular orbital (MO) analysis of their lowest excited states, are presented in Figure 5.2.

In the low-energy region (3.0-3.9 eV) of the NDI absorption spectrum, the dominant feature corresponds to the  $\pi$ - $\pi^*$  type  $S_0 \rightarrow S_1$  with the transition dipole moment oriented along the longer symmetry axis, peaking near 3.25 eV. Natural transition orbital (NTO) analysis indicates that this



transition is primarily composed (98%) of the HOMO  $\rightarrow$  LUMO single-electron excitation (Figure 5.2). Both the hole and electron orbitals are localized on the NDI core, consistent with only a minimal spectral shift between NDI monomers with different linkers e.g. a tiny red shift of approximately 0.012 eV is observed for NDI with the <sup>t</sup>BuPh linker relative to the system with Ada linker. The fine structure in the optical spectrum arises from vibronic excitations of the C-C stretching modes of the  $\pi$ -conjugated system, with computed frequencies of 1446 and 1640 cm<sup>-1</sup> and corresponding reorganization energies of 1132 and 674 cm<sup>-1</sup>, respectively. These values closely reproduce the experimentally observed vibronic peak separations of 1450 and  $\sim$ 1580 cm<sup>-1</sup>. The computed reorganization energies are slightly overestimated, leading to a lower intensity of the first vibronic peak in the simulated absorption spectrum compared to experiment, a well-known artifact of the vertical gradient approximation, which neglects small differences in normal modes between ground and excited states, and the DFT functional. The spectral shape can be further corrected by including Duschinsky rotation effects<sup>26,27,28</sup> (Figure 5.6). Despite these minor deviations, the computed NDI absorption spectra is in very good quantitative agreement with the experimental spectra without the need for arbitrary shifts or rescaling of the excitation energies. Note that the deviation between calculated and measured spectra in the high-energy region is due to the fact that only the lowest excited states were included in the calculations.

Similar properties can be observed for the optical spectrum of Pyrene. It is composed of three principal electronic transitions: the <sup>1</sup>L<sub>b</sub> ( $S_0 \rightarrow S_1$ ) state, composed of HOMO-1  $\rightarrow$  LUMO and HOMO  $\rightarrow$  LUMO+1 excitations; the <sup>1</sup>L<sub>a</sub> state corresponding to ( $S_0 \rightarrow S_2$ ) excitation, primarily a HOMO  $\rightarrow$  LUMO transition; and the higher-lying  $S_0 \rightarrow S_4$  transition, which gives rise to the intense UV absorption band around 4.5 eV. The first excited state <sup>1</sup>L<sub>b</sub> possesses a weak transition dipole moment oriented along the short molecular axis, while the <sup>1</sup>L<sub>a</sub> transition near 3.65 eV is polarized along the longer molecular axis. As in the case of NDI, TD-DFT slightly overestimates the reorganization energy, but the computed positions and relative intensities of both electronic and vibronic features are in very good agreement with experiment. Although the TD-DFT ( $\omega$ B97XD) calculations predict an incorrect ordering of the lowest excited states in solution, the correct ordering is restored upon applying the CC2-based energy corrections that account for dynamic electron correlation. The simulated fluorescence spectra also reproduce the experimental shapes well, albeit blue-shifted by about 0.2 eV, primarily due to the overestimated excitation energy of the <sup>1</sup>L<sub>b</sub> state, which experimentally lies near 3.3 eV<sup>29</sup>. A more accurate description of this state would require a higher-level method beyond the CC2 approach.

For Pyrene containing the amine-functionalized linkers (Ada and <sup>t</sup>BuPh), the low-energy region of the optical spectrum (2.6-3.5 eV) is dominated by a broad and featureless  $S_0 \rightarrow S_1$  transition with a maximum near 2.74 eV. This transition corresponds to the <sup>1</sup>L<sub>b</sub> excitation polarized along the shorter molecular axis, but with partial contribution from an intramolecular charge transfer (ICT) component<sup>30,31,32,33,34,35</sup>, as illustrated in Figure 5.2b. NTO analysis reveals that the amine substituent acts as an electron donor: the hole orbital is delocalized over the amine, Pyrene and partially also linker moieties, whereas the electron orbital remains localized on the Pyrene core. This results in partial charge transfer from the linker region to the Pyrene unit upon excitation. Consequently, the excitation energy is sensitive to the electronic properties of the linker. Both theoretical and experimental data confirm this trend. The computed absorption energy of the Ada-linked Pyrene is lower by 0.103 eV relative to the <sup>t</sup>BuPh-linked analogue, consistent with the experimentally observed difference of approximately 0.075 eV.

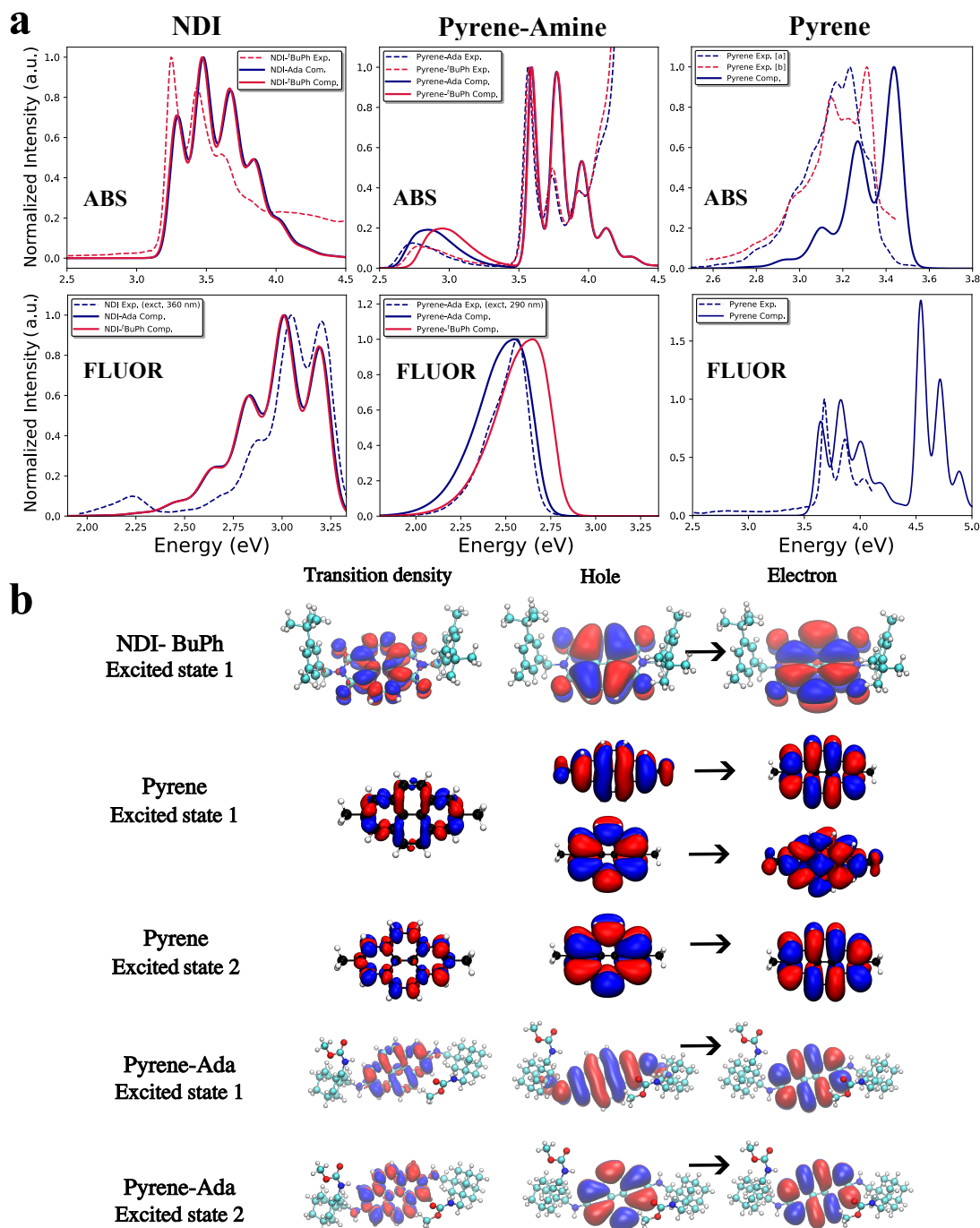


Figure 5.2: **Optical spectra and corresponding electronic excitations of the monomeric units.** (a) Computed and experimental absorption and fluorescence spectra of NDI, Pyrene and Pyrene with <sup>t</sup>BuPh and Ada linkers. The computed spectra show excellent agreement with the experimental ones without inclusion of arbitrary shifts. (b) Transition densities and natural transition orbitals for the lowest excited states of the monomeric units.



The higher-energy  $S_0 \rightarrow S_2$  transition (3.5-4.0 eV) exhibits clear vibronic structure and corresponds to the  $^1L_a$  excitation polarized along the longer molecular symmetry axis. Transition density and NTO analyses show that this excitation is localized entirely on the Pyrene unit, with negligible linker influence, evidenced by only an 8 meV shift in the vibronic 0-0 transition. This is in agreement with the experimentally observed shift of 3 meV. Similar to the NDI and unsubstituted Pyrene monomers, the computed reorganization energies for the C-C stretching modes are slightly overestimated, leading to stronger intensities of the higher vibrational transitions peaks compared to experiment. Nonetheless, the absolute excitation energies, spectral shapes, and fluorescence features are reproduced with excellent quantitative agreement. The lowest  $S_1 \rightarrow S_0$  fluorescence transition, which retains partial ICT character, exhibits a slightly broader band than in experiment due to the same reorganization energy overestimation, but its energy and overall spectral profile are accurately reproduced.

The excellent agreement between experimental and computed optical spectra for all monomeric systems validates the reliability of the employed computational protocol. This level of accuracy is particularly crucial for the subsequent modeling of heterodimeric PCPs, where differences in the absolute excitation energies of individual monomers directly determine the extent and character of electronic state mixing.

### 5.4.3 Optical Properties of the Homoparacyclophanes

From the perspective of their optical and electronic properties, as well as for interpreting their spectra, the PCPs can be regarded as two optically active chromophoric units held in defined positions and orientations by two linkers. Within this framework, their excited state properties can be investigated using two different approaches.

The first is the supermolecular approach, in which the entire PCP is treated as a single molecule, for which electronic and optical properties are computed directly. This approach provides the most accurate description of the system, as it naturally includes all mutual interactions between the two chromophoric units. However, this accuracy comes at a significant computational cost, particularly for the CC2 step, for which the scaling increases steeply with system size (roughly as  $N^5$ ). The computational demand becomes even more severe when simulating transient absorption spectra, which require calculations of higher-lying singly and doubly excited states.

An alternative approach is the Frenkel exciton model, which treats the PCP as a dimer composed of two interacting monomeric units. Here, the aggregate Hamiltonian is expressed in a basis of separate non-interacting units. The diagonal elements correspond to the excitation energies of each unit within its environment, including the solvent and the remainder of the PCP molecule. The off-diagonal elements describe the Coulomb coupling between the transition densities of the two units, evaluated within their respective solvent cavities (see Supporting Information for details). The limitations of this method arise when the inter-unit distance becomes small or when the excited states exhibit strong delocalization over the linkers. In such cases, a clear partitioning of the PCP into distinct, non-overlapping units becomes ambiguous, and a specific partitioning may be required for each electronic state.

In this section, we first demonstrate that the supermolecular approach reliably and quantitatively reproduces the experimental optical properties of the homo-PCPs. In fact, as for the case of the monomeric units, the computed absorption and fluorescence spectra agree very well with

experimental measurements for both NDI- and Pyrene-based homo-PCPs (Figure 5.3). Even the vibronic structures are faithfully reproduced, with well-resolved progressions that closely mirror experimental spectra, where individual electronic and vibronic bands are often difficult to distinguish.

The optical spectra of the homo-PCPs can be interpreted in terms of excitonic H-type dimers of the two chromophoric units. Parallel stacking of the  $\pi$ -systems leads to a splitting of the lowest  $\pi$ - $\pi^*$  excitations in the dimers: a lower-energy, optically dark  $S_1$  state and a higher-energy, bright  $S_2$  state. Deviations from perfect parallel alignment arising from steric effects or geometric constraints of the linker lead to redistributions of the transition dipole strength between these two excitonic states, rendering the lower  $S_1$  state partially allowed. This behavior is particularly evident in the NDI-based homo-PCPs.

For the NDI-Ada-NDI and NDI-*t*BuPh-NDI systems, where the NDI units remain nearly parallel, the transition dipole moment of the  $S_2$  state approaches the ideal H-type dimer limit,  $|d_{02}^{PCP}| = \sqrt{2} |d_{01}^{NDI}| = 3.38 a.u.$ , while  $|d_{01}^{PCP}| \approx 0$  for the  $S_1$  state (a summary is given in Table XX). This assignment is also supported by the transition density analysis for NDI-Ada-NDI shown in Figure 5.3b. The dark  $S_1$  state exhibits opposite transition dipole orientations on the two NDI units (antiparallel configuration), whereas the bright  $S_2$  state shows parallel dipoles (constructive configuration). Small deviations from the idealized H-dimer behavior arise from weak molecular orbital (MO) overlap, linker effects, and differences in the local dielectric environment due to the presence of the other unit.

In NDI-cyc-NDI, the two NDI units are rotated by approximately  $9^\circ$  with respect to each other, which prevents perfect cancellation of the transition dipoles in the  $S_1$  "antiparallel" state, resulting in a weakly allowed transition. This is manifested in the appearance of the small absorption peak near 3.1 eV corresponding to the  $S_0 \rightarrow S_1$  transition, in addition to the dominant  $S_0 \rightarrow S_2$  transition around 3.4 eV. Another important factor influencing the optical properties of PCPs is the inter-unit separation. NDI-Ada-NDI and NDI-*t*BuPh-NDI, with similar separations of 5.44 Å and 5.24 Å, respectively, show similar splitting energies and spectral shapes, whereas the shorter 2.9-4.0 Å separation in NDI-cyc-NDI increases the coupling strength, leading to larger exciton splitting, i.e. a blue-shift of the  $S_2$  state and a red-shift of the  $S_1$  state with respect to the Ada and *t*BuPh linkers.

The fluorescence spectra provide further insight into the nature of the lowest excited states. For NDI-*t*BuPh-NDI, the fluorescence intensity is significantly reduced relative to the monomer due to the weak transition dipole moment of the lowest exciton state, in line with the H-type dimer picture. The computed fluorescence spectrum within the vertical gradient approximation reproduces the experimental spectrum almost perfectly (Figure 5.3), indicating minimal structural relaxation upon excitation. The fluorescence profile is thus essentially the mirror image of the absorption spectrum, shifted by the solvent reorganization energy.

In contrast, the NDI-cyc-NDI system exhibits a large Stokes shift of approximately 0.65 eV between absorption and fluorescence maxima, which cannot be explained solely by solvent relaxation. The very short inter-unit distance, smaller than the sum of the van der Waals radii, introduces steric strain and mutual repulsion of the aromatic units in the ground state but favors excimer formation in the excited state manifold. Excitation leads to charge redistribution and perfect parallel alignment with smaller separation of the NDI units in the optimal excited state geometry compared

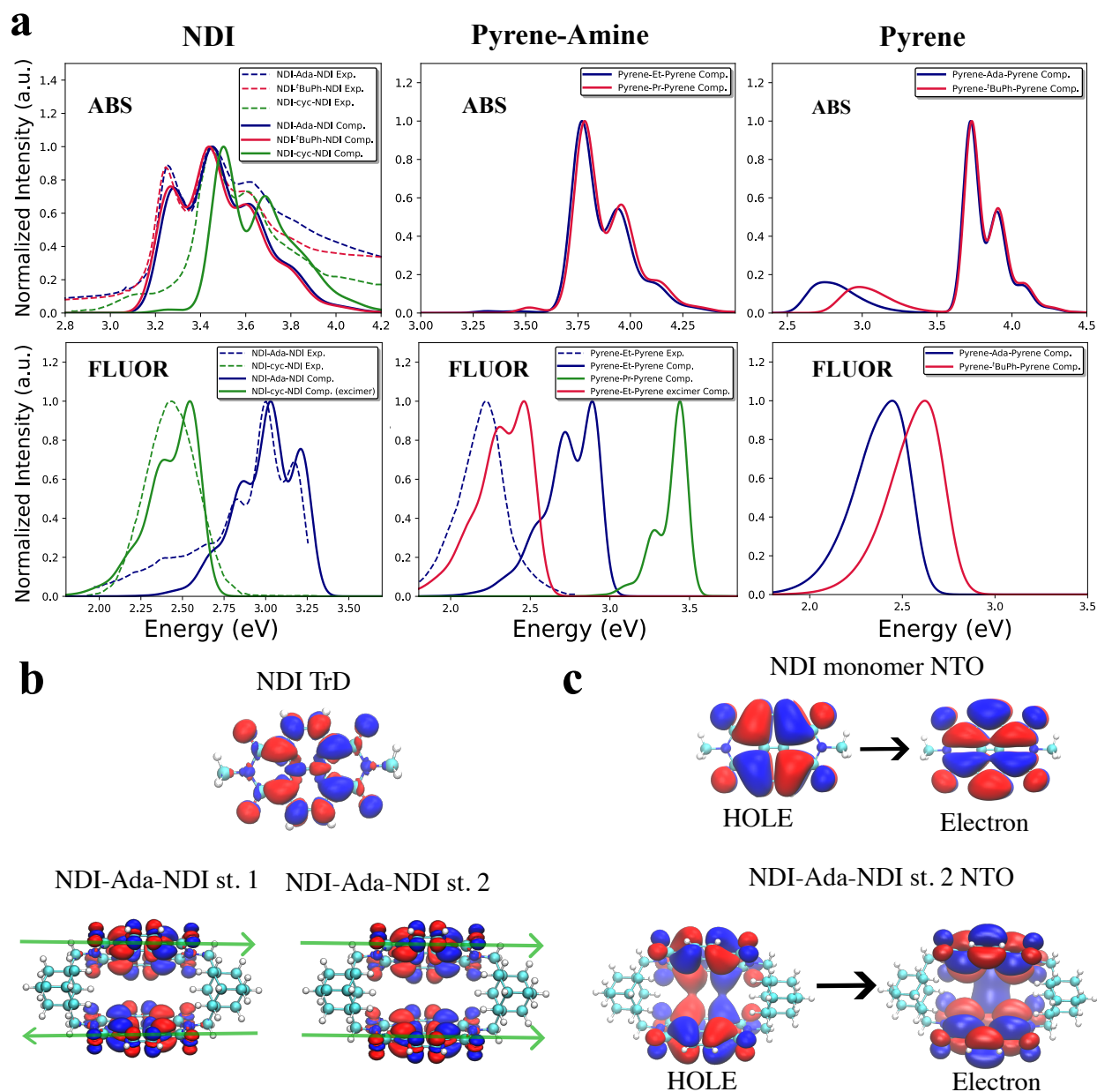


**Figure 5.3: Optical spectra and corresponding electronic excitations of the homoparacyclophanes.** (a) Computed and experimental absorption and fluorescence spectra of NDI, Pyrene and bis(aminomethyl)Pyrene homo-paracyclophanes. (b) Monomeric and NDI-Ada-NDI transition density for the corresponding lowest excited states. The green arrows represents the orientation of the transition dipole from the separate aromatic units. The lowest excited state of the H-type dimer is optically dark with unit transition dipoles oriented in opposite directions whereas the second excited state is bright with unit dipoles aligned. (c) Natural transition orbitals for the monomeric NDI and the second excited state for the NDI-Ada-NDI paracyclophane.

to the ground state one. Excitation relieves the ground state strain due to the shorter optimal interunit distance, leading to the planarization of the aromatic units and a stabilization of the excimer configuration (see Figure 5.7). The resulting structural relaxation significantly lowers the excited state energy, causing the pronounced fluorescence red-shift. Theoretical simulations confirm the presence of an intra-PCP excimer in NDI-cyc-NDI, with the computed fluorescence spectrum for the relaxed structure in the excited state matching the experimental data (Figure 5.3).

Excimer formation is not observed in NDI-*t*BuPh-NDI or NDI-Ada-NDI due to the bulky linkers maintaining interunit separations above 5 Å. At such distances, no ground state strain/repulsion exists, and both ground and excited state geometries remain planar with just weakly interacting aromatic units. Excimer formation for these systems could occur only under high concentrations, where the interaction between aromatic units from different PCP molecules (rather than intra-PCP) become significant, due to short inter-PCP separation compared to the interunit separation within the single PCP molecule.

Similar behavior is observed for Pyrene-based PCPs. Systems with short ethylene linkers exhibit clear excimer fluorescence, whereas those with longer linkers show primarily monomer-like emission. In Figure 5.3, the fluorescence spectra computed within the vertical gradient approximation are compared to those obtained after full excited state relaxation. The relaxed (excimer) spectra are significantly red-shifted by around 0.5 eV compared to the ones computed within the vertical gradient approximation and they well reproduce the experimentally observed emission band. The slight blue-shift of the calculated spectra relative to experiment is consistent with the systematic overestimation of excitation energies by the employed combined TD-DFT and CC2 levels of theory, as noted above for the Pyrene monomer.

Having validated the supermolecular approach, we next assess the performance of the Frenkel exciton model in reproducing the same optical and electronic properties from monomer-level data and their mutual interactions. The key parameters in this model are the site energies (monomeric unit excitation energies) and the electronic couplings between the units. The electronic couplings can be divided into two categories: (i) interactions between locally excited states (LE-LE coupling) and (ii) couplings between locally excited and charge transfer states (LE-CT coupling). The former can be expressed as Coulomb interaction of the corresponding transition densities, whereas the later one is related to molecular orbital overlap between the two units<sup>36</sup>. The different form of coupling originates from the different physical nature of the processes. The LE-LE coupling can be understood as an excitation transfer process between the two units ( $DA^* \rightarrow D^*A$ ), where the deexcitation of the molecule  $D$  is accompanied by excitation of the molecule  $A$ . Such coupling originates from Coulomb interaction between transition densities and is often approximated within multipole expansion by dipole-dipole interactions (Förster resonant energy transfer). Here we adopted a more rigorous approach and computed electronic couplings via the Poisson-TrESP method<sup>37,38</sup>, where transition densities are represented as distributed atomic transition charges in molecular cavities (Figure 5.4b), and their electrostatic interactions are evaluated in a dielectric environment using the APBS package<sup>39</sup>. More details concerning the calculation of the electronic couplings can be found in the SI.

The LE-CT coupling, corresponding to the process  $D^+A^- \rightarrow DA^*$  during which the electron is transferred between the two units, depends linearly on the HOMO orbital overlap between donor and acceptor units, reflecting its one-electron transfer character. For the simplest case of the  $\text{HOMO}^A \rightarrow \text{LUMO}^A$  excitation of the  $A^*$  and  $\text{HOMO}^D \rightarrow \text{LUMO}^A$  excitation for the  $D^+A^-$  CT

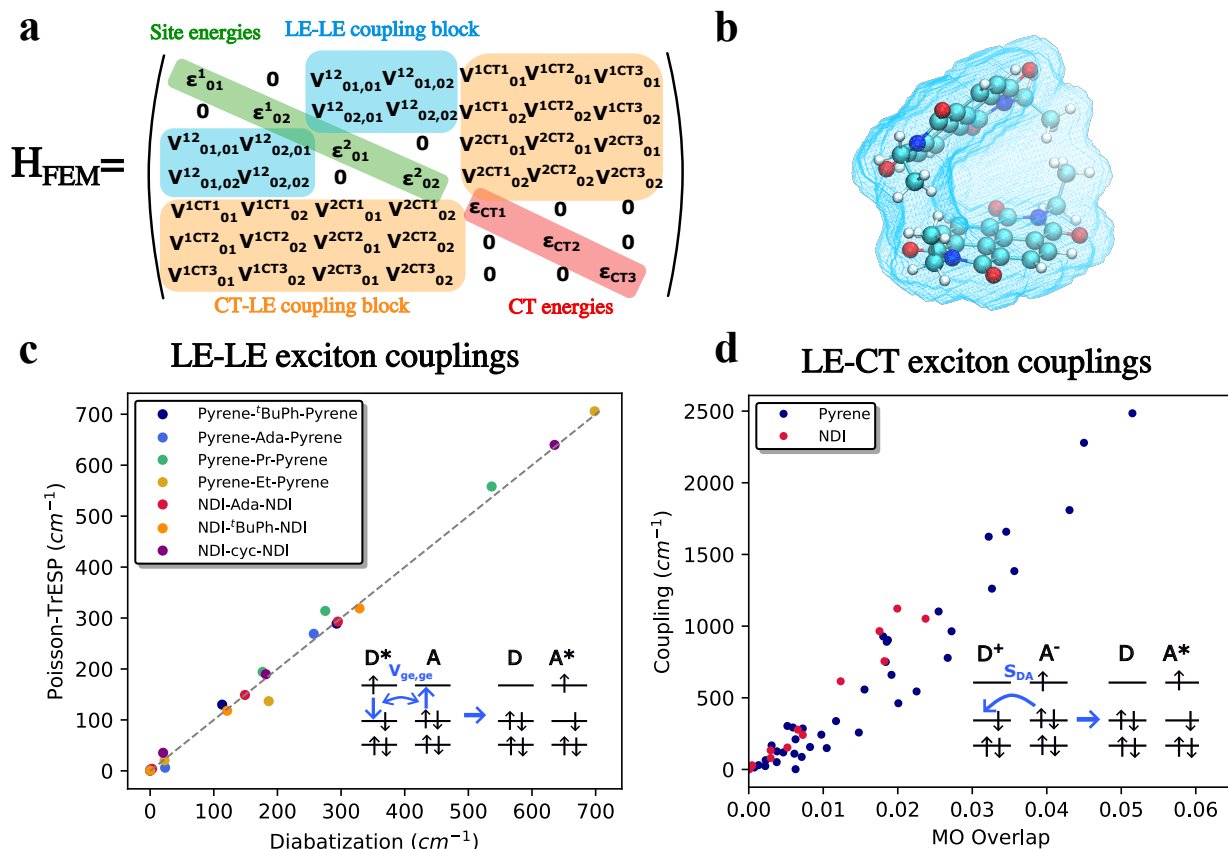


Figure 5.4: **Frenkel exciton model for the homo-paracyclophanes.** (a) Representation of the Frenkel exciton Hamiltonian and decomposition into LE-LE and CT-LE blocks. (b) Representation of the paracyclophane as two separate units embedded in a dielectric environment. The blue area represents the solvent cavity. (c) Comparison of the exciton couplings between locally excited states computed from the Poisson-TrESP method and from diabatization of the supermolecule excited states with correlation coefficient 0.997. (d) Correlation between calculated LE-CT couplings and corresponding molecular orbital overlaps between the individual separate units with correlation coefficient of 0.983 and 0.964 for the NDI and Pyrene based PCs, respectively.

state, the process  $D^+ A^- \rightarrow DA^*$  corresponds to electron transfer from the  $HOMO^D$  of the donor to the  $HOMO^A$  of the acceptor. This electron transfer is therefore dependent on the overlap of HOMO orbitals of the donor and acceptor, yielding a linear dependence of the CT-LE coupling on the corresponding MO overlap. The graphical representation of the processes is shown in Figure 5.4.

To compare the supermolecular approach with the Frenkel exciton model, the supermolecular excited states were diabatized using the Fragment Charge Difference (FCD) algorithm<sup>40</sup>, yielding distinct LE and CT diabatic states and their mutual couplings. The resulting LE-LE couplings agree exceptionally well with those obtained from the Poisson-TrESP method across all the investigated PCs, both for the NDI and Pyrene systems (Figure 5.4). The CT-LE couplings also follow a nearly perfect linear dependence on the corresponding MO overlaps for both NDI and Pyrene units with

only small deviations. Remarkably, this agreement holds even for the shortest inter-unit distances such as in NDI-cyc-NDI and Pyrene-Et-Pyrene, where substantial orbital overlap is present.

Overall, these results demonstrate the robustness and reliability of the Frenkel exciton model in describing a wide range of homo-PCPs, from weakly coupled dimers to systems with partial charge transfer character. This validates its use as an efficient and physically transparent framework for an understanding of the optical excitations and energy transfer processes in both homo- and hetero-paracyclophane architectures.

### 5.4.4 Transient Absorption

To investigate the effect of the linker on the ultrafast excited state dynamics of the NDI-based homodimers, femtosecond transient absorption (fTAS) measurements were performed with excitation at 380 nm, corresponding to the NDI  $S_1$  absorption band. The transient absorption spectra recorded at different delay times for NDI- $t$ BuPh-NDI and NDI-Ada-NDI in  $\text{CHCl}_3$  are shown in Figure 5.5a. Immediately following photoexcitation, both compounds exhibit similar transient

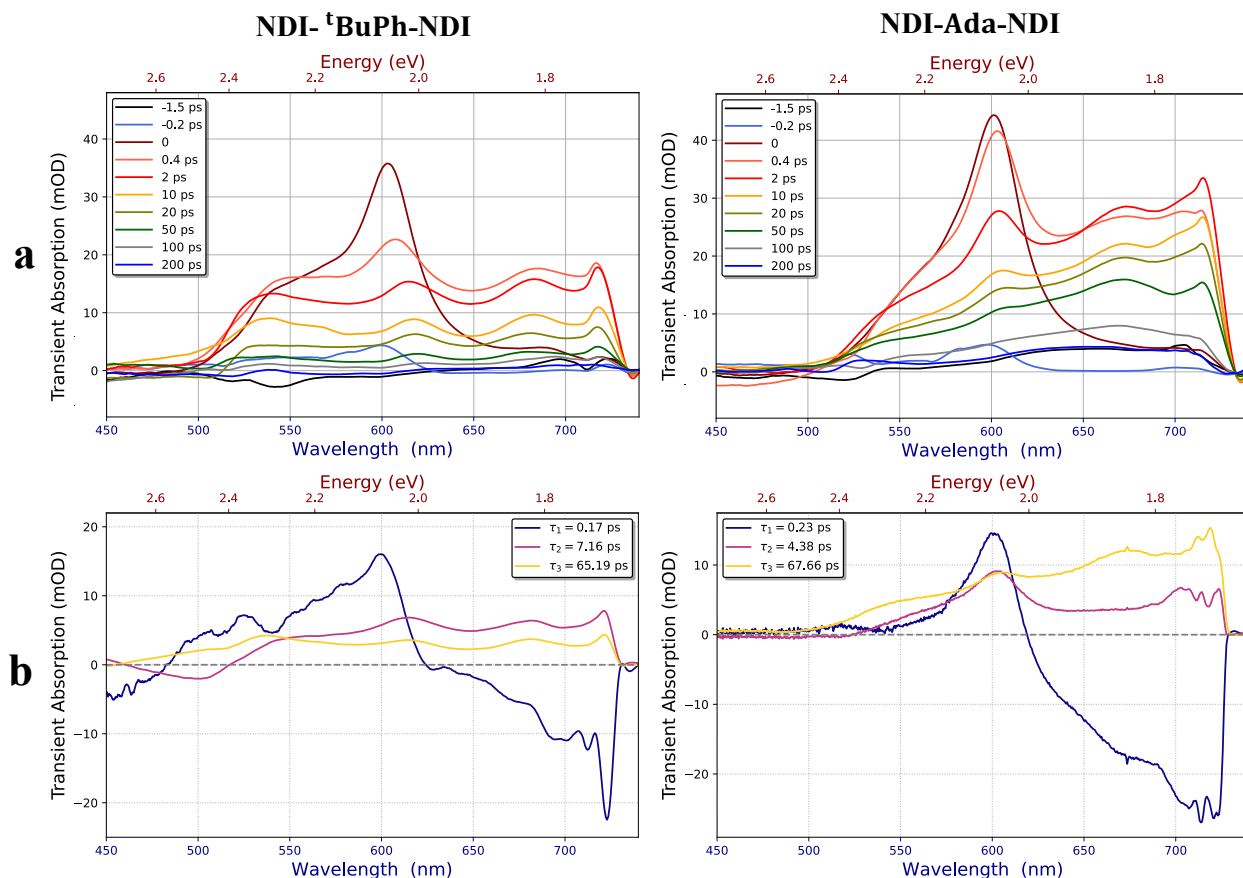


Figure 5.5: **a** Transient absorption spectra of NDI- $t$ BuPh-NDI and NDI-Ada-NDI recorded at various time delays excited at 380 nm. **b** Corresponding decay associated spectra (DASs).

spectral features. The positive signal in the transient absorption spectra is attributed to excited state absorption (ESA). At early delay times, the ESA displays a pronounced peak centered around



600 nm with a side band around 550 nm, whose relative intensity differs between the <sup>t</sup>BuPh- and Ada-linked PCPs. These features closely resemble the transient absorption spectrum of the NDI monomer<sup>41</sup> and can be assigned to the ESA from the NDI  $S_1$  state. At longer delay times, the ESA evolves into a much broader band with three prominent peaks around 550nm, 610nm and 680nm. Such pronounced spectral changes cannot be explained solely by vibrational relaxation, but indicate substantial electronic relaxation. The broad and structured character of the spectra at longer delay times suggest the formation of a lower energy excimer state arising from interaction between the nearby NDI units of two separate PCPs.

To quantify the underlying kinetics, the transient absorption data were analyzed using a global fitting procedure based on a sequential decay model. The best fit was obtained with three exponential decay components. The extracted lifetimes ( $\tau$ ) and their corresponding decay associated spectra are shown in Figure 5.5b. For NDI-<sup>t</sup>BuPh-NDI, the time constants are  $\tau_1 = 0.17$  ps,  $\tau_2 = 7.16$  ps, and  $\tau_3 = 65.19$  ps, while for the NDI-Ada-NDI corresponding values are  $\tau_1 = 0.23$  ps,  $\tau_2 = 4.38$  ps, and  $\tau_3 = 67.66$  ps.

The ultrafast component  $\tau_1$ , represents the decay of the NDI  $S_1$  ESA peak with a simultaneous rise of the broad band extending from 500nm to 750nm, near the edge of the spectral detection window. This process can be attributed to exciton relaxation from the lowest excited state  $S_1$  of the NDI PCP H-type dimer to the excimer state. Such rapid excimer formation is facilitated by the high concentration of the sample (5 mM), which likely promotes the formation of  $\pi$ -stacked PCP aggregates already in the electronic ground state, before initial excitation. Ultrafast excimer formation has also been reported for the NDI-cyc-NDI PCP, further supporting this assignment. The intermediate component  $\tau_2$  is associated with minor spectral evolution around 500nm and may be attributed to vibrational relaxation in the excimer state. The longest-lived component  $\tau_3$ , can be interpreted as the decay of the excimer back to the ground state.

Although minor differences in the transient absorption spectra between Ada- and <sup>t</sup>BuPh-linked PCPs are observed, their overall excited state dynamics is remarkably similar. In contrast, previously reported transient absorption spectra of NDI-cyc-NDI in Ref. 42, indicate longer excimer lifetimes and slower relaxation to the ground state. This observation is consistent with the steady state absorption and fluorescence data, as well as the computational results, which all suggest that the electronic and optical properties of the <sup>t</sup>BuPh- and Ada-linked PCPs are nearly identical, whereas the NDI-cyc-NDI system exhibits a substantially different behavior due to the shorter spatial separation between its chromophoric units.

### 5.4.5 Electrochemical Properties

The electrochemical properties of NDI-Ada-NDI, along with several monomeric units were investigated by cyclic voltammetry (CV), and differential pulse voltammetry (DPV) in CH<sub>2</sub>Cl<sub>2</sub> (Figures S5.10-S5.12). As summarized in Table 5.1, the NDI-Ada-NDI homodimer undergoes four reversible single-electron reduction processes at -0.62 V, -0.77 V, -1.21V and -1.25 V. It is expected that each NDI is sequentially reduced to the radical anion and the dianion species. The splitting of the first and second reductions suggests a strong electronic coupling between the two NDIs, resulting from the enforced interactions between their  $\pi$ -orbitals as previously reported for double-decker or multi-decker systems with NDI chromophores<sup>43,44</sup>.

To gain deeper insight into the electrochemical behavior of the PCPs and the MOs involved in



the redox processes, DFT calculations were performed. The geometries of the neutral, oxidized, and reduced species were independently optimized using the B3LYP functional with a 6-31+G(d,p) basis set including solvent effects from CH<sub>2</sub>Cl<sub>2</sub> via the polarizable continuum model (PCM). The adiabatic ionization potentials (IP) and electron affinities (EA) were then derived from the optimized structures according to  $IP = E_{+1}^{opt} - E_0^{opt}$  and  $EA = E_0^{opt} - E_{-1}^{opt}$  where  $E_i^{opt}$  denotes the total energy of the optimized structure with charge  $i$ . The computed IP and EA values show excellent quantitative agreement with experimental measurements, with deviations below 0.1 eV for all systems (Table 5.1). Accurate reproduction of the experimental redox properties critically depends on the inclusion of solvent effects, particularly in polar environments. For charged species, solvent reorientation stabilizes the charge, resulting in molecular orbital energy shifts exceeding 1 eV. Once again, the outstanding agreement between theory and experiment confirms the reliability of the computational methodology and its capability to accurately describe both geometric and electronic properties of PCPs.

Table 5.1: Redox properties for the monomeric units and homoparacyclophanes.

Compound	Experimental		Vertical gas-phase			Vertical PCM			Adiabatic PCM		
	$-IP_{exp}$ (eV)	$-EA_{exp}$ (eV)	$-IP_{comp}$ (eV)	$-EA_{comp}$ (eV)	$E_{g,comp}$ (eV)	$-IP_{comp}$ (eV)	$-EA_{comp}$ (eV)	$E_{g,comp}$ (eV)	$-IP_{comp}$ (eV)	$-EA_{comp}$ (eV)	$E_{g,comp}$ (eV)
NDI-Ada -	-	-	8.00	2.31	5.68	7.13	3.68	3.44	6.81	3.70	3.11
NDI- <sup>i</sup> BuPh -	-	3.82	7.72	2.45	5.27	6.81	3.76	3.06	6.66	3.80	2.86
NDI-cyc -	-	-	8.68	2.26	6.40	7.18	3.56	3.62	-	-	-
Pyrene-Ada -	4.76	-	6.20	0.31	5.89	5.05	1.75	3.31	4.82	1.94	2.88
Pyrene- <sup>i</sup> BuPh -	-	-	6.34	0.38	5.96	5.18	1.79	3.39	4.98	1.92	3.06
Pyrene -	-	-	7.00	0.29	6.70	5.67	1.84	3.38	5.56	1.59	3.62
NDI-Ada-NDI -	-	3.79	8.53	2.72	5.62	7.13	3.68	3.44	7.07	3.81	3.79
NDI- <sup>i</sup> BuPh-NDI-trans	-	-	7.80	2.74	5.06	6.81	3.76	3.06	6.73	3.85	2.88
NDI-cyc-NDI -	-	-	8.45	2.75	5.70	7.11	3.82	3.28	7.06	3.93	3.13
Pyrene-Ada-Pyrene	-	-	5.76	0.47	5.30	4.88	1.79	3.10	4.76	1.83	2.93
Pyrene- <sup>i</sup> BuPh-Pyrene	-	-	5.86	0.38	5.48	5.01	1.74	3.27	4.86	1.81	3.06
Pyrene-Eth-Pyrene	-	-	6.39	0.74	5.65	5.25	2.08	3.17	5.15	2.30	2.85
Pyrene-Pr-Pyrene	-	-	6.35	0.66	5.69	5.28	2.01	3.26	5.19	2.07	3.11

## 5.5 Conclusions

The excellent agreement between the simulated and experimental optical spectra demonstrates the robustness of the proposed computational methodology for a quantitative description of the optical and electronic properties of paracyclophanes (PCPs). Furthermore, representing PCPs as assemblies of interacting monomeric units has proven to be a powerful framework for interpreting both theoretical and experimental data. This fragment-based description also provides an efficient and accurate alternative for computing electronic and optical properties of a wide range of PCPs within the Frenkel exciton model.

Nevertheless, the fragment-based Frenkel exciton approach has inherent limitations. It cannot fully capture phenomena that intrinsically depend on dimer-specific characteristics, such as structural relaxation in the excited state leading to excimer formation. In such cases, the computationally more demanding supermolecular approach remains necessary. Additional challenges may arise when combining CC2 and TDDFT methods for systems where charge transfer (CT) states are energetically close to and strongly mixed with the locally excited (LE) states. Since CC2 and TDDFT can yield different relative energies for CT and LE states, their mixing and thus the resulting excited state composition may differ. This issue can be mitigated by working in a diabatic

basis, where pure CT and LE excitations are separated and the CC2 correction is applied prior to the back transformation to the adiabatic basis for the optical spectra calculations.

Despite these potential limitations, even for systems exhibiting mixed CT/LE character such as bis(aminomethyl)Pyrene, the calculated spectra show excellent agreement with the experimental data. Therefore, we believe that cases where the proposed methodology fails are expected to be rather rare exceptions than common cases, confirming the broad applicability and reliability of this approach for the study of paracyclophane-based systems.

## 5.6 Supplementary Information

### Computational Methods

#### Spectral density

The spectral density of the pigments was modeled by two contributions. The first contribution corresponds to the intramolecular vibrations coupled to the electronic excited states and is modeled by underdamped Brownian oscillator. The intramolecular normal modes were obtained with normal mode analysis and the corresponding Huang-Rhys factors through vertical gradient method<sup>24,45,46</sup>. The structure of the system was optimized with the B3LYP functional with DCM solvent included through polarization continuum model (PCM). At the optimal geometry the normal mode analysis was performed using the same approach as for the geometry optimization. The gradients of the excited and ground state potential surfaces were computed at the TD-DFT approach with the range separated  $\omega$ B97XD functional which reasonably well describes both LE and CT states. The excited state gradients were corrected to the different DFT functional used for geometry optimization by subtracting non-zero gradient of the ground state. This is within the harmonic approximation used also for computing the spectral density exact. The second contribution originates from the nuclear motion of the environment and it is modeled by an overdamped Brownian oscillator. Reorganization energy of the environment was estimated to  $\lambda \approx 200 \text{ cm}^{-1}$  from PCM calculation with equilibrium and non-equilibrium solvation. The computed reorganization energy well represents the broadening of the vibronic peaks as well as the fluorescence Stokes shift of the monomers.

#### Exciton couplings

The exciton couplings between two LE states were computed within Poisson-TrESP approach. First the paracyclophane is separated into two aromatic units (A and B) containing also some linker atoms which contribute to the excitation of interest. Then the transition densities are computed for each monomeric units separately within TD-DFT approach including the solvent effects within the PCM method. The transition densities are then integrated into point transition charges localized on nuclei coordinates. Assignment of the transition density contribution to the atomic center was performed based on the closest distance. The resulting transition charges are rescaled to obtain the correct quantum mechanical transition dipole as:

$$Q_{0j,a} = q_{0j,a} * \frac{|\mathbf{d}_0 \mathbf{i}^{(QM)}|}{|\sum_b q_{0j,b} \mathbf{r}_b|}, \quad (5.6)$$

where  $q_{0j,a}$  correspond to transition charge for the excitation from ground to  $j$ -the excited state and located on atom  $a$  at position  $\mathbf{r}_b$ , the  $\mathbf{d}_{0j}^{(QM)}$  represents the full quantum chemical transition dipole and  $Q_{0j,a}$  represents rescaled transition charges. The interaction energy in the dielectric environment was computed with APBS software package<sup>39</sup>, where the rescaled transition charges are placed into vacuum cavities within dielectric environment. The cavities are formed by combined van der Waals surfaces of the two monomeric units. In the next step potential  $\nu_{0j}^{(A)}(\mathbf{r}_b)$  of transition atomic charges from one unit ( $A$ ) at the atomic positions  $\mathbf{r}_b$  of the other unit ( $B$ ) was evaluated with optical dielectric constant of 2.032 for the dichloromethane environment. The final interaction energy is then computed as:

$$V_{0i,0j}^{AB} = \sum_a Q_{0i,a}^{(A)} * \nu_{0j}^{(B)}(\mathbf{r}_a), \quad (5.7)$$

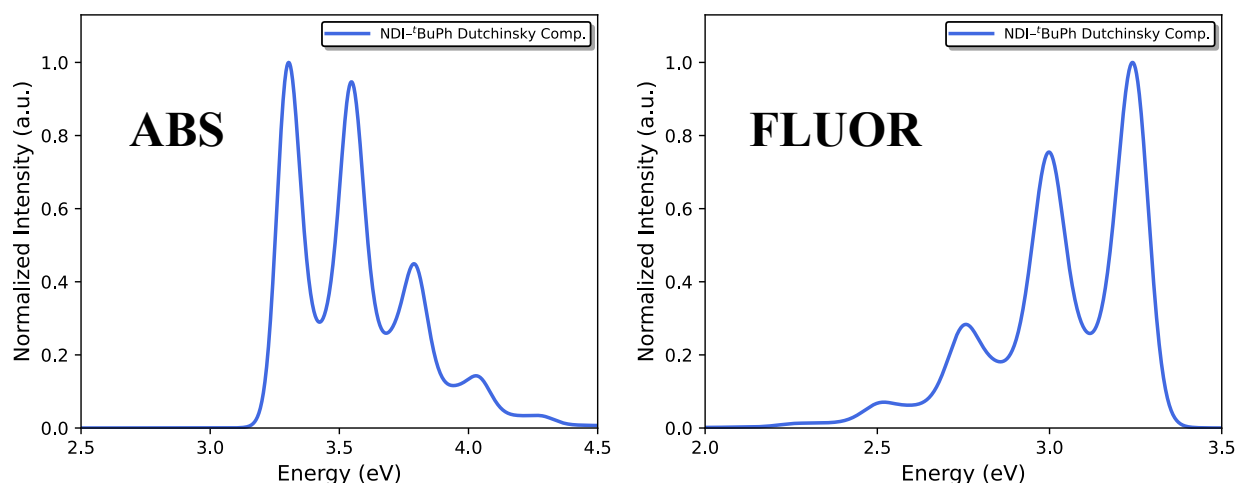


Figure 5.6: Absorption and fluorescence spectra for the NDI computed with Duschinsky rotation.

## Experimental Section

### Femtosecond Transient Absorption Spectroscopy (fTAS)

Femtosecond pump-probe TAS was carried out with a Ti:sapphire regenerative amplifier with the central wavelength 800 nm, pulse duration 87 fs, repetition rate 4 kHz, and pulse energy 0.55 mJ.

Figure 5.8 provides an overview of the experimental setup. Pump pulses were generated in a non-collinear optical parametric amplifier (NOPA) seeded with white light from the fundamental. The NOPA output at 760 nm was frequency-doubled in a 0.1 mm BBO crystal to produce excitation pulses centered at 380 nm. The pump energy at the sample was adjusted to 0.5  $\mu\text{J}$  per pulse to avoid multiphoton artifacts.

Probe pulses were obtained by focusing 0.05  $\mu\text{J}$  of the 800 nm fundamental into a 5 mm  $\text{CaF}_2$  plate, yielding a stable supercontinuum spanning 420-750 nm. The continuum was collimated and split into probe and reference arms to improve signal to noise ratio. A mechanical chopper

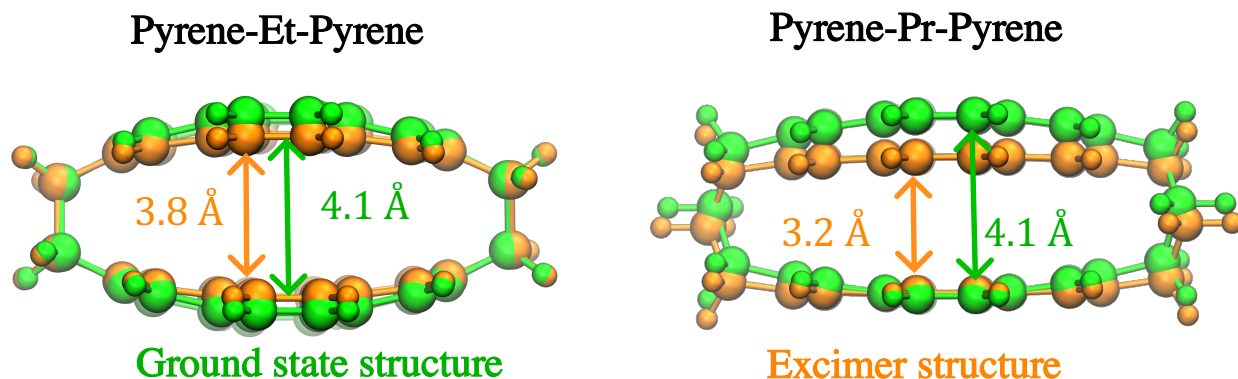


Figure 5.7: Comparison of the ground state and excimer geometry for the Pyrene homoparacyclophane with ethyl and propyl linkers.

at 2 kHz modulated the pump beam for alternating on/off acquisition. The instrument response function (IRF) was determined to be 200 fs (FWHM). Temporal delay between pump and probe was controlled by a motorized delay stage, covering to 1.9 ns. Transient absorption spectra were recorded and detected on a dual CMOS cameras, achieving a spectral resolution of around 3 nm and a noise floor of around 100  $\mu$ OD. Prior to analyzing the data, the raw signal must be corrected for the group velocity dispersion (GVD) of the probe pulse. This procedure is necessary to establish an accurate and consistent time-zero reference point for all wavelengths across the entire probe spectrum. Then data were analyzed using global fitting with IRF convolution to extract decay associated spectra (DAS) and characteristic lifetimes.

### Paracyclophane structural analysis and sample preparation

Air- and/or water-sensitive reactions were conducted under nitrogen and dry, freshly distilled solvents were used. Chemicals used to synthesize the compounds were purchased from commercial suppliers (Sigma-Aldrich, TCI, Alfa Aesar, or Thermo Fischer) and used without further purification. UV-Vis absorption spectra were measured on a Jasco V-730 spectrophotometer using quartz cuvettes with an optical path of 1 cm. Fluorescence spectra were collected on a Jasco spectrophotometer FP-8300. Automated flash chromatography (Silica gel) was performed with a Biotage Isolera Four instrument using a gradient of solvents that were given by the  $R_f$  values from the TLC.

$^1\text{H}$  and  $^{13}\text{C}$  NMR spectra were recorded on a Bruker Avance 300 or 400 spectrometer ( $^1\text{H}$  NMR = 300 MHz or 400 MHz;  $^{13}\text{C}$  NMR = 75 MHz or 101 MHz). Chemical shifts are reported in parts per million (ppm) and are referenced to the residual solvent peak ( $\text{CDCl}_3$ ,  $\delta_{^1\text{H}} = 7.26$  ppm, and  $\text{DMSO-d}_6$ ,  $\delta_{^1\text{H}} = 2.50$  ppm;  $\text{CDCl}_3$ ,  $\delta_{^{13}\text{C}} = 77.16$  ppm, and  $\text{DMSO-d}_6$ ,  $\delta_{^{13}\text{C}} = 39.52$  ppm). The following abbreviations were used: s (singlet), d (doublet), and m (multiplet).

High-resolution mass spectra (HR-MS) were measured by the Analytical Research and Services (ARS) of the University of Bern, Switzerland on a Thermo Fisher LTQ Orbitrap XL using Nano Electrospray Ionization. Cyclic voltammetry (CV) was performed in a three-electrode cell with a Pt working electrode, a glassy carbon counter-electrode, and an Ag/AgCl reference

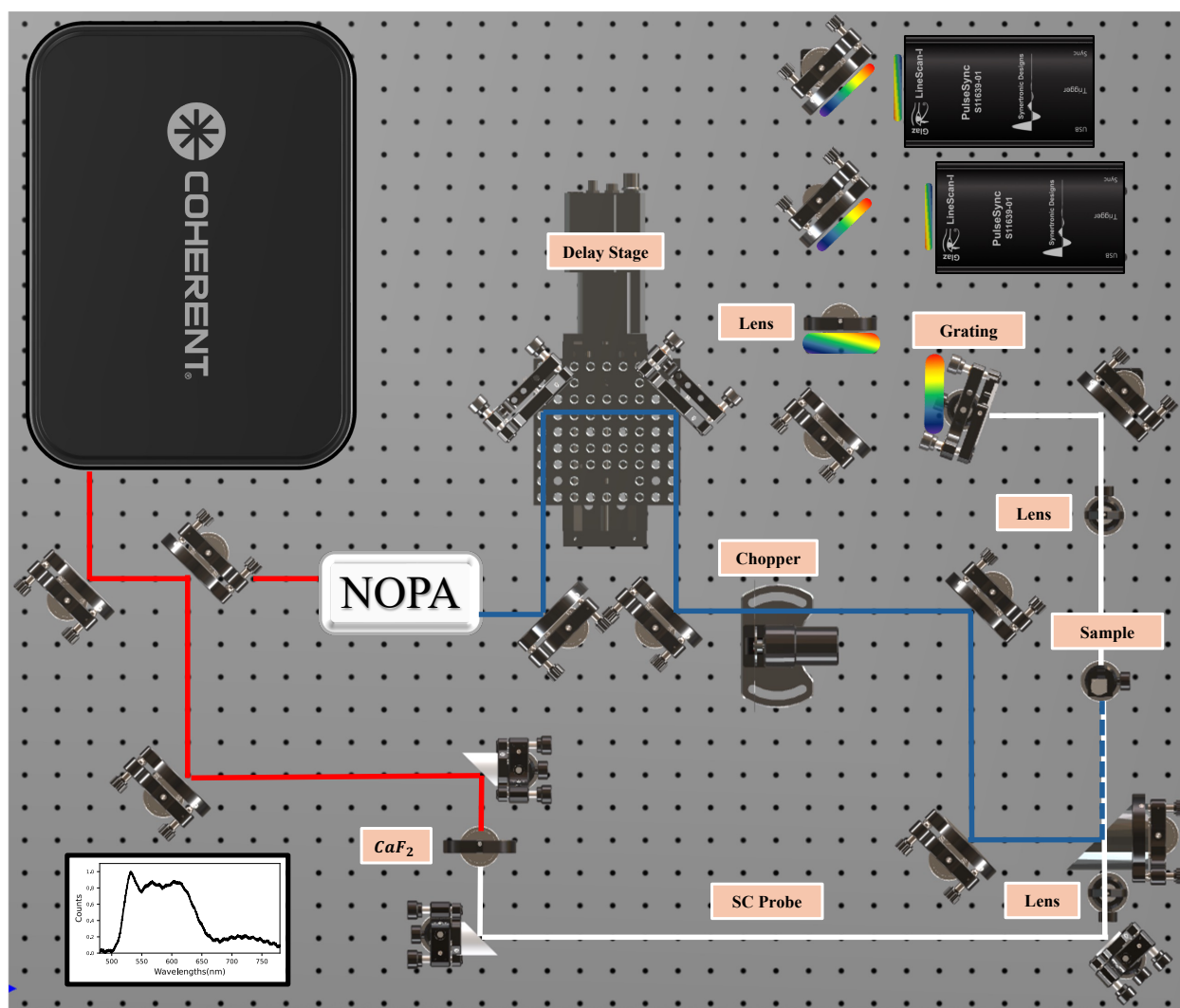


**Figure 5.8: Experimental setup for transient absorption spectroscopy (TAS) with a reference-corrected supercontinuum detection.** Pump pulses were generated in a noncollinear optical parametric amplifier (NOPA) and are spatially overlapped with femtosecond SC probe pulses generated in  $\text{CaF}_2$ . A mechanical chopper running at 2 kHz periodically interrupted the pump beam, allowing sequential acquisition of pump-on and pump-off traces for differential measurements.

electrode. The electrochemical experiments were conducted under an oxygen-free atmosphere in dichloromethane with  $\text{TBAPF}_6$  (0.1 M) as the supporting electrolyte.

## Synthetic procedures of paracyclophane

### Synthesis of Ada-CN (1)

In a 250 mL two-neck round-bottom flask equipped with a condenser, 1,3-Adamantanedicarboxylic acid (20 mmol, 4.48 g) was suspended in  $\text{CH}_3\text{CN}$  (120 mL), followed by dropwise addition of  $\text{H}_2\text{SO}_4$  (22 mL, 98% wt/wt) at room temperature. The reaction mixture was refluxed under con-

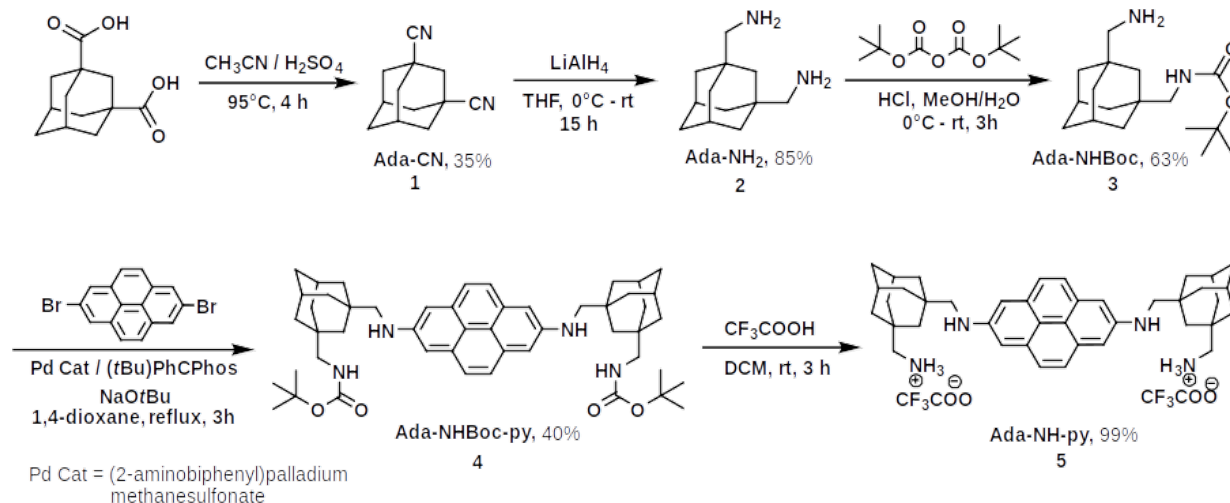


Figure 5.9: **Synthetic route to homoparacyclophanes and monomeric units with linkers.**

stant stirring for 4 h and then cooled to room temperature. The excess of  $\text{CH}_3\text{CN}$  was evaporated under vacuum, and the crude obtained was diluted with water (150 mL) and extracted with  $\text{CH}_2\text{Cl}_2$  (150 mL). The aqueous phase was further extracted with two portions of  $\text{CH}_2\text{Cl}_2$  (200 mL in total). The organic layers were combined and washed with saturated  $\text{NaHCO}_3$  followed by brine. The organic solution was dried over anhydrous  $\text{Na}_2\text{SO}_4$ , and the solvent was evaporated to obtain a solid crude that was purified by automated flash column chromatography (Rf: 0.29, EtOAc: n-heptane 1:4). White powder, 1.35 g, 35% yield.  $^1\text{H}$  NMR (300 MHz,  $\text{CDCl}_3$ )  $\delta$  2.30 (s, 2H), 2.28 - 2.13 (m, 2H), 2.04 (d,  $J = 3.1$  Hz, 8H), 1.73 (s, 2H).  $^{13}\text{C}$  NMR (75 MHz,  $\text{CDCl}_3$ )  $\delta$  123.17, 41.39, 38.49, 34.03, 29.89, 26.41.

### Synthesis of Ada-NH<sub>2</sub> (2)

In a well-dried two-neck round-bottom flask, a suspension of  $\text{LiAlH}_4$  in THF (1.0 M, 25 mL) was added under a nitrogen atmosphere. The mixture was cooled to  $0^\circ\text{C}$  with an ice bath, followed by the slow addition of **1** (466 mg, 2.5 mmol) dissolved in dry THF (20 mL). After 30 minutes, the reaction was slowly warmed up to room temperature and left to react for a further 15 hours under constant stirring. The white suspension formed was exposed to air and then cooled down to  $0^\circ\text{C}$ . After that, it was carefully quenched with the following in this order: water (1 mL, added drop by drop), then  $\text{NaOH}$  (0.6 mL, 15% wt/v), and finally water (3 mL, vapors and gas are released during this process). The mixture was stirred for another 30 minutes, and the inorganic precipitate was filtered off using a glass frit (pore size 4) and washed with THF. The organic phase was dried over anhydrous  $\text{Na}_2\text{SO}_4$  and then evaporated to obtain the product, which appeared as a colorless oil. No further purification was necessary. 0.44 g, 91%. Store the product under inert gas at a temperature below  $4^\circ\text{C}$  due to its instability under ambient conditions.  $^1\text{H}$  NMR (300 MHz,  $\text{CDCl}_3$ )  $\delta$  2.36 (s, 4H), 2.15 - 2.02 (m, 2H), 1.61 (m, 2H), 1.50 - 1.31 (m, 8H), 1.16 (m, 6H).  $^{13}\text{C}$  NMR (75 MHz,  $\text{CDCl}_3$ )  $\delta$  54.84, 42.57, 39.84, 36.96, 34.67, 28.70.

### Synthesis of Ada-NHBoc (3)



In a two-neck round-bottom flask and under a nitrogen atmosphere, 1 equivalent of **2** (1.96 mmol, 0.38 g) was dissolved in MeOH (15 mL). The solution was cooled to 0°C, followed by the slow addition of HCl solution in diethyl ether (1.0 M, 1.96 mL). After that, the mixture was warmed to room temperature and stirred for 30 minutes. Subsequently, water (4 mL) was added and stirred for a further 30 minutes. Following this, a solution of 1.5 equivalents of (Boc)<sub>2</sub>O (2.94 mmol, 0.64 g) in MeOH (20 mL) was added slowly over the course of 1 h, and the resulting solution was stirred for an additional hour. The mixture was concentrated under vacuum, then the residue was diluted with 10 mL of water. Next, the aqueous solution was extracted with two portions of Et<sub>2</sub>O (15 mL each) to remove unreacted amine and/or double-protected amine. After treating the aqueous phase with a solution of NaOH (2 equivalents in 10 mL of water), the monoprotected amine was extracted with CH<sub>2</sub>Cl<sub>2</sub> (3 x 30 mL). The organic phase was washed with brine, dried over anhydrous Na<sub>2</sub>SO<sub>4</sub>, and then evaporated to obtain a colorless oil, requiring no further purification. Oil, 0.40 g 69% yield. <sup>1</sup>H NMR (300 MHz, CDCl<sub>3</sub>) δ 4.57 (s, 1H), 2.84 (d, J = 6.5 Hz, 2H), 2.38 - 2.36 (m, 2H), 2.08 - 2.06 (m, 2H), 1.68 - 1.59 (m, 5H), 1.46 - 1.35 (m, 16H), 1.20 - 1.17 (m, 2H). <sup>13</sup>C NMR (75 MHz, CDCl<sub>3</sub>) δ 156.48, 54.83, 54.69, 52.25, 42.56, 39.86, 39.83, 39.59, 36.95, 36.68, 34.67, 34.63, 28.69, 28.57, 28.52. HR-MS (ESI, positive): m/z calcd. for [C<sub>17</sub>H<sub>30</sub>N<sub>2</sub>O<sub>2</sub>+H]<sup>+</sup> 295.2380; found: 295.2370.

#### Synthesis of Ada-Pyrene semicircle (**4**)

Following a literature procedure<sup>47</sup>, a mixture of 2,7-dibromopyrene (240 mg, 0.68 mmol, 1.00 equiv), Na<sub>2</sub>CO<sub>3</sub> (156 mg, 1.63 mmol, 2.40 equiv), 2-aminobiphenylpalladium methanesulfonate (10.5 mg, 2.0 mol %), (tBu)PhCPhos (5.5 mg, 2.0 mol %) and **3** (440 mg, 1.50 mmol, 2.20 equiv) dissolved in dry 1,4-dioxane (10 mL) was stirred at 100 °C under a positive flow of nitrogen gas. The mixture was monitored by TLC (EtOAc: n-heptane 3:7) and the reaction was stopped when the Pyrene precursor was completely consumed. The reaction was cooled to room temperature and diluted with EtOAc. The solution was filtered through Celite and concentrated in vacuo. The crude was purified by automated flash column chromatography (R<sub>f</sub>: 0.32, EtOAc: n-heptane 3:7). Yellow powder, 220 mg, 41% yield. <sup>1</sup>H NMR (300 MHz, CDCl<sub>3</sub>) δ 7.77 (s, 4H), 7.33 (s, 4H), 4.59 (s, 2H), 3.08 (s, 4H), 2.89 (d, J = 6.5 Hz, 4H), 2.13 (s, 4H), 1.69 - 1.60 (s, 14H), 1.49 - 1.40 (m, 30H). HR-MS (ESI, positive): m/z calcd. for [C<sub>50</sub>H<sub>66</sub>N<sub>4</sub>O<sub>4</sub>+H]<sup>+</sup> 787.5157; found: 787.513



**Cyclic voltammograms (CV) and differential pulse voltammograms (DPV)**

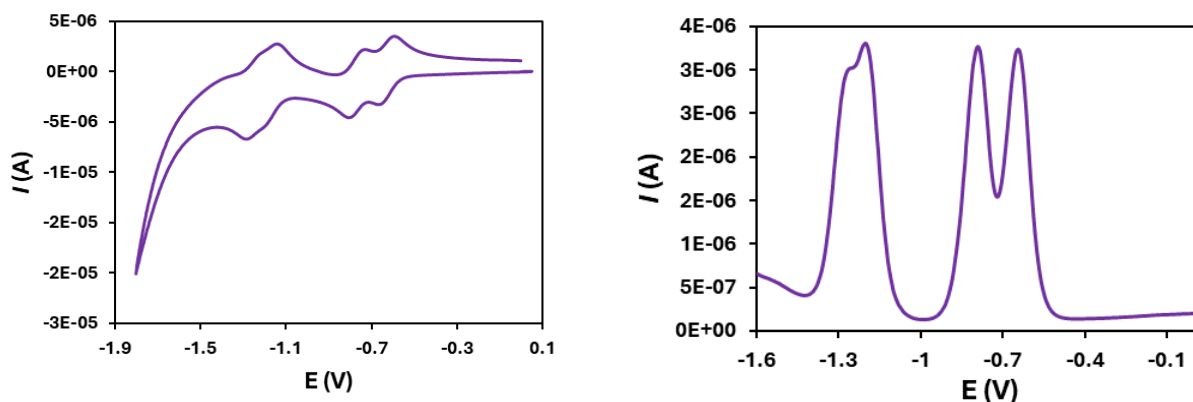


Figure 5.10: Cyclic voltammogram and differential pulse voltammogram of NDI-Ada-NDI.

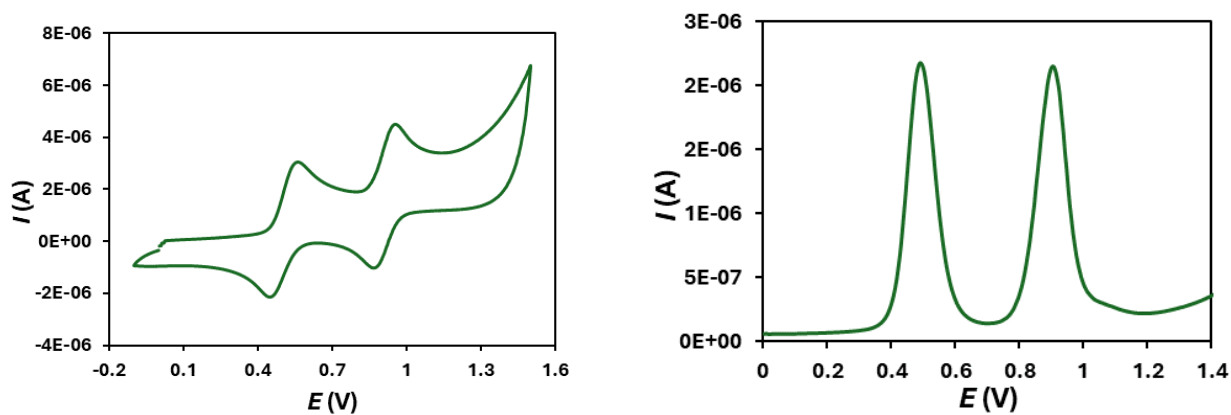


Figure 5.11: Cyclic voltammogram and differential pulse voltammogram of Pyrene-Ada.

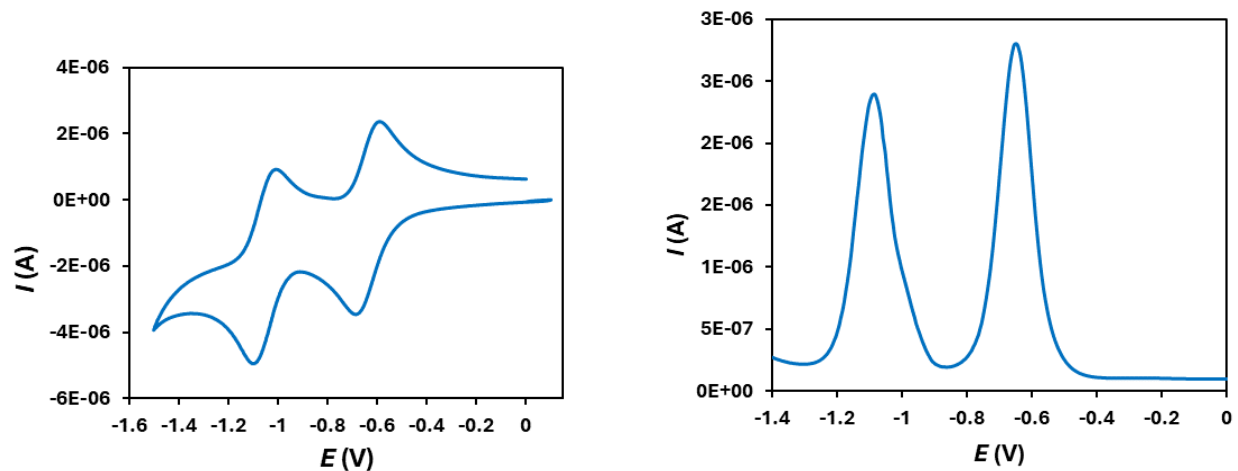


Figure 5.12: Cyclic voltammogram and differential pulse voltammogram of NDI-<sup>t</sup>BuPh.

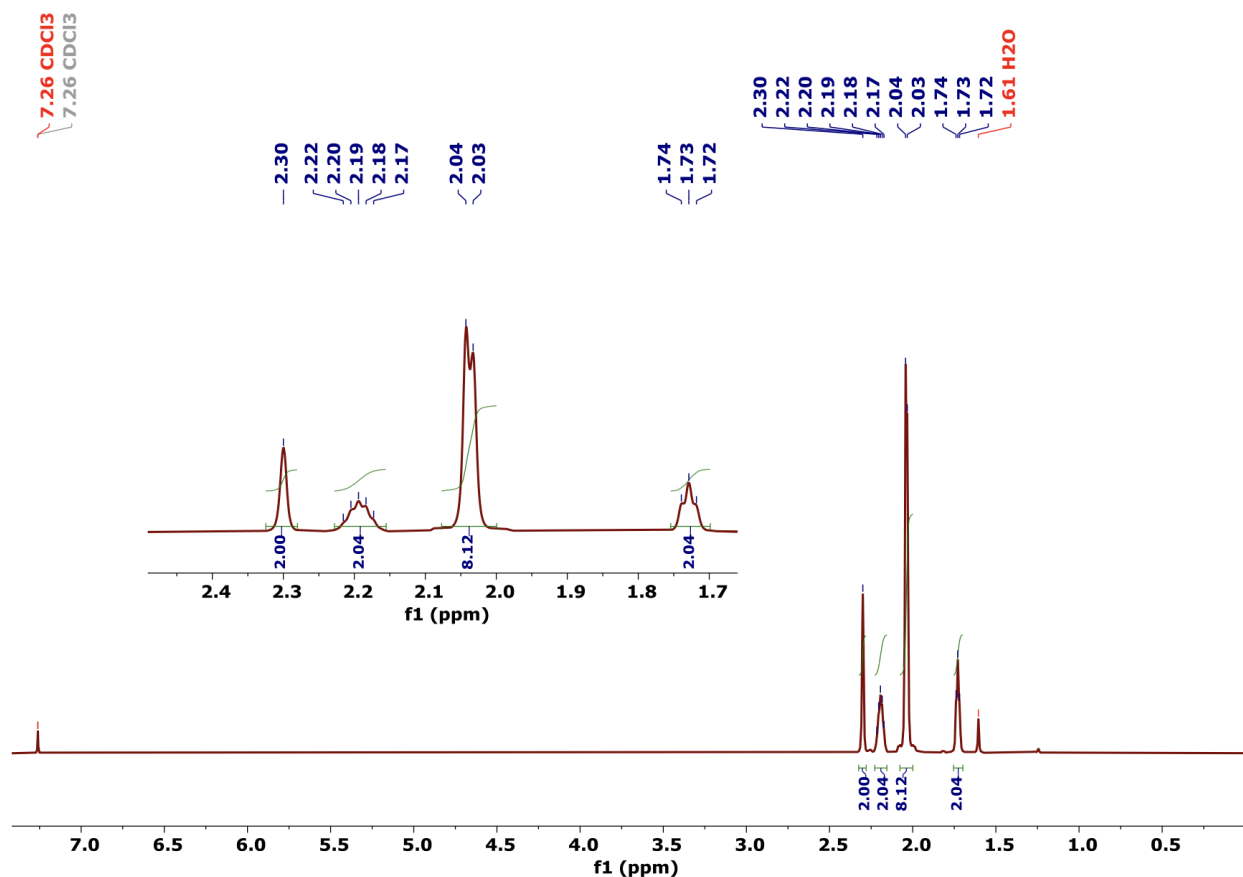


Figure 5.13: HNMR Ada-CN.

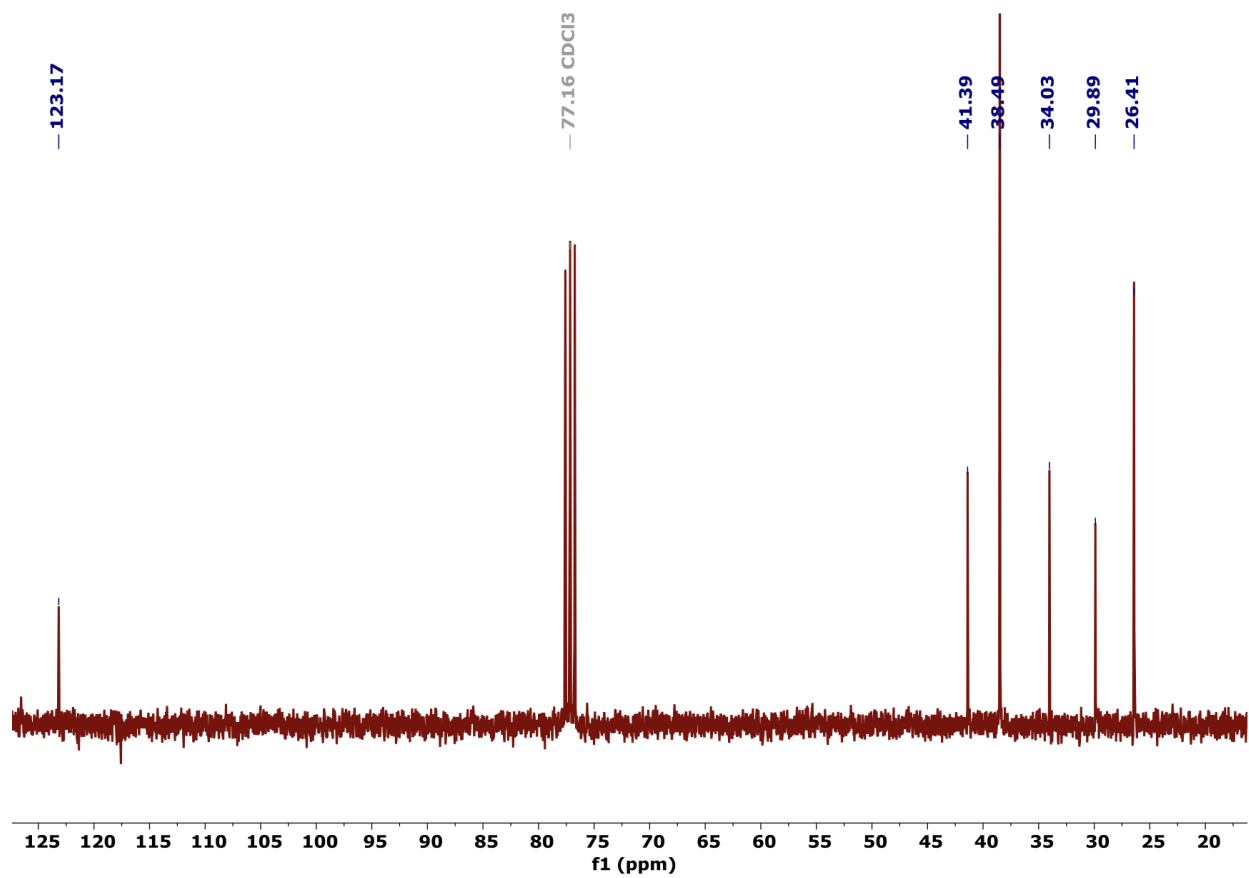


Figure 5.14: **CNMR Ada-CN.**

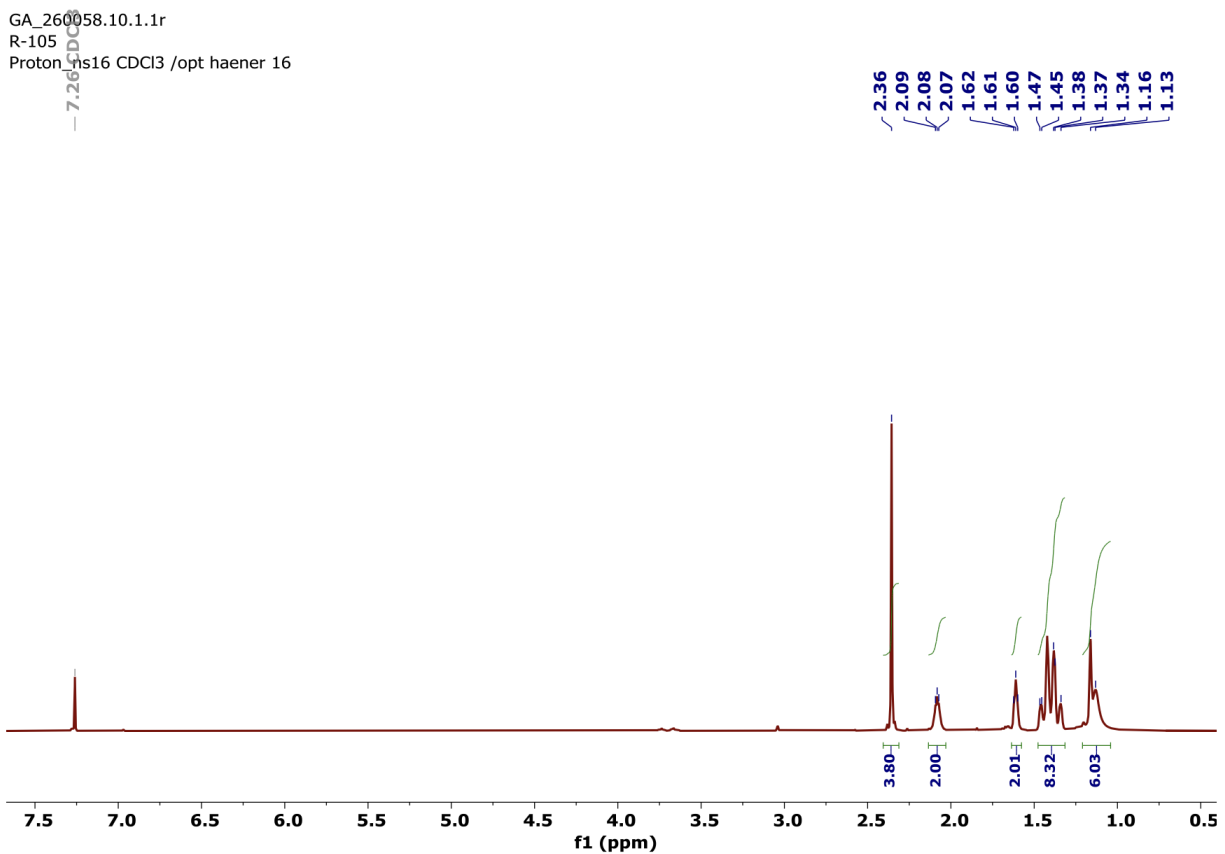


Figure 5.15: **<sup>1</sup>H NMR** Ada-NH<sub>2</sub>.

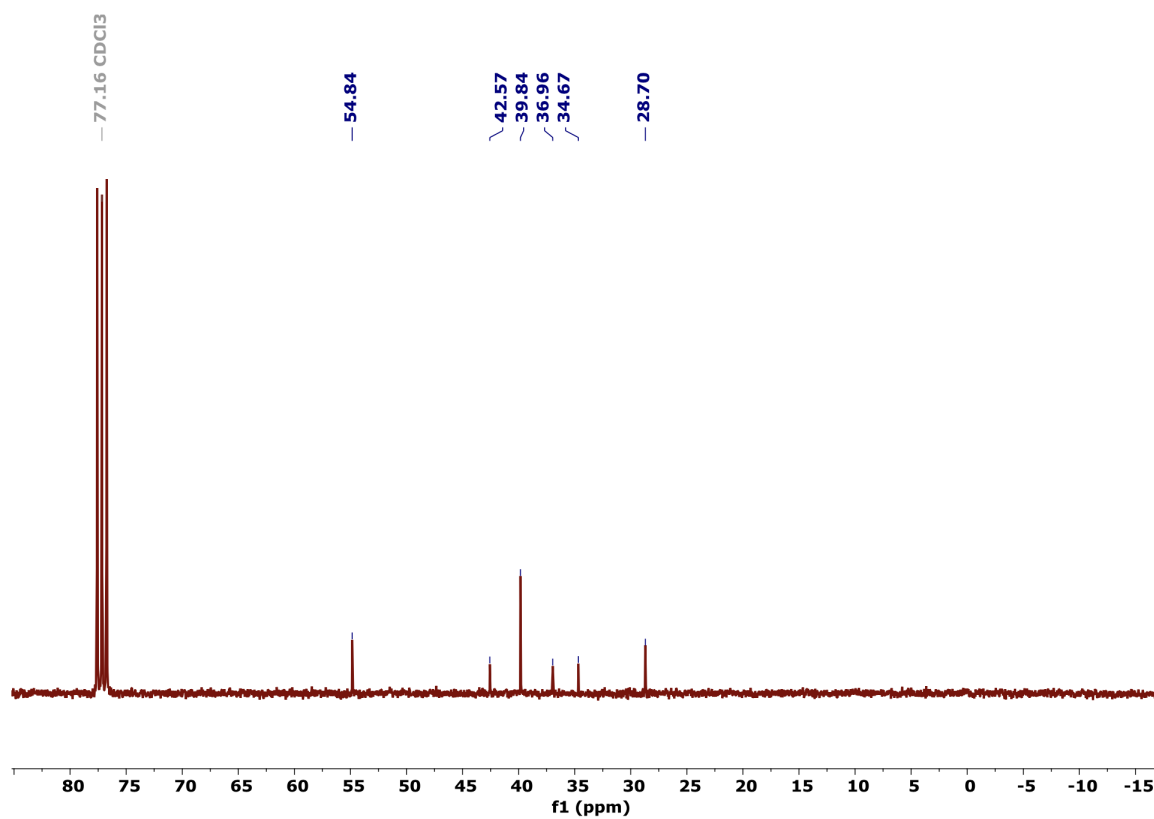


Figure 5.16: **CNMR Ada-NH<sub>2</sub>.**

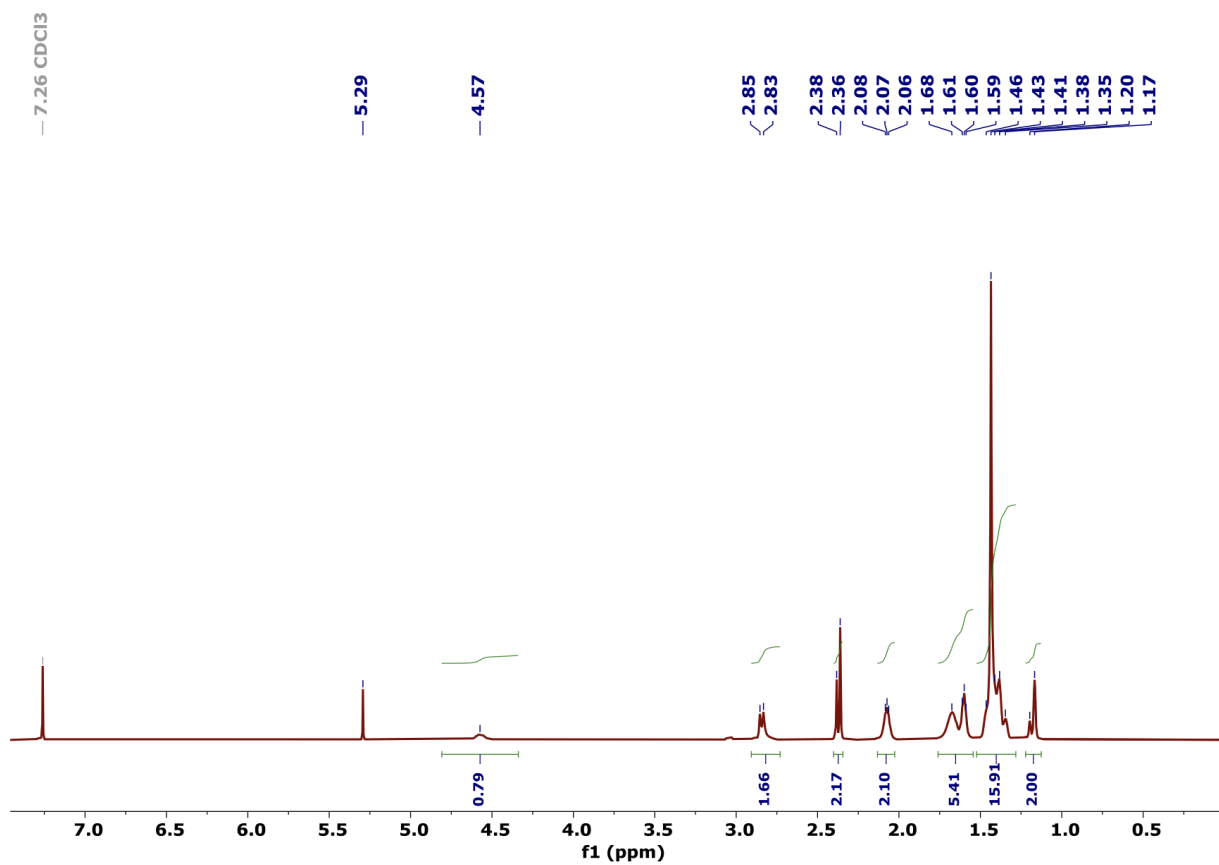


Figure 5.17: **<sup>1</sup>H NMR** Ada-NHBoc.

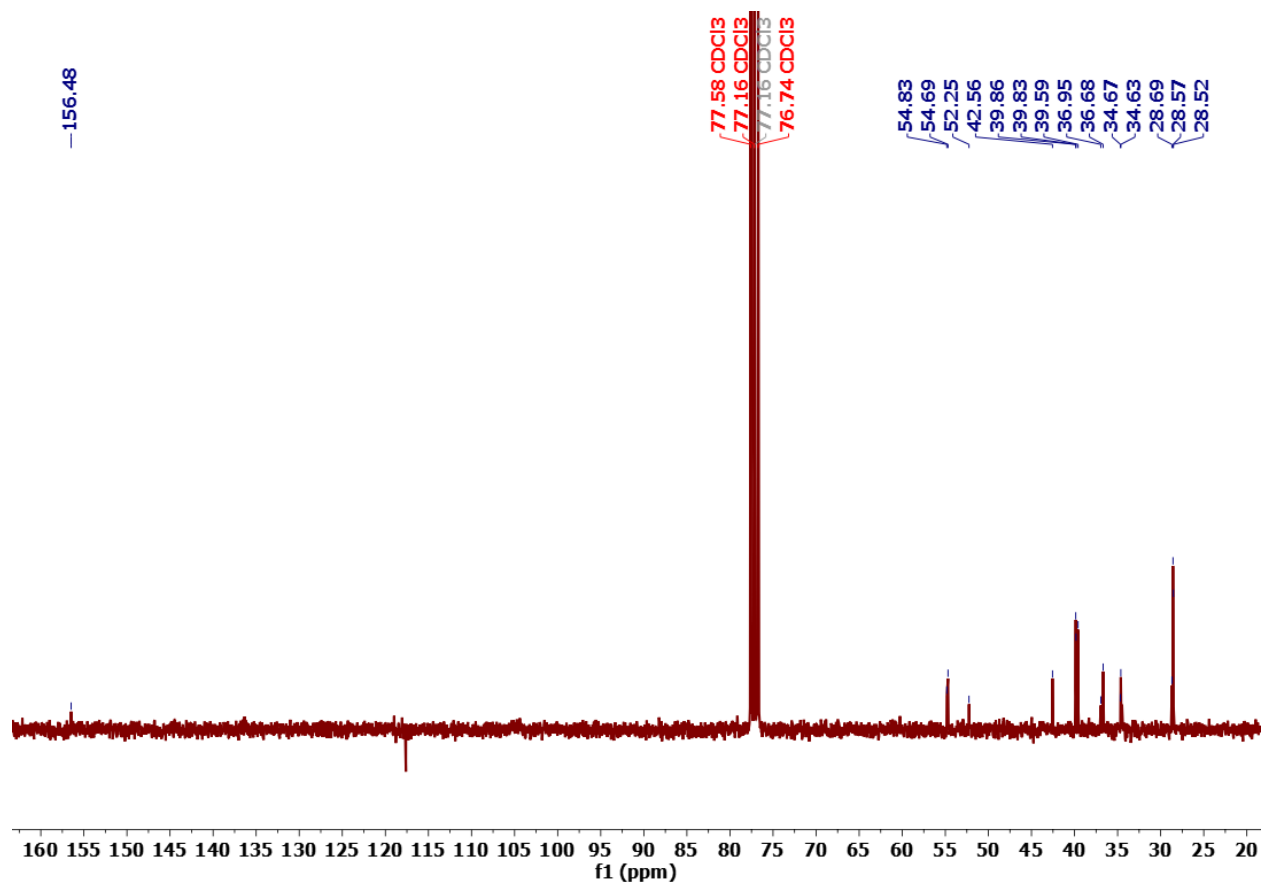


Figure 5.18: <sup>13</sup>C NMR Ada-NHBoc.



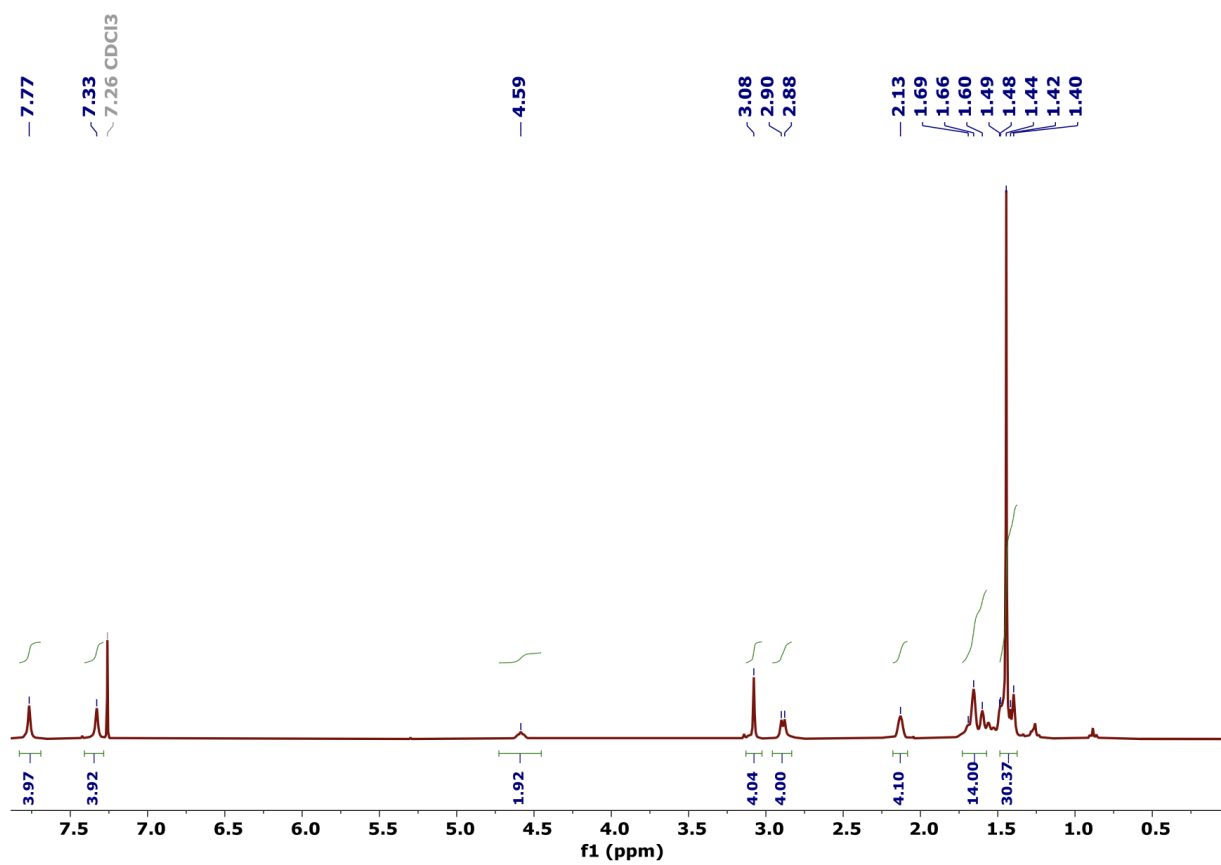


Figure 5.19: <sup>1</sup>H NMR Ada-NHBoc-py semicircle.

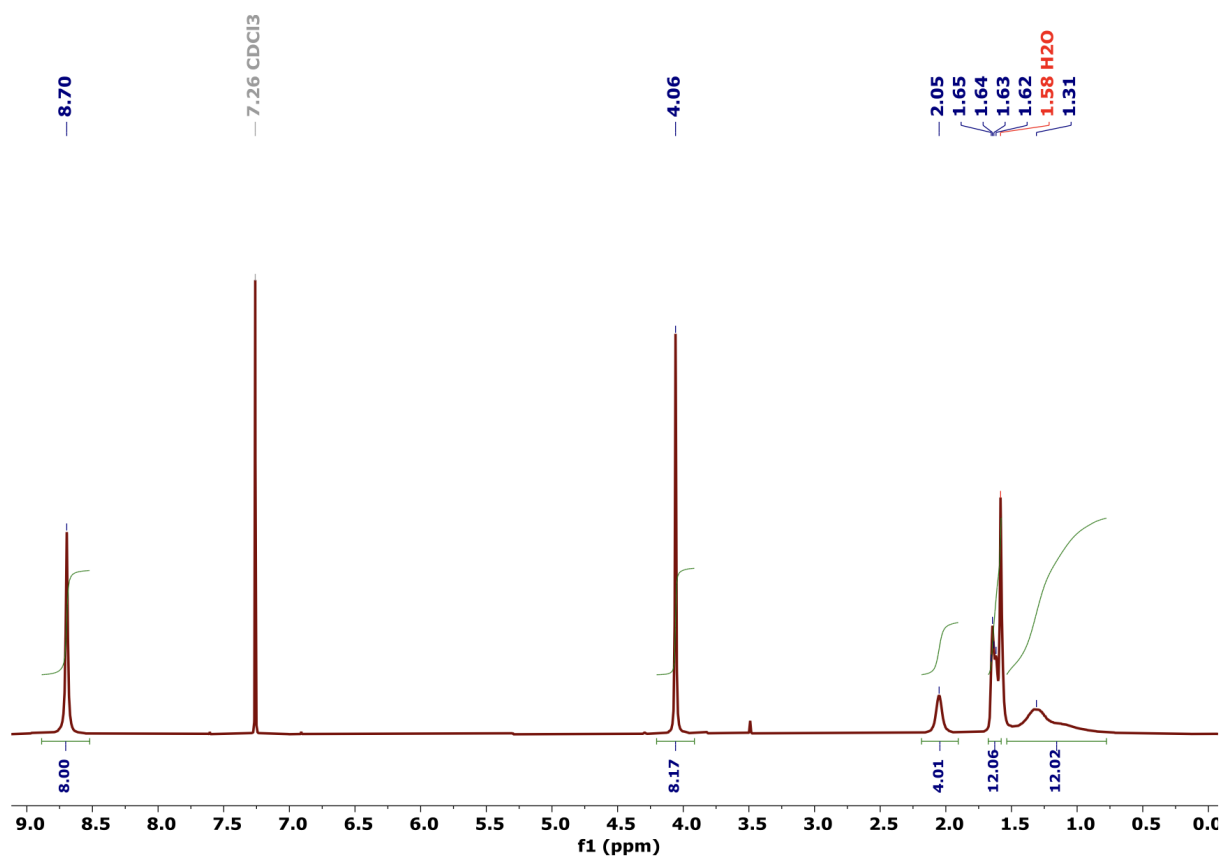


Figure 5.20:  $^1\text{H}$ NMR of NDI-Ada-NDI.

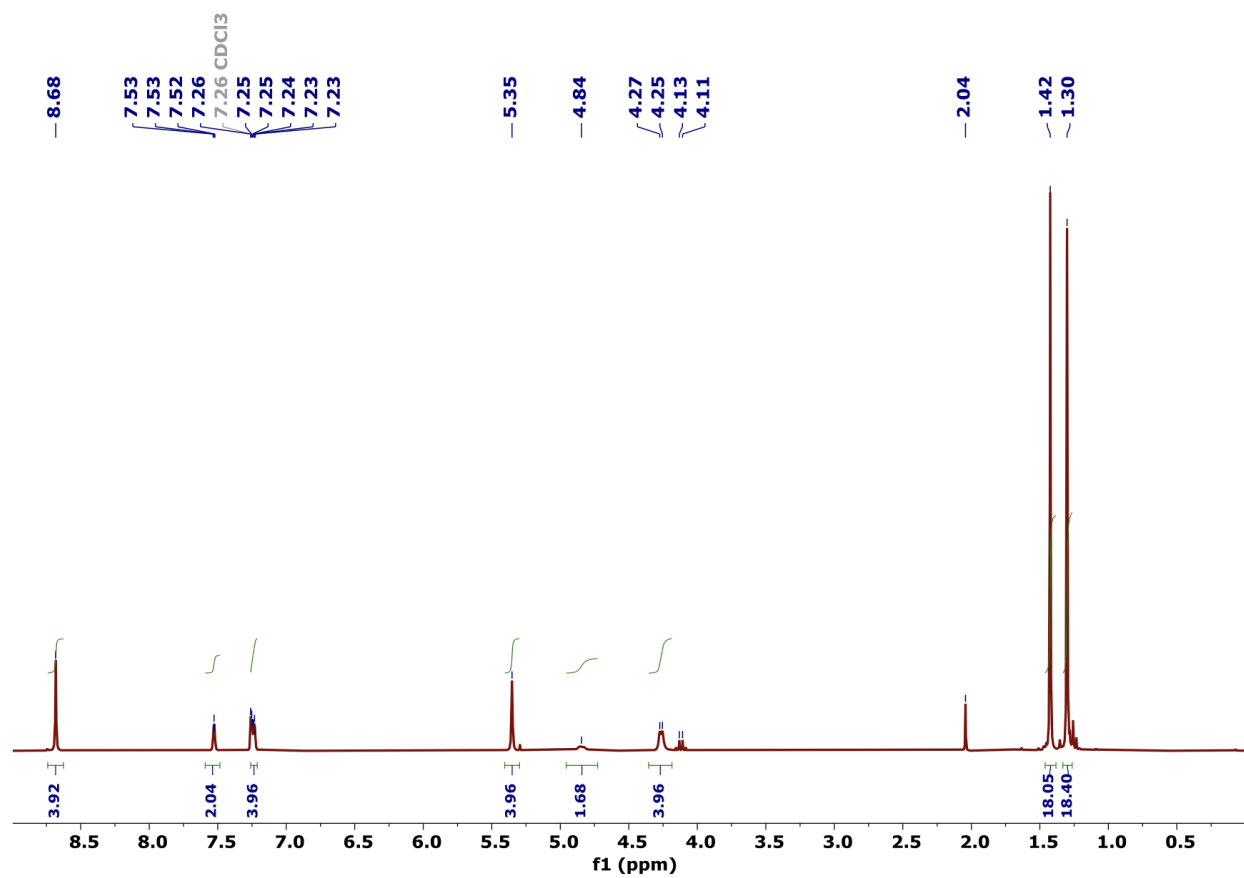


Figure 5.21: <sup>1</sup>H NMR of NDI-*t*BuPh monomer.

## Bibliography

- [1] Dennis A. Dougherty. The cation- $\pi$  interaction. *Accounts of Chemical Research*, 46(4): 885–893, 2013. doi: 10.1021/ar300265y.
- [2] Beatriz Bueschbell, Carlos A. V. Barreto, Ant3nio J. Preto, Anke C. Schiedel, and Irina S. Moreira. A complete assessment of dopamine receptor- ligand interactions through computational methods. *Molecules*, 24(7), 2019.
- [3] J.P. Allen and J.C. Williams. Photosynthetic reaction centers. *FEBS Letters*, 438(1):5–9, 1998. ISSN 0014-5793. doi: [https://doi.org/10.1016/S0014-5793\(98\)01245-9](https://doi.org/10.1016/S0014-5793(98)01245-9).
- [4] Michael R. Wasielewski. Self-assembly strategies for integrating light harvesting and charge separation in artificial photosynthetic systems. *Accounts of Chemical Research*, 42(12):1910–1921, 2009. doi: 10.1021/ar9001735.
- [5] Itaru Osaka and Kazuo Takimiya. Backbone orientation in semiconducting polymers. *Polymer*, 59:A1–A15, 2015. ISSN 0032-3861. doi: <https://doi.org/10.1016/j.polymer.2014.12.066>.
- [6] Antonio Facchetti.  $\pi$ -conjugated polymers for organic electronics and photovoltaic cell applications. *Chemistry of Materials*, 23(3):733–758, 2011. doi: 10.1021/cm102419z.
- [7] Azzaya Khasbaatar, Zhuang Xu, Jong-Hoon Lee, Gonzalo Campillo-Alvarado, Changhyun Hwang, Brandon N. Onusaitis, and Ying Diao. From solution to thin film: Molecular assembly of  $\pi$ -conjugated systems and impact on (opto)electronic properties. *Chemical Reviews*, 123(13):8395–8487, 2023. doi: 10.1021/acs.chemrev.2c00905.
- [8] Chengliang Wang, Huanli Dong, Wenping Hu, Yunqi Liu, and Daoben Zhu. Semiconducting  $\pi$ -conjugated systems in field-effect transistors: A material odyssey of organic electronics. *Chemical Reviews*, 112(4):2208–2267, 2012. doi: 10.1021/cr100380z.
- [9] Yayu Wu, Guilin Zhuang, Shengsheng Cui, Yu Zhou, Jinyi Wang, Qiang Huang, and Pingwu Du. Through-space  $\pi$ -delocalization in a conjugated macrocycle consisting of [2.2]paracyclophane. *Chem. Commun.*, 55:14617–14620, 2019. doi: 10.1039/C9CC06492C.
- [10] Henning Hopf. [2.2]paracyclophanes in polymer chemistry and materials science. *Angewandte Chemie International Edition*, 47(51):9808–9812, 2008. doi: <https://doi.org/10.1002/anie.200800969>.
- [11] Konstantin A. Lyssenko, Mikhail Yu. Antipin, and Dmitry Yu. Antonov. The transannular interaction in [2.2]paracyclophane: Repulsive or attractive? *ChemPhysChem*, 4(8):817–823, 2003. doi: <https://doi.org/10.1002/cphc.200200597>.

- [12] Ksenia Reznikova, Chunwei Hsu, Werner M. Schosser, Almudena Gallego, Katawoura Beltako, Fabian Pauly, Herre S. J. van der Zant, and Marcel Mayor. Substitution pattern controlled quantum interference in [2.2]paracyclophane-based single-molecule junctions. *Journal of the American Chemical Society*, 143(34):13944–13951, 2021. doi: 10.1021/jacs.1c06966.
- [13] Remigiusz Grykien, Beata Luszczynska, Ireneusz Glowacki, Lada Puntus, Irina Pekareva, Konstantin Lyssenko, François Kajzar, Ileana Rau, and Cosmina A. Lazar. Electric field tunable light emitting diodes containing europium  $\beta$ -diketonates with [2.2]paracyclophane moiety. *Optical Materials*, 57:114–119, 2016. ISSN 0925-3467. doi: <https://doi.org/10.1016/j.optmat.2016.04.034>. URL <https://www.sciencedirect.com/science/article/pii/S0925346716302142>.
- [14] YunHui L. Lin, Michael A. Fusella, and Barry P. Rand. The impact of local morphology on organic donor/acceptor charge transfer states. *Advanced Energy Materials*, 8(28):1702816, 2018. doi: <https://doi.org/10.1002/aenm.201702816>.
- [15] Giovanni F. Caramori and Sérgio E. Galembeck. Computational study about through-bond and through-space interactions in [2.2]cyclophanes. *The Journal of Physical Chemistry A*, 111(9):1705–1712, 2007. doi: 10.1021/jp066863h.
- [16] Zhengyan Wang, Yiping Liu, Xiuni Quan, Wenxuan Zhang, Renjun Tan, Hao Gu, Chunqi Sheng, Chunbo Duan, Pengyao Xing, and Jun-Hua Wan. Planar chiral charge-transfer cyclophanes: Convenient synthesis, circularly polarized light-responsive photothermal conversion and supramolecular chiral assembly. *Angewandte Chemie International Edition*, 64(1):e202413295, 2025. doi: <https://doi.org/10.1002/anie.202413295>.
- [17] Lin-Tao Bao, Rui-Hua Zhang, Xiaoyue Yuan, Xueli Wang, Peicong Wu, Xu-Qing Wang, Jinqian Chen, Anwei Zhu, Hai-Bo Yang, and Wei Wang. Rigidly locked pyrene excimers in planar chiral pyrenophanes for intense and stable circularly polarized photoluminescence and electrochemiluminescence. *Angewandte Chemie International Edition*, 64(15):e202500472, 2025. doi: <https://doi.org/10.1002/anie.202500472>.
- [18] Hsin-Chieh Lin and Bih-Yaw Jin. Three-dimensional through-space/through-bond delocalization in cyclophane systems: A molecule-in-molecule approach. *The Journal of Physical Chemistry A*, 112(13):2948–2954, 2008. doi: 10.1021/jp0763127.
- [19] Andreas Dreuw and Martin Head-Gordon. Failure of time-dependent density functional theory for long-range charge-transfer excited states: The zincbacteriochlorin-bacteriochlorin and bacteriochlorophyll-spheroidene complexes. *Journal of the American Chemical Society*, 126(12):4007–4016, 2004. doi: 10.1021/ja039556n.
- [20] Mark E. Casida, Christine Jamorski, Kim C. Casida, and Dennis R. Salahub. Molecular excitation energies to high-lying bound states from time-dependent density-functional response theory: Characterization and correction of the time-dependent local density approximation ionization threshold. *The Journal of Chemical Physics*, 108(11):4439–4449, 03 1998. doi: 10.1063/1.475855.

- [21] Vladislav Sláma, Lorenzo Cupellini, Vincenzo Mascoli, Nicoletta Liguori, Roberta Croce, and Benedetta Mennucci. Origin of low-lying red states in the lhca4 light-harvesting complex of photosystem i. *The Journal of Physical Chemistry Letters*, 14(37):8345–8352, 2023. doi: 10.1021/acs.jpclett.3c02091.
- [22] R. Ahlrichs, M. Bär, M. Häser, H. Horn, and C. Kölmel. Electronic structure calculations on workstation computers: The program system turbomole. *Chem. Phys. Lett.*, 163(3):165–169, 1989.
- [23] M. J. Frisch, G. W. Trucks, H. B. Schlegel, G. E. Scuseria, M. A. Robb, J. R. Cheeseman, G. Scalmani, V. Barone, G. A. Petersson, H. Nakatsuji, X. Li, M. Caricato, A. V. Marenich, J. Bloino, B. G. Janesko, R. Gomperts, B. Mennucci, H. P. Hratchian, J. V. Ortiz, A. F. Izmaylov, J. L. Sonnenberg, D. Williams-Young, F. Ding, F. Lipparini, F. Egidi, J. Goings, B. Peng, A. Petrone, T. Henderson, D. Ranasinghe, V. G. Zakrzewski, J. Gao, N. Rega, G. Zheng, W. Liang, M. Hada, M. Ehara, K. Toyota, R. Fukuda, J. Hasegawa, M. Ishida, T. Nakajima, Y. Honda, O. Kitao, H. Nakai, T. Vreven, K. Throssell, J. A. Montgomery, Jr., J. E. Peralta, F. Ogliaro, M. J. Bearpark, J. J. Heyd, E. N. Brothers, K. N. Kudin, V. N. Staroverov, T. A. Keith, R. Kobayashi, J. Normand, K. Raghavachari, A. P. Rendell, J. C. Burant, S. S. Iyengar, J. Tomasi, M. Cossi, J. M. Millam, M. Klene, C. Adamo, R. Cammi, J. W. Ochterski, R. L. Martin, K. Morokuma, O. Farkas, J. B. Foresman, and D. J. Fox. Gaussian~16 Revision A.03, 2016. Gaussian Inc. Wallingford CT.
- [24] Edoardo Cignoni, Vladislav Slama, Lorenzo Cupellini, and Benedetta Mennucci. The atomistic modeling of light-harvesting complexes from the physical models to the computational protocol. *The Journal of Chemical Physics*, 156(12):120901, 03 2022. ISSN 0021-9606. doi: 10.1063/5.0086275.
- [25] Yilei Wu, Marco Frasconi, Daniel M. Gardner, Paul R. McGonigal, Severin T. Schneebeli, Michael R. Wasielewski, and J. Fraser Stoddart. Electron delocalization in a rigid cofacial naphthalene-1,8:4,5-bis(dicarboximide) dimer. *Angewandte Chemie International Edition*, 53(36):9476–9481, 2014. doi: <https://doi.org/10.1002/anie.201403816>.
- [26] Fritz Duschinsky. Zur deutung der elektronenspektren mehratomiger moleküle. *Acta physicochimica URSS*, 7:551–566, 1937.
- [27] Fabrizio Santoro, Alessandro Lami, Roberto Improta, Julien Bloino, and Vincenzo Barone. Effective method for the computation of optical spectra of large molecules at finite temperature including the duschinsky and herzbeg–teller effect: The qx band of porphyrin as a case study. *The Journal of Chemical Physics*, 128(22):224311, 06 2008. ISSN 0021-9606. doi: 10.1063/1.2929846.
- [28] G. Olbrich and H. Kupka. The duschinsky effect and optical spectra. *Zeitschrift für Naturforschung A*, 38(8):937–946, 1983. doi: doi:10.1515/zna-1983-0819. URL <https://doi.org/10.1515/zna-1983-0819>.

- [29] Takahito Nakanishi, Ken ichi Mizuno, Atsuo Matsui, and Hitoshi Nishimura. Reabsorption of excitonic luminescence in pyrene crystals. *Journal of Luminescence*, 47(6):303–308, 1991. ISSN 0022-2313. doi: [https://doi.org/10.1016/0022-2313\(91\)90054-Y](https://doi.org/10.1016/0022-2313(91)90054-Y).
- [30] Andrew G. Crawford, Austin D. Dwyer, Zhiqiang Liu, Andreas Steffen, Andrew Beeby, Lars-Olof Pålsson, David J. Tozer, and Todd B. Marder. Experimental and theoretical studies of the photophysical properties of 2- and 2,7-functionalized pyrene derivatives. *Journal of the American Chemical Society*, 133(34):13349–13362, 2011. doi: 10.1021/ja2006862.
- [31] Julia Merz, Julian Fink, Alexandra Friedrich, Ivo Krummenacher, Hamad H. Al Mamari, Sabine Lorenzen, Martin Haehnel, Antonius Eichhorn, Michael Moos, Marco Holzapfel, Holger Braunschweig, Christoph Lambert, Andreas Steffen, Lei Ji, and Todd B. Marder. Pyrene molecular orbital shuffle—controlling excited state and redox properties by changing the nature of the frontier orbitals. *Chemistry – A European Journal*, 23(53):13164–13180, 2017. doi: <https://doi.org/10.1002/chem.201702594>.
- [32] Ryohei Kurata, Kazuyoshi Tanaka, and Akihiro Ito. Isolation and characterization of persistent radical cation and dication of 2,7-bis(dianisylamino)pyrene. *The Journal of Organic Chemistry*, 81(1):137–145, 2016. doi: 10.1021/acs.joc.5b02425.
- [33] Dipanwita Jana and Sankar Jana. Donor–pyrene–acceptor distance-dependent intramolecular charge-transfer process: A state-specific solvation preferred to the linear-response approach. *ACS Omega*, 5(17):9944–9956, 2020. doi: 10.1021/acsomega.0c00265.
- [34] Sun-Sun Li, Ke-Jian Jiang, Chun-Chun Yu, Jin-Hua Huang, Lian-Min Yang, and Yan-Lin Song. A 2,7-pyrene-based dye for solar cell application. *New J. Chem.*, 38:4404–4408, 2014. doi: 10.1039/C4NJ00421C.
- [35] Ryohei Kurata, Akihiro Ito, Masayuki Gon, Kazuo Tanaka, and Yoshiki Chujo. Diarylamino- and diarylboryl-substituted donor–acceptor pyrene derivatives: Influence of substitution pattern on their photophysical properties. *The Journal of Organic Chemistry*, 82(10):5111–5121, 2017. doi: 10.1021/acs.joc.7b00315.
- [36] Souloke Sen and Lucas Visscher. Towards the description of charge transfer states in solubilised lhci using subsystem dft. *Photosynthesis Research*, 156:39–57, 2023. doi: 10.1007/s11120-022-00950-7.
- [37] Julia Adolphs and Thomas Renger. How proteins trigger excitation energy transfer in the fmo complex of green sulfur bacteria. *Biophysical Journal*, 91(8):2778–2797, 2006. ISSN 0006-3495. doi: <https://doi.org/10.1529/biophysj.105.079483>. URL <https://www.sciencedirect.com/science/article/pii/S0006349506719932>.
- [38] Julia Adolphs, Frank Müh, Mohamed El-Amine Madjet, and Thomas Renger. Calculation of pigment transition energies in the fmo protein. *Photosynthesis Research*, 95(8):197–209, 2008. ISSN 1573-5079. doi: 10.1007/s11120-007-9248-z.



- [39] Elizabeth Jurrus, Dave Engel, Keith Star, Kyle Monson, Juan Brandi, Lisa E. Felberg, David H. Brookes, Leighton Wilson, Jiahui Chen, Karina Liles, Minju Chun, Peter Li, David W. Gohara, Todd Dolinsky, Robert Konecny, David R. Koes, Jens Erik Nielsen, Teresa Head-Gordon, Weihua Geng, Robert Krasny, Guo-Wei Wei, Michael J. Holst, J. Andrew McCammon, and Nathan A. Baker. Improvements to the apbs biomolecular solvation software suite. *Protein Science*, 27(1):112–128, 2018. doi: <https://doi.org/10.1002/pro.3280>.
- [40] M. Nottoli, S. Jurinovich, L. Cupellini, T. A. Gardiner, R. Cogdell, and B. Mennucci. The role of charge-transfer states in the spectral tuning of antenna complexes of purple bacteria. *Photosynthesis Research*, 137(2):215–226, 2018. doi: 10.1007/s11120-018-0492-1.
- [41] Oleksandr Yushchenko, Giuseppe Licari, Sandra Mosquera-Vazquez, Naomi Sakai, Stefan Matile, and Eric Vauthey. Ultrafast intersystem-crossing dynamics and breakdown of the kasha–vavilov’s rule of naphthalenediimides. *The Journal of Physical Chemistry Letters*, 6(11):2096–2100, 2015. doi: 10.1021/acs.jpcllett.5b00882.
- [42] Yilei Wu, Siva Krishna Mohan Nalluri, Ryan M. Young, Matthew D. Krzyaniak, Eric A. Margulies, J. Fraser Stoddart, and Michael R. Wasielewski. Charge and spin transport in an organic molecular square. *Angewandte Chemie International Edition*, 54(41):11971–11977, 2015. doi: <https://doi.org/10.1002/anie.201504576>.
- [43] Sudhir Kumar Keshri, Atsuro Takai, Tomoya Ishizuka, Takahiko Kojima, and Masayuki Takeuchi. Conformational dynamics of monomer- versus dimer-like features in a naphthalenediimide-based conjugated cyclophane. *Angewandte Chemie International Edition*, 59(13):5254–5258, 2020. doi: <https://doi.org/10.1002/anie.201914414>.
- [44] Sudhir Kumar Keshri, Tomoya Ishizuka, Takahiko Kojima, Yoshitaka Matsushita, and Masayuki Takeuchi. Long-range order in supramolecular  $\pi$  assemblies in discrete multi-decker naphthalenediimides. *Journal of the American Chemical Society*, 143(8):3238–3244, 2021. doi: 10.1021/jacs.0c13389.
- [45] Francisco José Avila Ferrer and Fabrizio Santoro. Comparison of vertical and adiabatic harmonic approaches for the calculation of the vibrational structure of electronic spectra. *Phys. Chem. Chem. Phys.*, 14:13549–13563, 2012. doi: 10.1039/C2CP41169E.
- [46] Mi Kyung Lee, Pengfei Huo, and David F. Coker. Semiclassical path integral dynamics: Photosynthetic energy transfer with realistic environment interactions. *Annual Review of Physical Chemistry*, 67(Volume 67, 2016):639–668, 2016. doi: <https://doi.org/10.1146/annurev-physchem-040215-112252>.
- [47] Paula Ruiz-Castillo, Donna G. Blackmond, and Stephen L. Buchwald. Rational ligand design for the arylation of hindered primary amines guided by reaction progress kinetic analysis. *Journal of the American Chemical Society*, 137(8):3085–3092, 2015. doi: 10.1021/ja512903g.

## Chapter 6

# Tuning Charge Transfer in Novel NDI-Pyrene Paracyclophanes: The Role of Interchromophore Distance and Linker Structure

Camila Negrete-Vergara<sup>1</sup>, Elnaz Zyaee<sup>2</sup>, Vladislav Slama<sup>3</sup>, Hans-Martin Frey<sup>2</sup>, Ursula Röthlisberger<sup>3</sup>, Thomas Feurer<sup>2</sup>, Shi-Xia Liu<sup>1</sup>

<sup>1</sup> Department of chemistry, biochemistry and pharmaceutical sciences, University of Bern

<sup>2</sup> Institute of Applied Physics, University of Bern, 3012 Bern, Switzerland

<sup>3</sup> Laboratory of Computational Chemistry and Biochemistry, École Polytechnique Fédérale de Lausanne (EPFL)

[This work is in preparation for submission.](#)

---

### Abstract

Paracyclophanes (PCPs) offer a unique platform for studying through-space interactions in donor-acceptor (D-A) systems, crucial for molecular electronics. Here, we report the synthesis, structural characterization, and comprehensive photophysical investigation of novel PCPs comprising Pyrene (Py) donors and naphthalene diimide (NDI) acceptors, covalently linked by phenyl (Ph), tert-butylphenyl (<sup>t</sup>BuPh), or adamantyl (Ada) bridges. Steady state absorption spectroscopy reveals characteristic bands of the NDI and Py units, along with new, broad absorption features attributed to through-space charge transfer transitions, whose intensity correlates strongly with linker rigidity and interchromophore distance. A robust theoretical protocol combining time-dependent density functional theory (TD-DFT) and approximate coupled-cluster (CC2) methods with solvent corrections quantitatively reproduces the optical spectra and elucidates the nature of the low-lying charge transfer states. Femtosecond transient absorption spectroscopy across multiple excitation wavelengths reveals complex, multi-step excited state dynamics, characterized by ultrafast formation of an intramolecular charge transfer state. This work demonstrates the effective tuning of charge transfer properties via linker design in NDI-Py PCPs and provides detailed insight into their dynamics, crucial for the development of PCP-based molecular electronic components and informing future strategies for ultrafast state control.

---

## 6.1 Introduction

Understanding charge transfer (CT) and charge delocalization phenomena is indispensable for manufacturing molecular devices. Much effort has been devoted to preparing a variety of donor-acceptor (D-A) molecules as well as to intensively investigating their electronic properties<sup>1,2,3,4,5,6,7</sup>. A strategy to enhance electronic interaction between D and A chromophores is to covalently connect them through  $\pi$ -conjugated bridges, resulting in large  $\pi$ -extended skeletons that often cause solubility and aggregation issues<sup>2</sup>. Recently, single cocrystals featuring organic donor-acceptor pairs have become valuable tools for investigating the complexities of CT exciton dynamics within solid materials<sup>8</sup>. However, regulating the spatial arrangement of D and A moieties is challenging, and the inherent brittleness of crystals complicates the fabrication of optoelectronic devices. One effective method for precisely controlling the spatial arrangement of D and A fragments is to covalently link them with flexible spacers. This allows the D and A moieties to be in close proximity and interact through non-covalent bonds. This interaction can be demonstrated by through-space CT dynamics, which are primarily influenced by the intermolecular delocalization of neighboring  $\pi$ -electrons in stacked aromatic D and A units<sup>9,10</sup>. This approach also offers advantages over the through-bond interactions since it can provide a conformational locking effect, without compromising the solubility of the system.

The discovery of paracyclophane (PCP) and its derivatives marked the onset of the non-covalent interaction strategy for designing organic electronic materials<sup>11,12,13</sup>. Naphthalene diimide (NDI) derivatives have been chosen as building blocks to construct different self-assembled CT systems due to their electron-deficient properties, tendency to stack through  $\pi$ -interactions, and their n-type semiconducting behavior<sup>14,15,16,17,18,19,20,21,22</sup>. Consequently, NDI cyclophanes have been successfully synthesized and studied as representative models for supramolecular host and complexation structures<sup>23</sup>, sublimable compounds for Ultra High Vacuum STM investigations<sup>24,25,26</sup>, and excimer fluorescence research<sup>27</sup>. Incorporation of D and A moieties into a PCP skeleton can facilitate directional CT, leading to polar electronic displacement across the barrier, producing long-lived charge separated states upon photoexcitation<sup>10</sup>. However, investigating through-space CT dynamics remains a significant challenge due to the limited availability of asymmetric PCP systems, which is a result of the inherent complexity of tedious asymmetric synthesis, including multiple-step reactions, sophisticated purification, and poor yields. To the best of our knowledge, only one paper published very recently provides insight into the electronic couplings between NDI and a series of electron donors such as carbazole, benzodithiophene, and dihydroindole<sup>9</sup>. This study demonstrated that the CT interactions in the enforced D/A  $\pi$ -stacks lead to efficient photothermal conversion because of the active non-radiative decay processes, as confirmed by femtosecond transient absorption measurements. It is also well known that NDI and Pyrene have been used to create a range of CT functional materials, including supramolecular polymers<sup>28,29,30</sup>, single co-crystals and complexes<sup>8,31,32</sup>, and PCPs<sup>33</sup>. It is worth noting that only one example of PCPs consisting of these two chromophores fixed by methylene chains has been published so far, showing a broad absorption with a maximum of 520 nm ( $\epsilon = 1010 \text{ cm}^{-1}$  in  $\text{CHCl}_3$ ) due to a through-space CT caused by their face-to-face orientations with a separation of  $3.5 \text{ \AA}$ <sup>33</sup>. However, a comprehensive study of

the CT dynamics has not yet been conducted.

To tackle these challenges, we report herein the synthesis of new PCPs consisting of Pyrene (Py) and NDI chromophores, linked by different bridges such as phenyl and adamantane molecules, as shown in Figure 6.1. The optical and electrochemical properties of these PCPs, along with their reference compounds, were investigated in detail. Interestingly, the effect of the linker and the interchromophore distance plays a crucial role in modulating the CT absorption band. All PCPs exhibit a broad absorption band that peaks between 500 and 600 nm, which is attributed to a through-space charge transfer (TSCT) from the Py donor to the NDI acceptor. Cyclic voltammetry measurements indicate that the NDI moiety of all systems undergoes two reversible reduction processes. In contrast, the electrochemical behavior of the Py moiety varies depending on its chemical substituents. The observed photophysical and redox properties were further supported by extensive theoretical calculations, which provided deeper insight and quantitative description of its electronic structure, origin of the observed changes in the optical spectra and exciton relaxation. Furthermore, time-resolved transient absorption spectroscopy at different excitation wavelengths revealed complex dynamics.

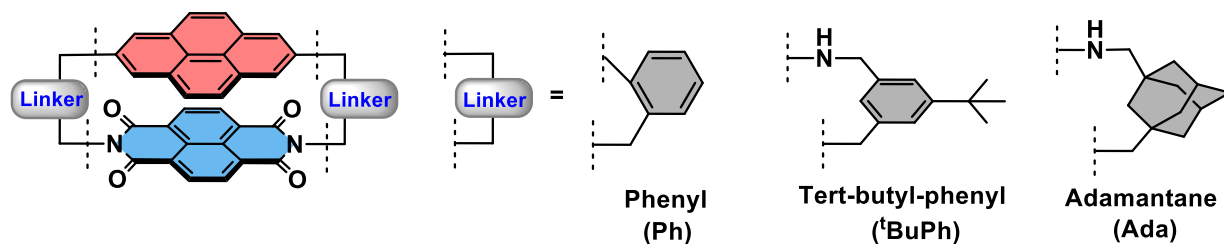


Figure 6.1: Schematic representation of the different PCP structures investigated in this work.

## 6.2 Results and Discussion

### 6.2.1 Synthesis and Characterization

The cyclization of asymmetric paracyclophanes was achieved via the condensation of naphthalenetracarboxylic dianhydride (NTDA) with the corresponding 2,7-substituted phenyl or adamantyl amine monomers in the presence of triethylamine (Et<sub>3</sub>N) under dilute conditions (~1 mM), as illustrated in Figure 6.2. The inherently low yields (10-17%) of these reactions are primarily attributed to the unavoidable formation of oligomeric by-products. The 2,7-substituted Pyrene building blocks were synthesized through palladium-catalyzed cross-coupling reactions: C-N Buchwald coupling for **Ada-Py** and <sup>t</sup>**BuPh-Py**, and Suzuki-Miyaura coupling for the **Ph-Py** moiety. All PCPs underwent extensive purification, including column chromatography, gel permeation chromatography, and, in some cases, high-temperature vacuum treatment to eliminate trace impurities. The structures of the resulting cyclophanes and reference compounds were unambiguously confirmed by <sup>1</sup>H and <sup>13</sup>C NMR spectroscopy, as well as high-resolution mass spectrometry. Notably, as shown in Figure 6.3, <sup>1</sup>H NMR measurements revealed that the aromatic protons of the NDI and

Py units in the D-A PCPs are significantly upfield shifted compared to their relative monomers, as shown in Figure 6.3. For example, the  $^1\text{H}$  NMR signals of the NDI moiety in **NDI- $^t\text{BuPh-Py}$**  PCP (8.06 ppm) were significantly upfield shifted compared to those of the **NDI-Ref** (8.68 ppm). Similarly, the protons of the Py monomer (7.79 and 7.38 ppm) were also significantly shifted compared to the D-A PCP (7.29 and 7.02 ppm). These findings indicate strong  $\pi$ - $\pi$  interactions, even in solution. Additionally, NDI and Py protons in all D-A PCPs appear as single peaks, revealing the symmetric nature of these systems.

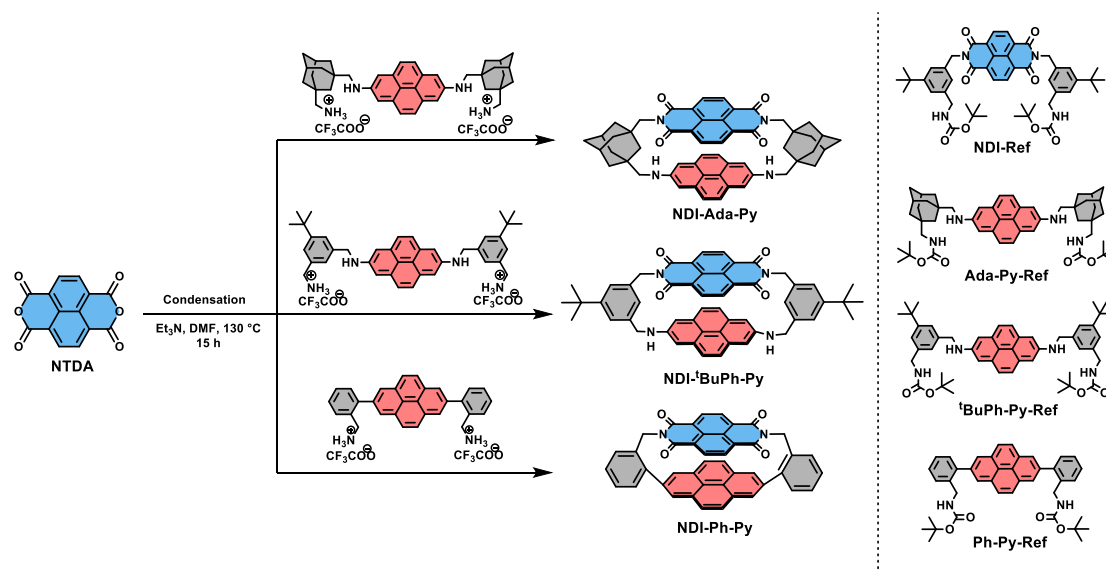


Figure 6.2: Synthetic routes to **NDI-Ada-Py**, **NDI- $^t\text{BuPh-Py}$** , and **NDI-Ph-Py** cyclophanes and structures of reference compounds.

## 6.2.2 Structure of the Paracyclophanes

The geometries of paracyclophanes were optimized using DFT with solvent effects modeled via the polarizable continuum model (PCM) approach in  $\text{CH}_2\text{Cl}_2$ . Structural features depend on the linker type and on the lengths of the chromophore units. The  $^t\text{BuPh}$  linker introduces greater flexibility, allowing parallel stacking of slightly mismatched units, whereas the more rigid adamantyl (Ada) linker causes a pronounced inclination between monomers. PCPs with amine groups can adopt *cis* or *trans* conformations, where amine hydrogens face the same or opposite directions, respectively. These conformers are nearly isoenergetic: for Ada-linked PCPs, the *cis* form is favored by 29.6 meV, while for  $^t\text{BuPh}$ -linked PCPs, the *trans* is slightly more stable by 38.3 meV (though *cis* is favored at 0 K by 13.6 meV). These small differences, comparable to thermal energy at room temperature ( $\sim 25.9$  meV), suggest both forms coexist. A length mismatch of  $\sim 1.8$  Å between the Py and NDI units leads to mutual rotation, allowing for accommodation of the geometry without excessive bending. Structures with *cis* amine groups show a greater inclination between the NDI and Py planes compared to the *trans* ones. In the **NDI-Ph-Py** system with the shortest phenyl linker, the inter-unit distance near the linker is 3.0 Å, shorter than the  $\sim 3.4$  Å van der Waals sum

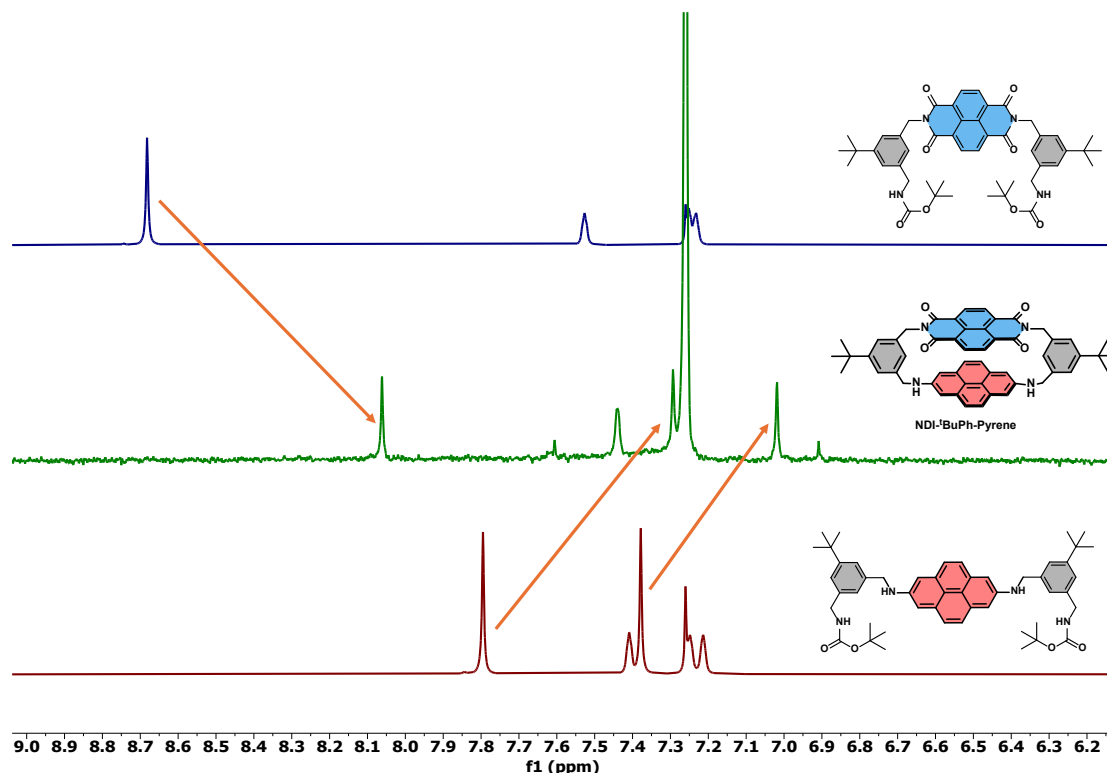


Figure 6.3: Partial  $^1\text{H}$  NMR spectra of NDI-Ref, NDI- $t\text{BuPh-Py}$ , and  $t\text{BuPh-Py}$  in  $\text{CDCl}_3$ .

for two carbon atoms, causing repulsion that bends the structure and increases the NDI-Py spacing to  $\sim 3.7 \text{ \AA}$  at the center (see Figure 6.4).

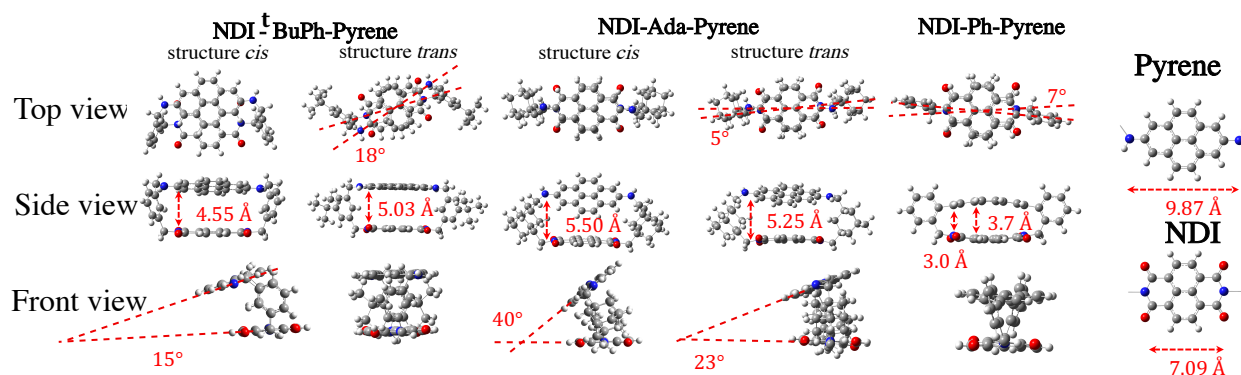


Figure 6.4: Optimized geometries for the three D-A paracyclophanes.

## 6.2.3 Optical Properties

The absorption spectra of the different PCPs in  $\text{CH}_2\text{Cl}_2$  are shown in Figure 6.5, along with those of their isolated constituent units (NDI and Py monomers) for comparison. In the blue and UV

region of the optical spectra (230-400 nm), all D-A PCPs present intense absorption bands that correspond to the  $\pi - \pi^*$  transitions of the NDI and Py units. Remarkably, the characteristic  $S_0 - S_1$  transition of the NDI chromophore at around 380 nm for **NDI-Ph-Py** PCP exhibited a pronounced red shift ( $\sim 6$  nm) and a loss of its vibronic progression compared to **NDI-Ref** (see Figure 6.5). For the Py unit, a notable loss of the vibronic progression of the  $S_0 - S_2$  band was also observed (ca. 340 nm). This behavior is likely due to the  $\pi$ - $\pi$  stacking enforced by the shorter, more rigid bridges, with **NDI-Ph-Py** having the shortest interchromophore distance. In contrast, the **NDI-Ada-Py** and **NDI-<sup>t</sup>BuPh-Py** PCPs, having a larger separation between chromophores, displayed subtler effects, with only minor broadening and negligible shifts in the main transition bands. Additionally, in the 400-500 nm region, the **Ada-Py** and **<sup>t</sup>BuPh-Py** reference compounds exhibit a broad, relatively weak absorption band, attributed to the short-axis polarized  $^1L_b$  transition, which includes a significant contribution from intramolecular charge transfer (ICT) from the amine group to the Py [ $\lambda_{\max}(\epsilon) \sim 453$  nm ( $\epsilon = 3850$  M $^{-1}$ cm $^{-1}$ )]. Similar behavior has been observed in other 2,7-diamino-substituted Py derivatives<sup>34,35,36,37,38,39</sup>. **NDI-Ada-Py** and **NDI-<sup>t</sup>BuPh-Py** display the same band, albeit it is slightly broadened and red-shifted compared to their reference compounds, as depicted in Figure 6.5. As expected for **Ph-Py** reference and **NDI-Ph-Py** PCP, no ICT is observed. Very interestingly, in all D-A PCPs, new broad and structureless bands at around 500-600 nm emerged, which are not observed in the spectra of the reference compounds. This feature cannot be attributed to the individual donor (Py) or acceptor (NDI) chromophores, but rather to a charge transfer (CT) transition from the Py to the NDI moiety. Furthermore, the intensity of these CT bands is directly correlated to the rigidity and interchromophore distance, in which **NDI-Ph-Py** with the shortest linker, exhibits the strongest band [ $\lambda_{\max}(\epsilon) \sim 520$  nm, ( $\epsilon = 1300$  M $^{-1}$ cm $^{-1}$ )], while **NDI-Ada-Py** [ $\lambda_{\max}(\epsilon) \sim 600$  nm, ( $\epsilon = 512$  M $^{-1}$ cm $^{-1}$ )], and **NDI-<sup>t</sup>BuPh-Py** [ $\lambda_{\max}(\epsilon) \sim 550$  nm, ( $\epsilon = 450$  M $^{-1}$ cm $^{-1}$ )] display a weak and very broad CT transition that extend to the near infrared region (NIR). The experimental results we observed closely matched the theoretical simulations, supporting our findings, which we will introduce in the section below.

The emission spectra of the three D-A PCPs and their corresponding reference compounds were recorded in CH<sub>2</sub>Cl<sub>2</sub> as shown in Figure 6.16-6.19. The reference compounds **Ada-Py** and **<sup>t</sup>BuPh-Py** exhibit strong, broad, and featureless emission bands centered around 480 nm. These compounds show clear solvatochromism, with a bathochromic shift observed when the solvent polarity increases from toluene to acetonitrile. This shift is characteristic of emission from a state with significant charge transfer character in polar solvents, whereas in nonpolar environments, the emission originates from a  $\pi - \pi^*$  excited state. In contrast, the **Ph-Py-Ref** compound displays an emission band centered at approximately 400 nm, attributed to a pure  $\pi - \pi^*$  transition. Notably, the fluorescence originating from both donor and acceptor chromophores in all three PCPs is dramatically reduced, suggesting that upon cyclization, a predominant photoinduced electron transfer is present to cause charge separation.

## 6.2.4 Electrochemical Properties

The electrochemical behavior of the D-A PCPs and their corresponding reference compounds was investigated using cyclic voltammetry (CV, shown in Figure 6.6) and differential pulse voltammetry (DPV) in CH<sub>2</sub>Cl<sub>2</sub> (Figures 5.10-5.12, 6.20, 6.21). As summarized in Table 6.1, the **NDI-<sup>t</sup>BuPh**



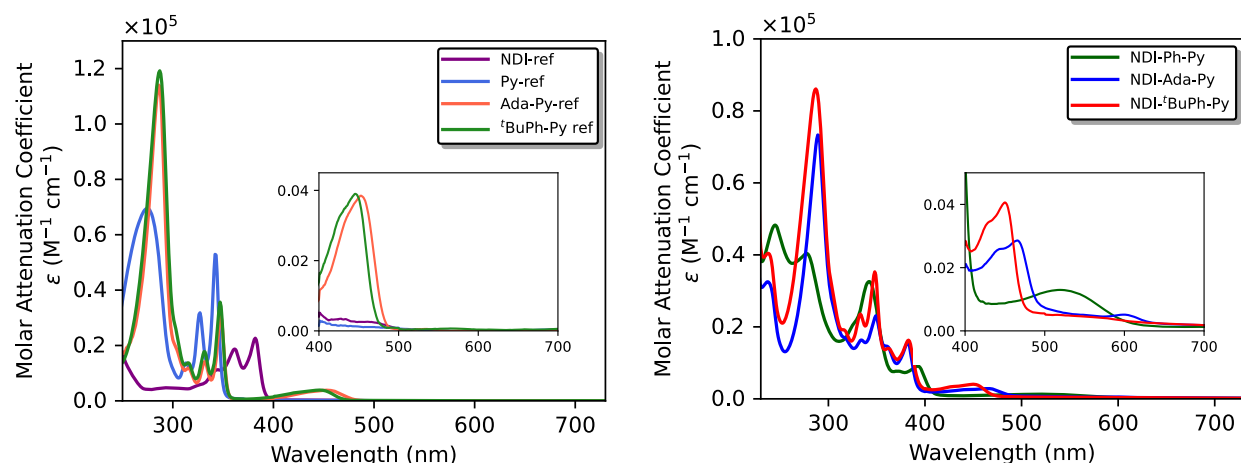


Figure 6.5: Absorption spectra of PCPs and their reference compounds in  $\text{CH}_2\text{Cl}_2$  at room temperature.

reference exhibits two reversible single-electron reduction processes at  $-0.63$  V and  $-1.05$  V, corresponding to the sequential reduction of the NDI unit to its radical anion and dianion forms. All three PCPs display similar reduction profiles; however, the first reduction potential is cathodically shifted by approximately 100 mV compared to the **NDI-*t*BuPh** reference. This shift suggests that the Py moiety influences the electronic properties of the adjacent NDI unit, likely through non-covalent interactions such as through-space charge transfer (CT), destabilizing the LUMO level. In the positive potential window, the Pyrene-based reference compounds exhibit distinct electrochemical behavior. **Ada-Py** shows two reversible single-electron oxidation processes at 0.50 V and 0.92 V, corresponding to the sequential formation of Pyrene radical cation and dication species<sup>35,36,40,41</sup>. In contrast, ***t*BuPh-Py** undergoes one irreversible oxidation at 0.59 V and a quasi-reversible oxidation at 1.02 V. The relatively low oxidation potentials observed for both compounds indicate their propensity to form radical cationic species. Notably, **NDI-Ada-Py** and **NDI-*t*BuPh-Py** PCPs exhibit two reversible oxidation processes, slightly shifted relative to their corresponding reference compounds. This shift suggests a modest electronic interaction between the donor and acceptor units, reflecting a small contribution to the HOMO energy level upon formation of the  $\pi$ -stacked D-A structure. In stark contrast, for the **Ph-Py** reference compound, a single irreversible oxidation process was observed at 1.34 V. Upon cyclization to form **NDI-Ph-Py**, this oxidation step shifted anodically by 70 mV. This stronger interaction is attributed to the shorter, more rigid linker in **NDI-Ph-Py**, which enforces closer spatial proximity between the donor and acceptor moieties. As a result, the HOMO level is stabilized. It is well established that in fused D-A systems that present ICT, it often results in HOMO stabilization and LUMO destabilization. For the **NDI-Ph-Py** structure, this effect is reflected in the anodic shift of the first oxidation potential and the cathodic shift of the first reduction potential, relative to the redox potentials of the individual D and A components. In contrast, **NDI-Ada-Py** and **NDI-*t*BuPh-Py** exhibit different behavior. In these cases, the HOMO level is influenced not only by the Py core but also by the ICT character introduced by the electron-donating amino groups at the 2,7-positions. This additional ICT contribution accounts for the opposite trend observed in the redox behavior of these two derivatives.

The experimental measurements were further supported by theoretical calculations based on DFT theory. The solvent effects of the  $\text{CH}_2\text{Cl}_2$  were included within implicit continuum polarizable model (PCM). The adiabatic electron affinities (EA) and ionization potentials (IP), obtained from the optimized structures as  $IP = E_{+1}^{opt} - E_0^{opt}$  and  $EA = E_0^{opt} - E_{-1}^{opt}$  where  $E_i^{opt}$  corresponds to the total energy of the optimized structure with the charge  $i$ , were in exceptional agreement with the experimental values with errors as low as 0.1 eV (Table 6.1). It should be noted that including the solvent effects is crucial for obtaining the quantitative description of the redox properties, because it can accounts for around 1eV changes of the energies of the charged systems compared to the gas phase results. Moreover the structural relaxation during the redox reactions leads to the shift of the HOMO orbitals to the higher energies meanwhile the LUMO energy is lowered reducing the band gap by around 0.2-0.4 eV.

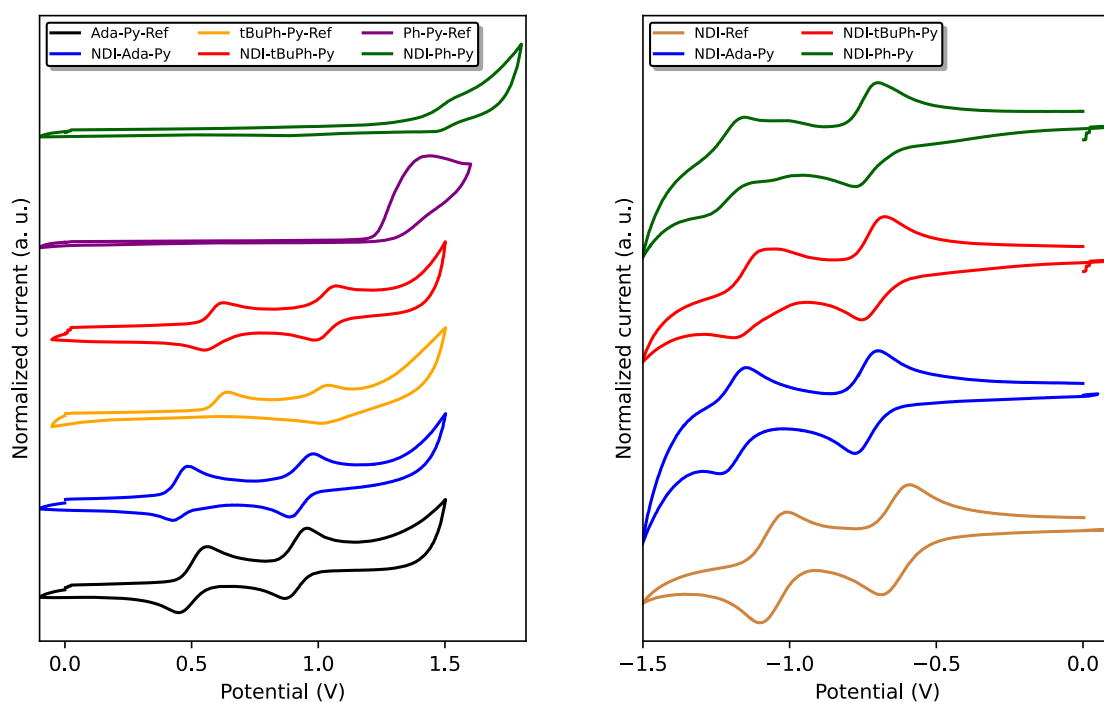


Figure 6.6: **Cyclic voltammograms of the different PCPs with their reference compounds measured in DCM with TBAPF<sub>6</sub> (0.1M) as the supporting electrolyte. Pt working electrode, glassy carbon as counter electrode, scan rate 0.1 V min<sup>-1</sup>.**

### 6.3 Theoretical Study

The combination of the electron-donating Py unit, specially conferred by the amino group at the 2,7 positions, and the electron-accepting NDI unit leads to the formation of several low-lying inter-unit (through-space) CT states. The inherently low transition dipole moments, molecular orbital (MO) overlap, and charge separation of the CT states make them challenging for both theoretical and experimental investigation. To overcome these challenges, we employed a two-step

Table 6.1: Electrochemical data of the target compound and references. Redox potentials (V) vs. Ag/AgCl in CH<sub>2</sub>Cl<sub>2</sub>.

Compound	$E_{1/2}^{\text{ox1}}$ (V)	$E_{1/2}^{\text{ox2}}$ (V)	$E_{1/2}^{\text{red1}}$ (V)	$E_{1/2}^{\text{red2}}$ (V)	HOMO (eV)	LUMO (eV)	$E_{\text{g}}^{\text{el}}$ (eV)	$E_{\text{g}}^{\text{op}}$ (eV)	IP <sub>comp</sub> (eV)	EA <sub>comp</sub> (eV)	$E_{\text{g}}^{\text{el}}$ (eV)
Ada-Py Ref	0.50	0.92	-	-	-4.76	-	-	-	-4.82	-1.94	2.88
<sup>t</sup> BuPh-Py Ref	0.58	0.99	-	-	-4.86	-	-	-	-4.98	-1.92	3.06
Ph-Py Ref	1.34	-	-	-	-5.56	-	-	-	-5.65	-2.04	3.61
NDI- <sup>t</sup> BuPh Ref	-	-	-0.63	-1.05	-	-3.82	-	-	-6.66	-3.80	2.86
NDI-Ada-Py	0.46	0.94	-0.73	-1.18	-4.71	-3.71	-1.00	-	-4.81	-3.68	1.13
NDI- <sup>t</sup> BuPh-Py	0.59	1.02	-0.76	-1.12	-4.87	-3.76	-1.10	-	-4.97	-3.72	1.25
NDI-Ph-Py	1.41	-	-0.73	-1.02	-5.72	-3.77	-1.95	2.02	-5.76	-3.71	2.05

The HOMO level was calculated from the onset of the first oxidation potential according to  $E_{\text{HOMO}} = [-e(E_{\text{onset, ox}} - (\text{Fc}^+/\text{Fc}) + 4.8)]$  eV. The LUMO level was calculated from the onset of the first reduction potential according to  $E_{\text{LUMO}} = [-e(E_{\text{onset, red}} - (\text{Fc}^+/\text{Fc}) + 4.8)]$  eV. 4.8 eV is the energy level of ferrocene below the vacuum level. The oxidation potential of Fc<sup>+</sup>/Fc against Ag/AgCl was recorded to be 0.45 V or 0.43 V.

computational procedure to obtain the excited state electronic properties with comparable accuracy for both CT and localized excited (LE) states. In the first step, linear-response time-dependent density functional theory (TD-DFT) using the range-separated wB97XD functional was applied. This method provides a reliable description of electron density redistribution upon excitation for both LE and CT transitions, while also allowing the inclusion of solvent effects via the polarizable continuum model (PCM) with state-specific solvation for CT states.

Although TD-DFT describes LE state energies with good accuracy often in quantitative agreement with experimental observations, it tends to underestimate or overestimate CT state energies, with typical absolute errors ranging from 0.1 to 1.0 eV. To correct this discrepancy, we calculated the gas-phase excitation energies using the approximate coupled-cluster method (CC2), which offers consistent accuracy for both LE and CT states. In our two-step approach, gas-phase excited state energies were obtained at the CC2 level, while solvent effects were subsequently incorporated from the TD-DFT calculations.

Validity of this approach was verified for the lowest intramolecular CT state of amino-substituted Py, where the two-step approach within the linear-response framework for solvent effects reproduced the same solvent shift of -64 meV from the gas-phase excitation energy as obtained ADC(2) with a COSMO solvent description. Further methodological details regarding the two step approach for computing the electronic and optical properties are provided in Chapter 5.

The vibronic absorption and fluorescence spectra were simulated from the excited state properties within the vertical gradient approximation and cumulant expansion approach<sup>42</sup>. This method is widely applied in modelling of organic molecules and super-molecular systems and efficiently accounts for vibronic effects in optical spectra without requiring extensive sampling of the molecular geometries.

### 6.3.1 Absorption Properties of Paracyclophanes

The optical and excited state properties of the three paracyclophane systems, **NDI-Ada-Py**, **NDI-<sup>t</sup>BuPh-Py**, and **NDI-Ph-Py**, were analyzed using the two-step computational approach mentioned above to simulate absorption and fluorescence spectra in dichloromethane (CH<sub>2</sub>Cl<sub>2</sub>) solvent. These spectra were compared to experimental data for validation (Figure 6.7), and their features were interpreted by decomposing the spectra into individual excited state contributions (Figure 6.8), sup-

ported by natural transition orbital (NTO) analysis. No arbitrary shifts or rescaling of the spectra was used for the calculation of the optical spectra. Exceptional quantitative agreement between the computed and experimental spectra demonstrates, strength of the applied two step methodology to quantitatively well describe properties of the heteroparacyclophanes with the same accuracy for both CT and LE states leading to reliable interpretation of the observed spectral effects.

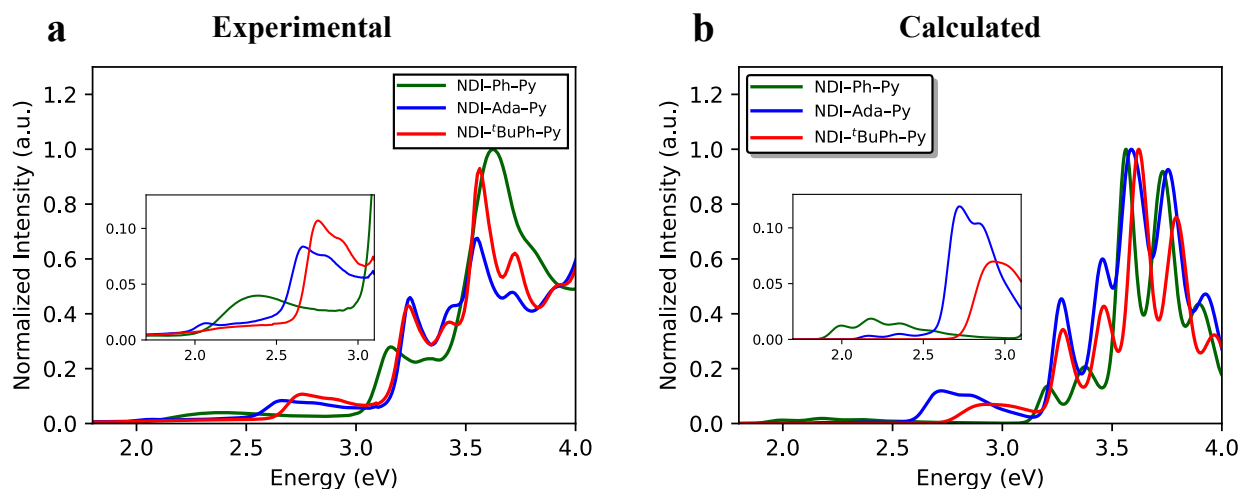


Figure 6.7: **Comparison of the experimental and computed absorption spectra.** Except of the broadening peak and slightly different redistribution of intensities among the vibronic modes the computed spectra quantitatively well agree with the experimental ones and all the observed effects are well captures.

### NDI-Ada-Py and NDI-*t*BuPh-Py Systems

The heteroparacyclophanes with Ada and *t*BuPh linkers between the NDI and Py aromatic units exhibit strong similarities in their optical and electronic properties and are therefore analysed together. The similarity of the electronic properties primarily arises from their similar chemical composition and spatial separation of the constituent units. The computed absorption spectra, alongside the experimental ones, are presented in Figure 6.7, while the decomposition of the full spectra into contributions from individual electronic transitions is shown in Figure 6.8. The optical spectra were simulated by including the lowest seven excited states, covering the infrared (IR), visible, and edge of the ultraviolet (UV) regions with an energy range below 4 eV. The lowest-energy region of the spectrum primarily arises from three low lying inter-unit CT states, corresponding to the electron transfer transfer from the Py highest occupied molecular orbitals (MO) to the NDI lowest unoccupied MO (LUMO).

The first excited state ( $S_1$ ), a CT state characterized by a large reorganization energy, resulting in a broad absorption band from 1.15 to 2.0 eV for both Ada and *t*BuPh linkers. The slightly lower energy by 12 meV of the CT state for Ada linker can be attributed to differences in the delocalization of the Py highest occupied MO (HOMO) over the linker, which is consistent with observations in the spectra of the monomeric Py with Ada and *t*BuPh linker (Chapter 5). Although the  $S_1$  transition corresponds to the low-energy tail of the experimental absorption spectra, the

calculated intensity is underestimated by approximately two orders of magnitude. This discrepancy arises from the use of the vertical gradient approach, in which excitation properties are computed at the optimized ground state geometry. Under these conditions, the  $S_0 \rightarrow S_1$  transition dipole moment is nearly zero due to molecular symmetry. In solution, however, thermal motion breaks this symmetry, enabling coupling between dark CT and bright locally excited (LE) states, thereby enhancing the transition dipole of the CT state, as seen in the experimental spectra.

The second CT state ( $S_2$ ) exhibits vibronic structure and corresponds to minor peaks at 2.08 and 2.35 eV in the experimental absorption spectra. The excitation energy for the  $^t\text{BuPh}$  linker is red-shifted by 154 meV relative the Ada-linked one, while in gas phase the excitation energies are nearly identical (Table 6.2). This shift can thus be attributed to different state-specific solvation effects. The same trend is obtained also for the other through-space CT states, suggesting that solvent cavity shape, influenced by the molecular geometry and unit separation, affect the solvation shifts of the Ada- and  $^t\text{BuPh}$ -linked PCPs. Like  $S_1$ , the calculated intensity of the  $S_2$  state is underestimated due to the neglect of thermal fluctuations.

The third CT state ( $S_3$ ), appearing between 2.4 and 3.3 eV in the absorption spectra, also exhibits low intensity and clear vibronic features including the pronounced double-peak structure arising from vibrational transitions. At the higher energies, the absorption bands mainly originate from excitations localized on the individual aromatic units. The  $S_4$  state, which shows weak absorption between 2.5-3.1 eV, is assigned to the Py  $^1\text{L}_b$  transition with partial intra-unit CT character. In agreement with experimental observations,  $S_4$  band is blue shifted for the Ada linker relative to the  $^t\text{BuPh}$  analogue. A similar blue shift was also observed for the monomeric units with Ada and  $^t\text{BuPh}$  linkers, (shown in Chapter 5), and it is attributed to the differences in delocalization of the Py HOMO across the linkers. For the heterodimers, the computed shift between the two linkers of 216 meV is slightly overestimated relative to the experimental value of  $\sim 100$  meV. This deviation arises mainly from differences in the linear-response solvent shift of 97 meV between the two linkers, suggesting that TD-DFT with linear response solvation tends to overestimate the solvent-shift differences between the **NDI-Ada-Py** and **NDI- $^t\text{BuPh}$ -Py**.

The strong absorption band corresponding to  $S_5$  excited state between 3.1-3.5 originates from the lowest excited state of the NDI moiety, while the intense absorption band between 3.5-4.0 eV ( $S_6$ ) corresponds to the Py  $^1\text{L}_a$  transition. Theoretical calculation also predicts higher intensity of the absorption spectra in  $S_6$  state region (Pyrene unit excitation) for the  $^t\text{BuPh}$ -linked PCPs compared to the Ada-linked one, consistent with the experimental findings. This enhancement arises from the shorter inter-unit separation in the  $^t\text{BuPh}$ -linked PCP, which increases the interaction energy between the Py  $^1\text{L}_a$  state and NDI lowest excited state from  $255\text{cm}^{-1}$  for the Ada linker to the  $293\text{cm}^{-1}$  for the  $^t\text{BuPh}$  linker, resulting in the transition dipole moment redistribution between these transitions. Furthermore, due to the spectral overlap with the  $S_7$  state corresponding to the second excited state of the NDI moiety, the increased transition dipole in the  $^t\text{BuPh}$ -linked PCP leads to enhanced absorption in the 3.5-4.0 eV spectral region.

Across all CT states, PCP with  $^t\text{BuPh}$  linkers exhibit larger reorganization energies than those with Ada linkers. This difference can be attributed to the greater structural flexibility of the  $^t\text{BuPh}$ -linked systems, which allows for larger geometric relaxation and conformational freedom in the excited state. A similar effect was reported for the NDI homo-paracyclophanes (shown in Chapter 5) and is supported by transient absorption measurement, which show faster relaxation to the ground state for the  $^t\text{BuPh}$ -linked PCP compared to the Ada-linked ones. This behavior arises from



the higher structural flexibility and, consequently, the lower energy barrier for geometric relaxation from the initial excited state and more efficient dissipation of excess energy into vibrational motion.

### NDI-Ph-Py System

A similar analysis was performed for the **NDI-Ph-Py** system, in which the NDI and Py units are connected by a phenyl (Ph) linker. Although this system exhibits overall spectral similarities to the **NDI-Ada-Py** and **NDI-<sup>t</sup>BuPh-Py** systems, several key differences arise from the distinct structural and electronic characteristics of the Ph linker. Notably, the Ph linker lacks the electron-donating amine groups present in the Ada- and <sup>t</sup>BuPh-linked systems, resulting in the absence of the HOMO delocalization over the amine-substituted Py and the linker. In the **NDI-Ada-Py** system, this delocalized HOMO contributes to both the lowest inter-unit CT state  $S_1$  and the intra-unit CT/LE state  $S_4$ . In contrast, in **NDI-Ph-Py** the corresponding MO is localized exclusively on the Py, lowering its energy and causing it to become HOMO-1. Consequently, also the ordering of the CT states is altered: the  $S_1$  and  $S_2$  CT states are interchanged relative to those from PCPs with Ada and <sup>t</sup>BuPh linkers, and the intra-unit CT/LE state  $S_4$  is eliminated, thereby modifying the spectral profile below 3 eV.

The low-energy region of the **NDI-Ph-Py** absorption spectrum arises from two inter-unit CT states involving electron transfer from Py to NDI. The lowest CT excited state,  $S_1$ , exhibits a broad absorption band spanning from 1.9 to 2.8 eV, in excellent agreement with the experimental spectrum, which displays a corresponding broad band in this range. This state corresponds to the electron transfer from the Py HOMO to NDI LUMO and is analogous in character to the  $S_2$  CT state in the Ada- and <sup>t</sup>BuPh-linked systems. However, it possesses a transition dipole moment approximately an order of magnitude larger. This enhancement arises not to the mixing with other LE state, but rather from the substantially shorter donor-acceptor spatial separation, which increases orbital overlap. Diabatization analysis using Fragment Charge Difference (FCD) algorithm<sup>43</sup> reveals that the couplings between the CT state and the two lowest excited states of the NDI are 0.34 cm<sup>-1</sup> and 0.84 cm<sup>-1</sup>, while the couplings to the two lowest excited states of Pyrene are 0.29 cm<sup>-1</sup> and 0.44 cm<sup>-1</sup>. These small coupling values, together with the large energy gap between CT and LE states, indicate the absence of delocalization and transition dipole moment redistribution. Nevertheless, the shorter spatial separation in **NDI-Ph-Py** (3.7 Å) results in a significantly larger HOMO-LUMO overlap of 0.039, compared to only 0.008 in **NDI-Ada-Py**, where the chromophores are separated by 5.44 Å. The increased orbital overlap in the Ph-linked system leads to partial delocalization of the Py HOMO and NDI LUMO orbitals and enhances the CT transition. In this case of strong molecular overlap, the transition density of the lowest CT state  $S_1$  for **NDI-Ph-Py** can be approximated as  $\rho_{ge}^{(S_1)}(r) \approx c_2 c_1 (\rho_{\text{LUMO}}^{\text{NDI}}(r) - \rho_{\text{HOMO}}^{\text{Py}}(r))$ , where  $\rho_{\text{LUMO}}^{\text{NDI}}(r)$  and  $\rho_{\text{HOMO}}^{\text{Py}}(r)$  represent the electron densities of the NDI LUMO and Pyrene HOMO orbitals, respectively, and  $c_i$  are the expansion coefficients of the **NDI-Ph-Py** HOMO orbitals into the Pyrene HOMO and NDI LUMO basis functions, quantifying the extent of the electron delocalization between the two units. This transition density gives rise to a transition dipole moment oriented perpendicular to the  $\pi$ -conjugated planes of the NDI and Pyrene moieties.

Exciton formation and transition dipole redistribution also significant contribute to the spectral differences between the two systems. In **NDI-Ada-Py**, the transition dipole moments are 2.08 a.u. and 2.07 a.u. for the NDI and Py lowest LE states, respectively, consistent with values for

isolated monomers of 2.39 and 2.06 a.u., respectively. In **NDI-Ph-Py**, however, short separation of the NDI and Pyrene units and resulting strong interaction between the corresponding transition densities leads to substantial state mixing and exciton formation, resulting in transition dipole strength redistribution: the NDI LE state dipole decreases to 1.32 a.u., while that of the Py LE state increases to 2.67 a.u. The coupling between the lowest LE states of the NDI and Pyrene obtained from diabaticization of the dimer states into the monomeric basis, is  $668\text{ cm}^{-1}$  closely matching the  $660\text{ cm}^{-1}$  coupling derived from localized fragments using Poisson-TrEsp method. This coupling is more than 2.6 times larger than coupling for the **NDI-Ada-Py**,  $255\text{ cm}^{-1}$  and  $259\text{ cm}^{-1}$  from the diabaticization and Poisson-TrEsp approach, respectively. The sum of the squares of the transition dipole moments remains nearly constant for both Ada and Ph linkers, confirming that the observed changes results from exciton formation and redistribution of the transition dipoles strength between NDI and Pyrene units. Finally, a small redshift of about 75 meV is observed for the first vibronic peak of the NDI absorption around 3.2 eV in **NDI-Ph-Py**. This shift originates from partial delocalization between the NDI LUMO and the Py HOMO orbitals, further supporting the enhanced interaction enabled by the Ph linker's reduced spatial separation.

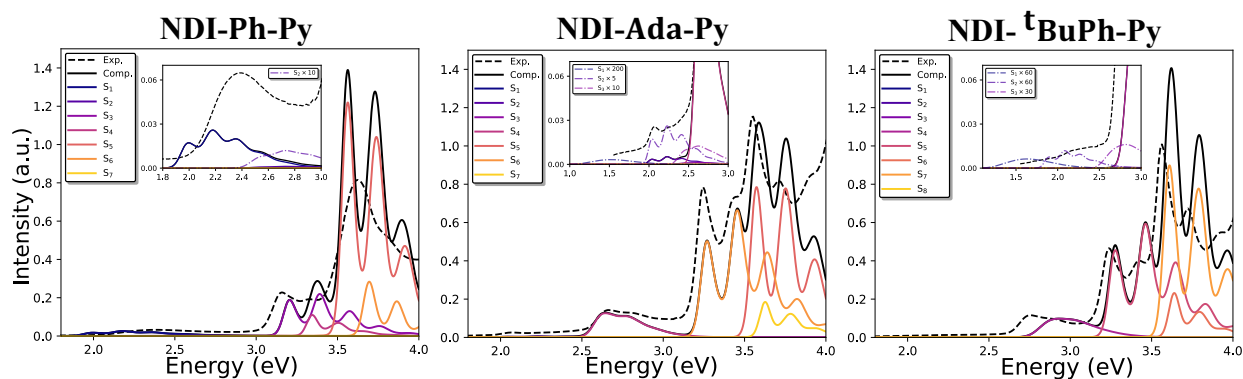


Figure 6.8: Absorption spectra decomposed to the individual transitions for the three different linkers.

## 6.4 Fluorescence

In addition to the absorption spectra, fluorescence measurements of **NDI-Ada-Py** were performed using three excitation wavelengths, 290 nm, 380 nm, and 460 nm, to selectively excite different electronic states within the molecule and investigate the resulting relaxation pathways. Excitation at 290 nm targets the  $S_2$  state of the Py unit (4.28 eV). The resulting very weak fluorescence spectrum closely matches the calculated emission from the  $S_4$  state of **NDI-Ada-Py**, which corresponds to the  $S_1$  state of isolated Py. This match indicates that, upon excitation, energy relaxes within the Py moiety itself ( $S_2 \rightarrow S_1$ ) without significant inter-unit transfer, leading to localized fluorescence. Excitation at 460 nm (2.7 eV) directly excites the  $S_1$  state of Py. The emission spectrum in this case aligns well with the calculated spectrum of the  $S_3$  charge transfer state, suggesting that after initial excitation on the Py unit, relaxation occurs to a CT state involving electron transfer to the NDI unit. This pathway represents an inter-unit charge transfer process.



Table 6.2: Transition dipole and excitation energy decomposition into individual contributions.

NDI-Ada-Py					
State	Gas-phase Energy CC2 (eV)	Solvent Shift (eV)	Reorganization Energy (eV)	Adiabatic Energy $E_{0-0}$ (eV)	Transition Dipole Moment $ \mu_{ge} $ (a.u.)
$S_1$	1.879	-0.315	-0.439	1.250	0.020
$S_2$	2.613	-0.282	-0.311	2.020	0.260
$S_3$	2.991	-0.386	-0.304	2.301	0.124
$S_4$	2.822	-0.057	-0.170	2.595	1.017
$S_5$	3.589	-0.067	-0.268	3.245	2.076
$S_6$	3.830	-0.053	-0.209	3.568	2.069
$S_7$	3.832	-0.069	-0.138	3.625	0.836

NDI-BuPh-Py					
State	Gas-phase Energy CC2 (eV)	Solvent Shift (eV)	Reorganization Energy (eV)	Adiabatic Energy $E_{0-0}$ (eV)	Transition Dipole Moment $ \mu_{ge} $ (a.u.)
$S_1$	2.093	-0.424	-0.532	1.137	0.055
$S_2$	2.642	-0.456	-0.320	1.866	0.057
$S_3$	3.257	-0.385	-0.265	2.607	0.085
$S_4$	2.981	0.040	-0.210	2.811	0.959
$S_5$	3.461	0.073	-0.265	3.269	2.064
$S_6$	3.695	0.094	-0.185	3.604	2.173
$S_7$	3.717	0.041	-0.120	3.638	0.930

NDI-Ph-Py					
State	Gas-phase Energy CC2 (eV)	Solvent Shift (eV)	Reorganization Energy (eV)	Adiabatic Energy $E_{0-0}$ (eV)	Transition Dipole Moment $ \mu_{ge} $ (a.u.)
$S_1$	2.504	-0.235	-0.311	1.958	0.671
$S_2$	2.999	-0.189	-0.345	2.465	0.137
$S_3$	3.454	-0.017	-0.239	3.198	1.321
$S_4$	3.543	-0.069	-0.132	3.342	0.739
$S_5$	3.805	-0.067	-0.180	3.558	2.672
$S_6$	3.822	-0.010	-0.122	3.690	1.076

Excitation at 380 nm (3.26 eV), targeting the  $S_1$  state of the NDI unit, produces a broad fluorescence band spanning more than 1 eV. This broad emission cannot originate from a single excited state, otherwise the same feature would be present also in the absorption spectra, which is not the case. Instead, it suggests that multiple excited states are populated during the relaxation. Based on spectral position, shape, and comparison with the computed fluorescence spectra, the most likely contributors are the  $S_3$  CT state,  $S_4$  (Py  $S_1$ ) with partial intra-unit CT/LE character, and  $S_5$  (NDI  $S_1$ ). Thus, a multiple state population appears more plausible.

Because the lowest CT states possess very small transition dipole moments, their exact contributions to the excited state relaxation are difficult to extract from the fluorescence data alone. Nonetheless, the significantly reduced emission observed in NDI-Ada-Py, compared to isolated monomers, strongly indicates that these CT states are populated during relaxation. These states may decay non-radiatively or emit weakly in the infrared region, beyond the spectrometer's detection range. A schematic representation of the proposed excited state relaxation pathways is shown in Figure 6.9.

## 6.5 Transient Absorption

To determine the exciton relaxation pathways of different excited states, investigate the effect of charge transfer (CT) states, and identify the final relaxed excited state, femtosecond transient absorption (TAS) measurements were performed. The TAS spectroscopy provides access to tran-

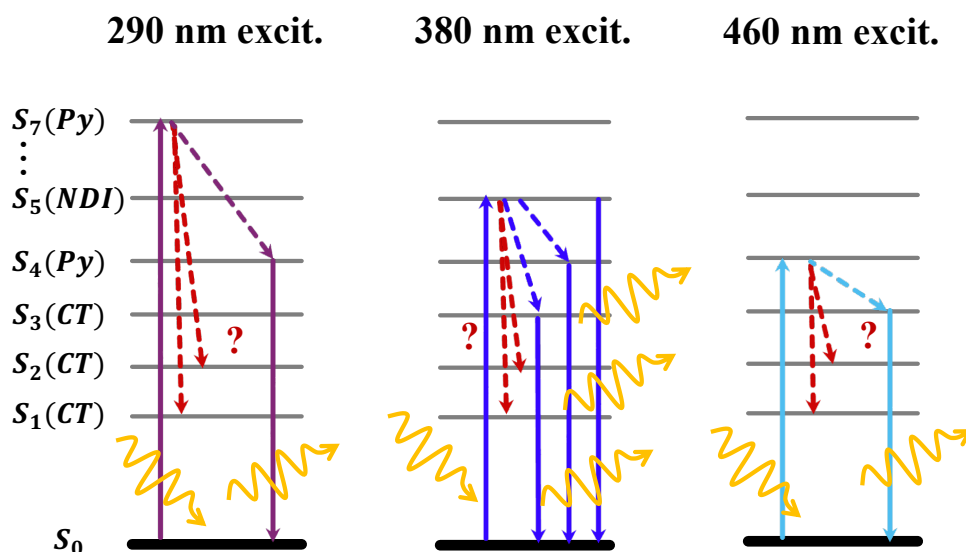


Figure 6.9: **The proposed exciton relaxation pathways for different excitation wavelengths of the NDI-Ada-Py based on a comparison of the computed and experimental fluorescence spectra.** Solid arrows indicate system excitation and fluorescence, while dashed lines show exciton relaxation. The red dashed lines represent expected relaxation pathways that could not be validated from the comparison of the experimental and computed spectra due to the small transition dipole moment of the final CT states.

sitions that are otherwise inaccessible in linear spectroscopies. Although CT states are optically dark in ground state excitations, they can exhibit significant excited state absorption (ESA) signals arising from transitions from the excited CT state to higher-lying electronic states with substantial CT character<sup>44</sup>. This makes TAS a powerful tool for probing not only relaxation dynamics but also the population and evolution of CT states.

Femtosecond TAS measurements were carried out using a Ti:sapphire regenerative amplifier system (800 nm central wavelength, 87 fs pulse duration, 4 kHz repetition rate, 0.55 mJ pulse<sup>-1</sup>). Three different pump wavelengths, 380 nm, 400 nm, and 266 nm, were employed to explore the influence of the excitation energy on exciton relaxation. These excitation wavelengths were selected to closely replicate the conditions used in the fluorescence experiments, although an exact match of the excitation frequencies was not possible with the current setup. The 380 nm pulses were generated by frequency-doubling the 760 nm output of a noncollinear optical parametric amplifier (NOPA) seeded with white light from the fundamental. The 400 nm pulses were generated as the second harmonic of the 800 nm fundamental in a BBO crystal, while the 266 nm pulses were produced via third-harmonic generation by sum-frequency mixing of the 800 nm and 400 nm beams. The pump energy at the sample was maintained at 0.5  $\mu$ J to suppress multiphoton effects. Probe pulses spanning 420-750 nm were produced as a supercontinuum in a 5 mm CaF<sub>2</sub> plate and collinearly overlapped with the pump within the sample. The instrument response function (IRF) was 200 fs (FWHM), and temporal delays up to 1.9 ns were introduced using a motorized delay

stage. Additional experimental details and a schematic of the setup are provided in the Supporting Information (Figure S5.8).

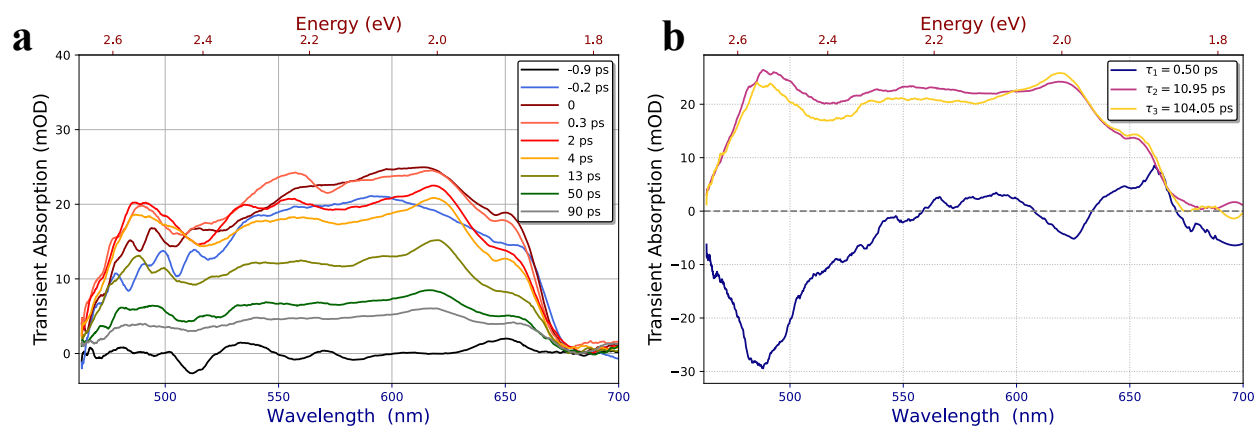


Figure 6.10: **Ultrafast excited state dynamics of NDI-Ada-Py upon excitation at 400 nm.**  
**a** Transient absorption spectra of NDI-Ada-NDI recorded at various time delays. **b** Corresponding decay associated spectra (DASs).

As in the fluorescence measurements, TAS measurements were performed on the NDI-Ada-Pyrene system using pump wavelengths of 400, 380, and 266 nm to selectively excite distinct electronic transitions within the donor-acceptor framework. Excitation at 400 nm primarily addresses the Pyrene  $S_1$  absorption band, while excitation at 380 nm corresponds mainly to the NDI  $S_1$  transition with a minor contribution from Pyrene. Excitation at 266 nm accesses higher-lying electronic states of both chromophores, enabling observation of relaxation pathways from the upper excited states.

The transient absorption spectra recorded at 380 nm and 400 nm excitation wavelengths exhibit remarkable similarities, despite the differing initial population of the NDI and Pyrene  $S_1$  states after the pump excitation. Immediately after photoexcitation, a broad positive transient signal attributed to ESA is observed, extending from approximately 520 to 700 nm, accompanied by a distinct sharp feature around 470 nm. At longer delay times, the transient spectra evolve slightly, with the 470 nm band becoming more pronounced while the broad ESA between 550 and 700 nm decreases in intensity. The broad ESA feature may correspond either to the formation of a CT state or relaxation to an excimer state, as reported for NDI homo-paracyclophanes with  $t$ BuPh- and Ada-linkers in Chapter 5. The sharp band at 470 nm could originate from several possible species. One possible assignment is the NDI triplet state, which exhibits ESA near this wavelength<sup>45</sup>, however, the reported lifetime of this state ( $\approx 82 \mu\text{s}$ ) is inconsistent with our transient absorption results. Another possible origin is the Pyrene  $S_1$  state<sup>46</sup>, though the transient absorption spectrum of amine-substituted Pyrene (which is present in NDI-Ada-Py) is red-shifted relative to the observed TAS signal for the NDI-Ada-Py paracyclophane, making this assignment unlikely. Alternatively, the emerging peak may indicate the formation of an NDI radical species<sup>9</sup>, consistent with photoinduced charge separation within the donor-acceptor framework.

Global fitting analysis using a sequential kinetic model was applied to the transient absorption data, revealing similar excited state dynamics for the 380 nm and 400 nm excitations. Three

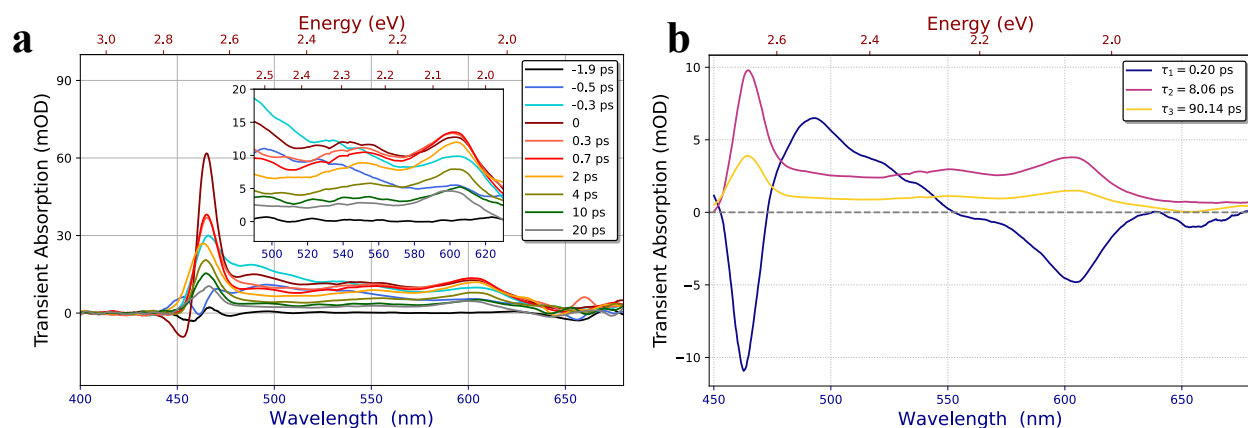


Figure 6.11: **Ultrafast excited state dynamics of NDI-Ada-Py upon excitation at 380 nm.**

**a** Transient absorption spectra of NDI-Ada-NDI recorded at various time delays. **b** Corresponding decay associated spectra (DASs).

exponential decay components were required to reproduce the experimental kinetics. The corresponding decay-associated spectra (DAS) and normalized population kinetics are shown in Figures 6.10 and 6.11. The extracted lifetimes for the 400 nm excitation,  $\tau_1 = 0.50$  ps,  $\tau_2 = 11$  ps, and  $\tau_3 = 105$  ps, are closely matching the 380 nm excitation results ( $\tau_1 = 0.20$  ps,  $\tau_2 = 8$  ps, and  $\tau_3 = 90$  ps). Minor differences were observed in the earliest component, particularly a slight decrease of the 500 nm band that appeared only for 380 nm excitation.

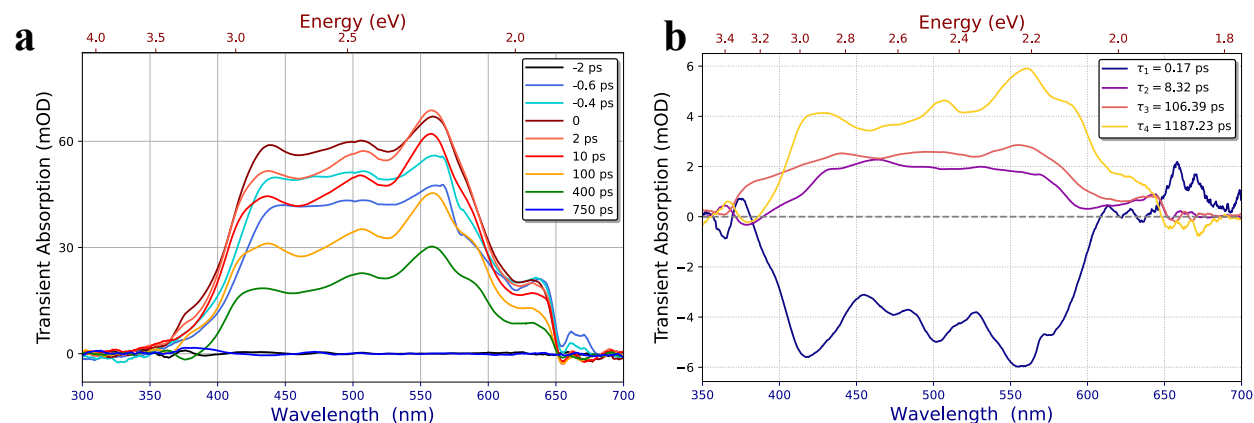


Figure 6.12: **Ultrafast excited state dynamics of NDI-Ada-Py upon excitation at 260 nm.**

**a** Transient absorption spectra of NDI-Ada-NDI recorded at various time delays. **b** Corresponding decay associated spectra (DASs).

In contrast, excitation at 266 nm yielded markedly different dynamics. Although a similarly broad ESA band was observed, the overall excited state lifetime was approximately an order of magnitude longer. DAS analysis of the 266 nm transient spectra revealed four kinetic components with lifetimes of 0.17 ps, 8.32 ps, 106.39 ps, and 1187.23 ps. The first three components display dynamics comparable to those at 380 nm and 400 nm, while the longest component suggests

population of a distinct excited state. This long-lived state likely arises from excitation into higher-energy electronic levels, providing excess energy that facilitates greater geometric reorganization during excited state relaxation.

No clear spectral signatures corresponding to the initially excited NDI or Pyrene  $S_1$  states were detected, indicating ultrafast exciton relaxation occurring within the temporal resolution of our TAS setup. The absence of these features at longer delay times suggests that only a small fraction of the population remains in the locally excited states, with most of the excitation residing in CT or excimer-like states. This observation is consistent with fluorescence measurements, which show significantly reduced emission intensity compared to the monomeric units. Furthermore, the TAS spectra reveal excitation-wavelength-dependent relaxation dynamics, particularly between the low-energy excitations (380 nm and 400 nm) and the high-energy excitation (266 nm), in agreement with the trends observed in the fluorescence spectra.

A more detailed assignment of the observed spectral features would require further investigation, which lies beyond the scope of the present work and will be addressed in a subsequent publication.

## 6.6 Supplementary Information

### Experimental Section

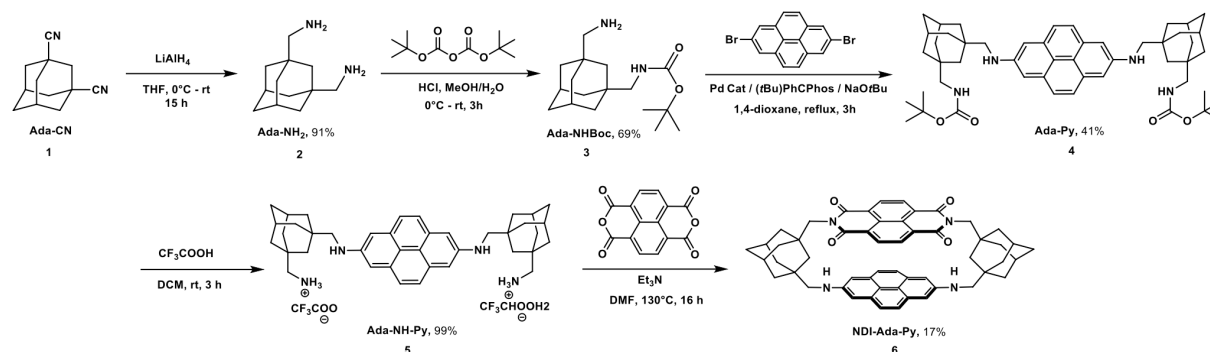


Figure 6.13: Synthetic procedures for NDI-Ada-Pyrene

### Synthesis of NDI-Ada-Pyrene

A solution of naphthalenetetracarboxylic dianhydride (NDI, 32 mg, 0.123 mmol) in anhydrous DMF (50 mL) was slowly added (over one hour) to a solution of **5** (120 mg, 0.147 mmol) in a mixture of  $\text{Et}_3\text{N}$  (1 mL) in warm anhydrous DMF at 90 °C (70 mL) under a nitrogen atmosphere. The mixture was then heated at 130 °C with constant stirring for 15 h. After that, the solvent was evaporated under reduced pressure. The remaining solid was dissolved with  $\text{CHCl}_3$  (50 mL) and filtered with a frit (pore size 4). The resulting brown solution was evaporated under a high

vacuum to eliminate any residual DMF. The dark residue was initially purified by silica gel column chromatography (eluent: DCM/isopropanol = 100:3, v/v). This was followed by gel permeation chromatography (THF, Bio-Beads S-X1 Support). Finally, the purified compound was heated at 180 °C under a high vacuum ( $1 \times 10^{-6}$  bar) to give the title compound as a dark solid (17 mg, 17% yield).

$^1\text{H}$  NMR (400 MHz,  $\text{CDCl}_3$ )  $\delta$  8.48 (s, 4H), 7.45 (s, 4H), 7.07 (s, 4H), 3.90 (s, 4H), 3.17 (s, 4H), 2.10 (s, 4H), 1.67–1.58 (m, 17H), 1.49–1.43 (m, 9H).

$^{13}\text{C}$  NMR (101 MHz,  $\text{CDCl}_3$ )  $\delta$  163.85, 146.06, 130.85, 130.38, 126.67, 126.17, 125.87, 118.10, 109.25, 77.36, 54.67, 51.64, 43.35, 41.98, 41.50, 37.02, 36.45, 36.22, 29.22.

HR-MS (ESI, positive):  $m/z$  calcd. for  $[\text{C}_{54}\text{H}_{50}\text{N}_4\text{O}_4+\text{H}]^+$  819.3905; found: 819.3927.

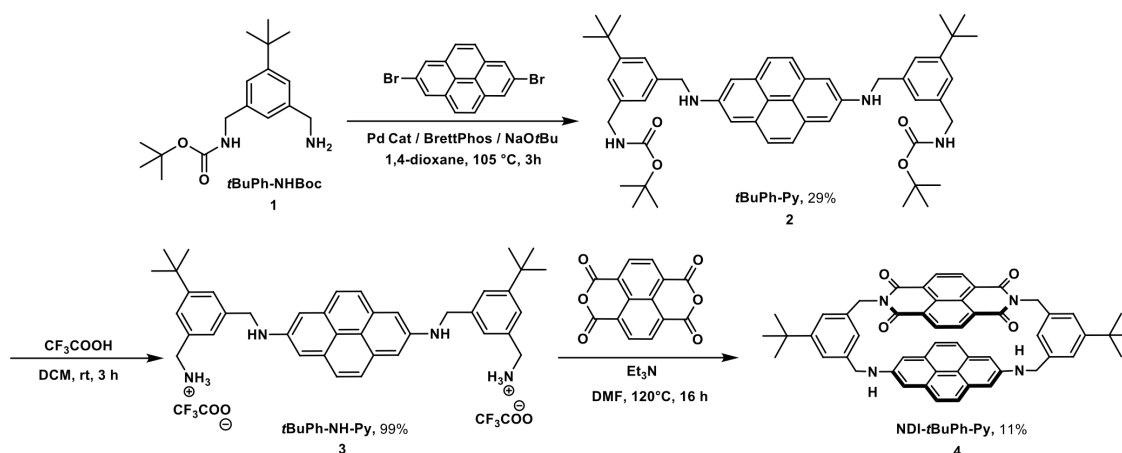


Figure 6.14: Synthetic procedures for NDI-*t*BuPh-Pyrene

### Synthesis of NDI-*t*BuPh-Py

A solution of naphthalenetetracarboxylic dianhydride (NDTA, 45 mg, 0.167 mmol) in anhydrous DMF (70 mL) was slowly added (over one hour) to a solution of *t*BuPh-NH-Py (160 mg, 0.200 mmol) with  $\text{Et}_3\text{N}$  (1 mL) in warm anhydrous DMF at 90 °C (80 mL) under a nitrogen atmosphere. The mixture was then heated at 130 °C with constant stirring for 15 h. After that, the solvent was evaporated under reduced pressure. The resulting brown residue was purified by silica gel column chromatography (eluent: DCM/EtOAc = 95:5, v/v), and the obtained solid was washed with diethyl ether to give the title compound as a brown solid (15 mg, 11%).

$^1\text{H}$  NMR (400 MHz,  $\text{CD}_2\text{Cl}_2$ )  $\delta$  8.08 (s, 4H), 7.43–7.40 (m, 4H), 7.30–7.28 (m, 6H), 7.03 (s, 4H), 5.16 (s, 4H), 4.59 (s, 4H), 1.41 (s, 18H).

$^{13}\text{C}$  NMR (101 MHz,  $\text{CD}_2\text{Cl}_2$ )  $\delta$  31.66. (Solubility was not sufficient to record a full spectrum.)

HR-MS (ESI, positive):  $m/z$  calcd. for  $[\text{C}_{54}\text{H}_{47}\text{N}_4\text{O}_4]^+$  = 815.3592; found: 815.3586.

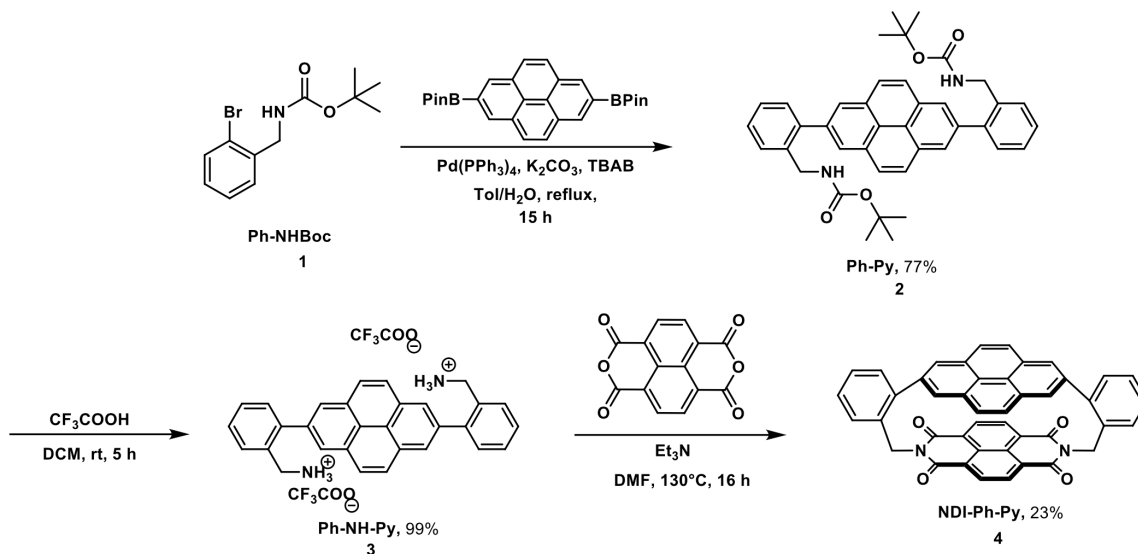


Figure 6.15: Synthetic procedures for NDI-Ph-Pyrene

### Synthesis of NDI-Ph-Py

A solution of naphthalenetetracarboxylic dianhydride (NTDA, 70 mg, 0.260 mmol) in anhydrous DMF (70 mL) was slowly added (over one hour) to a solution of Ph-Py (200 mg, 0.312 mmol) with Et<sub>3</sub>N (1 mL) in warm anhydrous DMF at 90 °C (80 mL) under a nitrogen atmosphere. The mixture was then heated at 130 °C with constant stirring for 15 h. After that, the solvent was evaporated under reduced pressure.

The pink residue was purified by silica gel column chromatography (eluent: DCM/EtOAc = 95:5, v/v) to give the title compound as a pink solid (38 mg, 23%).

<sup>1</sup>H NMR (300 MHz, CDCl<sub>3</sub>)  $\delta$  8.11 (s, 4H), 7.75 (s, 4H), 7.61 (s, 4H), 7.52–7.51 (m, 4H), 7.39–7.38 (m, 4H), 5.67 (s, 4H).

Solubility was not sufficient to record a <sup>13</sup>C NMR spectrum.

HR-MS (ESI, positive):  $m/z$  calcd. for [C<sub>44</sub>H<sub>24</sub>N<sub>2</sub>O<sub>4</sub>+Na]<sup>+</sup> = 667.1635; found: 667.1629.

### Emission spectra



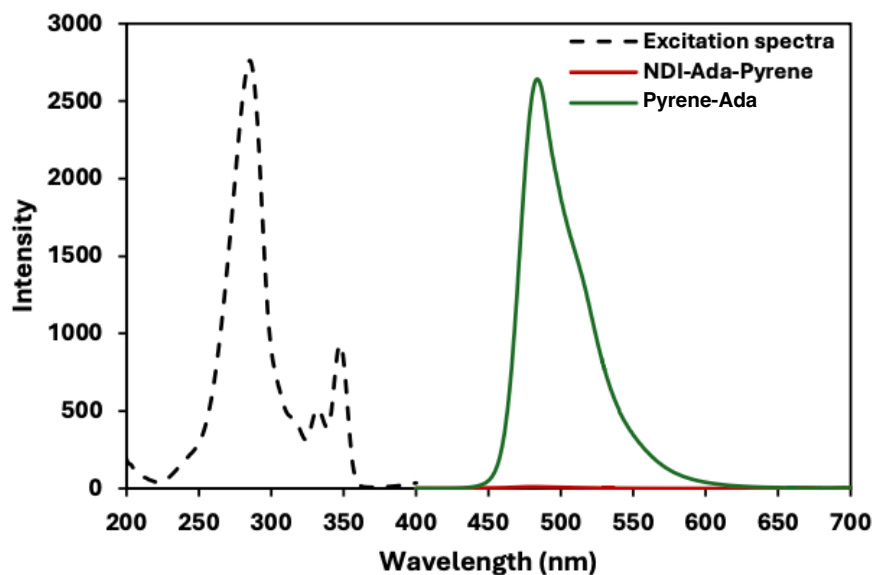


Figure 6.16: Fluorescence spectra of NDI-Ada-Pyrene and reference compound Pyrene-Ada ( $\lambda_{exc} = 290$  nm) and excitation spectra of Pyrene-Ada.

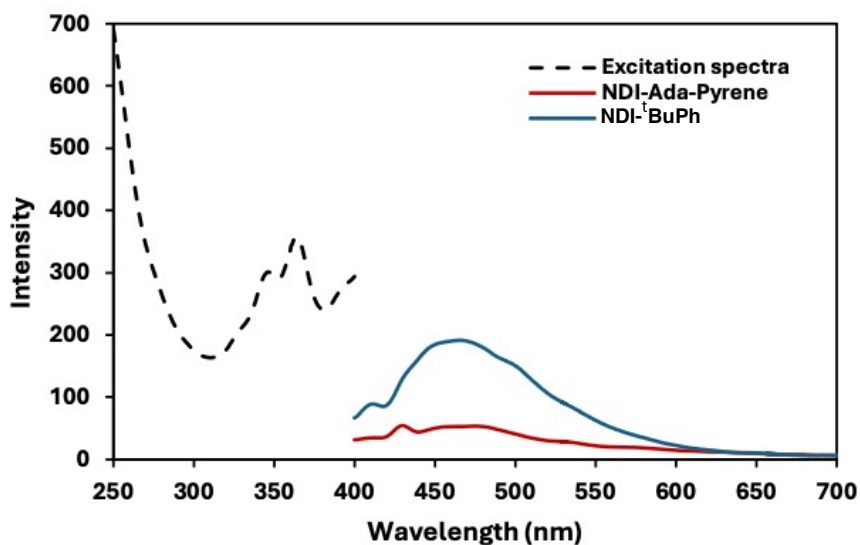


Figure 6.17: Fluorescence spectra of NDI-Ada-Pyrene and reference compound NDI-<sup>t</sup>BuPh ( $\lambda_{exc} = 380$  nm) and excitation spectra of Pyrene-NDI-<sup>t</sup>BuPh.

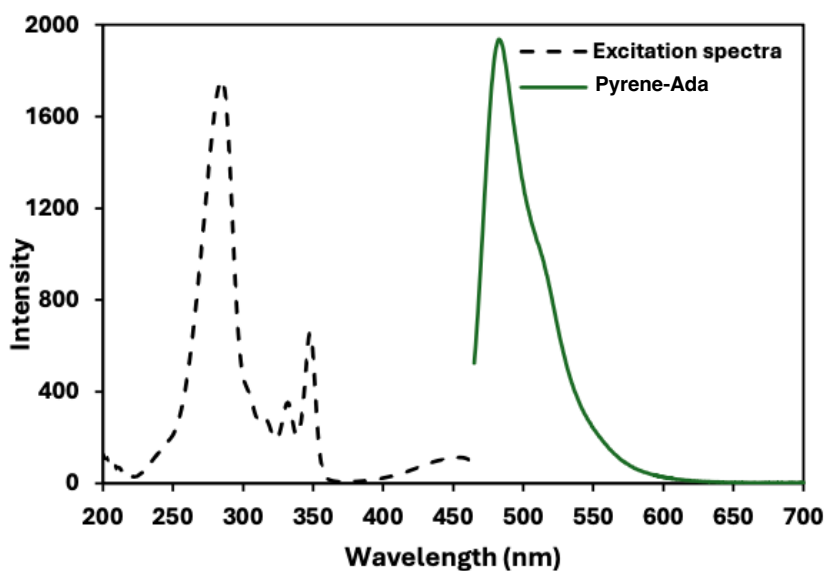


Figure 6.18: Fluorescence and excitation spectra of reference compound Pyrene-Ada ( $\lambda_{exc} = 450$  nm).

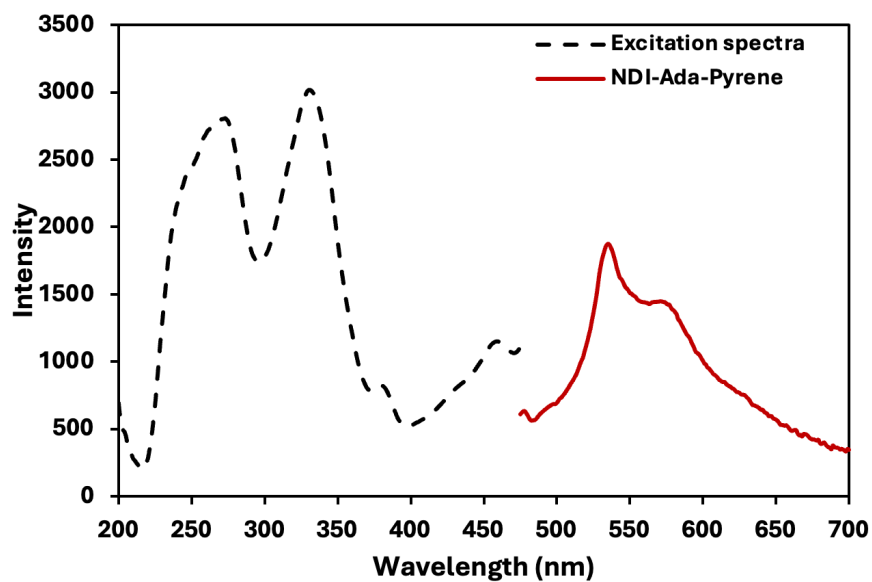


Figure 6.19: Fluorescence and excitation spectra of NDI-Ada-Pyrene ( $\lambda_{exc} = 460$  nm).

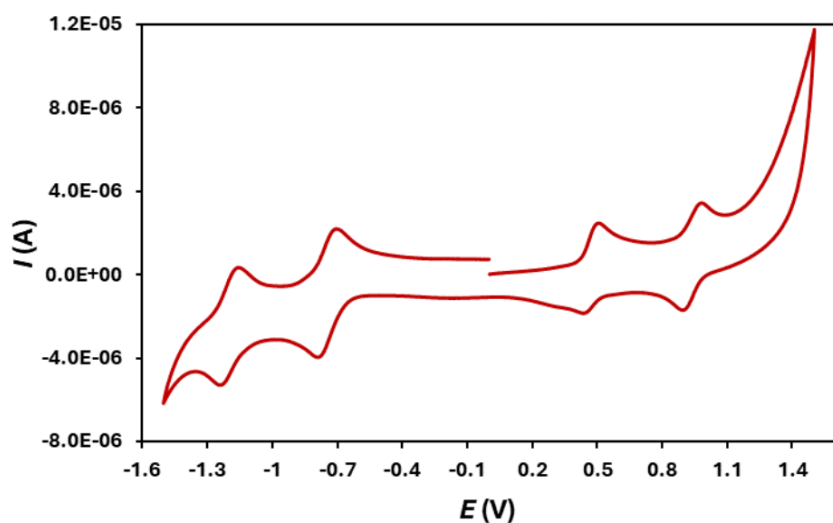


Figure 6.20: Cyclic voltammogram of NDI-Ada-Pyrene.

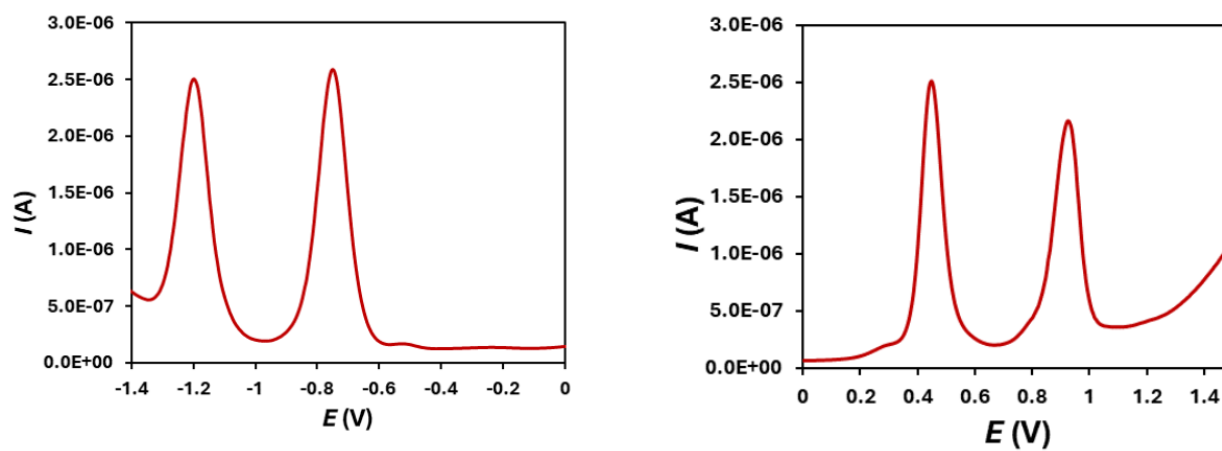


Figure 6.21: Differential pulse voltammograms of NDI-Ada-Pyrene.

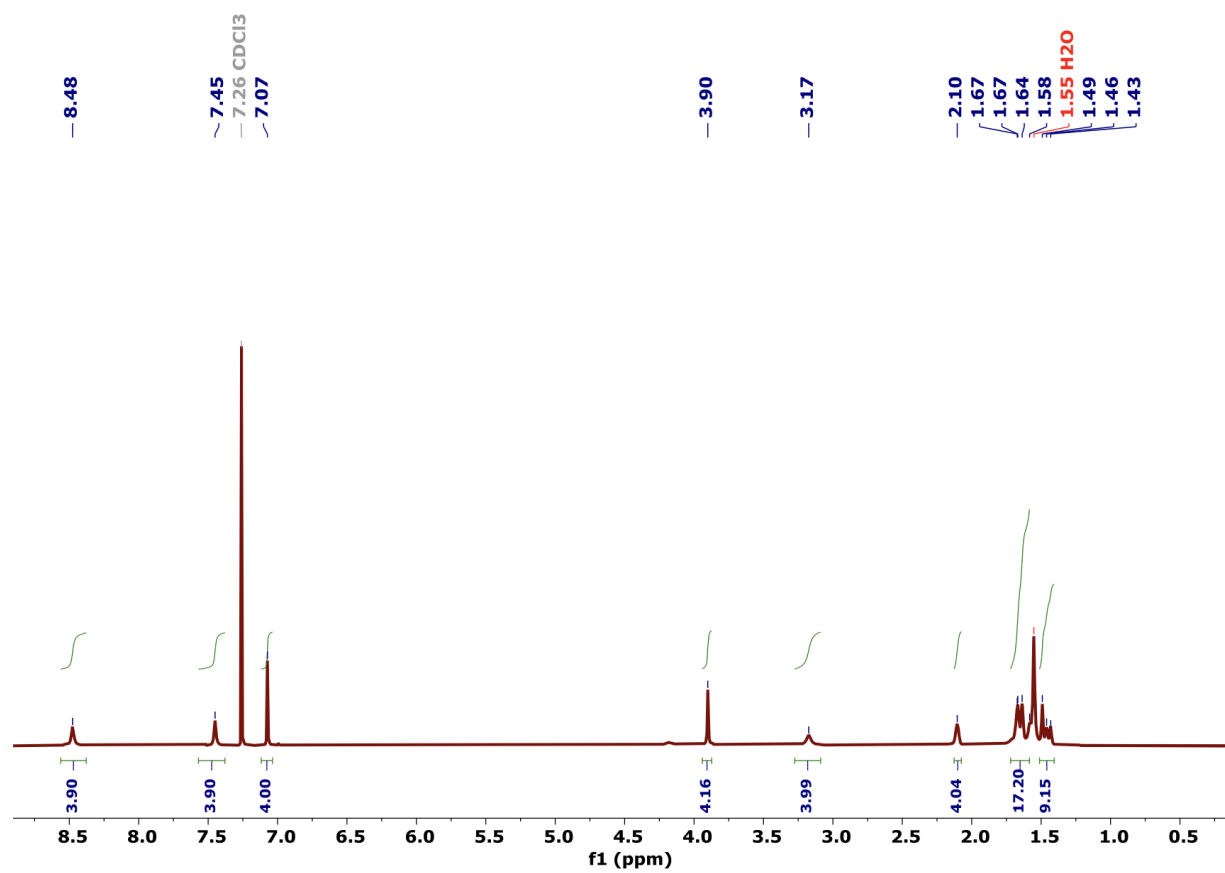


Figure 6.22: <sup>1</sup>H NMR NDI-Ada-Pyrene.

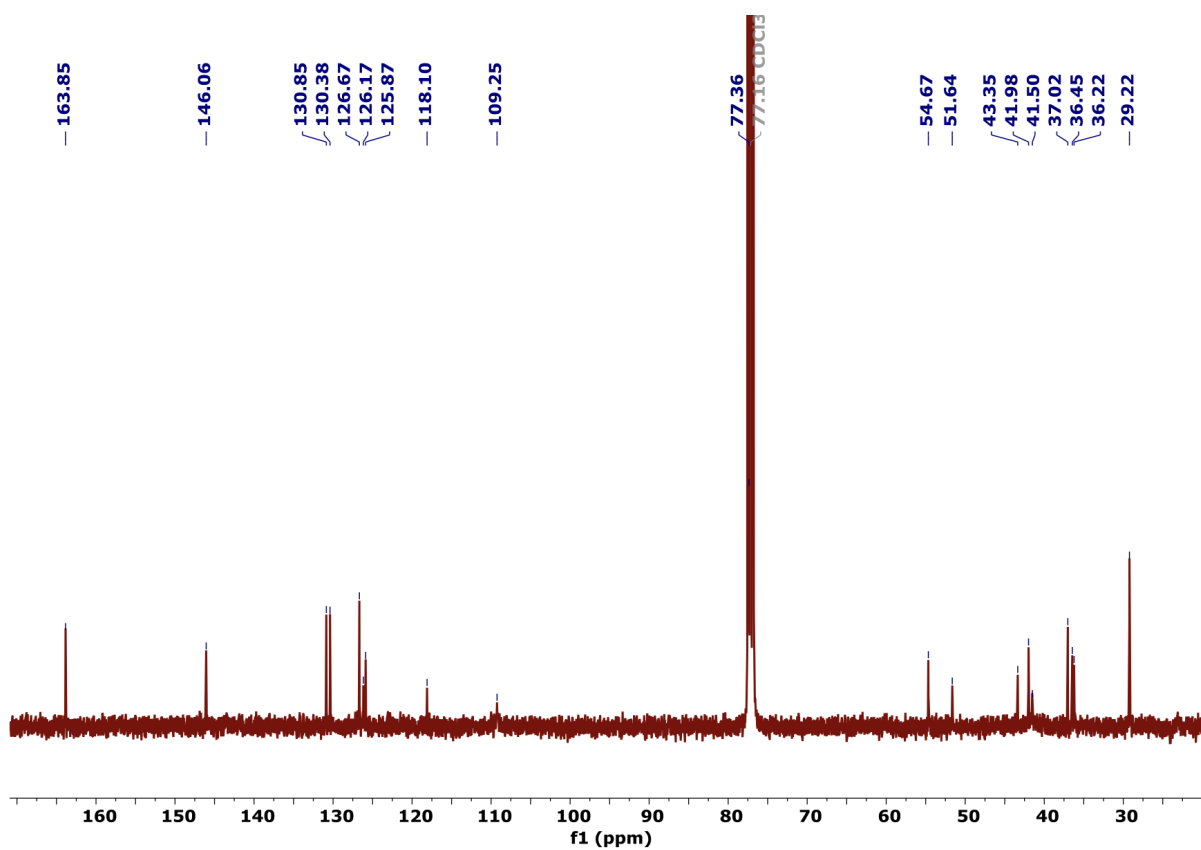


Figure 6.23: <sup>13</sup>C NMR NDI-Ada-Pyrene.

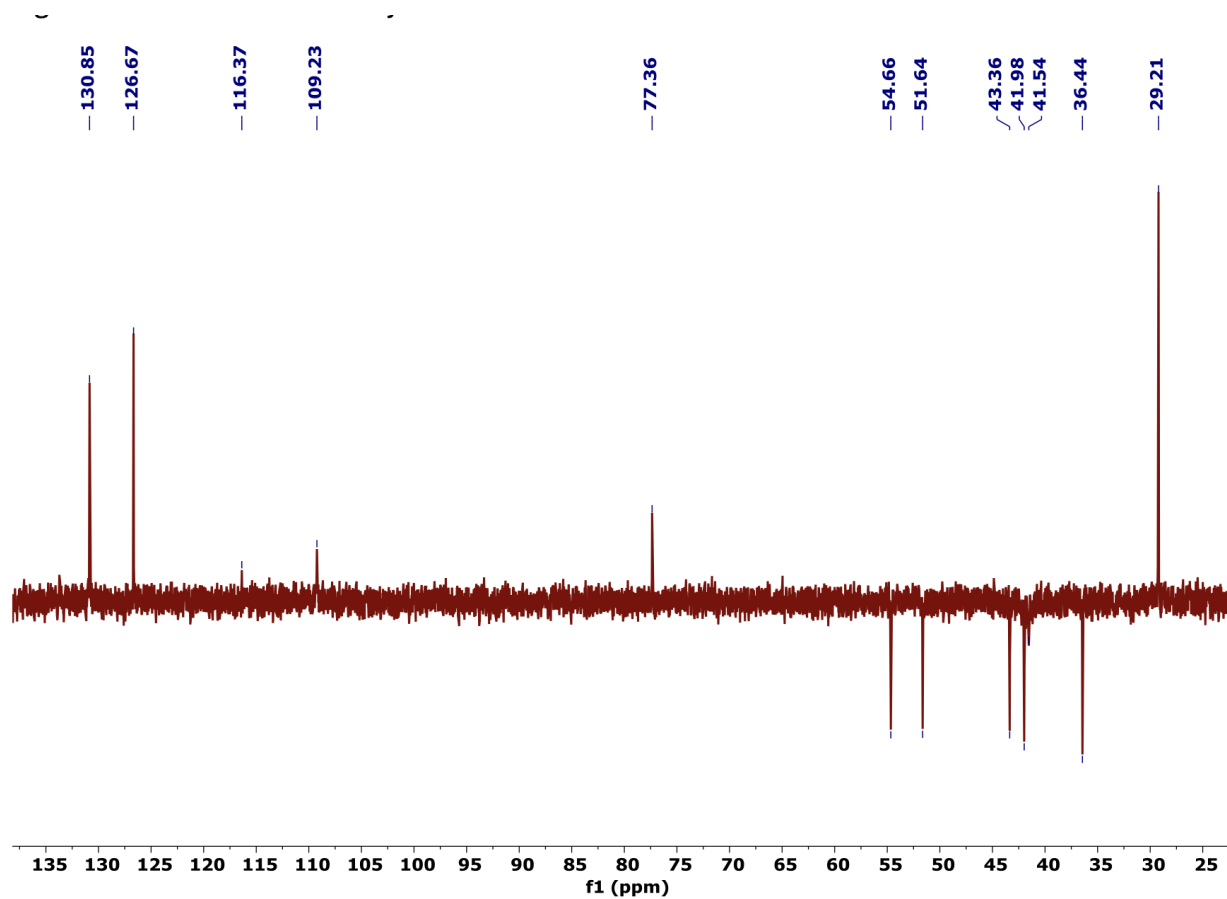


Figure 6.24: DEPT135 NDI-Ada-Pyrene.

## Theoretical Section

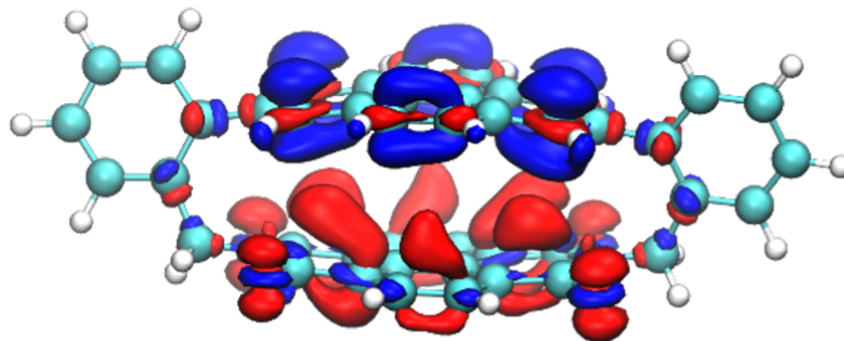


Figure 6.25: **Iso-surface representation of the transition density of the NDI-Ph-Pyrene lowest charge transfer (CT) state  $S_1$ .** The positive part (red) of the transition density is localized on the NDI unit, whereas the negative part (blue) is localized on the pyrene moiety. This spatial separation leads to a transition dipole moment oriented perpendicular to the planes of the NDI and pyrene units.



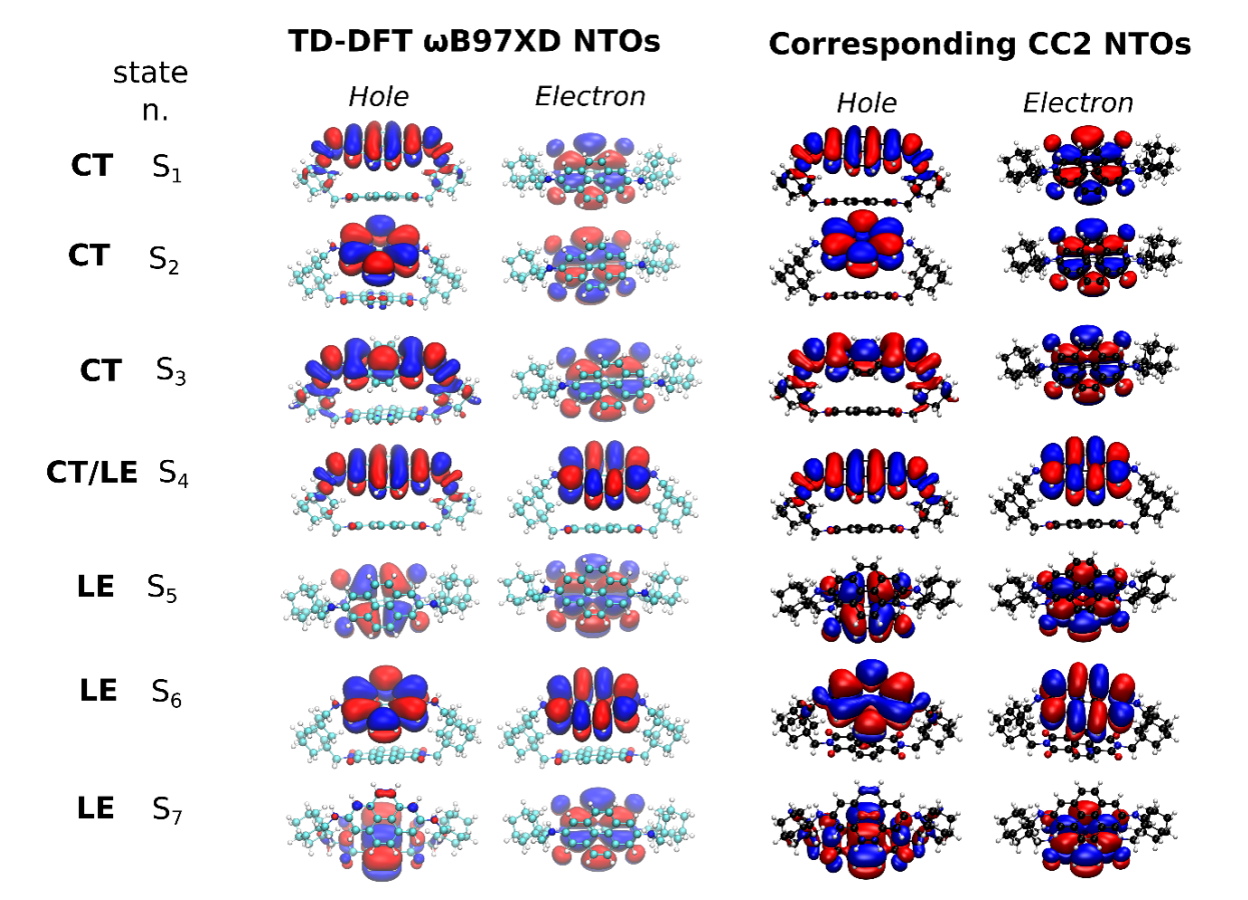


Figure 6.26: Comparison of the NTO analysis between TD-DFT with  $\omega$ B97XD functional and the corresponding states from CC2 method for the excited states of the NDI-Ada-Pyrene paracyclophane.

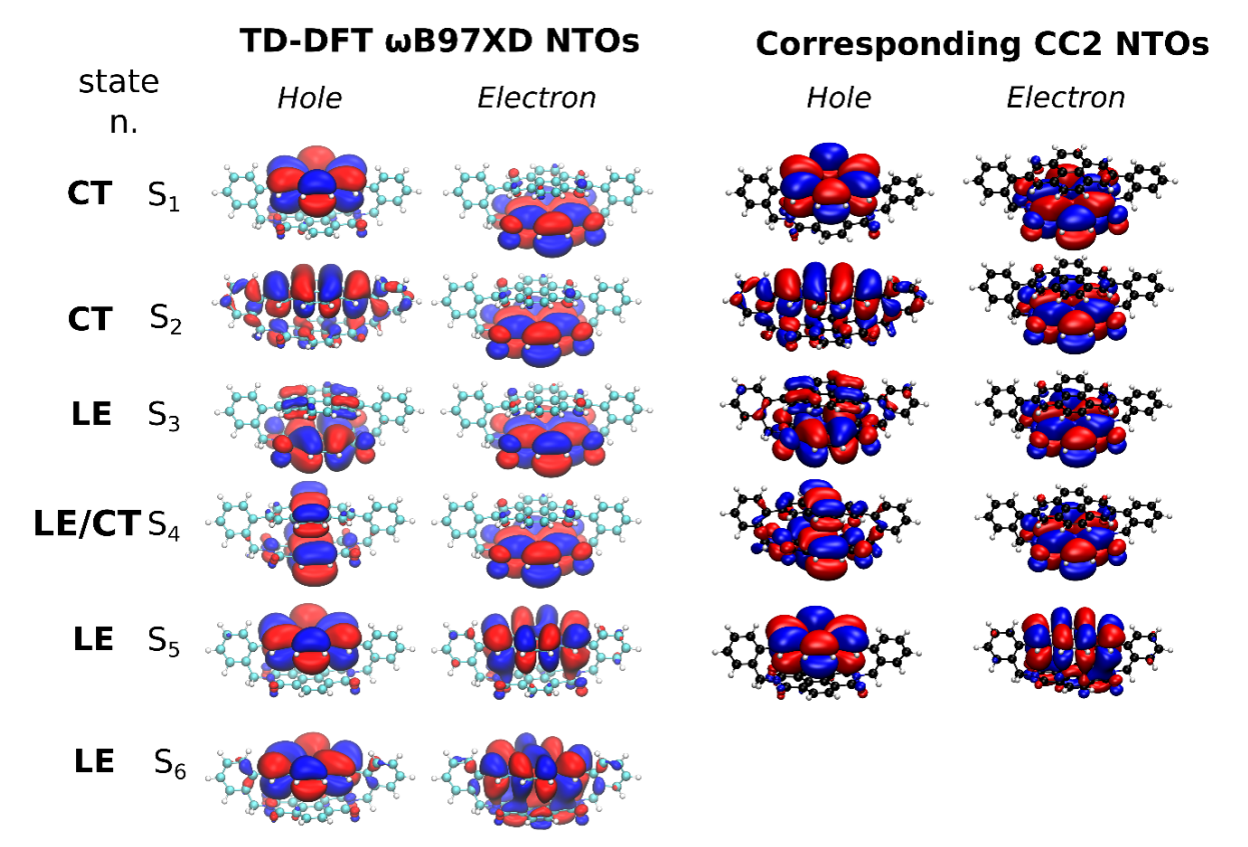


Figure 6.27: Comparison of the NTO analysis between TD-DFT with  $\omega$ B97XD functional and the corresponding states from CC2 method for the excited states of the NDI-Ph-Pyrene paracyclophane.

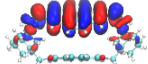
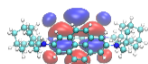
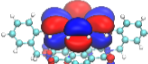
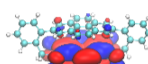
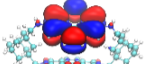
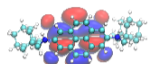
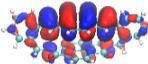
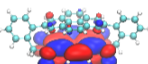
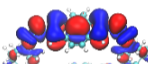
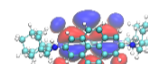
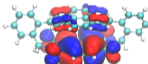
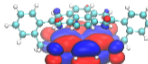
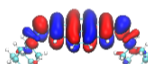
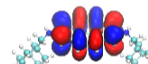
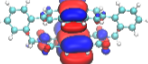
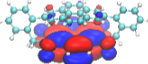
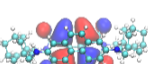
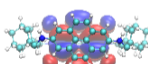
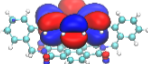
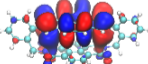
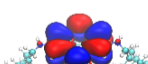
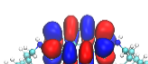
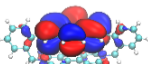
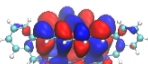
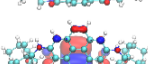
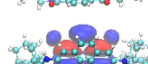
NTO NDI-Ada-Pyrene				NTO NDI-Ph-Pyrene			
state n.	Hole	Electron	$E_{0-0}$ [eV]	state n.	Hole	Electron	$E_{0-0}$ [eV]
CT $S_1$			1.250	CT $S_1$			1.958
CT $S_2$			2.144	CT $S_2$			2.465
CT $S_3$			2.489	LE $S_3$			3.198
CT/LE $S_4$			2.673	LE/CT $S_4$			3.342
LE $S_5$			3.261	LE $S_5$			3.558
LE $S_6$			3.568	LE $S_6$			3.690
LE $S_7$			3.625				

Figure 6.28: Natural Transition Orbital analysis for the NDI-Ada-Pyrene and NDI-Ph-Pyrene paracyclophane hetero-structures together with corresponding adiabatic energies.

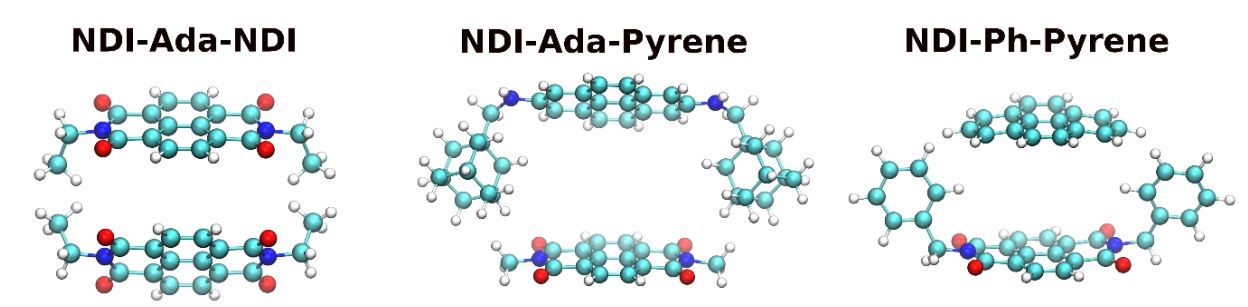


Figure 6.29: Individual fragments for calculation of the couplings between transition densities and molecular orbital overlaps for the paracyclophane homo- and hetero-structures.

## Bibliography

- [1] R. P. Sullivan, J. T. Morningstar, E. Castellanos-Trejo, R. W. Berryman III, Y. J. Hofstetter, Y. Vaynzof, M. E. Welker, and O. D. Jurchescu. Intermolecular charge transfer enhances the performance of molecular rectifiers. *Science Advances*, 8:eabq7224, 2022.
- [2] T. Kim, G. Shin, T. Park, and M. Kim. Molecular design leveraging non-covalent interactions for efficient light-emitting organic small molecules. *Advanced Functional Materials*, 2024. doi:10.1002/adfm.202412267.
- [3] J. Peng, L. Hou, D. Liu, Z. Zhao, J. Zhang, Z. Qiu, and B. Z. Tang. Organic optoelectronic devices based on through-space interaction. *ACS Applied Optical Materials*, 2(1):15–27, 2024. doi: 10.1021/acsaom.3c00370.
- [4] Y. K. Qu, D. Y. Zhou, Q. Zheng, P. Zuo, Z. L. Che, L. S. Liao, and Z. Q. Jiang. Linearly arranged multi- $\pi$ -stacked structure for efficient through-space charge-transfer emitters. *Angewandte Chemie International Edition*, 2024. doi:10.1002/anie.202408712.
- [5] S. Y. Yang, Y. K. Qu, L. S. Liao, Z. Q. Jiang, and S. T. Lee. Research progress of intramolecular  $\pi$ -stacked small molecules for device applications. *Advanced Materials*, 34(22):2104125, 2022. doi: 10.1002/adma.202104125.
- [6] Q. Zheng, X. Q. Wang, Y. K. Qu, G. Xie, L. S. Liao, and Z. Q. Jiang. Solution-processable through-space charge-transfer emitters via solubilizing groups modification. *npj Flexible Electronics*, 6:83, 2022. doi: 10.1038/s41528-022-00212-5.
- [7] R. T. Ayinla, M. Shiri, B. Song, M. Gangishetty, and K. Wang. The pivotal role of non-covalent interactions in single-molecule charge transport. *Materials Chemistry Frontiers*, 7(17):3524–3542, 2023. doi: 10.1039/d3qm00210a.
- [8] M. L. Williams, I. Schlesinger, R. M. Jacobberger, and M. R. Wasielewski. Mechanism of ultrafast triplet exciton formation in single cocrystals of  $\pi$ -stacked electron donors and acceptors. *Journal of the American Chemical Society*, 144(40):18607–18618, 2022. doi: 10.1021/jacs.2c08584.
- [9] Z. Wang, Y. Liu, X. Quan, W. Zhang, R. Tan, H. Gu, C. Sheng, C. Duan, P. Xing, and J. H. Wan. Planar chiral charge-transfer cyclophanes: Convenient synthesis, circularly polarized light-responsive photothermal conversion and supramolecular chiral assembly. *Angewandte Chemie International Edition*, 2024. doi:10.1002/anie.202413295.
- [10] M. L. Williams, A. F. Coleman, K. R. Peinkofer, R. M. Young, and M. R. Wasielewski. Structure-enabled long-lived charge separation in single crystals of an asymmetric donor–acceptor perylenediimide cyclophane. *Chemical Science*, 15(29):11472–11479, 2024. doi: 10.1039/d4sc03359k.
- [11] P. G. Ghasemabadi, T. Yao, and G. J. Bodwell. Cyclophanes containing large polycyclic aromatic hydrocarbons. *Chemical Society Reviews*, 44(18):6494–6518, 2015. doi: 10.1039/c5cs00274e.

- [12] M. Watanabe, K. Goto, M. Shibahara, and T. Shinmyozu. Synthesis, structure, and electronic and photophysical properties of two- and three-layered [3.3]paracyclophane-based donor–acceptor systems. *Journal of Organic Chemistry*, 75(18):6104–6114, 2010. doi: 10.1021/jo100688m.
- [13] Y. J. Chang, M. Watanabe, P. T. Chou, and T. J. Chow. [2.2]paracyclophane as a bridging unit in the design of organic dyes for sensitized solar cells. *Chemical Communications*, 48(5):726–728, 2012. doi: 10.1039/c1cc16248a.
- [14] S. V. Bhosale, M. Al Kobaisi, R. W. Jadhav, P. P. Morajkar, L. A. Jones, and S. George. Naphthalene diimides: Perspectives and promise. *Chemical Society Reviews*, 50(17):9845–9998, 2021. doi: 10.1039/d0cs00239a.
- [15] A. Diac, M. Matache, I. Grosu, and N. D. Hădade. Naphthalenediimide – a unique motif in macrocyclic and interlocked supramolecular structures. *Advanced Synthesis & Catalysis*, 360(5):817–845, 2018. doi: 10.1002/adsc.201701362.
- [16] M. Al Kobaisi, S. V. Bhosale, K. Latham, A. M. Raynor, and S. V. Bhosale. Functional naphthalene diimides: Synthesis, properties, and applications. *Chemical Reviews*, 116(19):11685–11796, 2016. doi: 10.1021/acs.chemrev.6b00160.
- [17] P. Gawrys, D. Djurado, J. Rimarčík, A. Kornet, D. Boudinet, J. M. Verilhac, V. Lukeš, I. Wielgus, M. Zagorska, and A. Pron. Effect of n-substituents on redox, optical, and electronic properties of naphthalene bisimides used for field-effect transistors fabrication. *Journal of Physical Chemistry B*, 114(5):1803–1809, 2010. doi: 10.1021/jp908931w.
- [18] N. Kumari, S. Naqvi, and R. Kumar. Naphthalene diimide self-assembled ribbons with high electrical conductivity and mobility without doping. *Journal of Materials Science*, 53(6):4046–4055, 2018. doi: 10.1007/s10853-017-1829-4.
- [19] L. Tan, G. Zhang, D. Zhang, and D. Zhu. Linear and cyclic tetrathiafulvalene–naphthalenediimide donor–acceptor molecules: Metal ions-promoted electron transfer. *Journal of Organic Chemistry*, 76(21):9046–9052, 2011. doi: 10.1021/jo201802p.
- [20] X. Peng, L. Wang, and S. Chen. Donor–acceptor charge transfer assemblies based on naphthalene diimides (ndis). *Journal of Inclusion Phenomena and Macrocyclic Chemistry*, 99(3–4):131–154, 2021. doi: 10.1007/s10847-021-01044-y.
- [21] S. K. Keshri, A. Takai, T. Ishizuka, T. Kojima, and M. Takeuchi. Conformational dynamics of monomer- versus dimer-like features in a naphthalenediimide-based conjugated cyclophane. *Angewandte Chemie International Edition*, 59(13):5254–5258, 2020. doi: 10.1002/anie.201914414.
- [22] S. K. Keshri, T. Ishizuka, T. Kojima, Y. Matsushita, and M. Takeuchi. Long-range order in supramolecular  $\Pi$  assemblies in discrete multidecker naphthalenediimides. *Journal of the American Chemical Society*, 143(8):3238–3244, 2021. doi: 10.1021/jacs.0c13389.

- [23] M. Tominaga, M. Kawahata, T. Itoh, and K. Yamaguchi. Spherical aggregates and crystal structure of naphthalenediimide-based macrocycle and complexation with perylene. *Crystal Growth & Design*, 18(1):37–41, 2018. doi: 10.1021/acs.cgd.7b01361.
- [24] S. Gabutti, M. Knutzen, M. Neuburger, G. Schull, R. Berndt, and M. Mayor. A rigid sublimable naphthalenediimide cyclophane as model compound for uhv stm experiments. *Chemical Communications*, pages 2370–2372, 2008. doi: 10.1039/b719796a.
- [25] F. Matino, G. Schull, F. Köhler, S. Gabutti, M. Mayor, and R. Berndt. Electronic decoupling of a cyclophane from a metal surface. *Proceedings of the National Academy of Sciences*, 108(3):961–964, 2011. doi: 10.1073/pnas.1006661107.
- [26] N. L. Schneider, F. Matino, G. Schull, S. Gabutti, M. Mayor, and R. Berndt. Light emission from a double-decker molecule on a metal surface. *Physical Review B*, 84(15):153403, 2011. doi: 10.1103/PhysRevB.84.153403.
- [27] S. Gabutti, S. Schaffner, M. Neuburger, M. Fischer, G. Schäfer, and M. Mayor. Planar chiral asymmetric naphthalenediimide cyclophanes: Synthesis, characterization and tunable fret properties. *Organic & Biomolecular Chemistry*, 7(16):3222–3229, 2009. doi: 10.1039/b905945h.
- [28] A. Das and S. Ghosh. Stimuli-responsive self-assembly of a naphthalene diimide by orthogonal hydrogen bonding and its coassembly with a pyrene derivative by a pseudo-intramolecular charge-transfer interaction. *Angewandte Chemie*, 126(4):1110–1115, 2014. doi: 10.1002/ange.201308396.
- [29] H. R. Yang, Y. Y. Chen, H. S. Sun, S. H. Tung, S. L. Huang, P. C. Huang, J. J. Lee, and Y. Y. Lai. Strengthening the intrachain interconnection of polymers by the naphthalene diimide–pyrene complementary interactions. *Macromolecules*, 54(15):7282–7290, 2021. doi: 10.1021/acs.macromol.1c00308.
- [30] K. Jalani, M. Kumar, and S. J. George. Mixed donor–acceptor charge-transfer stacks formed via hierarchical self-assembly of a non-covalent amphiphilic foldamer. *Chemical Communications*, 49(45):5174–5176, 2013. doi: 10.1039/c3cc41911h.
- [31] M. P. Parker, C. A. Murray, L. R. Hart, B. W. Greenland, W. Hayes, C. J. Cardin, and H. M. Colquhoun. Mutual complexation between  $\pi$ - $\pi$  stacked molecular tweezers. *Crystal Growth & Design*, 18(1):386–392, 2018. doi: 10.1021/acs.cgd.7b01376.
- [32] M. D. Gujrati, N. S. S. Kumar, A. S. Brown, B. Captain, and J. N. Wilson. Luminescent charge-transfer complexes: Tuning emission in binary fluorophore mixtures. *Langmuir*, 27(11):6554–6558, 2011. doi: 10.1021/la2012809.
- [33] H. A. Staab, D.-Q. Zhang, and C. Krieger. [3](n,n’)-1,8;4,5-naphthalenetetracarboxdiimido-[3](2,7)pyrenophane and its [4,4] cyclophane homologue. *Liebigs Annalen der Chemie*, pages 1551–1556, 1997.

- [34] A. G. Crawford, A. D. Dwyer, Z. Liu, A. Steffen, A. Beeby, L. O. Pålsson, D. J. Tozer, and T. B. Marder. Experimental and theoretical studies of the photophysical properties of 2- and 2,7-functionalized pyrene derivatives. *Journal of the American Chemical Society*, 133(34): 13349–13362, 2011. doi: 10.1021/ja2006862.
- [35] J. Merz, J. Fink, A. Friedrich, I. Krummenacher, H. H. Al Mamari, S. Lorenzen, M. Haehnel, A. Eichhorn, M. Moos, M. Holzapfel, H. Braunschweig, C. Lambert, A. Steffen, L. Ji, and T. B. Marder. Pyrene molecular orbital shuffle—controlling excited state and redox properties by changing the nature of the frontier orbitals. *Chemistry—A European Journal*, 23(53): 13164–13180, 2017. doi: 10.1002/chem.201702594.
- [36] R. Kurata, K. Tanaka, and A. Ito. Isolation and characterization of persistent radical cation and dication of 2,7-bis(dianisylamino)pyrene. *Journal of Organic Chemistry*, 81(1):137–145, 2016. doi: 10.1021/acs.joc.5b02425.
- [37] D. Jana and S. Jana. Donor-pyrene-acceptor distance-dependent intramolecular charge-transfer process: A state-specific solvation preferred to the linear-response approach. *ACS Omega*, 5(17):9944–9956, 2020. doi: 10.1021/acsomega.0c00265.
- [38] S. S. Li, K. J. Jiang, C. C. Yu, J. H. Huang, L. M. Yang, and Y. L. Song. A 2,7-pyrene-based dye for solar cell application. *New Journal of Chemistry*, 38(9):4404–4408, 2014. doi: 10.1039/c4nj00421c.
- [39] R. Kurata, A. Ito, M. Gon, K. Tanaka, and Y. Chujo. Diarylamino- and diarylboryl-substituted donor–acceptor pyrene derivatives: Influence of substitution pattern on their photophysical properties. *Journal of Organic Chemistry*, 82(10):5111–5121, 2017. doi: 10.1021/acs.joc.7b00315.
- [40] B. R. Kaafarani, C. Risko, T. H. El-Assaad, A. O. El-Ballouli, S. R. Marder, and S. Barlow. Mixed-valence cations of di(carbazol-9-yl) biphenyl, tetrahydropyrene, and pyrene derivatives. *Journal of Physical Chemistry C*, 120(6):3156–3166, 2016. doi: 10.1021/acs.jpcc.5b11061.
- [41] B. R. Kaafarani, A. O. El-Ballouli, R. Trattnig, A. Fonari, S. Sax, B. Wex, C. Risko, R. S. Khnayzer, S. Barlow, D. Patra, T. V. Timofeeva, E. J. W. List, J.-L. Brédas, and S. R. Marder. Bis(carbazolyl) derivatives of pyrene and tetrahydropyrene: Synthesis, structures, optical properties, electrochemistry, and electroluminescence. *Journal of Materials Chemistry C*, 1(8):1638–1650, 2013. doi: 10.1039/c2tc00474g.
- [42] Edoardo Cignoni, Vladislav Slama, Lorenzo Cupellini, and Benedetta Mennucci. The atomistic modeling of light-harvesting complexes from the physical models to the computational protocol. *The Journal of Chemical Physics*, 156(12):120901, 2022. doi: 10.1063/5.0086275.
- [43] Michele Nottoli, Sandro Jurinovich, Lorenzo Cupellini, Alastair T. Gardiner, Richard Cogdell, and Benedetta Mennucci. The role of charge-transfer states in the spectral tuning of antenna complexes of purple bacteria. *Photosynthesis Research*, 137(2):215–226,



- Aug 2018. doi: 10.1007/s11120-018-0492-1. URL <https://doi.org/10.1007/s11120-018-0492-1>.
- [44] Roman G. Fedunov, Anastasiia V. Plotnikova, Anatoly I. Ivanov, and Eric Vauthey. Simulations of the ultrafast transient absorption dynamics of a donor–acceptor biaryl in solution. *The Journal of Physical Chemistry A*, 121(2):471–481, 2017. doi: 10.1021/acs.jpca.6b11581. URL <https://doi.org/10.1021/acs.jpca.6b11581>. PMID: 28010064.
- [45] Muhammad Imran, Huaiman Cao, Jianzhang Zhao, and Gloria Mazzone. Does twisted molecular structure always induce intersystem crossing? a case study with near-ir absorbing 1,8-diazabicyclo[5.4.0]undec-7-ene-fused naphthaldiimide. *The Journal of Physical Chemistry A*, 127(22):4856–4866, 2023. doi: 10.1021/acs.jpca.3c02161. URL <https://doi.org/10.1021/acs.jpca.3c02161>. PMID: 37226449.
- [46] M. Raytchev, E. Pandurski, I. Buchvarov, C. Modrakowski, and T. Fiebig. Bichromophoric interactions and time-dependent excited state mixing in pyrene derivatives. a femtosecond broad-band pump-probe study. *The Journal of Physical Chemistry A*, 107(23):4592–4600, 2003. doi: 10.1021/jp027356c. URL <https://doi.org/10.1021/jp027356c>.

# Chapter 7

## Conclusion and Outlook

### Conclusion

This thesis presents a contribution towards the goal of realizing molecular electronic devices, specifically focusing on the potential of donor-acceptor (D-A) paracyclophanes (PCPs) as molecular switches and manipulated by terahertz (THz) electric fields. Achieving this objective requires a detailed understanding of both the interaction between THz fields and molecular systems and the intrinsic properties of the PCPs. This work addressed these prerequisites through complementary spectroscopic investigations.

Firstly, time-resolved THz Stark spectroscopy was employed to understand the fundamental interactions between THz electric fields and molecules in solution. The studies described in Chapter 3 demonstrated the capability of it to extract the electronic properties of donor-acceptor (D-A) type molecule, such as TTF-BTD, in nonpolar solvents. This work successfully provided quantitative measurements of key parameters like the change in dipole moment ( $\Delta\mu$ ) and polarizability ( $\text{Tr}(\Delta\alpha)$ ), demonstrating the applicability of the technique for this type of molecules. Subsequently, Chapter 4 extended the application of time-resolved THz Stark spectroscopy, demonstrating its feasibility and robustness even in the challenging environment of a highly polar solvent like water.

Secondly, the optical characterization of newly synthesized PCP systems, designed as potential molecular building blocks, was performed using Transient Absorption Spectroscopy (TAS) combined with theoretical modeling. Chapter 5 focused on homo-PCPs (NDI-NDI and Pyrene-Pyrene), providing insights into fundamental processes like excimer formation dynamics in stacked  $\pi$ -systems, while also validating the theoretical framework used. Building on this, Chapter 6 investigated the D-A hetero-PCPs (NDI-Pyrene). TAS measurements revealed the ultrafast dynamics of intramolecular charge transfer (ICT). These studies demonstrated that the kinetics and pathways of ICT are systematically tunable by modifying the molecular linker structure, which dictates the D-A separation and orientation.

In summary, this thesis provides two critical sets of foundational insight. The time-resolved THz Stark Spectroscopy investigations (Chapters 3 and 4) contributed to essential experience and understand that how THz fields interact with molecules, particularly D-A systems, in solution. Complementarily, the TAS and theoretical studies (Chapters 5 and 6) delivered a detailed charac-

terization of the excited state and ICT dynamics of the D-A PCPs, quantifying key parameters such as state lifetimes and relaxation pathways.

### Outlook

The immediate next step is the deposition of the characterized PCP systems onto conductive surfaces under ultra-high vacuum conditions. The detailed solution-phase dynamics, including charge transfer state lifetimes and relaxation pathways determined through TAS and theoretical modeling, serve as a baseline. Understanding how the molecule-surface interaction modifies these properties is essential. Techniques, such as Scanning Tunneling Microscopy (STM) and Atomic Force Microscopy (AFM), will be valuable for determining adsorption geometries, probing the local electronic structure, and assessing the influence of substrate coupling on the excited state dynamics previously studied in solution. Following successful surface characterization, the goal is to achieve coherent control over the intramolecular charge transfer states of individual PCP molecules using THz pulses. The envisioned experimental framework integrates these elements into a THz-STM setup. In this advanced configuration, THz pulses could deliver a localized, ultrafast voltage bias to a single adsorbed molecule. Synchronizing THz excitation with STM probing capabilities could enable the direct triggering and observation of switching between molecular states (e.g., neutral and ICT states).

Extending these investigations to molecules on surfaces will be a key step toward exploring THz-induced phenomena in molecular assemblies on surfaces relevant to molecular electronics. Furthermore, achieving precise quantum control over molecular states on surfaces could open opportunities in quantum information science, where the bi-stable states of these D-A molecules might serve as novel platforms for qubits. This thesis establishes a first step, providing the fundamental spectroscopic insight into molecular dynamics required as a prerequisite for any future attempt at coherent control on surfaces.